UNIVERSITY OF SOUTHAMPTON

Dynamic Light Scattering and Freedericksz Transition in Novel Nematic Liquid Crystals

Author: Cécile Schott

A thesis submitted for the degree of Doctor of Philosophy
Department of Physics and Astronomy
Faculty of Science
June 2002

UNIVERSITY OF SOUTHAMPTON

ABSTRACT

FACULTY OF SCIENCE

PHYSICS AND ASTRONOMY

Doctor of Philosophy

DYNAMIC LIGHT SCATTERING AND FREEDERICKSZ TRANSITION IN NOVEL NEMATIC LIQUID CRYSTALS

Cécile Schott

This thesis describes the implementation of two well-known experimental techniques, dynamic light scattering (DLS) and Freedericksz transition (FT), to measure the visco-elastic properties of a wide variety of nematic liquid crystalline systems.

In this work, DLS in the presence of an electric field is used to determine the twist k_{22} and splay k_{11} elastic constants as well as the rotational viscosity coefficient γ_1 of materials with positive dielectric anisotropy $\Delta\varepsilon$. FT experiments are performed in some cases to obtain the bend elastic constant k_{33}; using the bend visco-elastic ratios measured by DLS, it is therefore possible to deduce the bend viscosity η_{bend}. Static dielectric constants and associated anisotropy $\Delta\varepsilon$, required in both methods, are measured separately. The nematic orientational order parameter is calculated from refractive index data.

After calibration, the DLS technique is applied to evaluate the visco-elastic parameters for a series of mixtures, which differ in their chemical nature and thus exhibit different optical anisotropies. Then, the values of k_{22} and γ_1 are measured for mesogenic and non-mesogenic guest molecules added to a commercial host mixture in order to improve the in-plane switching mode.

In the next part, the influence of dichroic dopants on the visco-elastic constants and on the order parameter of the host is investigated for low concentrations of azo and anthraquinone dyes dissolved in 5CB. The temperature dependence of k_{11}, k_{22} and γ_1 is discussed for the series containing azo dye. The bend elastic constant and corresponding viscosity are determined for the anthraquinone dye guest-host samples. The data for the dichroic ratio and dye's order parameter are also included for the two dyes.

The nematic materials, studied in the final section, are characterised by a dielectric anisotropy $\Delta\varepsilon$, which changes sign either as a function of frequency or temperature. To illustrate the first case, mixtures of a novel phenylbenzoate compound in a neutral host are found to behave as 'dual-frequency' materials for a certain range of concentration. The dielectric, optical and visco-elastic properties are measured for the pure host mixture. The second case refers to mixtures of new symmetrical difluorobiphenyl bimesogens, characterised by low $\Delta\varepsilon$. These dimers present improved switching for the flexoelectro-optic effect in short pitch chiral nematics. Dielectric and DLS experiments are carried out on these systems. For the two types of materials, the measurements of $\Delta\varepsilon$ are performed on chiral-doped samples because of the difficulty to align them homeotropically.

TABLE OF CONTENTS

DECLARATION

This thesis is the work done by the author whilst in registered postgraduate candidature at the University of Southampton. Most of the work presented in this thesis is original and has not been submitted in support of an application for another degree or qualification at this or any other university or institution of learning. Results obtained in collaboration with others are clearly indicated and have been submitted by them for another degree.

ACKNOWLEDGEMENTS

I would like to express my gratitude to the following people without whom the work presented in this thesis would not have been possible:

First of all, my supervisor Prof. Harry Coles for his continuous support and for giving me the opportunity to work within in his research group.

Dr. Carlo Carboni for his encouragement during my first year and for his enthusiasm in the lab.

Dr. Seb Meyer for his useful advice in many experimental issues in particular on good clean room practice and for his help on setting up the Freedericksz transition experiment.

Dr. Bronje Musgrave for improving my English during our crossword lunches, for valuable comments on the thesis manuscript and most importantly for her friendship.

Marcus Coles, Dean Shoosmith and Matt Clarke for their patience in solving my numerous IT problems and explaining to me how a computer works!

Dr. Steve Perkins and Dr. Andrew Blatch for synthesising the dual-frequency material and the homologous series of dimers; Dr. Doina Ionescu from Merck for providing different nematic mixtures.

Dr. Noboru Kunimatsu from Hitachi for a fruitful and enjoyable collaboration using DLS.

Leona Hope for assistance in all sorts of admin matters; I am also grateful to Colin, Vince, Chad and all the staff from the Physics workshop in particular Mark for showing me that the machines there do not bite and Erik for great discussion on samba, capoeira and salsa.

I would like to acknowledge the University of Southampton for a three-year studentship and Toshiba for supplying the dye guest-host samples as well as financial support

A special thank to all the other past or present members of the group for their kindness and their support during my PhD and the write-up stage: Wendy, Petra, Chris, Anna, Piers, Jon, Steve M, Yong-Il, Mikhail and Oliver.

I would like to thank all my housemates for their friendship and for being so understanding, in particular a big thank to Cosmin, Ana Paula and Susana, who have shared with me the ups and downs of life as a PhD student.

Thank to all my friends from Soton and from France, especially to Alice (Dr. D.), who showed me that everything is possible.

At last but not least, un grand merci à ma famille pour leur soutien moral et pour leurs encouragements.

CHAPTER 1: INTRODUCTION

1.1 Definitions[1]

Liquid crystals (referred to as LCs) represent an intermediate state of matter between a solid crystal and an isotropic liquid that is observed in some organic materials. The LC phase, also called *mesomorphic phase* or *mesophase*, is characterised by the absence or partial reduction of positional order while orientational order is still present to some extent. This results for the mesophase in an interesting combination of anisotropic properties with a certain degree of fluidity. Liquid crystals can be classified as *thermotropic* mesophases, that are formed by changing the temperature of a compound and *lyotropic* mesophases, that occur by dissolving an appropriate concentration of surfactant or amphiphilic molecules in a solvent. An *enantiotropic* mesophase is thermodynamically stable over a certain range of temperature (defined by the *melting point* and the *clearing point* of the material) and pressure. A molecule that forms LC phases is known as a *mesogen* and a molecular group that promotes the existence of mesophases is called a *mesogenic unit*. The main requirement for the formation of liquid crystalline phases is a pronounced shape anisotropy of their constituent molecules, which can be either rod-like (*calamitic*) or disc-like (*discotic*). The work presented in this thesis is primarily focused on the properties of thermotropic calamitic liquid crystals.

Calamitic LCs are composed of elongated molecules, which generally consist of a rigid core unit with a flexible alkyl chain attached at one end and which typically have a length-to-width ratio of four to one or greater.[2] These molecules can form a diversity of mesophases that display varying degrees of orientational and positional order.

A *liquid crystal oligomer* contains more than one mesogenic group, each of which is sometimes designated as monomer; in the course of this work both the terms *dimers* and *bimesogens* will be used interchangeably to describe a LC oligomer with two mesogenic groups separated by a flexible spacer. By contrast with *LC polymers*, compounds with a single mesogenic unit are referred to as *low-molar mass LCs*.

Section 1.2 introduces the most common liquid crystalline phases i.e. the nematic and the principal smectic phases. The anisotropic nature of the different physical properties of the nematic phase is discussed in Section 1.3; then the concept of orientational order parameter is defined and related to the macroscopic parameters that can be measured experimentally. Finally, the work presented in this thesis is outlined in Section 1.4 of this chapter.

1.2 Description of the principal liquid crystalline phases

1.2.1 The nematic phase

In the nematic phase (abbreviated as N), the rod-shaped molecules are oriented on average with their long axes parallel to each other but without long-range translational correlation between their centres of mass. The local direction of alignment or preferred axis can be described by introducing a unit vector **n** called the director. A uniformly aligned nematic sample exhibits macroscopically rotational symmetry about the director and is said to be uniaxial. Furthermore, the axis of uniaxial symmetry has no polarity and thus **n** = -**n**. The nematic phase and the director **n** are illustrated in Figure 1.1.

Optically active molecules may form a chiral nematic phase, denoted as N^*, characterised by a spontaneous twist of the director in addition to the long-range orientational order. A schematic diagram of the chiral nematic phase is sketched in Figure 1.2. The local arrangement of the molecules is similar to the nematic phase within any plane normal to the helical axis. The main difference is that the direction of preferred orientation is slightly rotated in adjacent planes and the director **n** is given by:[2, 3, 4]

$$\begin{aligned} n_x &= \cos\phi, \\ n_y &= \sin\phi, \\ n_z &= 0. \end{aligned} \tag{1.1}$$

In this case, the director is confined to the (x, y) plane and its direction rotates about the helical axis, which is parallel to the z-axis. The rotation angle ϕ can be related to the natural pitch of the helix P_0 using the following equation:

$$\phi = \frac{2\pi}{P_0} z. \tag{1.2}$$

P_0 is chosen positive for a right-handed helix and negative for a left-handed helix. The pitch is several orders of magnitude greater than the molecular dimensions with typical values ranging from 0.2 μm to infinity for the nematic phase. Therefore, the local order is nematic. The energy associated with the twisted structure represents only a small fraction of the total energy associated with the parallel alignment of the molecules and a small quantity of chiral compound is sufficient to produce a chiral nematic phase.

Some chiral nematic materials with short pitch (less than 0.5 μm) may also form blue phases, which exist over a small temperature interval of about 1 °C between the chiral nematic and the isotropic phases.[3] There are three different types of blue phases BP I, BP II and BP III, occurring in this order as the temperature is increased. These phases are optically active but optically isotropic.

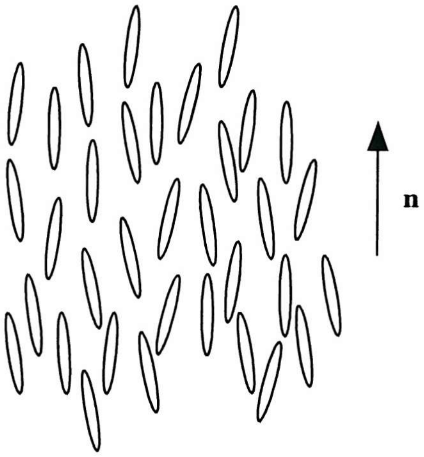

Figure 1.1: Schematic diagram of the nematic phase.

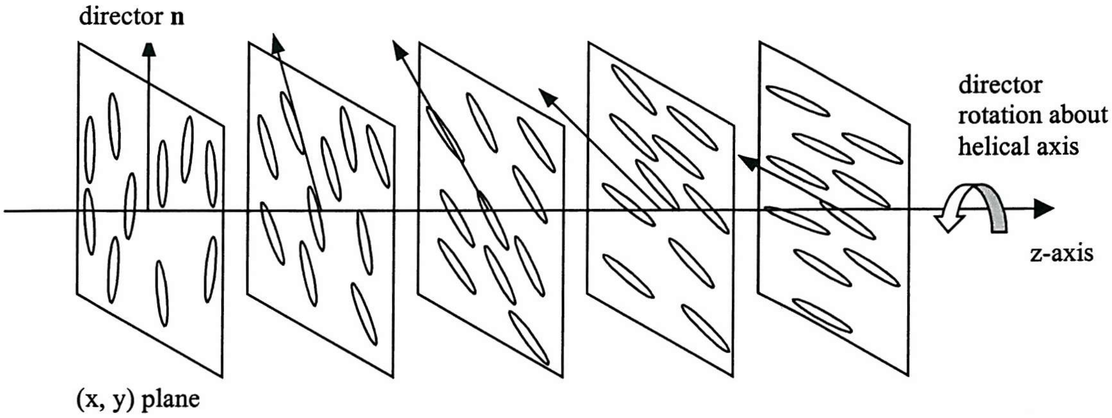

Figure 1.2: Schematic representation of the chiral nematic phase.

1.2.2 The smectic phases

The smectic phases possess stratified structures, characterised by a density distribution function and an additional translational order. Consequently, they are usually more viscous than the nematic phase. There are several possible molecular arrangements within the layers; as a result, over a dozen smectic mesophases have been identified.

The least ordered smectic phase is the smectic A phase, which is also referred to as S_A, and is shown in Figure 1.3 (a); in the S_A phase, the director lies perpendicular to the layers and behave like a two-dimensional liquid in the plane of the layers. The smectic C (S_C), illustrated in Figure 1.3 (b) is similar to the S_A phase except that the director is tilted at a temperature-dependent angle with respect to the layer normal.

By analogy, chiral molecules may form a chiral smectic A^* (S_A^*) or C^* (S_C^*) phases. The S_C^* phase, depicted schematically in Figure 1.4, has a helical structure with the molecules precessing about the layer normal and it is characterised by remarkable ferroelectric properties when aligned in a surface stabilised geometry due to the existence of a spontaneous dipole moment as the helix is suppressed.

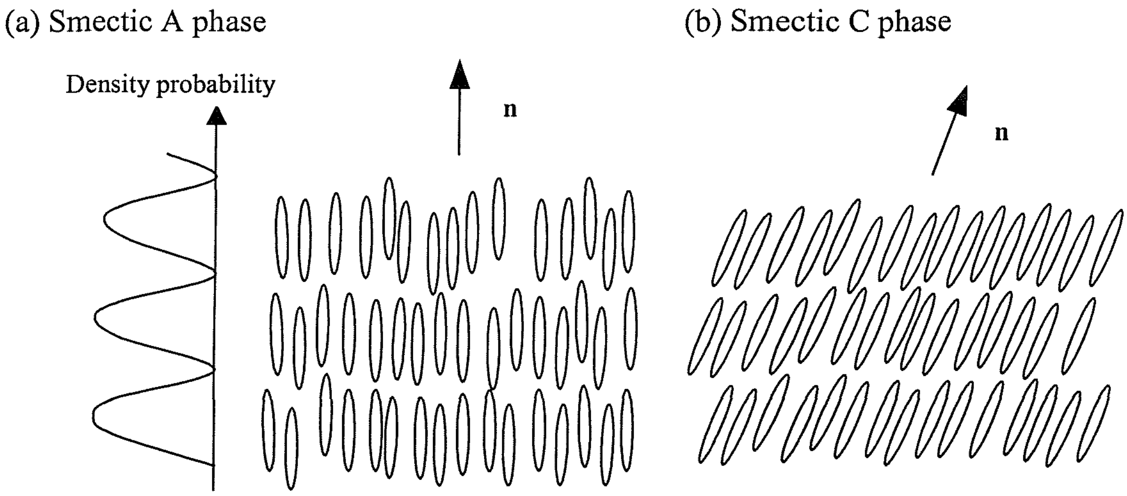

Figure 1.3: Schematic representation of the different smectic phases

(a) S_A (b) S_C.

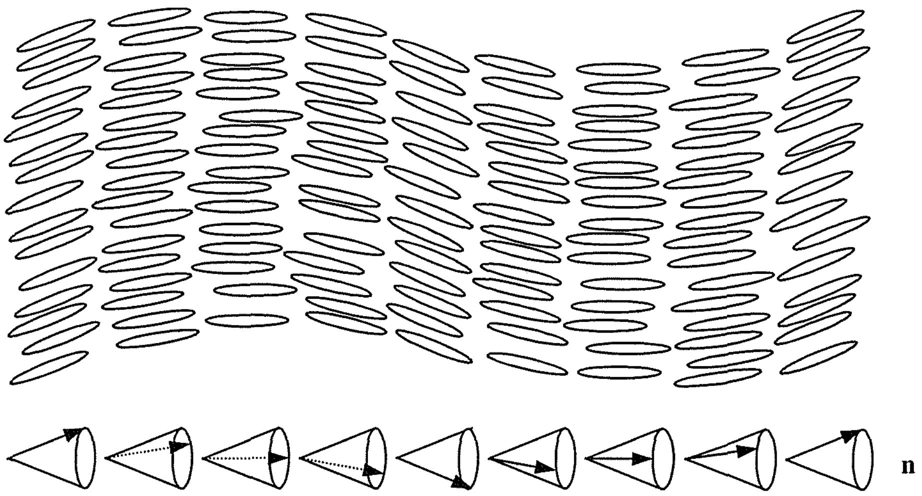

Figure 1.4: Schematic structure of the molecular arrangement and associated director pattern in the S_C* phase.

1.3 Physical properties of nematic liquid crystals

1.3.1 Anisotropic nature

Some of the anisotropic macroscopic properties of mesophases can be represented by using second-rank tensors or 3 x 3 matrices. These tensors can be further simplified by taking into account the unixial nature of the nematic phase, which exhibits cylindrical symmetry about the director **n**; as a consequence, they have only two independent components.[5] For instance, in a Cartesian coordinate system with the z-axis parallel to the director **n**, the tensors describing the magnetic susceptibility and the dielectric permittivity properties are respectively

$$\underline{\underline{\chi}} = \begin{pmatrix} \chi_\perp & 0 & 0 \\ 0 & \chi_\perp & 0 \\ 0 & 0 & \chi_\parallel \end{pmatrix} \tag{1.3}$$

$$\text{and} \quad \underline{\underline{\epsilon}} = \begin{pmatrix} \varepsilon_\perp & 0 & 0 \\ 0 & \varepsilon_\perp & 0 \\ 0 & 0 & \varepsilon_\parallel \end{pmatrix}, \tag{1.4}$$

where the subscripts $\parallel$ and $\perp$ refer to the component parallel and perpendicular to the director.

It is also useful to introduce two physical quantities, namely the anisotropy and the mean value of the property, which in the case of the magnetic susceptibility are expressed as

$$\Delta\chi = \chi_{\parallel} - \chi_{\perp} \tag{1.5}$$

and $$\bar{\chi} = \frac{1}{3}(\chi_{\parallel} + 2\chi_{\perp}). \tag{1.6}$$

The relation between the macroscopic dielectric permittivities and the microscopic parameters will be established in Chapter 2, Section 2.3. The magnetic and dielectric anisotropies allow the reorientation of the liquid crystal's molecules by externally applied fields; this coupling will be discussed in Chapter 2, Section 2.5.

Refractive indices

Nematic liquid crystals are uniaxial positive birefringent materials: their unique axis of symmetry, the optic axis, is parallel to the director **n**. Thus, the polarisation components of light propagating in a direction along the optic axis experience the same refractive index and therefore they remain unchanged. Strong double refraction occurs when the light propagates within the birefringent medium in a direction perpendicular to the optic axis; its polarisation vector can be decomposed into components parallel and normal to the optic axis, which see different refractive indices. A single ray may be split into two beams of different polarisations.

The optical properties of liquid crystals can be described by three independent principal refractive indices, which form a refractive index ellipsoid also called optical indicatrix.[5] For a uniaxial phase, there are only two independent refractive indices; in a Cartesian coordinate system with the optic axis taken along the z-axis, we have $n_z = n_e$ and $n_x = n_y = n_o$, where n_e and n_o are the extraordinary and ordinary refractive indices. The equation for the ellipsoid becomes

$$\frac{x^2}{n_o^2} + \frac{y^2}{n_o^2} + \frac{z^2}{n_e^2} = 1. \tag{1.7}$$

The refractive indices of nematic liquid crystals range typically from 1.4 to 1.9 and the associated birefringence varies from 0.02 to 0.5.[5]

1.3.2 Orientational order parameter

As mentioned in 1.2.1, the director **n** defines the preferred direction of the molecules. However, it does not contain any information about the degree of orientational order of the liquid crystalline phase. Its constituent molecules usually experience thermal fluctuations, collisions and intermolecular interactions. In the nematic phase, the long-range orientational order parameter S is defined in the following manner:[2, 3, 4]

$$S = \frac{1}{2}\left\langle 3\cos^2\theta - 1\right\rangle, \qquad \textbf{(1.8)}$$

where θ is the angle between the long axis of a molecule and the director **n**. The angular brackets denote a thermal average and the mesogenic molecules are assumed to behave as rigid rods.

$S = 1$ in a perfect crystal with no thermal fluctuations, whereas $S = 0$ in an isotropic liquid with randomly oriented molecules. The order parameter increases with decreasing temperature: in the nematic phase, its values vary between 0.3 in the vicinity of the isotropic transition and 0.8 at lower temperatures.[4] While in the smectic phases, S may be as high as 0.9.[3]

In principle, the orientational order parameter S can be determined from any anisotropic property. There are two ways commonly used to calculate the order parameter. S can be determined from experimental refractive index data using various extrapolation methods, such as Haller's analysis technique. This particular procedure will be explained in Chapter 2, Section 2.2. S is also directly related to the magnetic susceptibility $\Delta\chi$, since this physical quantity remains unaffected by molecular interactions.[2] In this case,

$$S \propto \Delta\chi = \chi_{\parallel} - \chi_{\perp}\,. \qquad \textbf{(1.9)}$$

1.4 Outline of the work presented in this thesis

In this chapter, the most important liquid crystalline phases have been presented. The nematic phase is a birefringent uniaxial phase which possesses cylindrical symmetry about the director **n**. Its macroscopic properties, such as the magnetic susceptibility and the dielectric permittivity, are described by the use of second-rank tensors. Its optical behaviour depends on the extraordinary and ordinary refractive indices. The orientational order parameter of the nematic phase has been defined microscopically and has been related to the magnetic susceptibility anisotropy.

Chapter 2 begins with a description of an extrapolation procedure widely employed to calculate the order parameter from refractive index data. The static dielectric permittivities are discussed using Maier and Meier's theory and the elastic constants are introduced in the context of curvature elasticity developed by Frank. After a short review of fluid dynamics in isotropic liquids, the Miesowicz viscosity coefficients are defined for nematic LCs. The reorientation of molecules in magnetic or electric fields, known as Freedericksz transition, is considered and the expressions for the threshold fields are established in both instances. In dynamic light scattering, the time variation of the scattered field is derived in the context of the electro-magnetic theory and is directly related to fluctuations in the optical dielectric tensor; these fluctuations arise from two modes associated with director distortions. Therefore, the visco-elastic constants of the materials can be directly measured from the linewidth of the autocorrelation function in DLS experiments using specific scattering geometries and a quenching electric field.

Freedericksz transition and dynamic light scattering can be implemented to determine the visco-elastic constants of nematic liquid crystals. This is explained in Chapter 3 alongside with a detailed description of both experiments. Dielectric constants and refractive indices, which are required to calculate the visco-elastic parameters, are measured respectively by a capacitance method and using an Abbé refractometer. This chapter also includes the methods for preparation of uniformly aligned nematic samples and their characterisation.

In Chapter 4, the procedure followed to align the DLS spectrometer is described as well as the calibration of the apparatus using a well-known nematic material, namely 4-pentyl 4'-cyanobipnenyl, known as 5CB. The evaluation of the DLS technique is carried out by measuring the splay and twist visco-elastic parameters for a series of mixtures, based on cyanobiphenyls (A), phenylbenzoates (B) and dicyclohexyls (C). Their different chemical compositions result in different polarities, birefringences and viscosity coefficients. The last part of this chapter is devoted to the measurement of the twist elastic constant and viscosity for a mixture with different additives for the improvement of the in-plane switching mode (IPS).[6] The host mixture chosen is a commercial mixture

ZLI-4792 and the four dopants investigated contain either phenylcyclopentenone or cyanobiphenyl moities.

Chapter 5 is dedicated to the study of novel dye guest-host nematic mixtures (DGH), which consist of a few percent azo or anthraquinone dyes dissolved in 5CB. First, we define D as the dichroic ratio and S_{Tcorr} as the corrected order parameter of the transition moment for the dye's absorption. The next section shows the influence of the two dyes on the splay and twist visco-elastic constants of the host. The temperature dependence of these parameters is examined for the azo-doped samples. It is interesting to compare the values of S_{Tcorr} and D obtained for the two dyes with similar systems reported in the literature. The bend elastic constant and viscosity coefficient are measured for the anthraquinone DGH mixtures by combining both DLS and FT techniques.

Chapter 6 deals with more complex nematic systems, which exhibit a sign reversal in $\Delta\varepsilon$. These materials do not align homeotropically using conventional surfactants. Consequently, the dielectric constants are measured using chiral-doped mixtures in two specific configurations. The second part of this chapter reports on the measurement of dielectric anisotropy for the "dual-frequency" compound 4-n-pentylphenyl 2-fluoro-4-(4-n-pentylbenzoyloxy) benzoate (referred to as 5PFP5) dissolved in different concentrations in a nematic host mixture, MDA-00-984, which is characterised by low and negative $\Delta\varepsilon$. An analogous material to 5PFP5 was found to exhibit a change of sign of its dielectric anisotropy $\Delta\varepsilon$ at the cross-over frequencies f_c between 1 and 20 kHz.[7] The next section is concerned with bimesogens for the flexoelectric effect in short pitch chiral nematics. In the uniformly lying helix geometry (ULH), an electric field applied across the cell causes a linear in-plane rotation of the optic axis.[8] Low dielectric anisotropy is necessary to avoid helix unwinding. High rotation angles have been achieved with the odd members of the series 4, 2'-difluorobiphenyl-4'-yloxyalkanes doped with a chiral additive.[9] The dielectric anisotropy and bend visco-elastic ratio are investigated for binary mixtures of bimesogens.

To conclude, Chapter 7 summarises the most important results of this work and gives an overview of future directions, in particular concerning the redesign of the light scattering apparatus and the developments of novel materials for the flexoelectric effect, including dye-doped bimesogenic systems.

REFERENCES

[1] Baron M., Definitions of Basic Terms Relating to Low-Molar Mass and Polymer Liquid Crystals (IUPAC Recommendations), *Pure Appl. Chem.*, **73(5)**, pp. 845-895 (2001)

[2] de Gennes P. G. and Prost J., *The Physics of Liquid Crystals*, 2nd edition, Oxford Science Publications, Oxford (1993)

[3] Chandrasekhar S., *Liquid Crystals*, 2nd edition, Cambridge University Press, Cambridge (1992)

[4] de Jeu W. H., *Physical Properties of Liquid Crystalline Materials*, Gordon and Breach, New-York (1980)

[5] Dunmur D. and Toriyama K., Chapter 7 in the *Handbook of Liquid Crystals*, **1**, pp. 189-280, edited by Demus D., Goodby J., Gray G. W., Spiess H-W. and Vill V., Wiley-VCH, New-York (1998)

[6] Coles H. J., Dunmur D. A., Kagawa H., Kondo K., Kunimatsu N., Luckhurst G. R. and Schott C., *Mol. Cryst. Liq. Cryst.*, **347**, pp. 157-166 (2000)

[7] Bücher H. K., Klingbiel R. T. and VanMeter J. P., *Appl. Phys. Lett.*, **25(4)**, pp. 186-188 (1974)

[8] Patel J. S. and Meyer R. B., *Phys. Rev. Lett.*, **58**, pp. 1538-1540 (1987)

[9] Musgrave B., Coles M. J., Perkins S. P. and Coles H. J., *Mol. Cryst. Liq. Cryst.*, Proceedings for ILCC Sendai 2000, **366**, pp. 735-742 (2001)

CHAPTER 2: THEORY

2.1 Introduction

The aim of this work is to investigate the visco-elastic properties of a wide-range of nematic liquid crystals, using two well-known experimental techniques, namely Freedericksz transition (FT) and dynamic light scattering (DLS). In the first case, a magnetic or electric field induces a reorientation of the director above a certain threshold; the elastic constants can be deduced from the measurement of this critical field. The second method relies upon the fact that light is scattered from the director fluctuations. By analysing the spectrum of scattered light, it is possible to determine the visco-elastic ratios of a given nematic material. In this chapter, we will review the key theoretical considerations, necessary to interpret the experimental data.

The beginning of this chapter relates the nematic orientational order parameter to measured refractive indices. In Section 2.3, static dielectric permittivities are explicitly introduced. In the following part, the elastic and viscous properties of nematics are discussed using the continuum theory. Section 2.5 describes the Freedericksz effect with external magnetic and electric fields. The next part is divided into six subsections grouped around two main themes: the general theory of DLS and the application of DLS to nematic liquid crystals. After presenting Rayleigh light scattering in subsection 2.6.1, time autocorrelation functions are defined in 2.6.2 and the different detection methods are outlined in 2.6.3. In nematic materials, light scattering arises from fluctuations in the optical dielectric constant tensor, which are in turn related to two modes of long-range distortions of the director pattern as will be shown in Section 2.6.4. In this case, the autocorrelation function represents the relaxation of those director modes and visco-elastic ratios can be deduced from DLS experiments in specific scattering geometries, detailed in subsection 2.6.5. Furthermore, individual elastic constants and viscosity coefficients can be derived if the measurements are performed in the presence of a stabilising electric field as explained in paragraph 2.6.6. In the last section 2.7, the experimental scattering configurations that isolate each fluctuation mode are defined.

2.2 Orientational order parameter and refractive indices

The nematic orientational order parameter S, introduced in Chapter 1 Section 1.3.2, may be obtained from refractive index data using Haller's extrapolation method.[1] This technique is founded on three assumptions:

1. Even in an anisotropic medium, the local field is isotropic. S is related to the refractive indices n_e and n_o via the relation

$$S\frac{\Delta\alpha}{\overline{\alpha}} = \frac{n_e^2 - n_o^2}{\overline{n^2} - 1}, \qquad \textbf{(2.1)}$$

   where $\overline{n^2} = (n_e^2 + 2n_o^2)/3$ is the mean refractive index, $\overline{\alpha} = (\alpha_{\parallel} + 2\alpha_{\perp})/3$ is the mean polarisability and $\Delta\alpha = \alpha_{\parallel} - \alpha_{\perp}$ is the polarisability anisotropy ($\Delta\alpha > 0$ for rod-like molecules[2]); $\alpha_{\parallel}$ and $\alpha_{\perp}$ are respectively the longitudinal and transverse components of the optical polarisability.

2. The extrapolation of the experimental data to absolute zero, which corresponds to S = 1, leads to $\Delta\alpha/\overline{\alpha}$.

3. The temperature dependence of the order parameter can be written as

$$S = \left(1 - \frac{T}{T^*}\right)^{\beta}. \qquad \textbf{(2.2)}$$

   T^* represents the temperature in Kelvin at which S would fall continuously to zero in the absence of a first order nematic-to-isotropic transition.

Combining Equations (2.1) and (2.2) results in the following expression

$$\log_{10}\left(\frac{n_e^2 - n_o^2}{\overline{n^2} - 1}\right) = \beta \log_{10}\left(1 - \frac{T}{T^*}\right) + \log_{10}\left(\frac{\Delta\alpha}{\overline{\alpha}}\right). \qquad \textbf{(2.3)}$$

The exponent β is quasi-universal and usually takes values between 0.17 and 0.23 while T^* depends on each material. Finally, S(T) is calculated from Equation (2.2).
It should be mentioned that the adjustable parameters T^* and β are independent of the wavelength at which refractive indices are measured[1] and no dispersion effects occur in the calculated order parameter S. For instance, refractive indices, measured experimentally at wavelengths ranging from 546.1 nm to 632.8 nm, yield values of S within 1%.[3]

Therefore, the accurate determination of S depends mainly on the fitting procedure employed and requires a quite broad temperature range i.e. ideally greater than 10-15°C.[1] Haller's analysis may give inconsistent and unreliable results close to the nematic-isotropic transition temperature since Equation (2.2) is not valid in the pretransitonal region.[4] In this work, the limitation of the Haller's extrapolation procedure will be examined in Chapter 5 Section 5.5 when the order parameter data are used to study the temperature dependence of the visco-elastic parameters.

2.3 Dielectric properties

The following discussion is based on the Maier and Meier's theory of static dielectric permittivities of nematic liquid crystals. Consider the polarisation **P** of an anisotropic medium by an electric field **E**:[2]

$$\mathbf{P} = \varepsilon_0\left(\underline{\underline{\varepsilon}} - \underline{\underline{\mathbf{I}}}\right)\mathbf{E}\,, \tag{2.4}$$

where ε_0 is the permittivity of vacuum, $\underline{\underline{\mathbf{I}}}$ is the second rank unit tensor and $\underline{\underline{\varepsilon}}$ is the relative dielectric constant tensor of the nematic material. As explained in Chapter 1 Section 1.3.1, if a suitable coordinate system is chosen, the components of this tensor can be reduced to $\varepsilon_{||}$ and $\varepsilon_{\perp}$, the static relative dielectric constants measured parallel and perpendicular to the director **n**.

For polar LC molecules, the total polarisation is given by[2]

$$\mathbf{P} = \mathrm{N}\left(\left\langle \underline{\underline{\alpha}}.\mathbf{E}_i \right\rangle + \left\langle \bar{\mu} \right\rangle\right), \tag{2.5}$$

where N is the number density of molecules, $\underline{\underline{\alpha}}$ is the polarisability tensor of a molecule, $\mathbf{E}_i$ is the internal electric field in the bulk material and $\bar{\mu}$ represents the average permanent molecular dipole moment. The brackets indicate that the terms are averaged over the orientations of all molecules. For non-polar LC molecules, only the first term on the right hand side subsists in expression (2.5) and the induced polarisation includes solely the contributions of the electronic and ionic polarisations.

Combining Equations (2.4) and (2.5) yields:

$$(\underline{\underline{\varepsilon}} - \underline{\underline{\mathbf{I}}}).\mathbf{E} = \frac{\mathrm{N}}{\varepsilon_0}\left(\left\langle \underline{\underline{\alpha}}.\mathbf{E}_i \right\rangle + \left\langle \bar{\mu} \right\rangle\right). \tag{2.6}$$

Maier and Meier evaluated Equation (2.6) by extending Onsager's theory for isotropic liquids and by using the following approximations:[5, 6]

- the molecules are considered to be spherical but with a positive polarizability anisotropy $\Delta\alpha = \alpha_{\parallel} - \alpha_{\perp}$, defined in Section 2.2;
- the dipole moment makes an angle ψ with the molecular long axis, as illustrated in Figure 2.1;
- the nematic orientational order parameter S, given by Equation (1.8) in Chapter 1, is not influenced by the external electric field;
- the dielectric anisotropy is small, i.e. $\Delta\varepsilon = \varepsilon_{\parallel} - \varepsilon_{\perp} << \bar{\varepsilon}$ where $\bar{\varepsilon} = (\varepsilon_{\parallel} + 2\varepsilon_{\perp})/3$ is the mean permittivity;
- the intermolecular interactions are neglected;
- the cavity field factor h and the reaction field factor f are assumed isotropic and their expressions are $h = 3\bar{\varepsilon}/(2\bar{\varepsilon}+1)$ and $f = (N/3\varepsilon_0)\left[(2\bar{\varepsilon}-2)/(2\bar{\varepsilon}+1)\right]$;
- the anisotropy of the polarisability is ignored in the calculation of the field factor F, which is defined by $F = 1/(1 - f\bar{\alpha})$.

Then, the static dielectric components are expressed as

$$\varepsilon_{\parallel} - 1 = \varepsilon_0^{-1} N F h \left\{ \bar{\alpha} + \frac{2}{3}\Delta\alpha S + \frac{F\mu^2}{3k_B T}\left[1 - (1 - 3\cos^2\psi)S\right] \right\}$$

and $$\varepsilon_{\perp} - 1 = \varepsilon_0^{-1} N F h \left\{ \bar{\alpha} - \frac{1}{3}\Delta\alpha S + \frac{F\mu^2}{3k_B T}\left[1 + \frac{1}{2}(1 - 3\cos^2\psi)S\right] \right\}. \qquad \textbf{(2.7)}$$

The corresponding dielectric anisotropy is therefore

$$\Delta\varepsilon = \varepsilon_{\parallel} - \varepsilon_{\perp} = \varepsilon_0^{-1} N F h S \left[\Delta\alpha - \frac{F\mu^2}{2k_B T}(1 - 3\cos^2\psi) \right]. \qquad \textbf{(2.8)}$$

For molecules with a large longitudinal dipole moment, i.e. for ψ less than 54.7°, the positive dipolar contribution results in positive $\Delta\varepsilon$. While for molecules with a significant transverse dipole moment, i.e. with ψ greater than 54.7°, the negative dipolar term may yield positive or negative $\Delta\varepsilon$, depending on the relative magnitude of the two terms.[5] The parameters N, F and h show little change with temperature. From Equation (2.8), the temperature variation of $\Delta\varepsilon$ is mainly determined by the contribution from the polarisability anisotropy, which is proportional to S and by the orientation polarisation, which scales as S/T. For specific combination of molecular properties, the dielectric anisotropy may also change sign as a function of temperature.[7]

Maier and Meier's model can be further improved by taking into account dipole-dipole interactions via the Kirkwood correlation factor g.[2, 6]

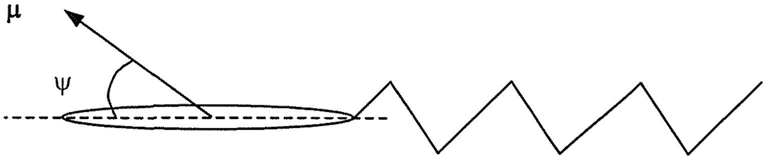

Figure 2.1: Schematic drawing of a LC mesogen exhibiting a dipole moment μ, which makes an angle ψ with the molecular long axis.

2.4 Visco-elastic properties of nematic liquid crystals

In the nematic phase, the physical properties of liquid crystals can be described using the continuum theory initially developed by Leslie and Ericksen.[2, 8, 9] The theory of curvature elasticity introduced by Frank is presented here.[10, 11]

2.4.1 Curvature strains of the director

In a nematic liquid crystal, the director orientation at a point **r** in space is given by

$$\mathbf{n}(\mathbf{r}) = \mathbf{n}_0 + \delta\mathbf{n}(\mathbf{r}), \qquad \textbf{(2.9)}$$

where $\mathbf{n}_0$ is the average director configuration and $\delta\mathbf{n}(\mathbf{r})$ is the fluctuating part. For fluctuations of small amplitude, $\mathbf{n}_0.\delta\mathbf{n}(\mathbf{r}) \approx 0$.

Consider a Cartesian coordinate system (x, y, z) with the equilibrium orientation of the director $\mathbf{n}_0$ along the z-axis at the origin. For infinitesimal deformations, a Taylor expansion around $\mathbf{n}_0$ gives the components of curvature strains for $\mathbf{n}(\mathbf{r})$:[10]

$$\begin{aligned} n_x(\mathbf{r}) &= \delta n_x(\mathbf{r}) = \frac{\partial n_x}{\partial x}\delta x + \frac{\partial n_x}{\partial y}\delta y + \frac{\partial n_x}{\partial z}\delta z + O(r^2), \\ n_y(\mathbf{r}) &= \delta n_y(\mathbf{r}) = \frac{\partial n_y}{\partial x}\delta x + \frac{\partial n_y}{\partial y}\delta y + \frac{\partial n_y}{\partial z}\delta z + O(r^2), \qquad \textbf{(2.10)} \\ n_z(\mathbf{r}) &= 1 + O(r^2), \end{aligned}$$

where $r^2 = x^2 + y^2 + z^2$.

The partial derivatives represent three fundamental elastic distortions, namely:

$$\begin{aligned} &\text{splay} \quad a_1 = \frac{\partial n_x}{\partial x} \qquad a_5 = \frac{\partial n_y}{\partial y}; \\ &\text{twist} \quad a_2 = \frac{\partial n_x}{\partial y} \qquad a_4 = -\frac{\partial n_y}{\partial x}; \\ &\text{bend} \quad a_3 = \frac{\partial n_x}{\partial z} \qquad a_6 = \frac{\partial n_y}{\partial z}. \end{aligned} \tag{2.11}$$

Any elastic distortion can be decomposed into a combination of splay, twist and bend deformations. The three fundamental deformations and the associated director curvature strains are shown in Figure 2.2.

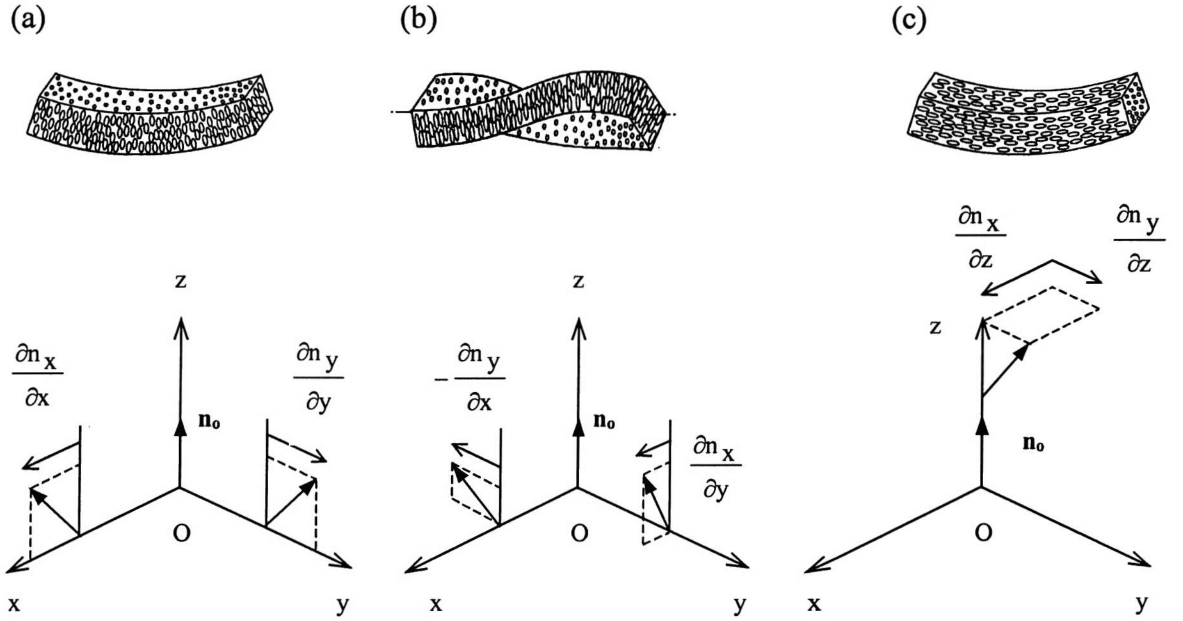

Figure 2.2: The three fundamental distortions and the associated curvature strains (a) Splay (b) Twist (c) Bend.

2.4.2 Elastic constants

In liquid crystals, restoring torques oppose the curvature strains of the director. By analogy with the theory of elasticity in solids, the equivalent of Hooke's law can be applied for small deformations. Thus, the free energy density that corresponds to distortions from a uniform director orientation is assumed to be a quadratic function of the curvature strains:

$$f_{\text{elastic}} = \sum_{i=1}^{6} k_i a_i + \frac{1}{2} \sum_{i=1}^{6} \sum_{j=1}^{6} k_{ij} a_i a_j, \tag{2.12}$$

where k_i and $k_{ij} = k_{ji}$ are the elastic moduli; they represent a change of energy with change of curvature. The free energy expression can be further simplified if specific transformations that preserve the symmetry of the phase are taken into account.[9-11] For an uniaxial non-polar achiral nematic phase, these transformations are summarised in Table 2.1.

Phase properties	Symmetry	Associated transformations
Uniaxial	Cylindrical	Rotations about z-axis
Non-polar	Inversion (**n**=-**n**)	Rotation about x-axis or y-axis
Achiral	Mirror image	Left-handed coordinate system

Table 2.1: Properties, symmetries and corresponding transformations for the nematic phase.

k_i and k_{ij} should remain invariant under these transformations. This condition reduces the number of independent non-zero elastic moduli to four terms. Furthermore, if the bulk of the nematic material is considered, the surface elastic modulus k_{24} can be ignored. The distortion free energy becomes

$$\begin{aligned} F_{\text{elastic}} &= \frac{1}{2}\int_V \left[k_{11}\left(\frac{\partial n_x}{\partial x} + \frac{\partial n_y}{\partial y}\right)^2 + k_{22}\left(\frac{\partial n_x}{\partial y} - \frac{\partial n_y}{\partial x}\right)^2 + k_{33}\left(\left(\frac{\partial n_x}{\partial z}\right)^2 + \left(\frac{\partial n_y}{\partial z}\right)^2\right)\right] dV \\ &= \frac{1}{2}\int_V \left[k_{11}(\nabla\cdot\mathbf{n})^2 + k_{22}(\mathbf{n}\cdot(\nabla\times\mathbf{n}))^2 + k_{33}(\mathbf{n}\times(\nabla\times\mathbf{n}))^2\right] dV \end{aligned} \quad ,\mathbf{(2.13)}$$

where V represents the volume studied and k_{11}, k_{22}, k_{33} are the Frank elastic constants associated with the splay, twist and bend deformations respectively. $k_{ii} > 0$ for $i = 1, 2, 3$. In S.I. units, k_{ii} are expressed in Newtons (N) and their order of magnitude is usually 10^{-11}-10^{-12} N for most low molar mass liquid crystals.

The fluctuating quantities $n_x(\mathbf{r})$ and $n_y(\mathbf{r})$ can be analysed in terms of their Fourier components according to[8]

$$n_x(\mathbf{r}) = \sum_{\mathbf{q}} n_x(\mathbf{q})\, e^{i(\mathbf{q}\cdot\mathbf{r})}$$

$$\text{and} \quad n_y(\mathbf{r}) = \sum_{\mathbf{q}} n_y(\mathbf{q})\, e^{i(\mathbf{q}\cdot\mathbf{r})} . \qquad \mathbf{(2.14)}$$

Hence, the curvature strains can be expressed as a function of wavevector components q_x, q_y and q_z. For instance,

$$\left(\frac{\partial n_x}{\partial x}\right)^2 = \sum_q |n_x(\mathbf{q})|^2 q_x^2 . \tag{2.15}$$

As will be shown in Section 2.6.4, the notation using wavevector components is extremely useful to interpret light scattering from nematic liquid crystals.

2.4.3 Viscosity coefficients

Basic concepts from fluid dynamics applied to isotropic liquids[2, 12]

The fluid is regarded as a continuous medium. Consider a fluid region that is a volume large enough to contain many molecules but is still small with respect to the characteristic length scale of the flow. Assume the fluid region has a velocity $\mathbf{v}(\mathbf{r}, t)$ at a point $\mathbf{r}$ in space at time t. In the next section, the notation x_i with $i = 1, 2, 3$ is used for the variables x, y, z respectively.

For incompressible fluids, such as liquids, the fluid density $\rho(\mathbf{r}, t)$ is constant and the law of conservation of mass leads to

$$\nabla \cdot \mathbf{v} = \frac{\partial v_i}{\partial x_i} = 0 , \tag{2.16}$$

where $\mathbf{v}(\mathbf{r}, t)$ is the fluid velocity.

The second-rank velocity gradient tensor is defined as

$$G_{ij} = \frac{\partial v_i}{\partial x_j} = A_{ij} + W_{ij} , \tag{2.17}$$

$$\text{with } A_{ij} = \frac{1}{2}\left(\frac{\partial v_i}{\partial x_j} + \frac{\partial v_j}{\partial x_i}\right) \tag{2.18}$$

$$\text{and } W_{ij} = \frac{1}{2}\left(\frac{\partial v_i}{\partial x_j} - \frac{\partial v_j}{\partial x_i}\right) . \tag{2.19}$$

$\underline{\underline{A}}$ is a symmetric tensor related to the rate-of-strain; the trace of this tensor is equal to zero for incompressible fluids. $\underline{\underline{W}}$ is an asymmetric tensor associated with the vorticity of the flow i.e. with the rotation of the fluid. In general, any shear flow may be decomposed locally into an irrotational part ($\underline{\underline{W}} = 0$) and a rotational contribution ($\underline{\underline{A}} = 0$) as can be seen in Figure 2.3.[2]

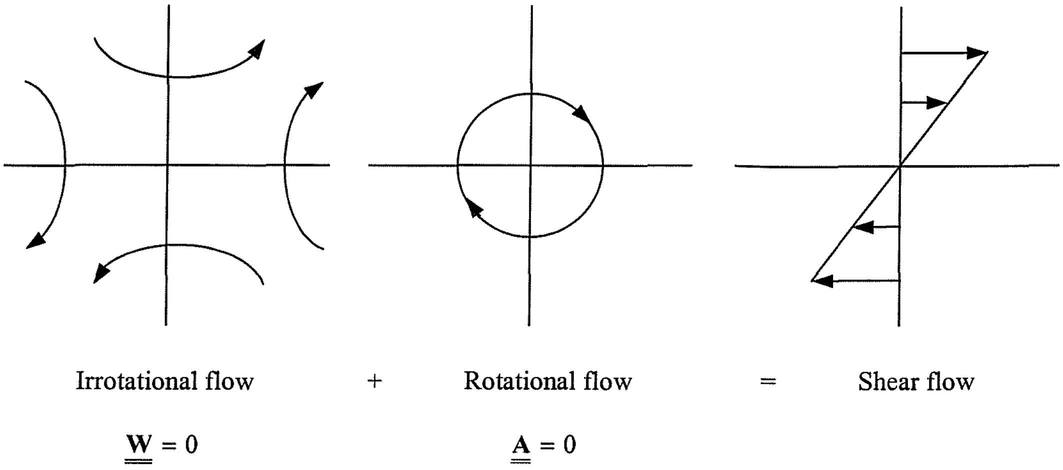

Figure 2.3: Decomposition of shear flow into rotational and irrotational flows.

Newton's second law of motion can be derived:[12]

$$\rho \frac{Dv}{Dt} = \mathbf{f} + \nabla \cdot \underline{\underline{\sigma}}, \tag{2.20}$$

where **f** is the resulting force per unit volume acting on a fluid particle (e.g. gravity, electrostatic, electro-magnetic, etc.) and $\underline{\underline{\sigma}}$ is the second-rank stress tensor.

For an isotropic fluid, the components of the stress tensor $\underline{\underline{\sigma}}$ are given by:

$$\sigma_{ij} = -p\delta_{ij} + \sigma'_{ij}, \tag{2.21}$$

where $-p\delta_{ij}$ is the hydrostatic pressure, δ_{ij} being the Kronecker delta function ($\delta_{ij} = 1$ for $i = j$ and $\delta_{ij} = 0$ for $i \neq j$). $\underline{\underline{\sigma}}'$ represents the viscous stress tensor. For Newtonian fluids, the viscous stress tensor $\underline{\underline{\sigma}}'$ is proportional to the rate-of-strain tensor $\underline{\underline{A}}$ as follows[12]

$$\sigma'_{ij} = 2\eta A_{ij} = \eta\left(\frac{\partial v_i}{\partial x_j} + \frac{\partial v_j}{\partial x_i}\right), \tag{2.22}$$

where η is the viscosity of the fluid.

Application to nematic liquid crystals

In this case, the situation is more complex due to the coupling between flow and director orientation $\mathbf{n}(\mathbf{r},t)$. It is necessary to introduce a new vector $\mathbf{N}$ that describes the rate of change of the director with respect to the flow:[2]

$$N_i = \frac{Dn_i}{Dt} - W_{ij}n_j . \qquad \textbf{(2.23)}$$

For $\mathbf{N} = 0$, $\frac{Dn_i}{Dt} = W_{ij}n_j$. In this case, the molecules' orientation rotates at the same angular velocity as the flow. As a result, the relative position of the molecules is unchanged and no viscous dissipation occurs.[2]

The viscous stress tensor $\underline{\underline{\sigma}}'$ is assumed to depend linearly on $\underline{\underline{\mathbf{A}}}$ and on $\mathbf{N}$. Furthermore, by symmetry, $\underline{\underline{\sigma}}'(-\mathbf{n}) = \underline{\underline{\sigma}}'(\mathbf{n})$. According to the Leslie and Ericksen theory, for an incompressible nematic liquid crystal, the general form for $\underline{\underline{\sigma}}'$ satisfying these conditions can be expressed as[2, 9]

$$\sigma'_{ij} = \alpha_1(n_k A_{kl} n_l)n_i n_j + \alpha_2 N_i n_j + \alpha_3 N_j n_i + \alpha_4 A_{ij} + \alpha_5(n_k A_{ki})n_j + \alpha_6 n_i(n_k A_{kj}) , \textbf{(2.24)}$$

α_i are six viscosity coefficients known as Leslie coefficients and they are expressed in Pa.s in S.I. units. Parodi showed that only five of these coefficients are independent:[9]

$$\alpha_2 + \alpha_3 = \alpha_6 - \alpha_5 . \qquad \textbf{(2.25)}$$

In the isotropic phase, the viscous stress tensor is reduced to $\sigma'_{ij} = \alpha_4 A_{ij}$ and therefore, the value of the isotropic viscosity coefficient is

$$\eta_{iso} = \alpha_4 / 2 . \qquad \textbf{(2.26)}$$

The rotational or twist viscosity is defined as

$$\gamma_1 = \alpha_3 - \alpha_2 . \qquad \textbf{(2.27)}$$

In order to understand the physical meaning of the Leslie coefficients, it is interesting to relate these to the Miesowicz viscosities η_1, η_2 and η_3, that are obtained in shear experiments using three different director configurations depicted in Figure 2.4:[13]

a. **n** parallel to the velocity gradient

$$\eta_1 = \frac{1}{2}(-\alpha_2 + \alpha_4 + \alpha_5) ; \qquad \textbf{(2.28)}$$

b. **n** parallel to the flow direction

$$\eta_2 = \frac{1}{2}(\alpha_3 + \alpha_4 + \alpha_6) = \frac{1}{2}(\alpha_2 + 2\alpha_3 + \alpha_4 + \alpha_5); \qquad \textbf{(2.29)}$$

c. **n** normal to the flow and to the velocity gradient

$$\eta_3 = \eta_{iso} = \frac{1}{2}\alpha_4. \qquad \textbf{(2.30)}$$

The Miesowicz viscosity coefficients are positive and generally $\eta_2 < \eta_3 < \eta_1$.

The sign of some of the Leslie coefficients can be discussed taking into account the previous derivations. Firstly, the rotational and isotropic viscosities should be positive and therefore $\alpha_2 < 0$ and $\alpha_4 > 0$. The coefficient α_3 can either be positive or negative; its absolute value has been predicted to be rather small or negligible compared to the other viscosity coefficients[14] and this has been confirmed experimentally.[15, 16]

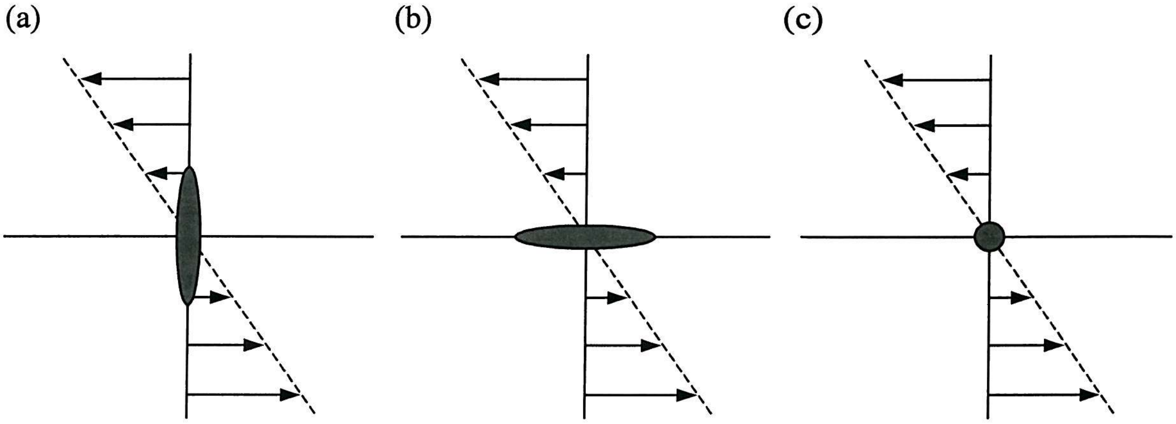

Figure 2.4: Definition of the Miesowicz viscosity coefficients in different geometries

(a) **n** ll velocity gradient (η_1)

(b) **n** ll flow (η_2)

(c) **n** ⊥ flow direction and velocity gradient (η_3).

2.5 Freedericksz transition

The application of a magnetic or electric field causes a reorientation of the LC molecules above a certain threshold value if their initial orientation with respect to the field does not correspond to a state of minimum free energy.[5] This field-induced deformation is also referred to as Freedericksz transition (FT).[17] This technique is widely used to measure the Frank elastic constants.[2, 5, 8, 9, 11, 18, 19] There are three possible geometries, as shown in Figure 2.5.

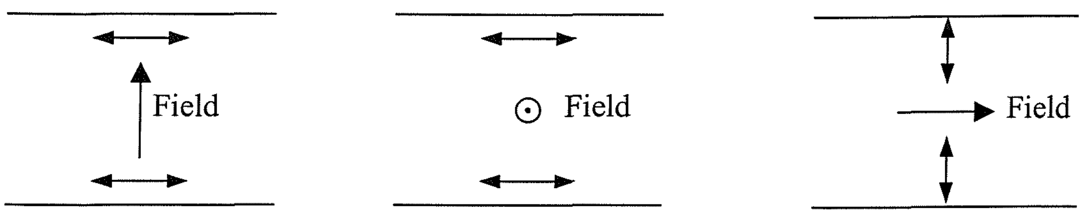

Figure 2.5: The three different geometries for the Freedericksz transition
(a) Splay (b) Twist (c) Bend
The double arrows indicate the director alignment at the boundaries.

2.5.1 Magnetic field

In an anisotropic phase, the magnetisation or magnetic moment per unit volume **M** in S.I. units can be defined in terms of the magnetic induction **B** as[2, 20]

$$\mathbf{M} = \mu_0^{-1}\underline{\underline{\chi}}\mathbf{B}, \qquad \textbf{(2.31)}$$

where μ_0 is the vacuum permeability and $\underline{\underline{\chi}}$ is the second-rank tensor for the magnetic susceptibility. In this work, the magnetic induction **B** is called the magnetic field; this quantity is measured experimentally in Tesla (T).

In the presence of a magnetic field applied at an arbitrary angle to the director **n**, the magnetisation becomes[8]

$$\mathbf{M} = \mu_0^{-1}\chi_\perp\mathbf{B} + \mu_0^{-1}\Delta\chi(\mathbf{B}\cdot\mathbf{n})\mathbf{n}, \qquad \textbf{(2.32)}$$

where $\Delta\chi = \chi_\parallel - \chi_\perp$ is the magnetic susceptibility anisotropy with $\chi_\parallel$ and $\chi_\perp$ being respectively the components parallel and perpendicular to the director. Most nematic liquid crystals consist of organic molecules and thus they are diamagnetic materials i.e. their values of $\chi_\parallel$ and $\chi_\perp$ are negative and of the order of 10^{-5} S.I. units; since $|\chi_\parallel| < |\chi_\perp|$, $\Delta\chi > 0$.

The free energy density of a nematic placed in a magnetic field is:[8, 20]

$$\begin{aligned} f_{\text{magn}} &= -\int \mathbf{M}\cdot d\mathbf{B} \\ &= -\frac{1}{2}\mu_0^{-1}\chi_\perp\mathbf{B}^2 - \frac{1}{2}\mu_0^{-1}\Delta\chi(\mathbf{B}\cdot\mathbf{n})^2. \end{aligned} \qquad \textbf{(2.33)}$$

In this expression, the first term can be ignored since it is independent of the director orientation. The second term is important because it takes into account the relative orientation of the director with respect to the applied field.

The general expression for the critical field in the splay, twist or bend configurations (see Figure 2.5 (a), (b) and (c)) can be derived by minimising the distortion free energy at the transition, which includes the magnetic and the elastic contributions:[8, 9]

$$(B_C)_i = \frac{\pi}{d}\left(\frac{k_{ii}\mu_0}{\Delta\chi}\right)^{1/2} \quad i = 1, 2, 3. \tag{2.34}$$

For instance in the bend geometry, the director is initially uniformly aligned perpendicular to the cell walls and the magnetic field **B** is applied parallel to these walls, as represented in Figure 2.6. The field will induce a bend deformation of the nematic slab above a threshold field $\mathbf{B}_c$ given by

$$B_C = \frac{\pi}{d}\left(\frac{k_{33}\mu_0}{\Delta\chi}\right)^{1/2}. \tag{2.35}$$

At the threshold field, the distortion is due solely to the bend term. It is possible to determine k_{33} from Equation (2.35), provided $\Delta\chi$ is known. When the field becomes significantly greater than the threshold field, the deformation involves both bend and splay elastic terms, enabling in principle the determination of the splay elastic constant;[9] this will be explained in greater detail in Chapter 3 Section 3.4.2.

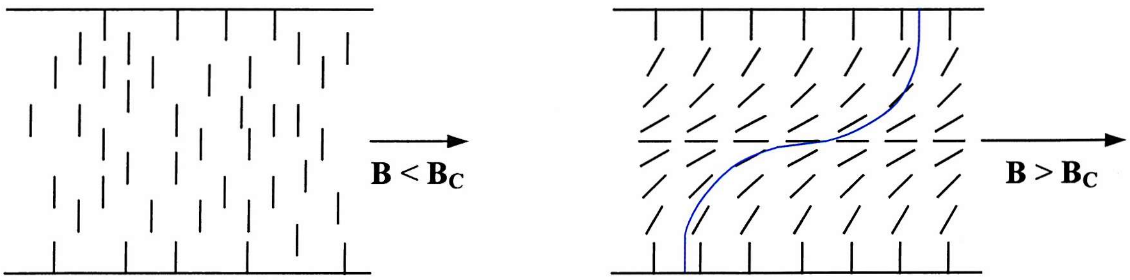

Figure 2.6: Schematic representation of the bend Freedericksz transition induced by a magnetic field (the blue line corresponds to the director profile)

(a) For $\mathbf{B} < \mathbf{B}_C$, the initial orientation of the molecules is unchanged

(b) For $\mathbf{B} > \mathbf{B}_C$, the bend deformation occurs.

2.5.2 Electric field

The coupling between an applied electric field **E** and the director fluctuations results in an energy density term[8]

$$f_{elec} = -\int \mathbf{D} \cdot d\mathbf{E}. \tag{2.36}$$

where the electric displacement **D** is defined in nematic liquid crystals by

$$\mathbf{D} = \varepsilon_0 [\varepsilon_\perp \mathbf{E} + \Delta\varepsilon(\mathbf{n} \cdot \mathbf{E}) \cdot \mathbf{n}], \quad \mathbf{(2.37)}$$

where $\Delta\varepsilon = \varepsilon_\| - \varepsilon_\perp$ is the static dielectric anisotropy of the material, defined in Section 2.3.

The electric energy can be rewritten as

$$f_{elec} = -\frac{1}{2}\varepsilon_0 \varepsilon_\perp E^2 - \frac{1}{2}\varepsilon_0 \Delta\varepsilon(\mathbf{n} \cdot \mathbf{E})^2. \quad \mathbf{(2.38)}$$

As in Equation (2.33), only the second term of this expression depends on the director orientation:

- for $\Delta\varepsilon > 0$, **n** tends to align itself along **E**
- for $\Delta\varepsilon < 0$, **n** tends to be perpendicular to **E**.

The analogy to the magnetic Freedericksz transition is illustrated in Figure 2.7 for electric fields applied perpendicular to the cell walls. Similar methods can be applied to calculate the threshold voltage. In practice, there are two interesting cases:[21]

- for $\Delta\varepsilon < 0$ with the director initially oriented normal to the walls, the critical voltage is given by

$$V_C = \pi \left(\frac{k_{33}}{|\varepsilon_\| - \varepsilon_\perp| \, \varepsilon_0} \right)^{1/2}; \quad \mathbf{(2.39)}$$

- for $\Delta\varepsilon > 0$ with the director initially aligned parallel to the walls, the critical voltage is then

$$V_C = \pi \left(\frac{k_{11}}{(\varepsilon_\| - \varepsilon_\perp) \, \varepsilon_0} \right)^{1/2}. \quad \mathbf{(2.40)}$$

However, certain difficulties may arise with the use of electric fields, which are not seen when a magnetic field is applied instead. Above its threshold value, the electric field becomes non-uniform inside the liquid crystal due to the induced distortion. Space charge and flexoelectric effects may also occur. Additionally, it must be ensured that the sample is pure to avoid conduction-induced instabilities.[2, 9]

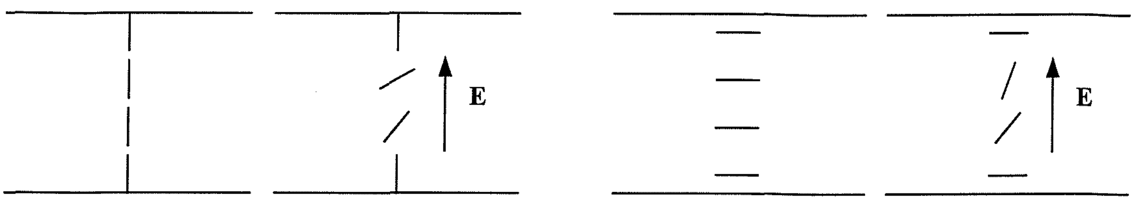

(a) $\Delta\varepsilon < 0$, bend distortion (b) $\Delta\varepsilon > 0$, splay distortion

Figure 2.7: Geometries used for the electric field induced Freedericksz transition.

2.6 Dynamic light scattering (DLS)

2.6.1 Rayleigh scattered light intensity

For the purpose of this thesis, the light scattering theory can be derived from simple electromagnetic calculations.[22, 23] An incident electromagnetic (EM) field acts as a force on the charges present in the scattering volume; these charges are accelerated and therefore radiate light. This light is in turn scattered as a result of local fluctuations in the optical dielectric constant of the medium.

Consider a non-magnetic, non-conducting and non-absorbing medium. The local optical dielectric constant tensor is of the form

$$\underline{\underline{\varepsilon}}(\mathbf{r},\,t) = \varepsilon_{ave}\underline{\underline{\mathbf{I}}} + \delta\underline{\underline{\varepsilon}}(\mathbf{r},\,t)\,, \tag{2.41}$$

where ε_{ave} is the average dielectric constant, $\underline{\underline{\mathbf{I}}}$ is the second-rank unit tensor and $\delta\underline{\underline{\varepsilon}}(\mathbf{r},\,t)$ is the dielectric constant fluctuations tensor at a point $\mathbf{r}$ in space at time t.

Assume a plane EM wave incident upon this medium; the electric field with polarisation direction $\hat{\mathbf{i}}$, amplitude E_0, wavevector $\mathbf{k}_i$ and angular frequency ω_i can be expressed as

$$\mathbf{E}_i(\mathbf{r},\,t) = \hat{\mathbf{i}}E_0\exp i(\mathbf{k}_i.\mathbf{r} - \omega_i t)\,. \tag{2.42}$$

By applying Maxwell's equations, it is possible to show that for a singly scattered wave with polarisation $\hat{\mathbf{f}}$ and wavevector $\mathbf{k}_s$, the scattered electric field at a large distance R from the scattering volume is given by:[22, 23]

$$E_S(\mathbf{R},\,t) = \frac{E_0}{4\pi R\varepsilon_0}e^{i(\mathbf{k}_s.\mathbf{R}-\omega_i t)}\int_{\text{Scatt. vol.}}\hat{\mathbf{f}}\,e^{i\mathbf{q}.\mathbf{r}}\cdot\left\{\mathbf{k}_s\times\left[\mathbf{k}_s\times(\delta\underline{\underline{\varepsilon}}(\mathbf{r},\,t)\cdot\hat{\mathbf{i}})\right]\right\}d^3\mathbf{r}\,. \tag{2.43}$$

$E_S(\mathbf{R},\,t)$ results from the superposition of the contributions from the whole scattering volume as sketched in Figure 2.8.

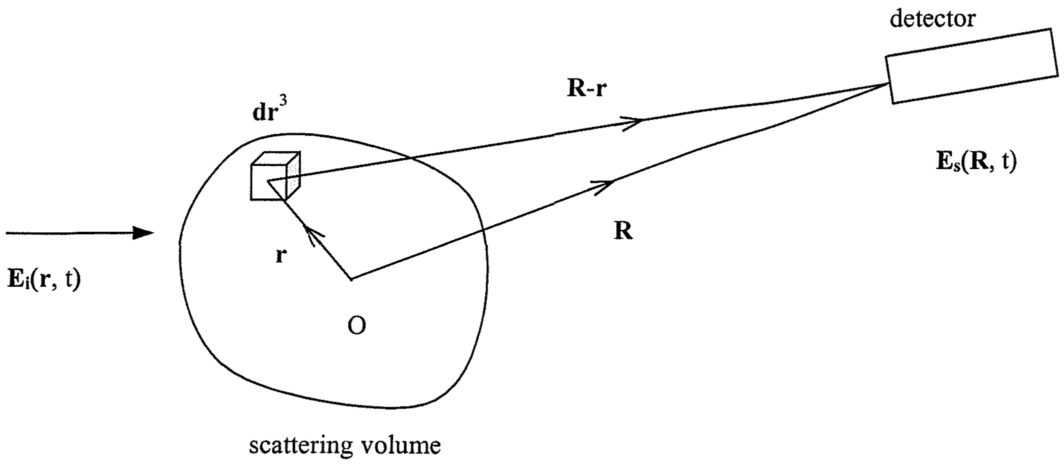

Figure 2.8: Definition of the electric field associated with the scattered light at the detector.

The scattering wavevector **q** is defined as

$$\mathbf{q} = \mathbf{k}_i - \mathbf{k}_s , \qquad (2.44)$$

where $\mathbf{k}_i$ and $\mathbf{k}_s$ are respectively the direction of propagation of the incident and scattered waves.

In quasi-elastic scattering, there is little change in energy between the scattered and incident photons. In an isotropic medium, this can be written:

$$|\mathbf{k}_i| \approx |\mathbf{k}_s| = \frac{2\pi n}{\lambda_i} , \qquad (2.45)$$

where n is the refractive index of the scattering medium and λ_i is the wavelength in vacuum of the incident EM wave. As a consequence,

$$|\mathbf{q}| = \frac{4\pi n}{\lambda_i} \sin(\theta_{LC}/2) , \qquad (2.46)$$

θ_{LC} is the angle between $\mathbf{k}_i$ and $\mathbf{k}_s$ measured within the scattering medium. Equation (2.46) specifies the Bragg condition, which determines the wavevector component of the optical dielectric constant fluctuations that gives rise to scattering at an angle θ_{LC}. The scattering geometry is summarised in Figure 2.9.

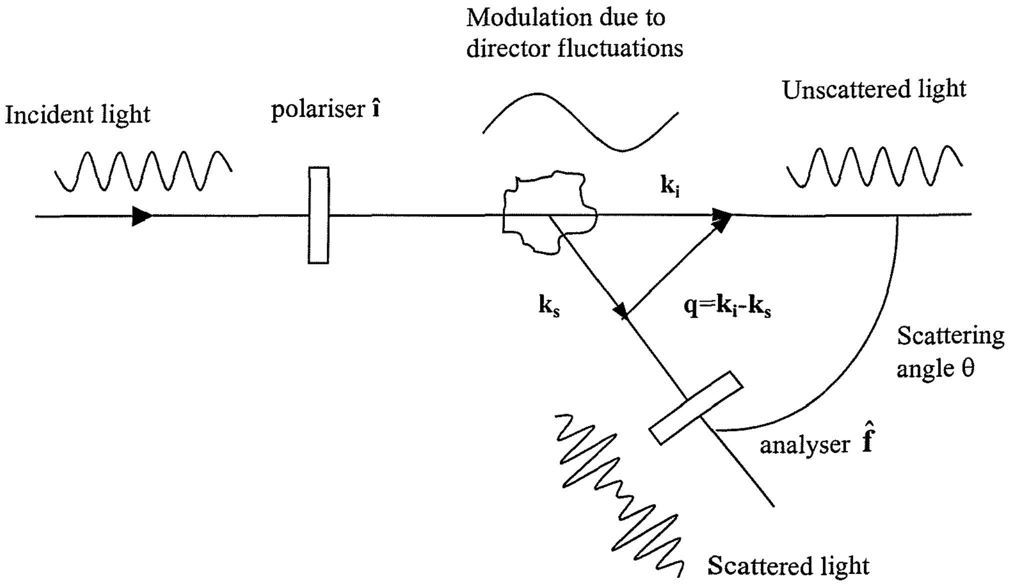

Figure 2.9: Light scattering geometry.

The spatial Fourier transform of the dielectric fluctuation tensor is

$$\delta\underline{\underline{\varepsilon}}(\mathbf{q},t) = \int_{\text{Scatt. vol.}} e^{i\mathbf{q}\cdot\mathbf{r}}\delta\underline{\underline{\varepsilon}}(\mathbf{r},t)\,d^3\mathbf{r}\,. \tag{2.47}$$

After substitution into Equation (2.43), the expression for the scattered field can be obtained[24]

$$E_S(\mathbf{R},t) = \frac{k_s{}^2E_0}{4\pi R\varepsilon_0}e^{i(\mathbf{k}_s\cdot\mathbf{R}-\omega_i t)}\left[\delta\varepsilon_{if}(\mathbf{q},t)\right], \tag{2.48}$$

$$\text{with}\quad \delta\varepsilon_{if} = \hat{\mathbf{f}}\cdot\delta\underline{\underline{\varepsilon}}(\mathbf{q},t)\cdot\hat{\mathbf{i}}\,. \tag{2.49}$$

$\delta\varepsilon_{if}$ corresponds to the component of the dielectric tensor along the initial and final polarisation directions. Equation (2.48) relates the Rayleigh scattered electric field to the fluctuations in local dielectric constant tensor.

2.6.2 Fluctuations and time autocorrelation functions

At the detector, the resulting scattered electric field fluctuates in time due to the thermal motion of the molecules in the scattering volume. These fluctuations can be described using time-dependent correlation functions.

Consider a dynamical property A(t) that depends on the positions and momenta of all the molecules in the system. A(t) is represented in Figure 2.10 (a) and is similar to a noise signal. Assume that A(t) is a stationary quantity, such that its average is independent of the time at which the measurement is started. The average value of A(t) over time T is

$$< A > = \lim_{T\to\infty}\frac{1}{T}\int_0^T A(t)dt\,. \qquad \textbf{(2.50)}$$

The autocorrelation function of the property A is defined as[22]

$$C(\tau) = < A(0)A^*(\tau) > = \lim_{T\to\infty}\frac{1}{T}\int_0^T A(t)A^*(t+\tau)dt\,, \qquad \textbf{(2.51)}$$

where A^* is the complex conjugate of A.

When τ is very small compared to the timescale of the fluctuations in A, $A^*(t+\tau)$ will be very close to A(t): $A^*(t+\tau)$ and A(t) are correlated. As τ increases, $A^*(t+\tau)$ will progressively differ from A(t): the correlation is lost for values of τ larger than the period of the fluctuations.[22] It can be shown that the autocorrelation function of a non-conserved and non-periodic quantity decays from complete correlation $<A^2>$ at $\tau = 0$ to non-correlation $<A>^2$ at large τ as illustrated in Figure 2.10 (b).

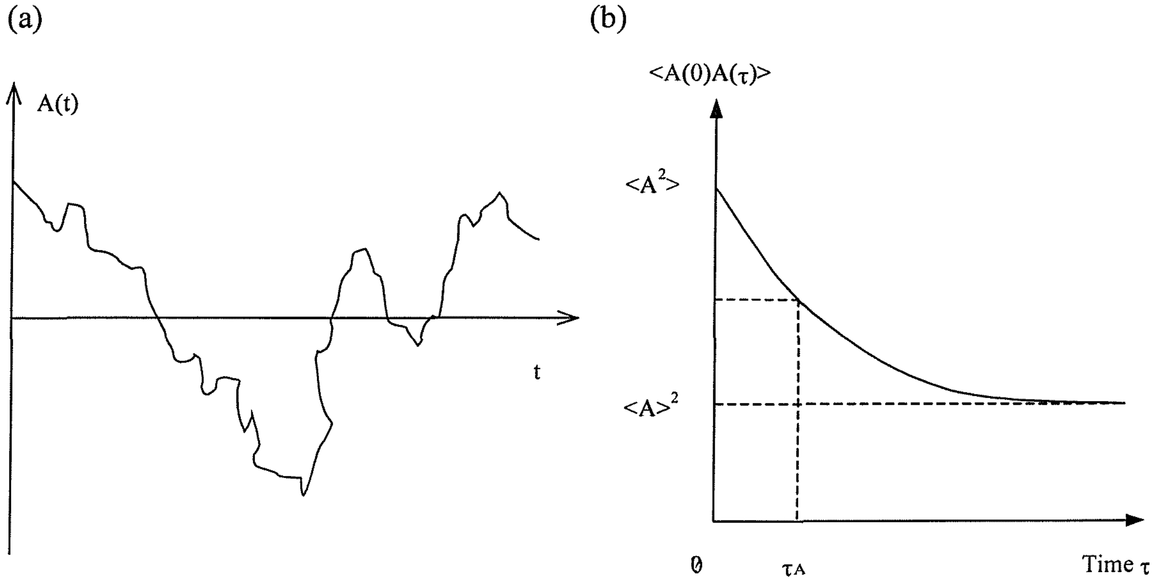

Figure 2.10: (a) Schematic representation of a fluctuating quantity A(t)
(b) Time-dependent autocorrelation function $<A(0)A^*(\tau)>$.

By definition, the time-dependent autocorrelation function $C(\tau) = <A(0)A^*(\tau)>$ and the frequency spectral density $s(\omega)$ of the signal are Fourier transforms of one another:[22]

$$s(\omega) = \frac{1}{2\pi}\int_{-\infty}^{+\infty} d\tau\, e^{-i\omega\tau} < A(0)A^*(\tau) > . \qquad \textbf{(2.52)}$$

If $C(\tau)$ is represented by a single exponential decay with a characteristic time $\tau_c = 1/\Gamma$ then $s(\omega)$ corresponds to a Lorentzian spectrum of half width Γ at half maximum as can be seen in Figure 2.11.

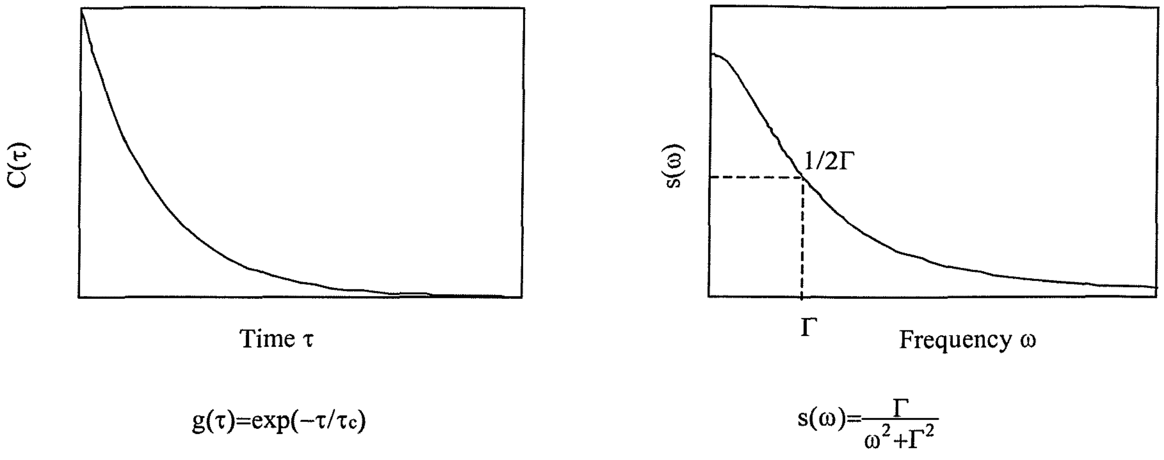

Figure 2.11: Autocorrelation function $C(\tau)$ and frequency spectrum $s(\omega)$ in the Lorentzian case.

In optical mixing experiments, a correlator analyses the time-dependent autocorrelation functions of the scattered field by dividing the time axis into very small intervals Δt over which the property A is constant. Let suppose that $t = j\Delta t$, $\tau = n\Delta t$ and $T = N\Delta t$, j, n and N are integers. To a good approximation, Equations (2.50) and (2.51) become respectively

$$< A > = \lim_{N\to\infty} \frac{1}{N} \sum_{j=1}^{N} A_j \tag{2.53}$$

and $$< A(0)A^*(\tau) > = \lim_{N\to\infty} \frac{1}{N} \sum_{j=1}^{N} A_j A^*_{j+n} \, , \tag{2.54}$$

where A_j is the value of A at the beginning of the j^{th} interval.

For the scattered field, two autocorrelation functions can be defined:[22]

- the first order field autocorrelation function

$$g_1(\tau) = < E_S(\mathbf{R}, t) E^*_S(\mathbf{R}, t+\tau) > ; \tag{2.55}$$

- the second order intensity autocorrelation function

$$g_2(\tau) = < I_S(\mathbf{R}, t)\, I_S(\mathbf{R}, t+\tau) > = < E_S(\mathbf{R}, t)\, E^*_S(\mathbf{R}, t)\, E_S(\mathbf{R}, t+\tau)\, E^*_S(\mathbf{R}, t+\tau) > . \tag{2.56}$$

2.6.3 Detection techniques

The instantaneous current output i(t) of a photomultiplier tube (PMT) is proportional to the square of the electric field E(t) and hence to the light intensity I(t) reaching the detector. This can be written as $i(t) \propto |E(t)|^2 \propto I(t)$.

A correlator computes the time autocorrelation function of the PMT output current as

$$< i(0)\, i(\tau) > = B < |E(0)|^2 |E(\tau)|^2 >, \qquad \textbf{(2.57)}$$

where B is a constant associated with the PMT efficiency.

Different autocorrelation functions are measured depending on whether homodyne or heterodyne detection techniques are used.[22]

Homodyne (or self-beat mode)

Only the scattered light impinges on the detector so that $E(\mathbf{R}, t) = E_S(\mathbf{R}, t)$.

The autocorrelation function of the PMT output current is given by

$$< i(0)\, i(\tau) > = B\, g_2(\tau). \qquad \textbf{(2.58)}$$

Assuming that $E_S(t)$ follows a Gaussian distribution (i.e. the scattering volume can be subdivided into many statistically independent regions), $g_2(\tau)$ is related to $g_1(\tau)$ via the Siegert relation:

$$g_2(\tau) = |g_1(0)|^2 + |g_1(\tau)|^2. \qquad \textbf{(2.59)}$$

In this particular case, homodyne detection yields the same information as the heterodyne mode.[22]

Heterodyne

The scattered field $E_S(t)$ is mixed with a portion of unscattered field $E_U(t)$ derived from the same laser source, which acts as a local oscillator. The autocorrelation function of the PMT output current becomes

$$< i(0)\, i(\tau) > = B < |E_U(0) + E_S(0)|^2 |E_U(\tau) + E_S(\tau)|^2 >. \qquad \textbf{(2.60)}$$

Let us assume that:

- the fluctuations of the unscattered field $E_U(t)$ are negligible;
- $E_S(t)$ and $E_U(t)$ are statistically independent, such that $<I_S I_U>=<I_S> <I_U>$;
- $I_U(t) >> I_S(t)$ can be achieved experimentally.

Under these conditions,[22]

$$< i(0)\, i(\tau) > = B\,[I_U{}^2 + 2I_U\, \mathrm{Re}\, g_1(\tau)]\,, \qquad \textbf{(2.61)}$$

where Re $g_1(\tau)$ represents the real part of the field correlation function $g_1(\tau)$.

Heterodyne detection offers important advantages over homodyne detection:

- no Gaussian approximations are necessary;
- for processes involving several relaxation times, $g_2(\tau)$ has a more complex form than $g_1(\tau)$, making homodyne spectra more difficult to analyse than heterodyne data;
- experimentally, in homodyne mode, static scattering from impurities inside the sample or due to glass flare will cause partial heterodyning and affect the measured linewidth.[24]

Note that the heterodyne method requires coherent mixing of the scattered light and of the local oscillator i.e. their wavefronts must be parallel at the detector surface.

Finally, the autocorrelation functions $g_1(\tau)$ and $g_2(\tau)$ can be expressed in terms of the dielectric constant fluctuation tensor $\delta\varepsilon_{if}(\mathbf{q}, t)$ by substituting Equation (2.48) into Equations (2.55) and (2.56):

$$g_1(\tau) = < \delta\varepsilon_{if}(\mathbf{q}, t)\, \delta\varepsilon^*_{if}(\mathbf{q}, t+\tau) > ; \qquad \textbf{(2.62)}$$

$$g_2(\tau) = < \left|\delta\varepsilon_{if}(\mathbf{q}, t)\right|^2 \left|\delta\varepsilon_{if}(\mathbf{q}, t+\tau)\right|^2 > . \qquad \textbf{(2.63)}$$

Using heterodyne detection, $g_1(\tau)$ can be obtained directly and thus the dynamic properties of the medium can be easily deduced.

2.6.4 Light scattering from two uncoupled modes of director fluctuations

In uniaxial nematics, the optical dielectric tensor component along the initial and final polarisation directions is:[25]

$$\varepsilon_{if}(\mathbf{r}) = \bar{\varepsilon} + \Delta\varepsilon\, [(\hat{\mathbf{i}}\cdot\mathbf{n})(\hat{\mathbf{f}}\cdot\mathbf{n}) - 1/3]\,, \qquad \textbf{(2.64)}$$

where $\bar{\varepsilon} = (\varepsilon_{\parallel} + 2\varepsilon_{\perp})/2$ represents the mean value of dielectric constant and $\Delta\varepsilon = \varepsilon_{\parallel} - \varepsilon_{\perp}$ is the dielectric anisotropy of the material.

Recalling Equation (2.9) for $\mathbf{n}(\mathbf{r})$, the fluctuating part of ε_{if} becomes

$$\delta\varepsilon_{if}(\mathbf{r}) = \Delta\varepsilon\, \left[(\mathbf{n}_0\cdot\hat{\mathbf{i}})(\delta\mathbf{n}\cdot\hat{\mathbf{f}}) + (\mathbf{n}_0\cdot\hat{\mathbf{f}})(\delta\mathbf{n}\cdot\hat{\mathbf{i}})\right]. \qquad \textbf{(2.65)}$$

The fluctuations of the local optical dielectric constant tensor arise from fluctuations in the director orientation.[25]

As explained in Section 2.4.1, the equilibrium orientation of the director $\mathbf{n}_0$ is assumed parallel to the z-axis, which is therefore an axis of symmetry. Two new unit vectors can be defined as[25]

$$\hat{\mathbf{e}}_2 = \frac{\mathbf{n}_0 \times \mathbf{q}}{|\mathbf{n}_0 \times \mathbf{q}|}$$

$$\text{and} \quad \hat{\mathbf{e}}_1 = \hat{\mathbf{e}}_2 \times \mathbf{n}_0 . \tag{2.66}$$

In this new coordinate system, the director fluctuations can be written

$$\delta\mathbf{n}(\mathbf{q}) = \mathrm{n}_1(\mathbf{q})\hat{\mathbf{e}}_1 + \mathrm{n}_2(\mathbf{q})\hat{\mathbf{e}}_2 , \tag{2.67}$$

where $\mathrm{n}_1(\mathbf{q})$ and $\mathrm{n}_2(\mathbf{q})$ correspond to respectively the splay-bend distortions (mode 1) confined to the ($\hat{\mathbf{e}}_1$, $\mathbf{n}_0$) plane and the twist-bend deformations (mode 2) confined to the ($\hat{\mathbf{e}}_2$, $\mathbf{n}_0$) plane. These two modes of director fluctuations are independent. The new coordinate system is illustrated in Figure 2.12 (a) and the two modes of director fluctuations are outlined in Figure 2.12 (b) and (c).

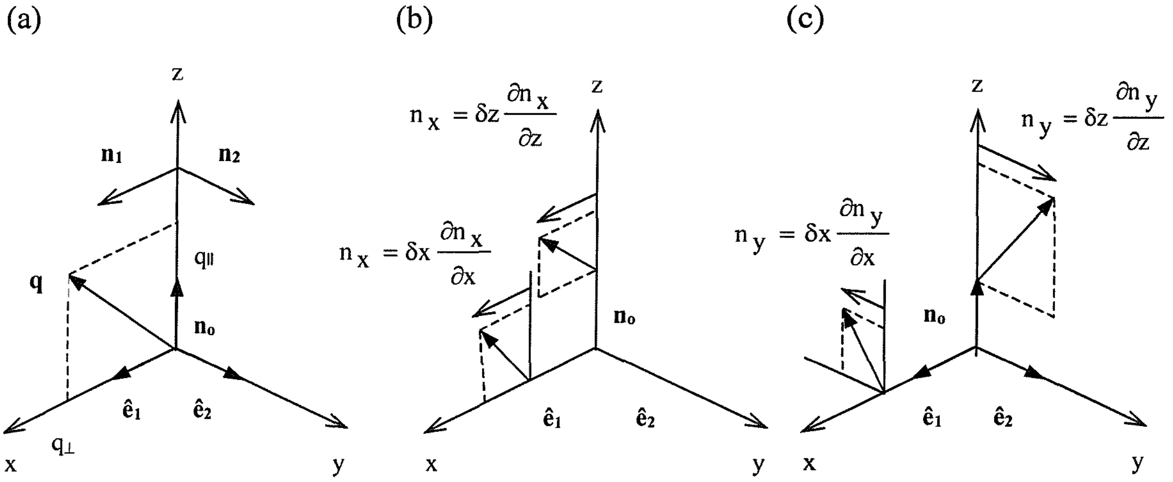

Figure 2.12: (a) Definition of the new coordinate system and of the two uncoupled modes of director fluctuations

(b) Splay-bend mode $\mathrm{n}_1(\mathbf{q})$

(c) Twist-bend mode $\mathrm{n}_2(\mathbf{q})$.

After expressing the curvature strains as a function of wavevector components in Equation (2.13), the elastic free energy becomes:

$$F_{\text{elastic}} = \frac{1}{2} V \sum_{\mathbf{q}} \left[|n_1(\mathbf{q})|^2 (k_{11} q_\perp^2 + k_{33} q_\parallel^2) + |n_2(\mathbf{q})|^2 (k_{22} q_\perp^2 + k_{33} q_\parallel^2) \right], \qquad \textbf{(2.68)}$$

where the component of **q** normal to the director, $q_\perp = q_x$, is related to either the splay or twist distortions while the component of **q** parallel to $\mathbf{n}_0$, $q_\parallel = q_z$ is associated with the bend deformations. In the frame defined by ($\hat{\mathbf{e}}_1$, $\hat{\mathbf{e}}_2$, $\mathbf{n}_0$), the scattering wavevector is in the (x, z) plane and $q_y = 0$.

Consider a classical system in thermal equilibrium. According to the equipartition theorem, the average energy per degree of freedom is $k_BT/2$, k_B being the Boltzmann constant. The thermal average associated with each mode of director fluctuations, $n_1(\mathbf{q}, t)$ and $n_2(\mathbf{q}, t)$, was derived by de Gennes as[26]

$$< |n_m(\mathbf{q}, t)|^2 > = \frac{k_B T}{V} \frac{1}{k_{mm} q_\perp^2 + k_{33} q_\parallel^2}, \text{ with } m = 1, 2. \qquad \textbf{(2.69)}$$

The fluctuations of the optical dielectric tensor can be related to $n_1(\mathbf{q}, t)$ and $n_2(\mathbf{q}, t)$ by substituting Equation (2.67) into Equation (2.65):

$$\delta\varepsilon_{if}(\mathbf{q}, t) = \Delta\varepsilon \sum_{m=1,2} n_m(\mathbf{q}, t)[(\hat{\mathbf{e}}_m \cdot \hat{\mathbf{i}})(\mathbf{n}_0 \cdot \hat{\mathbf{f}}) + (\hat{\mathbf{e}}_m \cdot \hat{\mathbf{f}})(\mathbf{n}_0 \cdot \hat{\mathbf{i}})]$$

$$\text{or} \quad \delta\varepsilon_{if}(\mathbf{q}, t) = \Delta\varepsilon \sum_{m=1,2} G_m \, n_m(\mathbf{q}, t), \qquad \textbf{(2.70)}$$

where the geometrical factors G_1 and G_2 depend on the scattering configuration and are given by

$$G_m = (\hat{\mathbf{e}}_m \cdot \hat{\mathbf{i}})(\mathbf{n}_0 \cdot \hat{\mathbf{f}}) + (\hat{\mathbf{e}}_m \cdot \hat{\mathbf{f}})(\mathbf{n}_0 \cdot \hat{\mathbf{i}}), \text{ for } m = 1, 2. \qquad \textbf{(2.71)}$$

The intensity of the light scattered by the two modes of director fluctuations is:

$$I_S = |E_S(\mathbf{R}, t)|^2 = C_{obs} \Delta\varepsilon^2 \frac{k_B T}{V} \left(\frac{G_1^2}{k_{11} q_\perp^2 + k_{33} q_\parallel^2} + \frac{G_2^2}{k_{22} q_\perp^2 + k_{33} q_\parallel^2} \right), \qquad \textbf{(2.72)}$$

$$\text{where } C_{obs} = \left(\frac{k_s^2 E_0}{4\pi R \varepsilon_0} \right)^2. \qquad \textbf{(2.73)}$$

Note that C_{obs} is a constant depending only on the conditions of observation.

Finally, the autocorrelation function of the scattered field is expressed in terms of the autocorrelation function associated with each fluctuation mode i.e.

$$< E_S(\mathbf{R},t)E_S^*(\mathbf{R},t+\tau) > = C_{obs}\Delta\varepsilon^2 \sum_{m=1,2} G_m^2 < n_m(\mathbf{q},t)n_m(\mathbf{q},t+\tau) >, \; m = 1, 2. \qquad \textbf{(2.74)}$$

2.6.5 Relaxation of the director fluctuations

The director fluctuations $\delta\mathbf{n}(\mathbf{r}, t)$ will relax towards zero with a characteristic time. This over-damped relaxation process is predicted to be purely viscous and can be described using the following equation:[2]

$$\underbrace{\eta_m{}^{eff}(\mathbf{q})\frac{\partial}{\partial t}n_m(\mathbf{q},t)}_{\text{viscous or damping term}} + \underbrace{(k_{mm}q_\perp^2 + k_{33}q_\parallel^2)n_m(\mathbf{q},t)}_{\text{elastic restoring term } (m = 1, 2)} = 0. \qquad \textbf{(2.75)}$$

The effective viscosity $\eta_m{}^{eff}(\mathbf{q})$ associated with each mode is[2]

$$\eta_1{}^{eff}(\mathbf{q}) = \gamma_1 - \frac{(q_\perp^2\alpha_3 - q_\parallel^2\alpha_2)^2}{q_\perp^4\eta_2 + q_\perp^2 q_\parallel^2(\alpha_1 + \alpha_3 + \alpha_4 + \alpha_5) + q_\parallel^4\eta_1},$$

$$\eta_2{}^{eff}(\mathbf{q}) = \gamma_1 - \frac{\alpha_2^2 q_\parallel^2}{q_\perp^2\eta_3 + q_\parallel^2\eta_1}, \qquad \textbf{(2.76)}$$

where γ_1 is the rotational viscosity, α_i (i = 1-6) are the Leslie coefficients and η_j (j = 1-3) are the Miesowicz viscosities defined in Section 2.4.3.

Equation (2.76) can be further simplified in two specific geometries

- $\mathbf{q} \parallel \mathbf{n}$, $q_\perp = 0$:

$$\text{bend mode} \quad \eta_1{}^{eff} = \eta_2{}^{eff} = \eta_{bend} = \gamma_1 - \frac{2\alpha_2^2}{-\alpha_2 + \alpha_4 + \alpha_5} \qquad \textbf{(2.77)}$$

- $\mathbf{q} \perp \mathbf{n}$, $q_\parallel = 0$:

$$\text{splay mode} \quad \eta_1{}^{eff} = \eta_{splay} = \gamma_1 - \frac{2\alpha_3^2}{\alpha_3 + \alpha_4 + \alpha_6} \qquad \textbf{(2.78)}$$

$$\text{twist mode} \quad \eta_2{}^{eff} = \gamma_1 = \alpha_3 - \alpha_2. \qquad \textbf{(2.79)}$$

It has been established experimentally that $\gamma_1 > \eta_{splay} > \eta_{bend}$.[15]

A solution for the time dependent director fluctuations, that satisfies Equation (2.75) is:

$$n_m(\mathbf{q},t) = n_m(\mathbf{q})\exp(-\Gamma_m t)\,, \qquad \textbf{(2.80)}$$

where Γ_m is the Lorentzian frequency broadening due to mode m. Γ_m is related to the decay time τ_m and to the visco-elastic parameters via:

$$\Gamma_m = \frac{1}{\tau_m} = \frac{k_{mm}q_\perp^2 + k_{33}q_\parallel^2}{\eta_m^{\text{eff}}(\mathbf{q})}\,,\ m = 1, 2. \qquad \textbf{(2.81)}$$

This equation is important because the linewidth Γ_m is usually the experimental quantity measured in DLS experiments.

The autocorrelation function for the scattered field becomes:

$$< E_S(\mathbf{R},t)E_S^*(\mathbf{R},t+\tau) > = C_{obs}\Delta\varepsilon^2\left[G_1^2 < |n_1(\mathbf{q})|^2 > e^{-\Gamma_1\tau} + G_2^2 < |n_2(\mathbf{q})|^2 > e^{-\Gamma_2\tau}\right]. \qquad \textbf{(2.82)}$$

This equation shows that the first order autocorrelation function decays exponentially. As will be discussed in Section 2.7, the splay, twist and bend mode of director fluctuations can be isolated using particular scattering geometries, for which the autocorrelation function can be reduced to a single exponential.

2.6.6 Electric field dynamic light scattering (EFDLS)

From the measured linewidth of the scattered intensity autocorrelation function, it is only possible to obtain visco-elastic ratios. In this case, the application of an electric field to dampen the director fluctuations only couples to the viscous term. This extra energy contribution allows the accurate determination of the individual elastic constants and viscosity coefficients.[3, 27, 28, 29] The stabilising electric field is applied along the equilibrium director orientation $\mathbf{n}_0$ for materials with $\Delta\varepsilon > 0$ and perpendicular to it for materials with $\Delta\varepsilon < 0$. Only the case $\Delta\varepsilon > 0$ will be considered in the following derivation.

From Equation (2.38), the electric energy density can be obtained:

$$f_{elec} = -\frac{1}{2}\varepsilon_0\,\Delta\varepsilon\,E^2\,. \qquad \textbf{(2.83)}$$

For the pure twist and bend modes, the situation in the presence of an electric field is adequately described by this equation. However, this expression has to be modified to account for the linewidth observed experimentally for pure splay distortions. Leslie and Waters considered the coupling between an applied dc electric field and the splay mode.

They also discussed the influence of conduction and flexoelectric effects on the measured linewidth. It was shown that conduction may lead to a second decay rate in the fluctuation spectrum and that flexoelectric effects can be ignored. An outline of the Leslie and Waters' calculations will be given for the splay distortions.[30]

Suppose the electric field can be decomposed into a uniform field $\mathbf{E}_0$ and a small perturbation $\delta\mathbf{E}$:

$$\mathbf{E}(\mathbf{r},t) = E_0\mathbf{n}_0 + \delta\mathbf{E}\, e^{i(q\cdot r-\omega t)}. \tag{2.84}$$

In nematics, the local director can similarly be written as the sum of two contributions:

$$\mathbf{n}(\mathbf{r},t) = \mathbf{n}_0 + \delta\mathbf{n}\, e^{i(q\cdot r-\omega t)}, \tag{2.85}$$

where $\mathbf{n}_0$ is the average orientation and $\delta\mathbf{n}$ is a fluctuation term, such that $\mathbf{n}_0.\delta\mathbf{n}(\mathbf{r}) \approx 0$.

The angle ϕ can be defined as the angle between $\mathbf{q}$ and $\hat{e}_1$ such that

$$\mathbf{n}_0 \cdot \mathbf{q} = q\sin\phi. \tag{2.86}$$

For a non-conducting and non-magnetic medium, the Maxwell's equations for **E** and **D** become

$$\nabla\times\mathbf{E} = 0 \tag{2.87}$$

$$\text{and}\quad \nabla\cdot\mathbf{D} = 0. \tag{2.88}$$

By using Equation (2.84), Equation (2.87) can be rewritten

$$\delta\mathbf{E} = \frac{\delta E}{|\mathbf{q}|}\mathbf{q}. \tag{2.89}$$

Furthermore, substituting Equation (2.37) into Equation (2.88) yields

$$\delta E = -\frac{\Delta\varepsilon\, E_0}{\varepsilon(\phi)q}(\delta\mathbf{n}\cdot\mathbf{q}), \tag{2.90}$$

$$\text{where}\quad \varepsilon(\phi) = \varepsilon_\perp + \Delta\varepsilon\sin^2\phi. \tag{2.91}$$

For pure twist mode, $\delta\mathbf{n} = \delta n_2\hat{\mathbf{e}}_2$ and $\mathbf{q} = q_\perp\hat{\mathbf{e}}_1$ hence $\delta\mathbf{n}\cdot\mathbf{q} = 0$. For pure bend mode, $\delta\mathbf{n} = \delta n_1\hat{\mathbf{e}}_1 + \delta n_2\hat{\mathbf{e}}_2$ and $\mathbf{q} = q_{\parallel}\mathbf{n}_0$: in this case, since $\mathbf{n}_0.\delta\mathbf{n}(\mathbf{r}) \approx 0$, so $\delta\mathbf{n}\cdot\mathbf{q} = 0$. However for a splay deformation, $\delta\mathbf{n} = \delta n_1\hat{\mathbf{e}}_1$ and $\mathbf{q} = q_\perp\hat{\mathbf{e}}_1$; in this case, $\delta\mathbf{n}\cdot\mathbf{q}$ is maximum and the electric field perturbation is only coupled to the splay fluctuations in mode 1. The three cases are illustrated in Figure 2.13.

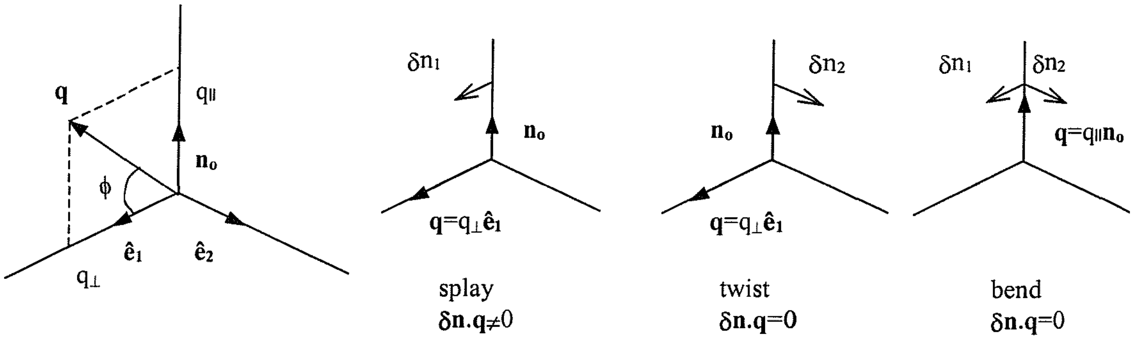

Figure 2.13: Coupling between the electric field perturbation and each fundamental distortion.

In the presence of a stabilising electric field, the scattered light intensity and the resulting frequency broadening for each fluctuation mode become:[24]

Mode 1

$$I_1 = C_{obs}\Delta\varepsilon^2 \frac{k_B T}{V} G_1^2 \left[k_{11}q_\perp^2 + k_{33}q_\parallel^2 + \frac{\varepsilon_0 \varepsilon_\parallel \Delta\varepsilon}{\varepsilon(\phi)} E^2 \right]^{-1};$$

$$\Gamma_1 = \frac{k_{11}q_\perp^2 + k_{33}q_\parallel^2}{\eta_1^{eff}(\mathbf{q})} + \left(\frac{\varepsilon_0 \varepsilon_\parallel \Delta\varepsilon}{\varepsilon(\phi)} \right) \frac{E^2}{\eta_1^{eff}(\mathbf{q})}. \qquad \textbf{(2.92)}$$

Mode 2

$$I_2 = C_{obs}\Delta\varepsilon^2 \frac{k_B T}{V} G_2^2 \left[k_{22}q_\perp^2 + k_{33}q_\parallel^2 + \varepsilon_0 \Delta\varepsilon E^2 \right]^{-1};$$

$$\Gamma_2 = \frac{k_{22}q_\perp^2 + k_{33}q_\parallel^2}{\eta_2^{eff}(\mathbf{q})} + \varepsilon_0 \Delta\varepsilon \frac{E^2}{\eta_2^{eff}(\mathbf{q})}. \qquad \textbf{(2.93)}$$

In practice, measurements of the linewidth associated with damping times are easier to implement and more accurate than measurements of the scattered intensity.[3, 24] A plot of Γ_1 or Γ_2 as a function of E^2 allows the viscosity coefficients η_1^{eff} and η_2^{eff} to be determined directly from the gradient of the curves. The visco-elastic ratios and hence the elastic constants can be deduced from the intercept of the plots at $E = 0$. $\varepsilon_\parallel$, $\varepsilon_\perp$ and $\Delta\varepsilon$ are measured from a separate experiment at the same frequency as the applied electric field.

In the heterodyne detection mode, Sefton showed that single exponential spectra were obtained for pure splay fluctuations at all amplitudes of applied ac fields and for a wide range of frequencies.[29] Nevertheless, the decay linewidth depends on the frequency of applied electric field for frequencies below 2.5 kHz. The values of dielectric permittivities are invariant in the frequency range 200 Hz-100 kHz. Above 2.5 kHz, the decay linewidth is independent of frequency and thus, accurate values for the splay elastic constant k_{11} and viscosity coefficient η_{splay} are obtained. Furthermore, conduction effects can be neglected for single exponential Lorentzian spectra and for electric fields of high enough frequency (in the kHz range). No such dependence on frequency exists for the twist or bend modes.

Equations (2.92) and (2.93) can be further simplified by using particular scattering geometries as will be demonstrated in the next section.

2.7 Experimental geometries for DLS studies

The splay, twist and bend mode can be isolated in specific scattering configurations characterised by:

- the equilibrium director alignment $\mathbf{n}_0$;
- the polarisations $\hat{\mathbf{i}}$ and $\hat{\mathbf{f}}$ of incident and scattered light such that either G_1 or G_2 can be cancelled;
- the scattering angles such that $q_\perp$ or $q_\parallel$ becomes negligible or zero.

For the experimental set up used in this work, only light at normal incidence to the cell is discussed. There are two preferred director orientations:

- homeotropic alignment with the director $\mathbf{n}_0$ normal to the substrate;
- planar or homogeneous alignment with the director $\mathbf{n}_0$ parallel to the substrate.

These orientations may be achieved by treating the glass substrates using various surface alignment agents (see Chapter 3, Section 3.2).

Van Eck investigated the available experimental geometries for the study of pure splay, twist and bend modes.[31] In the laboratory frame, the subsequent coordinate system was defined: the x-axis is chosen parallel to the incident light direction $\mathbf{k}_i$, the (x, y) plane is the scattering plane and the z-axis is perpendicular to this plane. Figure 2.14 shows schematically this geometry. In this section, Van Eck's convention has been adopted.

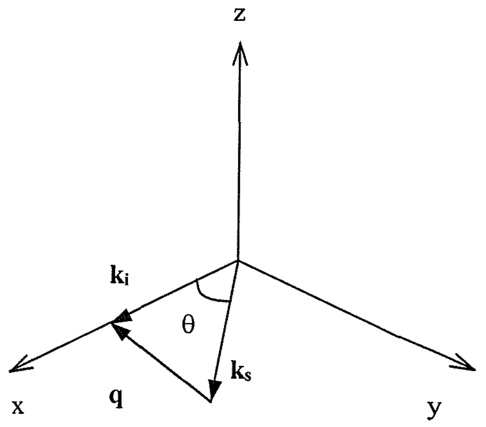

Figure 2.14: Coordinate system used by Van Eck to define the experimental geometries.

2.7.1 Homeotropic alignment

For convenience, the director orientation $\mathbf{n}_0$ is chosen parallel to the incident wavevector $\mathbf{k}_i$. In this configuration,

$$\mathbf{n}_0 = (1, 0, 0);$$

$$\hat{\mathbf{e}}_1 = \hat{\mathbf{e}}_2 \times \mathbf{n}_0 = (0, -1, 0);$$

$$\hat{\mathbf{e}}_2 = \frac{\mathbf{n}_0 \times \mathbf{q}}{q_\perp} = (0, 0, -1). \qquad \textbf{(2.94)}$$

The incoming light beam will not be refracted since it is at normal incidence to the glass walls; furthermore, it will experience the ordinary refractive index n_o of the nematic liquid crystal, whereas the output light beam scattered at an angle θ_{LC} will be refracted. If it is polarised perpendicular to the scattering plane, the scattered beam will encounter a refractive index n_o and if its polarisation is within the scattering plane then the ray will be subject to an effective refractive index[32]

$$n(\theta_{LC}) = n_o n_e (n_o^2 \sin^2 \theta_{LC} + n_e^2 \cos^2 \theta_{LC})^{-1/2}. \qquad \textbf{(2.95)}$$

To avoid any confusion, we consider two scattering angles: θ_{LC} is defined within the liquid crystal medium, while θ_{lab} is measured in the laboratory reference frame. These two angles are related via Snell's law:

$$n(\theta_{LC}) \sin\theta_{LC} = \sin\theta_{lab}. \qquad \textbf{(2.96)}$$

The polarisation or geometrical factors G_1 and G_2 are defined as:

$$G_m = \left[(\hat{\mathbf{e}}_m \cdot \hat{\mathbf{i}})(\mathbf{n}_0 \cdot \hat{\mathbf{f}}) + (\hat{\mathbf{e}}_m \cdot \hat{\mathbf{f}})(\mathbf{n}_0 \cdot \hat{\mathbf{i}})\right] \text{ for m = 1, 2.} \qquad \textbf{(2.71)}$$

To isolate mode 1 or mode 2, the input and output polarisations should be selected to cancel either G_2 or G_1. The states of polarisation are denoted VH or HH where V and H refer to the vertical (orthogonal to the scattering plane) and horizontal (within the scattering plane) polarisations, the first letter representing the plane of polarisation of the incident light and the second letter the polarisation of the scattered light.

Mode 1: splay-bend distortions (HH configuration)

Both the input and scattered light polarisations lie in the scattering plane (see Figure 2.15) and are given by

$$\hat{\mathbf{i}} = (0, 1, 0)$$

$$\text{and} \quad \hat{\mathbf{f}} = (-\sin\theta_{LC}, \cos\theta_{LC}, 0)\,. \qquad \textbf{(2.97)}$$

Then

$$G_1 = \sin\theta_{LC}$$

$$G_2 = 0\,. \qquad \textbf{(2.98)}$$

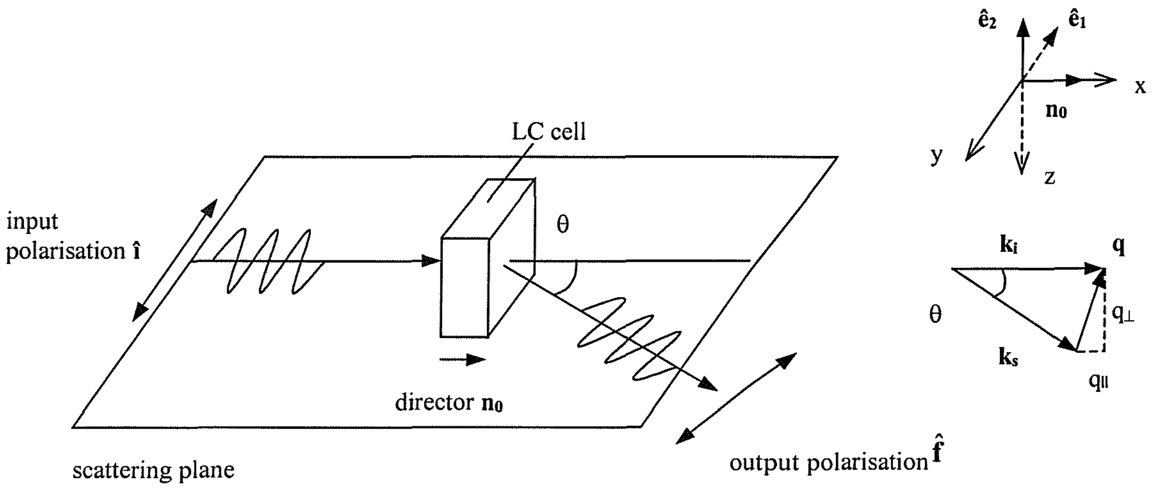

Figure 2.15: Experimental geometry for the study of pure splay distortions.

Mode 2: twist-bend deformations (VH configuration)

The incident light polarisation is perpendicular to the scattering plane while the scattered light polarisation lies in the scattering plane i.e.

$$\hat{\mathbf{i}} = (0, 0, 1)$$

$$\text{and} \quad \hat{\mathbf{f}} = (-\sin\theta_{LC}, \cos\theta_{LC}, 0)\,. \qquad \textbf{(2.99)}$$

This configuration is depicted in Figure 2.16. In this case:

$$G_1 = 0$$

$$\text{and} \quad G_2 = \sin\theta_{LC}\,. \tag{2.100}$$

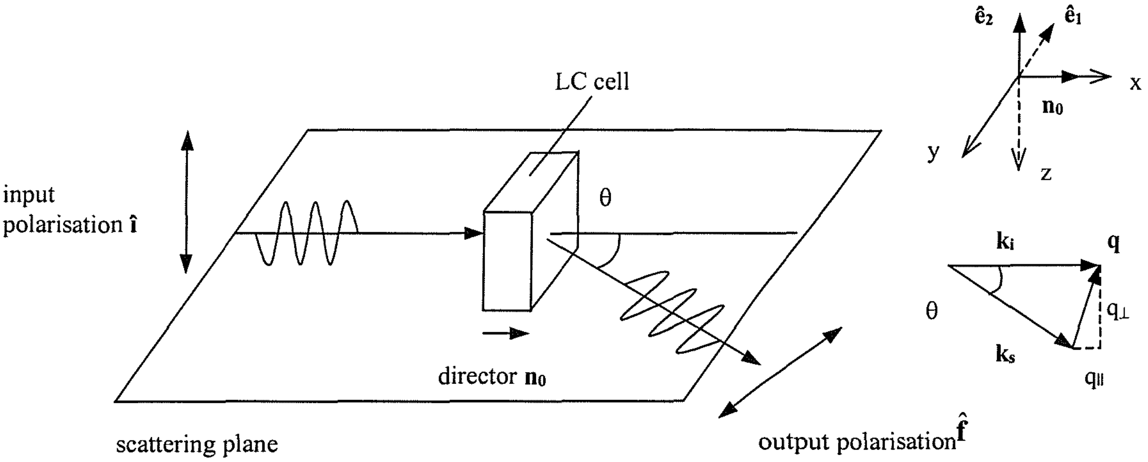

Figure 2.16: Experimental geometry for the study of pure twist distortions.

Minimisation of the bend component

The bend contribution to mode 1 or 2 can be neglected if certain restrictions are imposed on the scattering wavevector **q**. The expressions for the components $q_{||}$ and $q_\perp$ are:

$$q_{||} = \frac{2\pi}{\lambda}\left[n_o - n(\theta_{LC})\cos\theta_{LC}\right]$$

$$\text{and} \quad q_\perp = -\frac{2\pi}{\lambda} n(\theta_{LC})\sin\theta_{LC}\,. \tag{2.101}$$

In the isotropic medium approximation, $n(\theta_{LC}) = n_o = n_e$ and $k_i = k_s$. Thus

$$\frac{q_{||}^2}{q_\perp^2} = \frac{(1-\cos\theta_{LC})^2}{\sin^2\theta_{LC}}\,. \tag{2.102}$$

This function is plotted in Figure 2.17. For internal scattering angles θ_{LC} less than 15°, $q_{||}^2/q_\perp^2$ is less than 2%. Therefore, to a good approximation, $q_\perp^2 >> q_{||}^2$ and the bend contribution can be neglected.

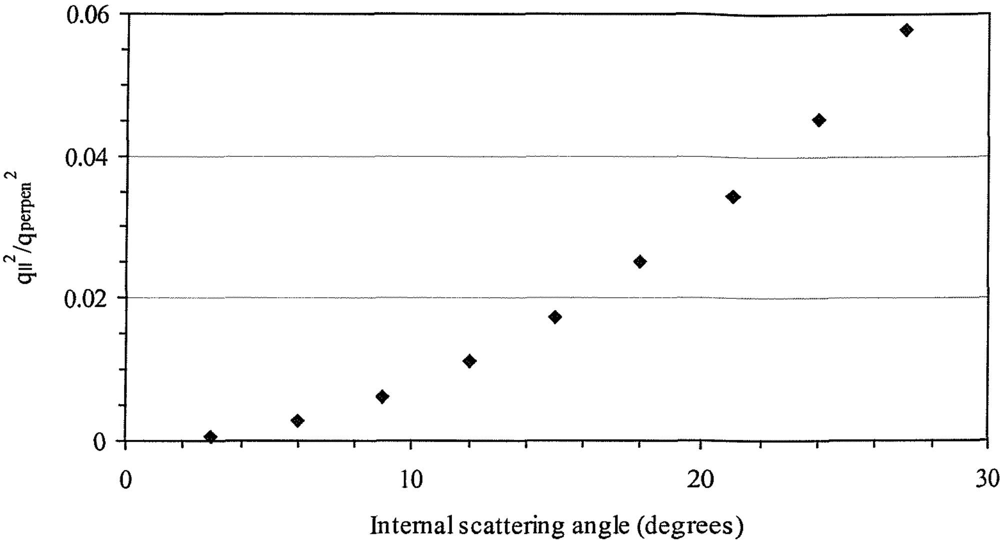

Figure 2.17: Plot of the function $q_{\|}^2/q_{\perp}^2$ versus internal scattering angle θ_{LC}.

For $\theta_{LC} < 15°$ and in the presence of an applied electric field, the linewidths for modes 1 and 2 are given by:

$$\Gamma_1 = \Gamma_{splay} = \frac{k_{11}}{\eta_{splay}} q_{\perp}^2 + \frac{\varepsilon_0 \Delta\varepsilon \varepsilon_{\|}}{\varepsilon(\phi)\eta_{splay}} E^2 \tag{2.103}$$

$$\Gamma_2 = \Gamma_{twist} = \frac{k_{22}}{\gamma_1} q_{\perp}^2 + \frac{\varepsilon_0 \Delta\varepsilon}{\gamma_1} E^2 . \tag{2.104}$$

In an isotropic medium, the angle ϕ is approximately equal to $\theta_{LC}/2$. By combining Equations (2.95) and (2.96), θ_{LC} can be obtained from the following expression:

$$\sin\theta_{LC} = (n_e \sin\theta_{lab})\,[(n_e^2 n_o^2 + (n_o^2 - n_o^2)\sin^2\theta_{lab}]^{-1/2} . \tag{2.105}$$

In practice, the scattering angles in the laboratory frame θ_{lab} are easily measured and the refractive indices are determined via a separate technique, described in Chapter 3 Section 3.5.

2.7.2 Planar alignment

Director normal to the scattering plane

In this scattering geometry, sketched in Figure 2.18, the scattering wavevector is perpendicular to $\mathbf{n}_0$ and consequently $q_{\|} = 0$. Its expression is given by

$$\mathbf{q} = (q_x, q_y, 0), \text{ with } |\mathbf{q}| = q_{\perp} = (q_x^2 + q_y^2)^{1/2} . \tag{2.106}$$

Van Eck's coordinate system becomes

$$\mathbf{n}_0 = (0, 0, 1);$$

$$\hat{\mathbf{e}}_1 = \hat{\mathbf{e}}_2 \times \mathbf{n}_0 = \frac{1}{q_\perp}(q_x, q_y, 0);$$

$$\hat{\mathbf{e}}_2 = \frac{\mathbf{n}_0 \times \mathbf{q}}{q_\perp} = \frac{1}{q_\perp}(-q_y, q_x, 0). \qquad \textbf{(2.107)}$$

The polarisations of incident and scattered light are respectively normal and parallel to the scattering plane (refer to Figure 2.18) i.e.

$$\hat{\mathbf{i}} = (0, 0, 1)$$

$$\text{and} \quad \hat{\mathbf{f}} = (-\sin\theta_{LC}, \cos\theta_{LC}, 0). \qquad \textbf{(2.108)}$$

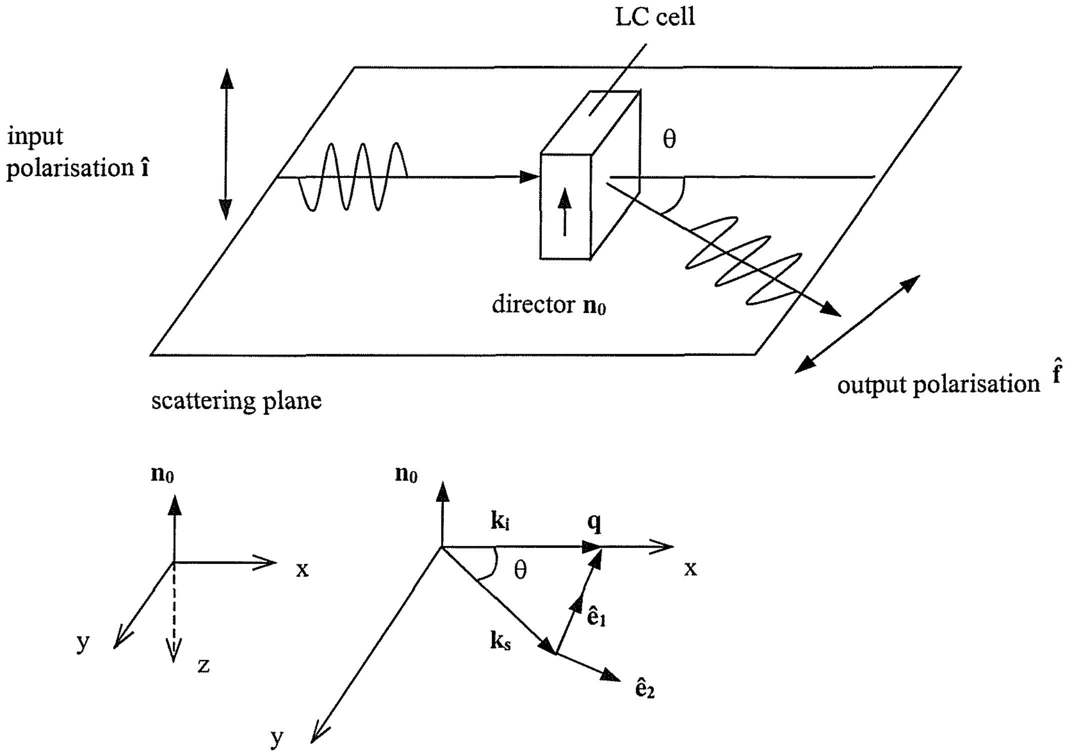

Figure 2.18: Experimental geometry for the study of pure splay distortions.

The polarisation factors G_1 and G_2 are derived from Equation (2.71) as:

$$G_1 = \frac{-q_x \sin\theta_{LC} + q_y \cos\theta_{LC}}{(q_x^2 + q_y^2)^{1/2}};$$

$$G_2 = \frac{q_y \sin\theta_{LC} + q_x \cos\theta_{LC}}{(q_x^2 + q_y^2)^{1/2}}. \qquad \textbf{(2.109)}$$

By expressing the components of q_x and q_y in the coordinate system (x, y, z), we obtain:

$$G_1 = \frac{-n_e \sin\theta_{LC}}{(n_e^2 + n_o^2 - 2n_e n_o \cos\theta_{LC})^{1/2}};$$

$$G_2 = \frac{n_e \cos\theta_{LC} - n_o}{(n_e^2 + n_o^2 - 2n_e n_o \cos\theta_{LC})^{1/2}}. \qquad \mathbf{(2.110)}$$

At a specific angle $\theta_{LC}^{splay} = \cos^{-1}(n_o / n_e)$, $G_2 = 0$ and thus pure splay distortions can be studied. The linewidth is given by:

$$\Gamma_{splay} = \frac{k_{11}}{\eta_{splay}} q_\perp^2 + \frac{\varepsilon_0 \Delta\varepsilon\varepsilon_{\|}}{\varepsilon(\theta_{LC}/2)\eta_{splay}} E^2, \qquad \mathbf{(2.103)}$$

with $q_\perp = \frac{2\pi}{\lambda}(n_e^2 - n_o^2)^{1/2}$.

This expression for the splay linewidth is identical to the one derived in the homeotropic case.

Director in the scattering plane

The coordinate system becomes:

$$\mathbf{n}_0 = (0, 1, 0);$$

$$\hat{\mathbf{e}}_1 = \hat{\mathbf{e}}_2 \times \mathbf{n}_0 = (1, 0, 0);$$

$$\hat{\mathbf{e}}_2 = \frac{\mathbf{n}_0 \times \mathbf{q}}{q_\perp} = (0, 0, -1). \qquad \mathbf{(2.111)}$$

The scattering wavevector **q** can be written as

$$\mathbf{q} = (q_\perp, q_\|, 0). \qquad \mathbf{(2.112)}$$

The polarisations of the incoming and scattered light are given by

$$\hat{\mathbf{i}} = (0, 0, 1)$$

$$\text{and} \quad \hat{\mathbf{f}} = (-\sin\theta_{LC}, \cos\theta_{LC}, 0). \qquad \mathbf{(2.113)}$$

This experimental configuration is illustrated in Figure 2.19. The resulting polarisation factors are

$$G_1 = 0$$

$$\text{and} \quad G_2 = -\cos\theta_{LC}. \qquad \mathbf{(2.114)}$$

The components of **q** can be deduced using the expression of $\mathbf{k}_i$ and $\mathbf{k}_s$:

$$q_{\perp} = (2\pi/\lambda)(n_o - n(\theta_{LC})\cos\theta_{LC})$$

$$\text{and} \quad q_{\parallel} = -(2\pi/\lambda)n(\theta_{LC})\sin\theta_{LC}, \qquad \textbf{(2.115)}$$

where $$n(\theta_{LC}) = n_o n_e (n_e^2 \sin^2\theta_{LC} + n_o^2\cos^2\theta_{LC})^{-1/2}. \qquad \textbf{(2.116)}$$

The bend deformations can be isolated when $q_{\perp} = 0$, which occurs at an angle defined by:

$$\theta_{LC}^{bend} = \cos^{-1}\left[\frac{n_e}{(2n_e^2 - n_o^2)^{1/2}}\right]. \qquad \textbf{(2.117)}$$

The linewidth becomes

$$\Gamma_{bend} = \frac{k_{33}}{\eta_{bend}} q_{\parallel}^2 + \frac{\varepsilon_0\Delta\varepsilon}{\eta_{bend}} E^2, \qquad \textbf{(2.118)}$$

$$\text{with} \quad q_{\parallel} = \frac{2\pi}{\lambda}(n^2(\theta_{LC}) - n_o^2)^{1/2}. \qquad \textbf{(2.119)}$$

There is another geometry, also represented in Figure 2.19, which is available to investigate the pure bend mode at low scattering angles;[31, 33] both input and output light polarisations are in the scattering plane i.e.

$$\hat{\mathbf{i}} = (0, 1, 0)$$

$$\text{and} \quad \hat{\mathbf{f}} = (-\sin\theta_{LC}, \cos\theta_{LC}, 0). \qquad \textbf{(2.120)}$$

In this case, the polarisation factors are:

$$G_1 = -\sin\theta_{LC}$$

$$\text{and} \quad G_2 = 0. \qquad \textbf{(2.121)}$$

The two components of scattering wavevector **q** are given by

$$q_{\perp} = (2\pi/\lambda)(n_e - n(\theta_{LC})\cos\theta_{LC})$$

$$\text{and} \quad q_{\parallel} = -(2\pi/\lambda)n(\theta_{LC})\sin\theta_{LC}. \qquad \textbf{(2.122)}$$

In the isotropic approximation, the function

$$\frac{q_{\perp}^{2}}{q_{\parallel}^{2}} = \frac{(1-\cos\theta_{LC})^2}{\sin^2\theta_{LC}} \qquad \textbf{(2.123)}$$

can be plotted against the scattering angle θ_{LC}. The roles of $q_{\parallel}$ and $q_{\perp}$ have been inverted compared to the homeotropic case (recall Equation (2.102)). For scattering angles θ_{LC} less than 15°, $q_{\perp}^2 << q_{\parallel}^2$ and the splay component of mode 1 can be ignored.

The linewidth for the pure bend distortions is given by Equation (2.118). However, in this configuration, there will be a minor contribution from the splay mode, since $q_{\perp} \neq 0$. Furthermore, the noise factor will be greater because of the parallel polariser arrangement.

The detection process for these two geometries is discussed below:

- Mode 1: Both input and scattered light polarisations are in the ($\mathbf{n_0}$, $\mathbf{q}$) plane (HH configuration) at low scattering angles θ_{lab} in the laboratory frame. For $\theta_{lab} \leq 10°$, the scattered light beats with the intense unshifted light in the $\theta_{lab} = 0°$ direction and full heterodyning occurs.[34]
- Mode 2: The incident and scattered light polarisations are respectively normal and parallel to the ($\mathbf{n_0}$, $\mathbf{q}$) plane (VH configuration) at sufficiently large θ_{lab}. In this case, the measured signal is purely homodyne and by recombining the scattered beam with a portion of unscattered light derived from the same laser source, heterodyne detection could be employed.[34]

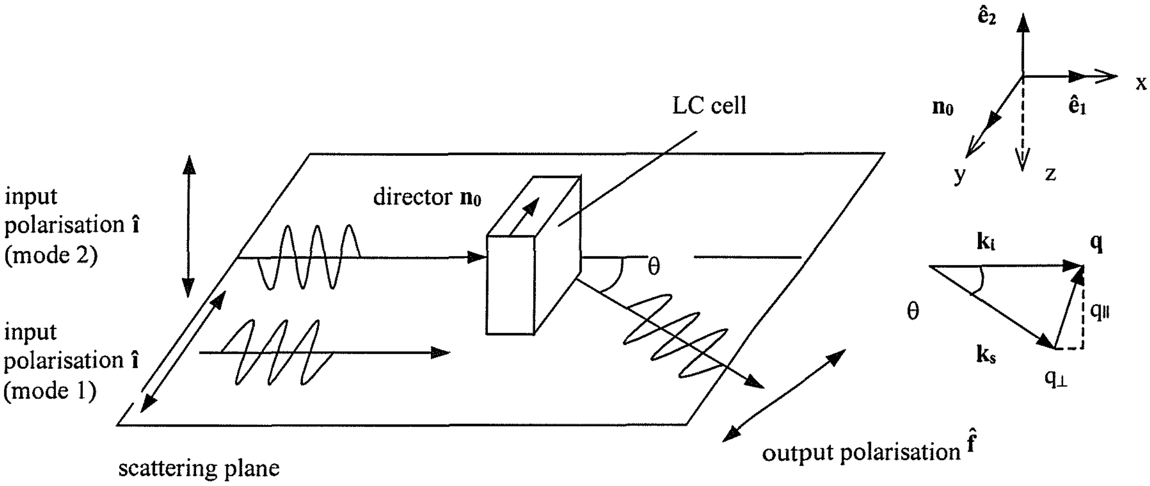

Figure 2.19: Experimental geometries for the study of pure bend distortions; the two input polarisations corresponding to mode 1 (HH geometry) and to mode 2 (VH geometry) are included in the same figure.

2.8 Conclusions

In this chapter, the relevant physical properties of nematic liquid crystals have been introduced and related to theoretical models.

First, the order parameter has been defined as

$$S = \left(1 - \frac{T}{T^*}\right)^{\beta}, \qquad \textbf{(2.2)}$$

where the exponent β and the temperature T^* are calculated using Haller's method and S is deduced from measured refractive indices.

The static dielectric permittivities parallel and normal to the director $\varepsilon_{||}$ and $\varepsilon_{\perp}$ have been derived from the Maier and Meier's theory. For polar LC molecules, the sign of the resulting dielectric anisotropy depends on the relative contributions of the dipolar term and of the polarisability term.

The free energy density (per unit volume) associated with the three fundamental elastic deformations can be expressed in terms of curvature strains of the director as

$$\begin{aligned} &\text{for splay} \quad f_{\text{splay}} = k_{11}(\nabla.\mathbf{n})^2, \\ &\text{for twist} \quad f_{\text{twist}} = k_{22}[\mathbf{n}.(\nabla \times \mathbf{n})]^2, \qquad \textbf{(2.124)} \\ &\text{for bend} \quad f_{\text{bend}} = k_{33}[\mathbf{n} \times (\nabla \times \mathbf{n})]^2, \end{aligned}$$

where k_{11}, k_{22} and k_{33} are the corresponding Frank elastic constants.

The Freedericksz transition describes the coupling of a magnetic or electric field to a uniformly aligned sample of nematic LC and this allows in principle each elastic constant to be determined separately using specific configurations. The magnetic field is applied in a direction perpendicular to the initial orientation of the nematic director. In this case, the field-induced reorientation of the LC molecules occurs above a threshold or critical field given by

$$(B_C)_i = \frac{\pi}{d}\left(\frac{k_{ii}\mu_0}{\Delta\chi}\right)^{1/2} \quad i = 1, 2, 3. \qquad \textbf{(2.34)}$$

For electric fields applied across the cell, the critical voltage can similarly be written

$$V_C = \pi\left(\frac{k_{ii}}{|\Delta\varepsilon|\varepsilon_0}\right)^{1/2} ; \qquad \textbf{(2.125)}$$

i = 1 for $\Delta\varepsilon > 0$ materials using planar aligned samples; i = 3 for $\Delta\varepsilon < 0$ materials using homeotropic aligned samples.

The theory associated with dynamic light scattering from nematic LCs has been examined thoroughly. The linewidths associated with the relaxation of the director fluctuations can easily be measured in DLS experiments. For each single mode, the linewidths become simply

$$\Gamma_{\text{splay}} = \frac{k_{11}}{\eta_{\text{splay}}} q_\perp^2 + \frac{\varepsilon_0 \Delta\varepsilon \varepsilon_{\parallel}}{\varepsilon(\theta_{LC}/2)\eta_{\text{splay}}} E^2, \qquad \textbf{(2.103)}$$

$$\Gamma_{\text{twist}} = \frac{k_{22}}{\gamma_1} q_\perp^2 + \frac{\varepsilon_0 \Delta\varepsilon}{\gamma_1} E^2, \qquad \textbf{(2.104)}$$

and $$\Gamma_{\text{bend}} = \frac{k_{33}}{\eta_{\text{bend}}} q_{\parallel}^2 + \frac{\varepsilon_0 |\Delta\varepsilon|}{\eta_{\text{bend}}} E^2, \qquad \textbf{(2.118)}$$

$\varepsilon(\theta_{LC}/2) = \varepsilon_\perp + \Delta\varepsilon \sin^2(\theta_{LC}/2)$

and $\sin\theta_{LC} = (n_e \sin\theta_{lab})\,[(n_e^2 n_o^2 + (n_e^2 - n_o^2)\sin^2\theta_{lab}]^{-1/2}$;

θ_{lab} is the scattering angle measured in the laboratory; n_e and n_o are the extraordinary and ordinary refractive indices of the nematic liquid crystal. The splay, twist and bend viscosities are related to the Leslie coefficients α_i with i = 1-6 in the following way:

$$\eta_{\text{splay}} = \gamma_1 - \frac{2\alpha_3^2}{\alpha_3 + \alpha_4 + \alpha_6}, \qquad \textbf{(2.78)}$$

$$\gamma_1 = \alpha_3 - \alpha_2, \qquad \textbf{(2.27)}$$

$$\eta_{\text{bend}} = \gamma_1 - \frac{2\alpha_2^2}{-\alpha_2 + \alpha_4 + \alpha_5}. \qquad \textbf{(2.77)}$$

The measurement of the frequency broadening allows the determination of the visco-elastic ratios. If an electric field is applied to quench the director fluctuations, the elastic constants and viscosity coefficients can be derived individually.

There are several possible scattering geometries to isolate each mode. In this thesis, the pure splay and twist modes associated with director fluctuations are studied using the configuration given below:

- homeotropic cells
- HH or VH polarisation states respectively
- scattering angles θ_{LC} less than 15° to minimise the bend contribution.

The bend mode can be isolated from either mode 2 or mode 1 using planar aligned samples using the scattering geometries shown in the table below:

Mode 2	Mode 1
VH polarisations $\theta_{LC}^{bend} = \cos^{-1}(n_o / n(\theta_{LC}))$	HH polarisations scattering angles $\theta_{LC} < 15°$

This time, $n(\theta_{LC}) = n_o n_e (n_e^2 \sin^2 \theta_{LC} + n_o^2 \cos^2 \theta_{LC})^{-1/2}$.

Although the values measured with VH polarisations are less noisy and more accurate, measurements of the bend visco-elastic constants in this scattering geometry are difficult with the current DLS spectrometer (see Chapter 3 Section 3.3) due limitations in the range of accessible scattering angles.

Experimental requirements, considered in the next chapter, will ultimately decide which technique is more accurate and/or easier to implement, depending on the LC material and on the type of deformation under investigation. For instance, DLS in the presence of an electric field is particularly suitable to measure accurately values of k_{11}, η_{splay}, k_{22} and γ_1 using cells with homeotropic configuration.

REFERENCES

[1] Haller I., *Prog. Solid St. Chem.*, **10**, pp. 103-118 (1975)

[2] de Jeu W. H., *Physical Properties of Liquid Crystalline Materials*, Gordon and Breach, New-York (1980)

[3] Coles H. J., Chapter 4 in *The Optics of Thermotropic Liquid Crystals*, edited by Elston S. and Sambles R., Taylor and Francis, London (1998)

[4] Tough R. J. A. and Bradshaw M. J., *J. Physique*, **44**, pp. 447-454 (1983)

[5] Blinov L. M., *Electro-Optical and Magneto-Optical Properties of Liquid Crystals*, John Wiley and Sons Ltd, Chichester (1983)

[6] Urban S., Chapter 6 in *Physical Properties of Liquid Crystals: Nematics*, pp. 267-276, edited by Dunmur D. A., Fukuda A. and Luckhurst G. R., INSPEC publication, London, (2001)

[7] Dunmur D. A., Hitchen D. A. and Hong Xi-Jun, *Mol. Cryst. Liq. Cryst.*, **140**, pp. 303-308 (1986)

[8] de Gennes P. G., and Prost J., *The Physics of Liquid Crystals*, 2nd edition, Oxford Science Publications, Oxford (1993)

[9] Chandrasekhar S., *Liquid Crystals*, 2nd edition, Cambridge University Press, Cambridge (1992)

[10] Frank F. C., *Disc. Faraday Soc.*, **25**, pp. 19-28 (1958)

[11] Stannarius R., Chapter 3 in the *Handbook of Liquid Crystals*, **2A**, pp. 60-90, edited by Demus D., Goodby J., Gray G. W., Spiess H.-W. and Vill V., Wiley-VCH, New-York (1998)

[12] Tritton D. J., Chapters 5 and 6 in *Physical Fluid Dynamics*, Van Nostrand Reinhold, New-York (1977)

[13] Miesowicz M., *Nature*, **158**, pp. 27 (1946)

[14] Helfrich W., *J. Chem. Phys.*, **50**, pp. 100 (1969)

[15] Orsay Liquid Crystal Group, *Mol. Cryst. Liq. Cryst.*, **13**, pp. 187-191 (1971)

[16] Chen G-P., Takezoe H. and Fukuda A., *Liq. Cryst.*, **5(1)**, pp. 341-347 (1989)

[17] Freedericksz V. and Zolina V., *Trans. Faraday Soc.*, **29**, pp. 919-930 (1933)

[18] Bradshaw M. J., Raynes E. P., Bunning J. D., and Faber, T.E., *J. Physique*, **46**, pp. 1513-1520 (1985)

[19] Allinson H. and Gleeson H. F., *J. Mater. Chem.*, **5(12)**, pp. 2139-2144 (1995)

[20] Dunmur D. A. and Toriyama K., Chapter 7 in the *Handbook of Liquid Crystals*, **1**, pp. 204-214, edited by Demus D., Goodby J., Gray G. W., Spiess H.-W. and Vill V., Wiley-VCH, New-York (1998)

[21] Helfrich W., *Mol. Cryst. Liq. Cryst.*, **21**, pp. 187-209 (1973)

[22] Berne B. J. and Pecora R., Chapters 1-4 in *Dynamic Light Scattering*, Wiley, New-York (1976)

[23] Lorrain P. and Corson D., *Electromagnetic Fields and Waves*, 2nd edition, W.H. Freeman and Company, New-York (1970)

[24] Birtwistle P., PhD Thesis, University of Manchester (1995)

[25] Groupe d'Etude des Cristaux Liquides, *J. Chem. Phys.*, **51(2)**, pp.816-822 (1969)

[26] de Gennes P. G., *C.R. Acad. Sc. Paris*, **266**, pp. B15-B17 (1968)

[27] Martinand J. L. and Durand G., *Sol. State Comm.*, **10**, pp. 815-818 (1972)

[28] Coles H. J. and Sefton M. S., *Mol. Cryst. Liq. Cryst. Lett.*, **1(5)**, pp. 151-157 (1985)

[29] Coles H. J. and Sefton M. S., *Mol. Cryst. Liq. Cryst. Lett.*, **3(3-4)**, pp. 63-68 (1986)

[30] Leslie F. M. and Waters C. M., *Mol. Cryst. Liq. Cryst.*, **123**, pp. 101-117 (1985)

[31] Van Eck D. C., PhD Thesis, University of Utrecht, Netherlands (1979)

[32] Dunmur D. A., Chapter 7 in *Physical Properties of Liquid Crystals: Nematics*, pp. 315-332, edited by Dunmur D. A., Fukuda A. and Luckhurst G. R., INSPEC publication, London, (2001)

[33] Hirakata J. I., Chen G. P., Toyooka T., Kawamoto S., Takezoe H. and Fukuda, A., *Jap. J. Appl. Phys.*, **25(7)**, pp. L607-L610 (1986)

[34] Orsay Liquid Crystal Group, *Phys. Rev. Lett.*, **22**, pp. 1361-1363(1969)

CHAPTER 3: EXPERIMENTAL APPARATUS AND TECHNIQUE

3.1 Introduction

This chapter describes the different experimental techniques employed in the course of this work to measure the physical parameters defined in Chapter 2. The first part deals with the sample preparation and characterisation. In Section 3.3, the apparatus used for dynamic light scattering (DLS) is presented. Section 3.4 introduces the Freedericksz transition (FT) set-up. The next two sections, 3.5 and 3.6, are dedicated respectively to the measurements of refractive indices and of dielectric constants.

3.2 Sample preparation and characterisation

3.2.1 Uniform alignment of the liquid crystal director

All the experiments discussed in this chapter require well-aligned samples:

- homeotropic cells where the director is perpendicular to the glass substrates
- planar (or homogeneous) cells where the director is parallel to the glass plates.

Homeotropic orientation

Surfactants are generally used to induce homeotropic alignment of liquid crystals. Surfactant molecules are made of two antagonistic parts: a polar (ionic or non-ionic) head group and long aliphatic carbon tails. The head group anchors itself to the glass substrate by polar interactions while the alkyl chains bind to the nematic molecules via steric interactions and force them to lie normal to the glass surface.[1, 2]

In this thesis, two different surfactant solutions were investigated:

- 0.25% wt/wt lecithin in chloroform[3]
- 1 g/100 ml cetyltrimethylammonium bromide (CTAB) in methanol.[1, 2]

These surfactant molecules do not react chemically with the surface of the glass and can be removed easily with acetone. Below 90 °C, lecithin gives a good and uniform homeotropic orientation for most low molar mass mesogens. Above this temperature, the lecithin starts to decompose and the uniform alignment may be destroyed. An alternative solution for the study of homeotropically-aligned high temperature liquid crystalline materials is to employ CTAB, which can withstand temperatures of up to 300 °C. Nevertheless, the quality of alignment is not as good as with lecithin; the texture appears grainy when viewed by polarising microscopy. Furthermore, problems may arise when electric fields are applied since CTAB is an ionic compound. Therefore, lecithin was employed as a homeotropic aligning agent for most materials investigated in this thesis. To deposit the alignment layer, a 0.25% wt/wt solution of lecithin in chloroform was drawn across the ITO surface of the glass plates using a lens cleaning tissue.

Planar orientation

Planar alignment is generally achieved by first coating the glass substrates with a polymer or surfactant and then by rubbing the treated surfaces unidirectionally to create a series of parallel microgrooves.[1] The liquid crystalline rod-like molecules will tend to orient parallel to the grooves since this corresponds to the lowest energy configuration. In order to form a polymeric planar alignment layer, a solution of 1% wt/wt of poly-vinyl alcohol (PVA) in deionised water was rubbed onto the glass plates and allowed to dry on a heating stage. A slide wrapped with lens cleaning tissue and impregnated with PVA was drawn parallel to the long edge of the cell using a guide to create straight microgrooves.

3.2.2 Cells used in DLS experiments: fabrication procedure

For DLS measurements, it is crucial to ensure that the sample cells are free from impurities. Thus, all cells were cleaned and prepared in a dust-free environment provided by an on-site clean room, specifically designed for working with liquid crystals.

To make the cells, glass carrying on one side an electrically conductive layer of indium-tin-oxide (ITO) was cut into rectangular pieces of 10 mm by 20 mm, using a diamond scriber and a ruler. These glass plates were wiped clean with a tissue to remove glass particles and then immersed for an hour in acetone to remove organic contaminants. The glass slabs were rinsed with distilled water and dried with a nitrogen air gun. The resistivity of the ITO side of the glass, measured with a multimeter, was found to be about 50 Ω per cm^2. At this stage, the alignment layer was applied to the conducting layer of the glass substrates by the techniques explained in the previous section. The spacers used were glass fibres of 43 μm diameter. Previous studies showed that above 40 μm, the measured visco-elastic ratio is independent of cell thickness and of scattering angle.[4]

Then, the two glass spacers were coated with rapid Araldite Epoxy glue and placed parallel to the long side of the glass at about 1 or 2 mm from each edge. The cell was assembled by positioning a second glass plate over the first with a small longitudinal displacement. Pressure was applied in different points of the cell in order to obtain parallel walls. This was achieved by checking under a sodium lamp ($\lambda = 589.6$ nm) the number of interference fringes across the cell. After approximately 20 minutes, the cell could be handled and more glue was applied to seal its edges, leaving two small gaps at each end.

Afterwards, the cell was heated to about 80 °C for at least 12 hours to ensure that the glue had fully cured. Otherwise, uncured glue would contaminate the liquid crystal material, modifying its physical properties, in particular causing a significant drop in its nematic-to-isotropic temperature.[4] The cell fabrication process is summarised in Figure 3.1.

Prior to filling, the LC sample was left under vacuum conditions to de-gas. The cell was filled by capillary action at a temperature above the material's clearing point; this was done to reduce the viscosity of the sample thereby increasing the rate at which the cell fills and, more importantly, to avoid flow alignment of the director. Before sealing the cells with rapid Araldite Epoxy glue, an air pocket was created by blowing compressed gas into the cell to prevent any contact between the LC and the glue.

Finally, thin wires were soldered to the ITO substrates using molten indium to enable the application of electric fields to the sample cell. A film of PTFE tape was wrapped around the connections to provide good electrical insulation.

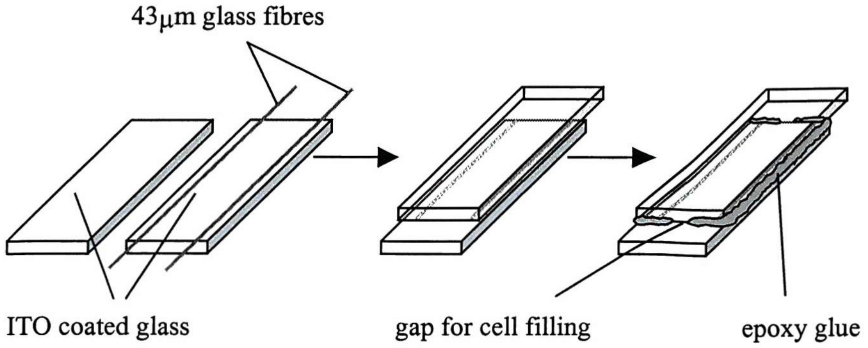

Figure 3.1: Cell fabrication procedure.

3.2.3 Cells used for other measurements

Freedericksz transition

In this work, the magnetic Freedericksz transition is usually performed to determine the bend elastic constant k_{33}, which requires homeotropically-aligned samples to be utilized. In order to measure the threshold field independently of any surface effects caused by the anchoring strength between the liquid crystal/surfactant/ITO glass interfaces, the thickness of the cells should be at least 40-50 μm.[5] Since the sample holder could accommodate cells of dimensions 10 mm by 20 mm, the cells used for FT are the same as the ones prepared for DLS experiments.

Dielectric constants

Accurate measurements of dielectric constants are ensured by employing cells with a well-defined electrode area. The Lucid cells manufactured by EEV[6] were available for the course of this work; their thickness is about 7.5 μm and they have a square active electrode area of 5 mm by 5 mm. Both the empty and filled cell capacitances are increased when measured in thinner cells since the capacitance is inversely proportional to cell thickness d. Furthermore, previous studies showed that in thin cells, the edge effects are minimised.[7]

The measurements of dielectric constants require homeotropic and planar alignment to determine respectively the dielectric components parallel $\varepsilon_{\parallel}$ and normal $\varepsilon_{\perp}$ to the director. The planar Lucid cells are supplied with a polyimide layer, which orients the liquid crystal molecules along the diagonal of the cell. Lucid cells without aligning agent were also available and they were filled by capillary action with the solution of 0.25% wt/wt lecithin in chloroform to obtain a homeotropic alignment layer. Short leads soldered to the Lucid cell allow the application of a probe voltage for the capacitance measurements.

3.2.4 Quality assessment and measurement of clearing points

After filling, the cells were inspected using an Olympus[8] BH-2 model microscope between crossed polarisers. The samples were placed on a Linkam[9] heating stage, directly mounted onto the microscope's rotation stage. This allows the quality of the alignment and the absence of impurities or disclinations in the cell to be checked. Cells with poor alignment i.e. those containing large domains with different director orientations were discarded. This thesis is mainly concerned with birefringent materials that exhibit a uniaxial nematic phase with the optic axis along the nematic director.

As the cell is rotated, planar-aligned samples exhibit a minimum in transmitted light intensity when the LC molecules lie parallel to either axis of the polarisers. Good homeotropic orientation is characterised by a uniformly dark texture between crossed polarisers. The texture should remain unchanged upon rotation of the cell, indicating that the optic axis is perpendicular to the glass substrates.

The uniaxial symmetry of homeotropically aligned cells can be assessed by conoscopy. A conoscopic figure is a characteristic interference pattern produced by the illumination of the sample with strongly convergent light. Experimentally, the polarising microscope can be employed as a conoscope by inserting a Bertrand lens between the analyser and the eyepiece to magnify the birefringence pattern formed by focusing light onto the material. As illustrated in Figure 3.2, when viewed between crossed polarisers the conoscopic figure of a homeotropic cell appears as a symmetric black or grey cross, which is invariant when the cell is rotated. Any deviation of the optic axis is seen as a non-symmetric pattern that changes with rotation of the sample. In this work, this technique is utilized in order to check if a dark optical texture can be attributed to a homeotropically aligned sample.

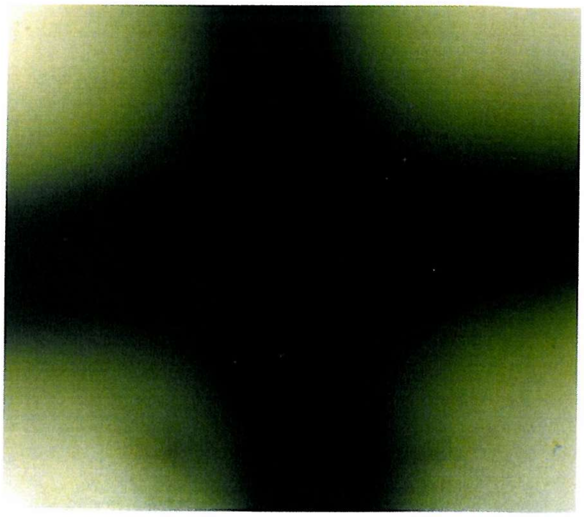

Figure 3.2: Conoscopic figure obtained for a homeotropic cell filled with 5CB.

The nematic-isotropic transition temperatures T_{NI} were measured using the heating stage on the polarising microscope and 7.5 μm planar Lucid cells.[6] The heating rate of the Linkam heating stage was 0.2 °C/min. The temperature of the Linkam can be controlled to an accuracy of ± 0.1 °C via the temperature controller TMS 90.[9]

3.2.5 Differential scanning calorimetry (DSC)

The temperature, nature and enthalpy of a given phase transition can be determined by differential scanning calorimetry or DSC. This technique is generally used as a complementary tool to polarising microscopy. In DSC experiments, the sample is heated or cooled at the same rate as an empty pan, taken as a reference. The energy flow into or out of the sample is monitored against the energy input into the reference as the temperature is changed.

DSC measurements were performed using a Perkin Elmer DSC 7.[10] Software supplied with the apparatus allows the experiment to be computer-controlled. The instrument calibration is carried out with indium. 5-10 mg of LC sample is weighed into a small aluminium pan. For the mesogenic materials investigated in this thesis, the temperature scan was performed at a heating/cooling rate of 5 °C/min over a temperature range of – 40 °C to 200 °C. The transition temperature and enthalpy are determined respectively as the onset and the peak area of the heat flow curve.[10]

3.2.6 UV-Visible spectrometer

A Hewlett Packard HP 8453 UV-Visible spectrophotometer[11] is employed to measure cell thicknesses and to record the absorption spectra of the dichroic materials, studied in Chapter 5. The built-in illumination sources are deuterium and tungsten lamps for ultraviolet and visible light respectively. The detector consists of a photodiode array, aligned with the incident beam, which detects wavelengths in the range 190 nm to 1100 nm with a resolution of 1 nm. The instrument is computer-controlled and the software displays the absorbance or transmittance spectra relative to a reference measurement.

Determination of cell thickness

In dynamic light scattering and Freedericksz transition experiments in the presence of an electric field, it is important to define accurately the applied electric field from the following relation:

$$E = \frac{V}{d}, \tag{3.1}$$

where V is the applied rms voltage and d is the distance between the two electrodes. Since the electrodes are the conductive surfaces of the glass substrates, the electrode gap d is equal to the cell thickness.

Cell thicknesses were determined by an interference method using the UV-Visible spectrophotometer. First, a reference measurement is run to correct for the background noise and to calibrate the instrument. The cell is placed normal to the incident beam and a uniform area is isolated by using a mask. As the wavelength λ is scanned (typically from 700 nm to 900 nm for a 45 μm cell), the transmitted intensity shows interference peaks and troughs that satisfy:

$$m\lambda_m = 2n_{cell}d, \tag{3.2}$$

where m is the peak (or valley) order corresponding to the wavelength λ_m and n_{cell} is the refractive index of the material inside the cell with $n_{cell} = 1$ for an empty cell.

Thus, the cell thickness d can be deduced from a linear fit of m plotted as a function of $2/\lambda_m$. For the cells used in this study, 44.0 μm < d < 46.0 μm; this indicates a good reproducibility in cell thickness during the fabrication process. The deviation from true parallelism is estimated to be of the order of 1 to 2 μm for cells with typically three to five broad interference fringes across their area. Therefore, the uncertainty in the measured cell thickness is about 5%. However, this variation will not influence the measurements since both DLS and FT techniques require only a very small area of sample, which is limited by the size of the laser beam spot (~ 0.1 mm).

Absorption spectra

In this instance, spectra are recorded at different temperatures (ranging from ambient to 45 °C) by inserting a Mettler FP82[12] sample stage into the light path. The controller FP80 allows the temperature to be set with an accuracy of 0.1 °C. The sample cell is securely enclosed between two heating elements, perforated with a 2 mm aperture. The Mettler heating stage, mounted on its side, is positioned within the spectrometer. It is crucial to ensure that the aperture of the stage is centred with respect to the light beam and also that the cell lies normal to the beam's direction.

A polaroid sheet is added in front of the light source. Lucid cells[6] with planar alignment and thickness of 7.5 μm are filled with dye guest-host materials. The absorbance spectra parallel $A_{\parallel}$ and perpendicular $A_{\perp}$ to the director can be observed by changing the pass direction of the polariser. Prior to any measurements, a reference measurement is recorded by using the Mettler stage containing a Lucid cell filled with the host LC material.

3.3 Light scattering experiment

Figure 3.3 (a) and Figure 3.3 (b) show two photographs of the experimental set-up utilized in this work. The light scattering spectrometer has four main components: a laser light source, the input and heterodyne optics, the sample holder and finally the collection optics. The detection equipment consists of a photomultiplier tube, an amplifier-discriminator unit and a correlator. The data from the correlator are collected and analysed using a PC computer. The spectrometer and detection equipment are depicted schematically in Figure 3.4. The alignment of the spectrometer and of the sample cell is essential to guarantee that reliable data are obtained. A description of the alignment procedure as well as an outline of the calibration procedure will be given in Chapter 4, Section 4.2.

(a) Overview of the light scattering apparatus and detection equipment

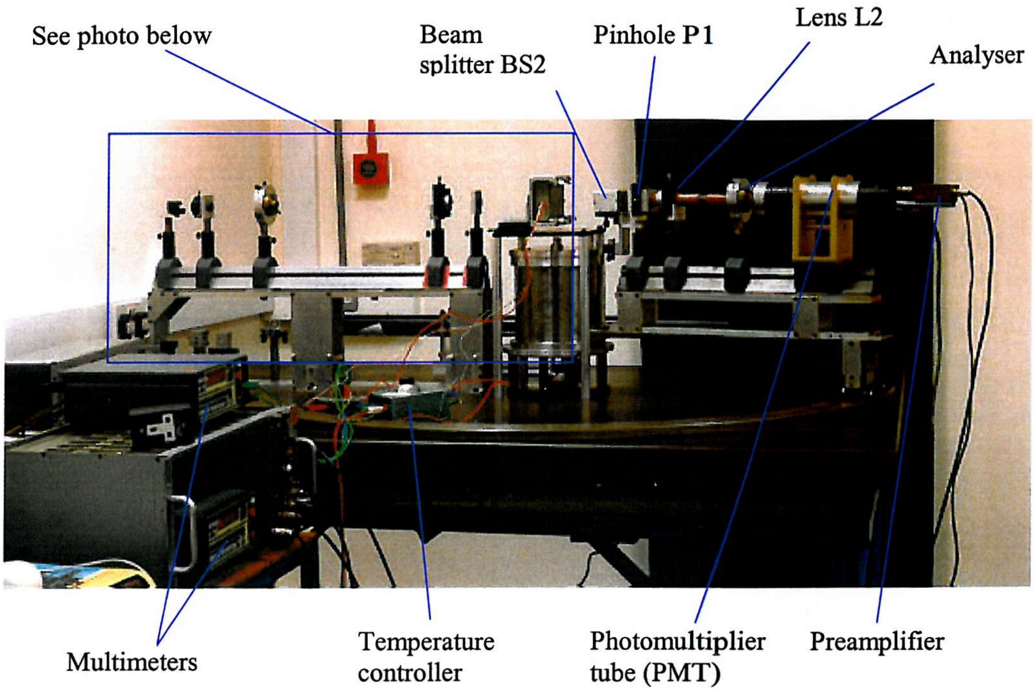

(b) Photograph of the laser source, input/heterodyne optics and sample holder

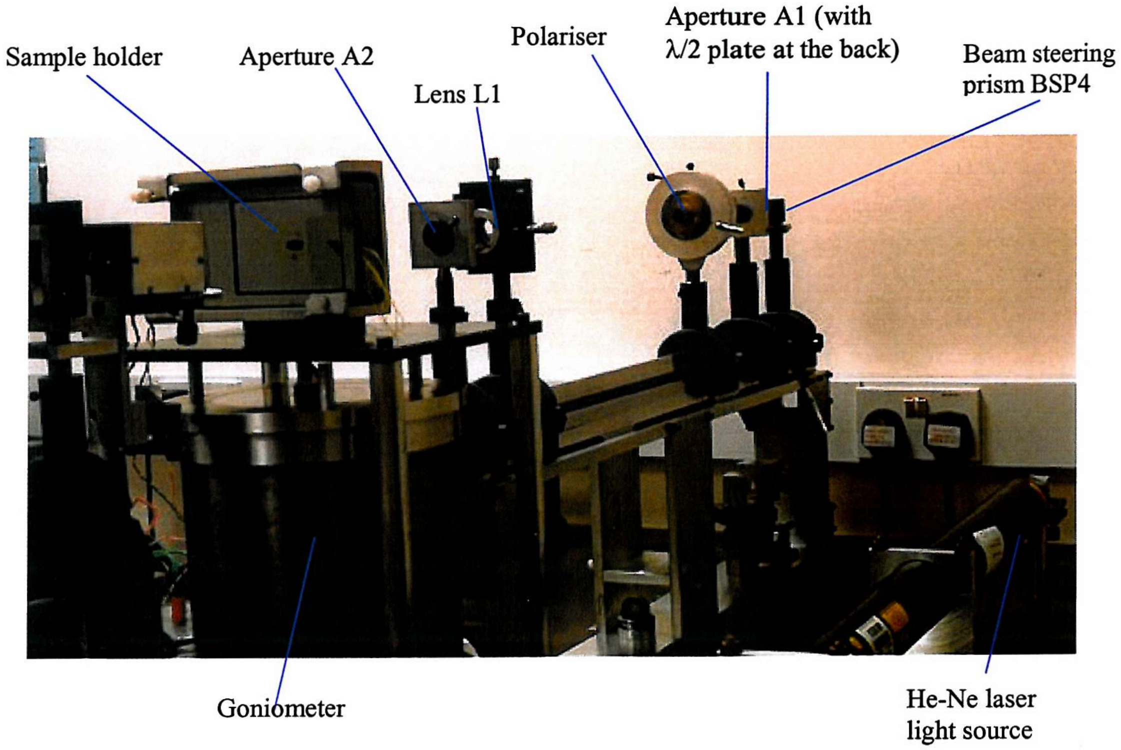

Figure 3.3: Photographs of the experimental set-up used to perform dynamic light scattering measurements.

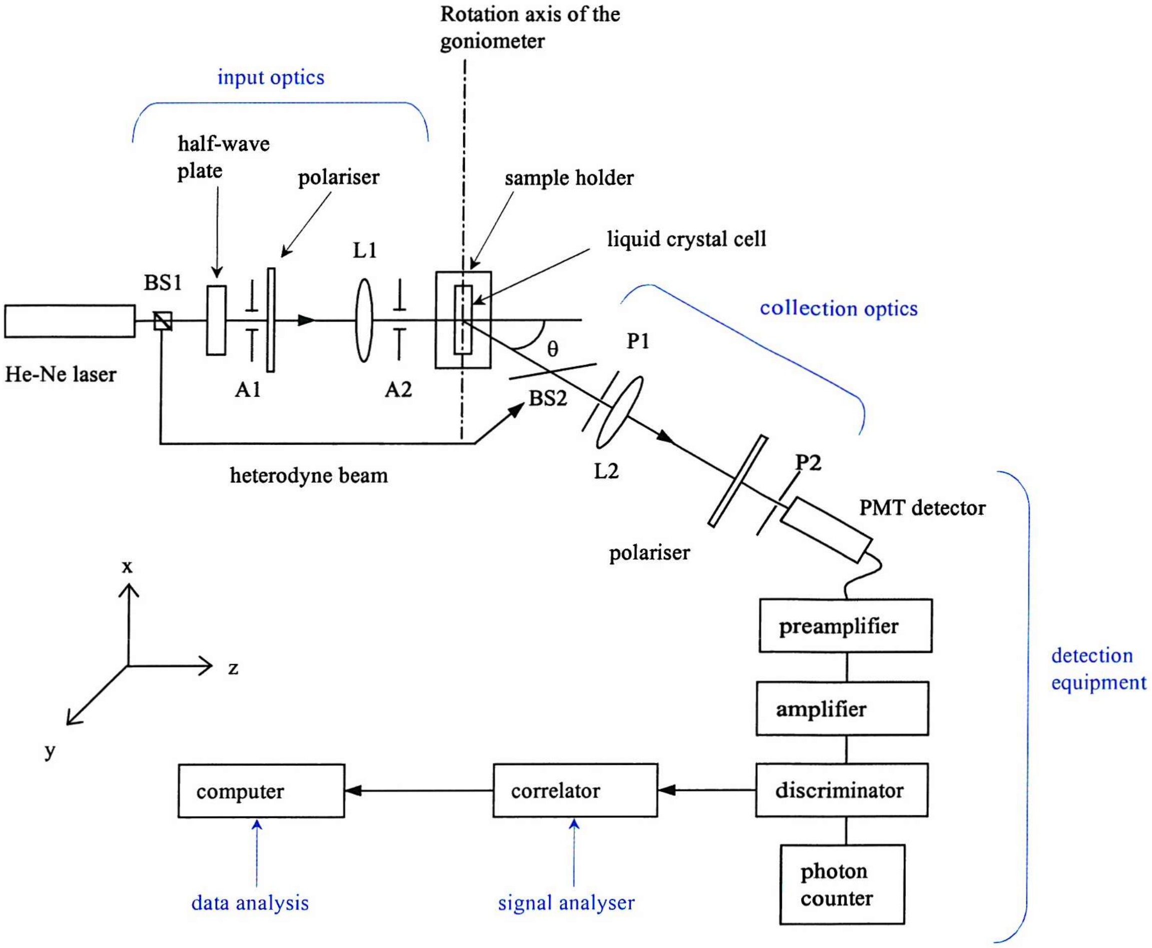

Figure 3.4: Schematic diagram of the light scattering experiment.

3.3.1 Spectrometer

The light scattering apparatus, represented in detail in Figure 3.5, will be described in this part. The apparatus is mounted on an optical table, which rests on a foam layer and the steel frame of the table is supported by pillars of sand (see photo (a) of Figure 3.3). This ensures that the spectrometer is isolated from any vibration or mechanical noise that may influence the measurements. The whole set-up was originally built at the University of Manchester for the study of the diffusion coefficients and particle sizes of dilute macromolecular solutions.[13] After minor transformations, the spectrometer could also be employed to measure accurately the twist and splay visco-elastic constants of low-molar mass nematic liquid crystals.[4, 14] Most of the subsequent investigations performed with this instrument were focused on the influence of the addition of a side-chain polymer to a nematic host, which caused a significant increase of the viscosity coefficients of the host.[3, 4, 7, 14] The original sample holder consisted of a glass annulus jacket to house the cell with an outer brass chamber, through which oil heated at the desired temperature was circulated. A new sample holder was designed to achieve thermal equilibrium more rapidly[3] and this was utilized in the course of this work.

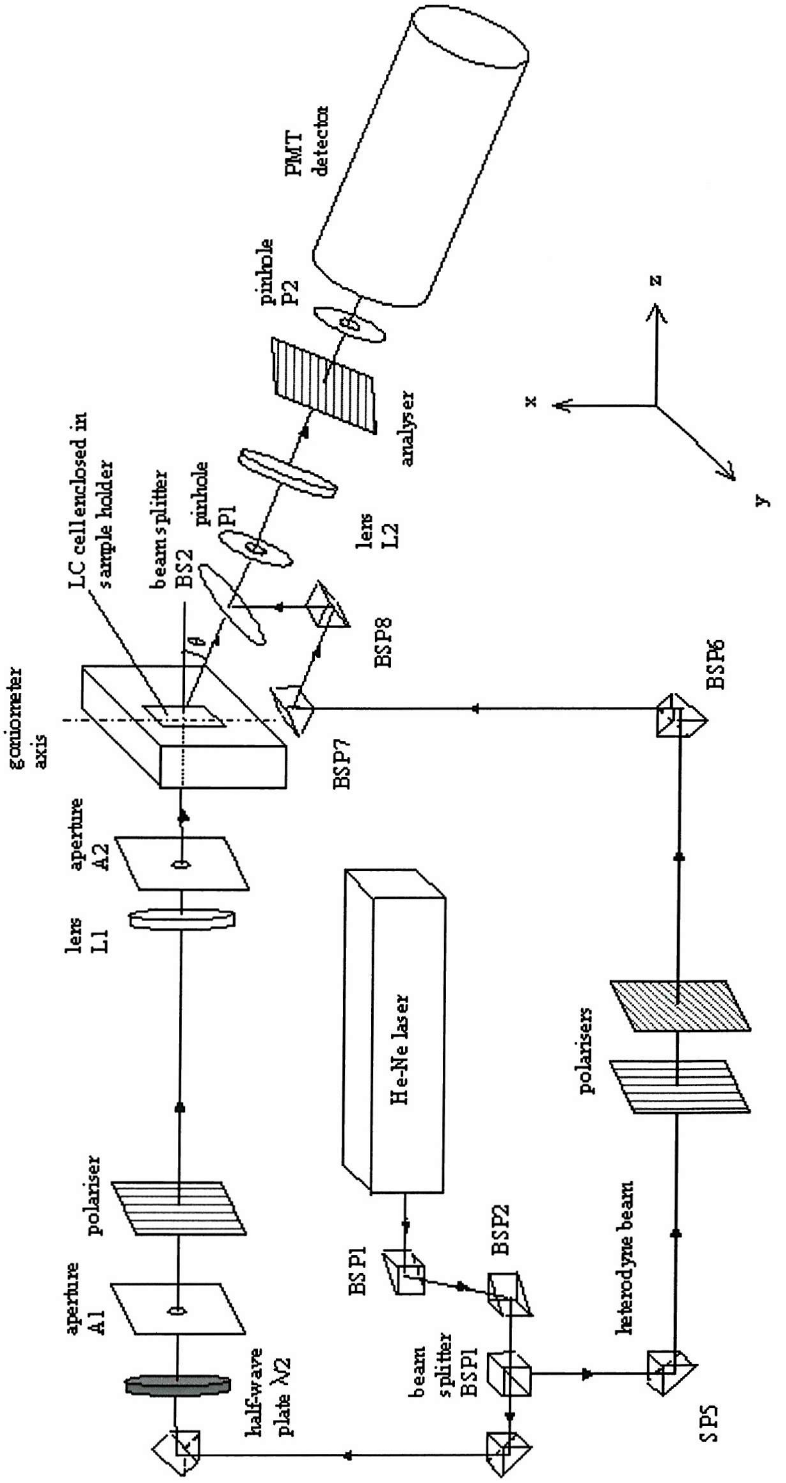

Figure 3.5: Detailed diagram of the optical components of the light scattering spectrometer (where BS refers to a beam splitter and BSP represents a beam-steering prism).

Laser source

Photon correlation experiments require a monochromatic laser light source operating in a single mode with a well-defined linear polarisation. Since nematic liquid crystals scatter light strongly, lasers of power lower than 50 mW are usually sufficient for accurate linewidth measurements. Nevertheless, they should be powerful enough to allow for the use of the heterodyne mode, to overcome transmission losses at the various optical interfaces and to compensate for the reduced efficiency of the photomultiplier in the red region of the electromagnetic spectrum.

The source employed in this work is a red helium-neon (He-Ne) laser model 05-LHP-927, manufactured by Melles Griot,[15] of wavelength $\lambda = 632.8$ nm operating in the TEM_{00} mode. Its polarisation ratio is greater than 500:1 and its maximum output power is 35 mW. The output beam is characterised by a Gaussian intensity profile with a waist diameter, measured at the $1/e^2$ points, of 1.25 ± 5% mm and an angular divergence of 0.66 ± 5% mrad.

Input optics

The laser light is guided by a series of prisms to the beam splitter BS1, which separates the beam into the input and heterodyne components of equal intensity. The beam-steering prisms BSP3 and BSP4 direct the input beam towards the input optical rail, as drawn in Figure 3.5. The polarisation of this beam can be defined precisely by first rotating a half wave plate to change the plane of polarisation and then by adjusting a polariser to select the desired polarisation state. Though Glan-Taylor polarisers have a higher extinction ratio ($> 1:10^5$), polaroid sheets are preferred since they do not displace the beam when rotated and their extinction ratio of $1:10^3$ is satisfactory for DLS experiments. As a consequence, the spectrometer does not have to be realigned each time the input polarisation is changed. Two variable apertures A1 and A2 allow the removal of off-axis light at the beginning and at the end of the input optical path. Finally, a converging lens L1 of focal length 20 cm is added before the aperture A2 to increase the power density at the scattering volume.

Heterodyne mode

After the beam splitter BS1, the heterodyne beam follows an optical path parallel to the input optical rail and of similar length (see Figure 3.3 (b)). The intensity of the heterodyne beam is adjusted to its correct value by the use of a pair of polarisers. This procedure will be explained in Chapter 4 Section 4.2.3. Then several beam-steering prisms guide the beam along the axis of rotation of the goniometer towards the pellicle beam splitter BS2 where it recombines with the scattered light.

Sample holder

The sample holder was specifically built for the study of the splay and twist visco-elastic constants. It is illustrated in Figure 3.6 and its design was based on the Mettler FP80 heating stage.[3] The presence of two aluminium plates containing nichrome heating wires, reduces the temperature gradient across the sample cell. A stabilised power supply was constructed to provide a steady noise-free dc current. A 5 mm by 2 mm hole is pierced in the centre of each plate for the incident light to enter the cell and for the scattered light to exit it. The long side of the rectangular hole is parallel to the scattering plane to enable the collection of the light at a wide range of scattering angles from – 13° to + 40°.[3]

A thermistor located close to the scattering volume measures the temperature. A thermistor is a semi-conductor device characterised by a temperature-dependent resistance R given by

$$R = A\exp(-E/k_B T), \tag{3.3}$$

where E represents the excitation energy from the valence band to the conduction band of the carriers, k_B is the Boltzmann constant and T is the temperature in Kelvin. The thermistor used here has a resistance ranging from 10 kΩ at 0 °C to 100 Ω at 100 °C and its nominal value is 3 kΩ at 25 °C. After calibration of the device, the change in temperature can be monitored to an accuracy of 0.05 °C by measuring the corresponding resistance with a multimeter. Good thermal coupling with the heating plates is achieved by coating the temperature sensor with heat sink compound. The temperature of the heating stage is controlled by a comparator circuit, described in detail in chapter 3 of reference 3. The voltage across the thermistor measured at the inverting input of the amplifier is compared to the reference voltage (corresponding to the required temperature) at the non-inverting input and the sample cell is heated accordingly. The temperature is very stable over long periods of time.

As can be seen in the photograph of Figure 3.6, the upper heating plate is attached to a door, which allows easy access to the sample cell. The size of the outer case containing the temperature jacket is approximately 14 cm × 8 cm × 4.5 cm. The case is mounted on a metal frame, which can be translated using a series of micro-positioners along the x- and y-axes to select a suitable area of the liquid crystal sample and along the z-axis to position the cell at the intersection of the input and scattered beams. Four screws placed at each corner of the metal frame hold the sample case in place and they can be adjusted so that the cell's walls are normal to the incident beam. The whole assembly is fixed to a small table support and stands over the goniometer (refer to Figure 3.3 (b)).

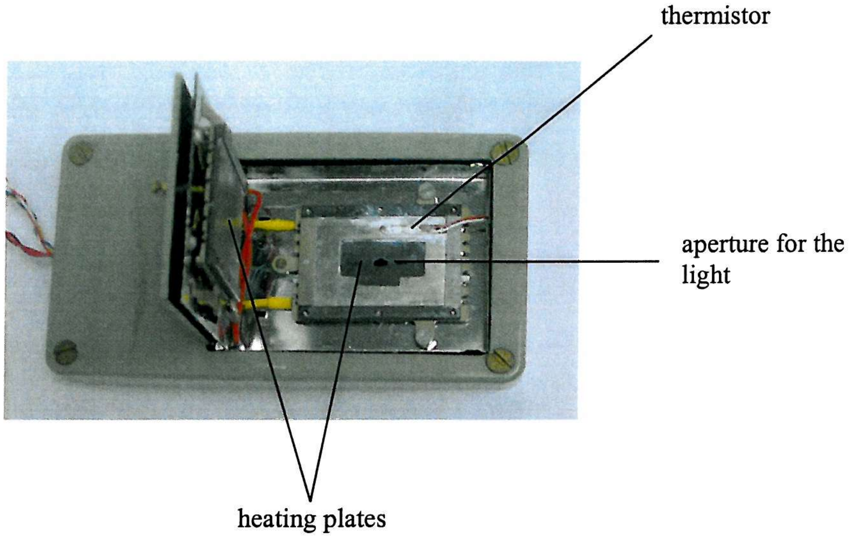

Figure 3.6: Photograph of the sample holder designed by Birtwistle for DLS experiments.[3]

Collection optics

The collection optics, mounted on an optical rail connected to the goniometer, can be rotated in the horizontal plane. The axis of the goniometer defines the rotation axis and a vernier scale gives the scattering angles with a precision of 0.1°. The scattered and heterodyne signals recombine at the pellicle beamsplitter BS2, which is inclined at 45° to the horizontal plane. The diameter of pinhole P1 defines the acceptance angle of the collection optics and thus the uncertainty in the measured scattering wavevector, as will be explained in the next paragraph. A focusing lens L2 produces an unmagnified image of the scattering volume onto the pinhole P2 located at the entrance of the PMT tube. A polariser sheet is placed between L2 and P2 and defines the polarisation of the scattered light. The scattered beam is guided through the different optical components between BS2 and the PMT detector via tubes to prevent any external signal from interfering with it. The amount of light detected is governed by the diameter of P2. From noise considerations, a diameter of 200 μm is chosen for both pinholes P1 and P2.[4]

The accuracy of the measured value of scattering wavevector **q** is related to the accuracy of the scattering angle and derives from:

- the finite size of the scattering volume;
- the focusing of the incident laser beam onto the sample using the converging lens L1;
- the diameter of the first pinhole P1 in the collection optics.

Recalling Equations (2.81) and (2.101), the uncertainty in the linewidth $\delta\Gamma$ depends on the uncertainty in scattering angle $\delta\theta_{lab}$ as:

$$\frac{\delta\Gamma}{\Gamma} = \frac{\delta q}{q} = \frac{\delta\theta_{lab}}{\tan\theta_{lab}}. \tag{3.4}$$

This relative uncertainty can be estimated to be around 0.5% for a scattering angle of 14°.

3.3.2 Detection equipment

Photomultiplier tube (PMT)

As mentioned in Chapter 2, Section 2.6.3, the output current of a photoelectric detector is proportional to the intensity or the square of the electric field incident upon it. Through the photoelectric detection process, the noise spectrum of the scattered light, centred about the optical frequency, is converted to a noise spectrum of the anode current, centred at zero Hz.[14, 16]

Scattered photons impinging on the photocathode of a photomultiplier tube generate photoelectrons via the photoelectric effect. These electrons produce more photoelectrons as they are accelerated through a series of dynodes. In this way, the anode photocurrent is multiplied by up to 10^7 times for an applied voltage of 2 kV. The PMT employed here is a Thorn[17] EMI 9863/100 characterised by an active photocathode area of 2.5 mm^2 and a low dark count rate of 40 Hz when operated at 2 kV. The PMT is contained in a cylindrical housing incorporating a mu-metal shield to protect it from stray magnetic fields. A 10 nm bandpass interference filter centred at 632.8 nm is used to remove extraneous light.

Amplifier and discriminator

The output pulses from the PMT are amplified by a factor of ten using an Ortec 9301 fast preamplifier,[18] which is connected directly to the detector to minimise the influence of noise. The signal is further increased by an Ortec 474 timing filter amplifier. An Ortec 473A discriminator eliminates small noise pulses, such as the dark count rate, that may affect the measurement of the linewidth. The lower level discrimination is set to 70 mV and a dead time of 80 ns is chosen to avoid double counting of the pulses. This dead time reduces the bandwidth of the detection system to approximately 10 MHz. In practice, since the pulses are randomly spaced in time, count rates should not exceed 1 MHz to prevent any saturation effects. Finally, the – 0.8 NIM and 5 V TTL outputs of the discriminator are fed respectively into the correlator and the photon-counter.

Correlator

The correlator counts the PMT output pulses n(t) arriving during a fixed time interval Δt called the sample time. Then, it calculates the autocorrelation function of the noise spectrum of the photo-detection current by using the following discrete approximation:[16]

$$g_2(\tau_m) = \frac{1}{N}\sum_{i=1}^{N} n(t_i)\, n(t_{i+m})\,. \tag{3.5}$$

$\tau_m = m\Delta t$ represents the time associated with the mth delay channel (m = 1, 2,....,L), L being the total number of channels of the correlator; $N = N_s - m$ where N_s is the total number of samples or sweeps defined as

$$N_s = \frac{T}{\Delta t}, \tag{3.6}$$

where T is the total duration or integration time.
For N_s sufficiently large, Equation (3.5) can be rewritten:

$$g_2(\tau_m) = \sum_{i=1}^{N_s} n(t_i)\, n(t_{i+m})\,. \tag{3.7}$$

This equation accurately describes the full unormalised correlation function, provided Δt is much smaller than the timescale of the fluctuations. Figures 3.7 (a) and (b) show schematically the operating principle of a correlator. First, the counter records a string of photocounts n(t) arriving during a sample time interval Δt, leading to N_s numbers for a total integration time T. The values of $n(t_i - m\Delta t)$ with $m = 1, \ldots, L$ are stored in the shift register and then multiplied by the currently measured value of $n(t_i)$.

The correlator used throughout the course of this work is a Malvern K7025 4-bit digital correlator[19] containing 128 delay channels equally spaced in time. The input prescaling divides the incoming signal by 2^0 to 2^7 so that the pulse rate remains lower than the maximum rate of 16 pulses per sample time. The sample times available Δt range from 100 ns to 990 ms and the experimental duration T can be set between 1 μs and 9000 s. An IEEE 488 bus interface that connects the correlator to a PC computer allows the autocorrelation function, initially stored in the delay channels, to be transferred for data analysis and the operating parameters to be set remotely.

(a) Example of the photocounting process and of the calculation of the autocorrelation function associated with the photoelectron pulses

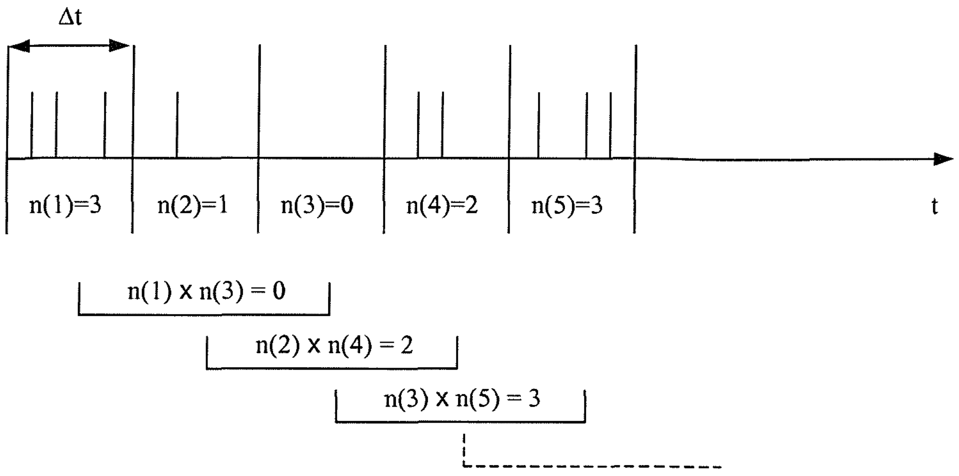

(b) Schematic representation of a correlator

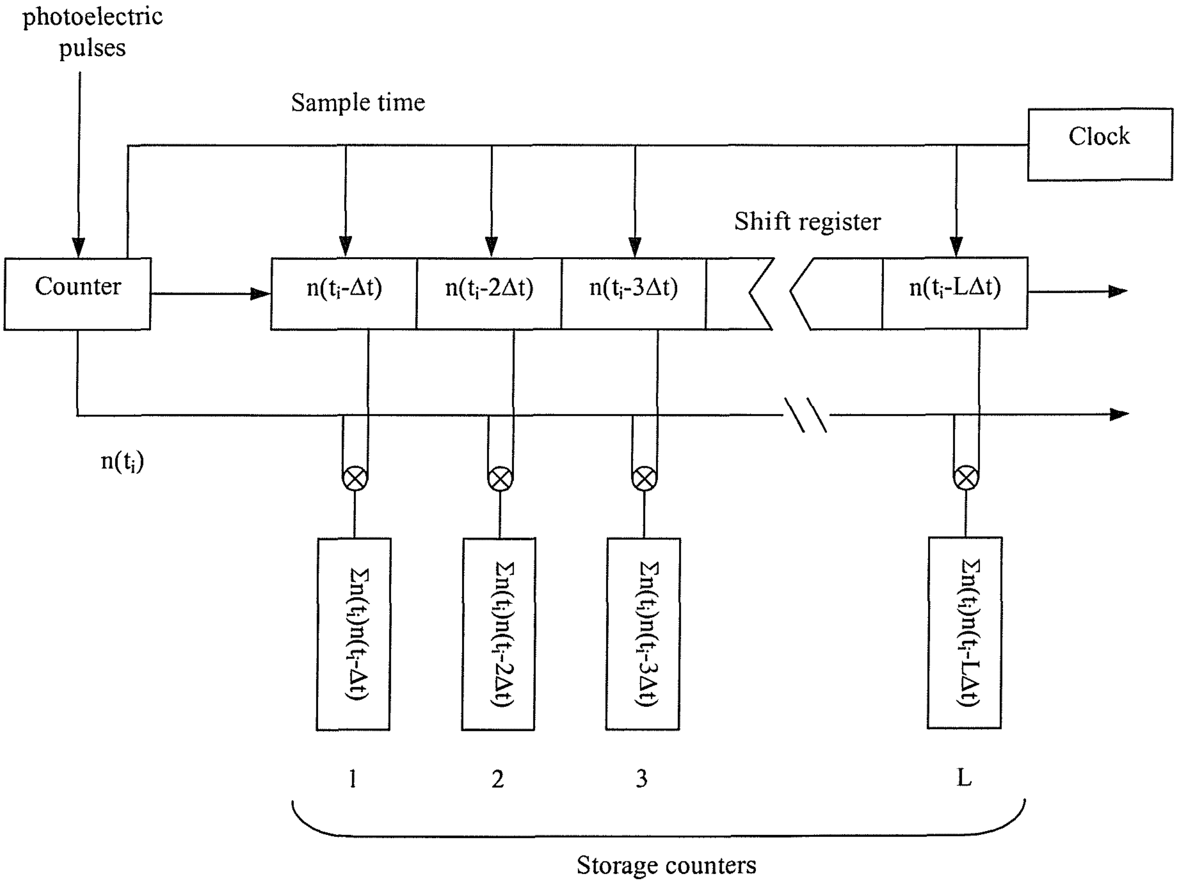

Figure 3.7: Operating principle of a correlator.

3.3.3 Data analysis

Fitting procedure

For a single mode of director fluctuations, the experimental autocorrelation function y_i can be described by a single exponential decay of the form

$$y_{fit}(a_j, \tau_i) = a_1 + a_2 \exp(-a_3\tau_i), \quad \textbf{(3.8)}$$

where τ_i is the delay time of the i^{th} correlator channel and a_j are the parameters to be determined by the fitting procedure: a_1 is the background signal, a_2 is the amplitude of the correlation function and $a_3 = \Gamma$ is the frequency broadening of the scattered light that is related to the visco-elastic properties of the liquid crystal.

The fitting routine, written by P. Birtwistle in C language, is based on a least-square fit method and uses the powerful Marquadt algorithm.[3] The main features of the data analysis program are summarised below:

- A function for the figure of merit χ^2 is introduced to account for the quality of the fit:

  $$\chi^2 = \sum_{i=1}^{L} \frac{(y_i - y_{fit}(a_j, \tau_i))^2}{\sigma_i^2}, \quad \textbf{(3.9)}$$

  where L represents the total number of delay channels (L = 128 for our correlator) and σ_i^2 is the estimated uncertainty on the experimental value y_i (assuming Poisson statistics, we have $\sigma_i^2 = y_i$). The best values for the parameters a_j are obtained by minimising the function χ^2 with respect to each a_j (j = 1, 2, 3).

- The Marquadt algorithm is run to increment the parameters in order to determine the minimum value of χ^2. This algorithm is fast and yields reliable results provided the initial values of the parameters are of the same order of magnitude as the final values.[3]

- The residuals to the single exponential fit and the noise factor f_n are displayed on the computer screen during data collection and enable the data quality to be continuously monitored. The residuals are the difference between the experimental and the fitted autocorrelation functions (y_i-y_{fit}).

The noise factor f_n is given by

$$f_n = \frac{\sigma_{rms}}{a_2}, \tag{3.10}$$

where σ_{rms} is the root mean square of the residuals to the fit defined as

$$\sigma^2_{rms} = \sum_{i=1}^{L} \frac{(y_i - y_{fit}(a_j, \tau_i))^2}{L}. \tag{3.11}$$

For a good data set, the residuals should be random and the noise factor is typically less than 0.02% when 5×10^6 counts are accumulated in each channel of the correlator. Figure 3.8 represents a typical autocorrelation function which was fitted by a single exponential decay. The corresponding residuals $y_i - y_{fit}(a_j, \tau_i)$ are plotted as an inset in the same figure.

Although care has been taken to ensure that a single fluctuation mode has been isolated, the correlation function could not be fitted to a single exponential on a few occasions. This was indicated as structured residuals and in these cases the data were fitted to a double exponential using Origin 6.0.

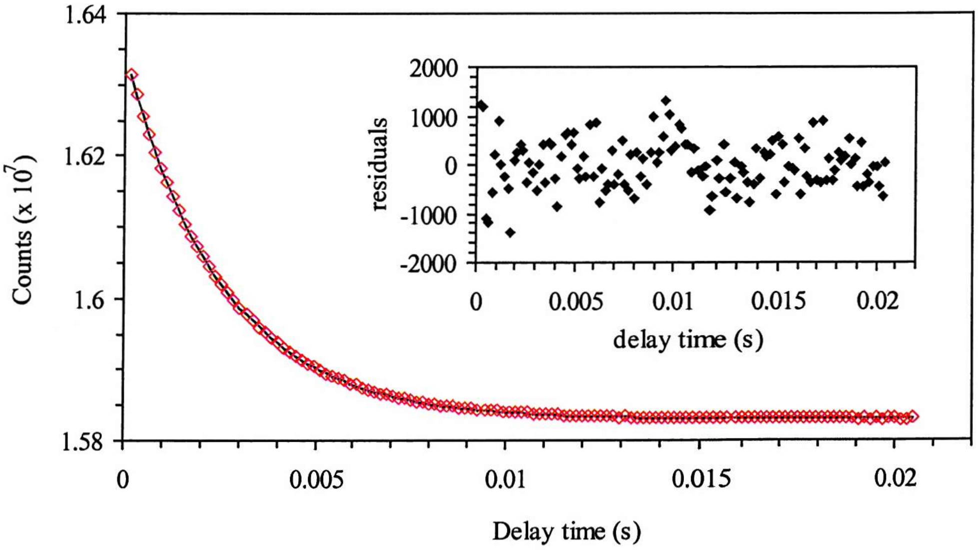

Figure 3.8: Typical correlation function fitted with a single exponential decay (data obtained for 5CB+1% anthraquinone after averaging 25 runs of 40 s each, at T = 34.5 °C, for the twist mode and with no voltage applied); the inset represent the residuals to the fit for the same experimental data.

Sample time and integration time

The sample time Δt and the integration time T are two important operating parameters of the correlator that control the accuracy of the linewidth calculated from the fitted autocorrelation function. In photon correlation spectroscopy, the optimum sample time Δt is chosen such that

$$2\tau_c \le L\,\Delta t \le 3\tau_c, \qquad \mathbf{(3.12)}$$

where $\tau_c = 1/\Gamma$ is the characteristic decay time of the exponential.[16]

However, previous studies showed that the uncertainty on the linewidth did not increase as rapidly for oversampling as for undersampling.[20] As a consequence, the sample time Δt should preferably be selected so that the correlation function spans at least 5 decay times in order to define accurately the background signal level. In the data analysis program, a quantity called U-value is defined as:

$$U = \exp(-\Gamma \Delta t), \qquad \mathbf{(3.13)}$$

with the best sample time corresponding to a U-value of 0.94.

Theoretical calculations estimate the uncertainty $\delta\Gamma$ on the measured frequency broadening Γ to be dependent on the integration time T and on the decay time of the fluctuations τ_c according to

$$\frac{\delta\Gamma}{\Gamma} \propto \left(\frac{\tau_c}{T}\right)^{1/2}; \qquad \mathbf{(3.14)}$$

this means that the relative uncertainty on an experimental linewidth of 500 Hz is 1% after an integration time of 20 s.

The spectrometer control program

The main functions performed by this program are outlined below:

- after each short run, it plots the autocorrelation function (experimental data plus fitted exponential) and corresponding residuals;
- it allows the user to remotely set and change the operating parameters of the correlator during the measurement i.e. prescale factor, sample time, duration time and number of experimental runs;
- all data are saved automatically under user-specified file names;

- it calculates and displays for each data set the noise factor, U-value, fitted linewidth, amplitude of the correlation function, and finally the visco-elastic ratio (using the value of scattering angle θ_{lab} provided by the user);
- it reads and displays continuously the temperature at the sample;
- it gives additional information such as the total number of input pulses, the background counts, the total number of samples, the number of counts per sample time and the PMT count rate.

At the end of a series of experimental runs, another existing program was used to add all data sets and to calculate the resulting linewidth.

3.3.4 Electric field dynamic light scattering (EFDLS)

For $\Delta\varepsilon > 0$ materials in the homeotropic configuration, voltages were applied across the cell to dampen the director fluctuations by means of a Thurlby Thandar[21] TG102 function generator. In this way, the splay and twist elastic constants and associated viscosities can be determined separately. All the measurements were carried out with an ac square wave signal of frequency 10 kHz since it was demonstrated that for both splay and twist modes at this frequency, the fitted linewidth does not depend upon frequency and is not affected by the waveform.[4] The amplitude of the signal can be further increased up to 130 V_{rms} through a high-voltage, wide-band amplifier EW1134B, designed at the University of Manchester. At each temperature for each splay or twist mode, five different amplitude voltages were applied in order to get an accurate fit.

k_{33} and η_{bend} can be determined solely from dynamic light scattering experiments in the presence of an electric field using planar aligned samples.[3] However, materials with $\Delta\varepsilon > 0$ require special cell design for the application of transverse damping fields and these cells were not available for this study. Furthermore, in this geometry, the high uncertainty in the variation of the electric field across the sample leads to experimental errors of about 30% on the bend elastic constant and viscosity coefficient obtained.[3] Therefore, the bend visco-elastic ratio k_{33}/η_{bend} was measured by dynamic light scattering without any applied electric field.

3.3.5 Experimental procedure

The measurements of the pure twist and splay modes were performed at a scattering angle in the laboratory frame $\theta_{lab} = 14°$ for which the bend contributions are negligible. For the determination of the bend visco-elastic parameters, the two geometries introduced in Chapter 2, Section 2.7.2 were investigated.

Depending on the scattering power of the material and on the voltage applied, the integration time is chosen between 40 s and 100 s for one run, so that the number of counts in each channel is about 10^5 counts. The final linewidth is derived after accumulating and fitting at least 25 to 50 individual runs. The relative uncertainty in the fitted linewidth is determined from the standard deviation calculated from these data sets and is evaluated to be less than 2% in most cases.

3.4 Freedericksz transition

Experimentally, the Freedericksz transition can be observed in a slab of uniformly aligned nematic material subject to sufficiently high fields by measuring the changes in any anisotropic macroscopic property, such as the capacitance, the thermal conductivity or the birefringence.[22] The latter method is employed in the course of this work since it is very accurate and offers the advantage that only a small region of well-aligned sample is required.[23]

3.4.1 Presentation of the apparatus

Figure 3.9 (a) shows the magnet, analyser and detector mounted on an optical rail. On picture (b), we can see the different elements used to control the voltage applied to the cell and to collect the data.

(a) Magnet and optical components

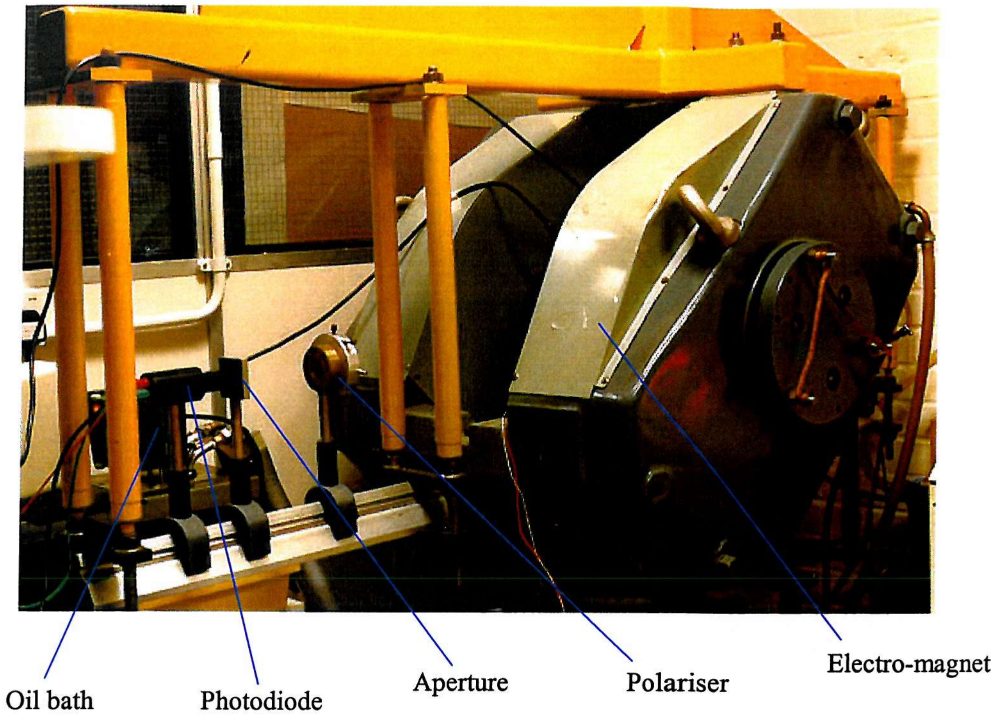

(b) Detection equipment

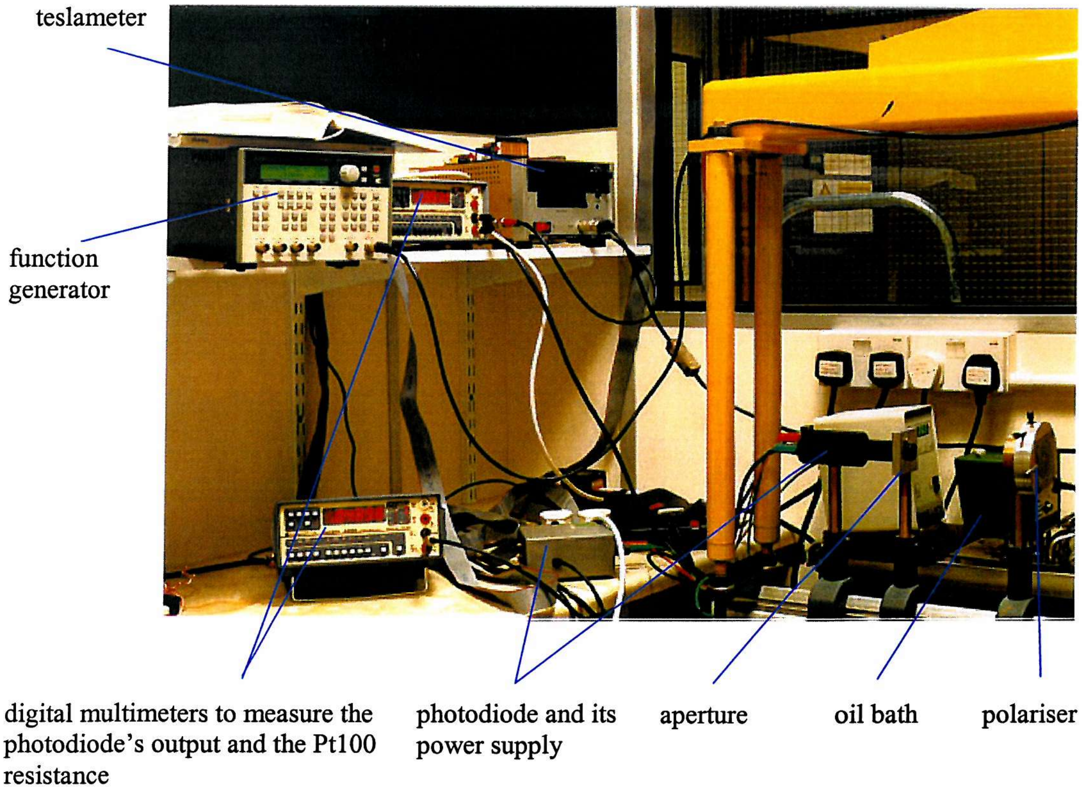

Figure 3.9: Photographs of the set-up for the magnetic Freedericksz transition experiment.

Overview

A schematic drawing of the apparatus is sketched below in Figure 3.10. The optical rail is divided into two parts, one on each side of the magnet. The monochromatic illumination source is provided by a linearly polarised He-Ne laser, operating at 632.8 nm with an output power of 10 mW. Both polariser and analyser consist of polaroid sheets, the polariser ensuring that the incident beam is linearly polarised at 45° with respect to the direction of the applied magnetic field. The sample holder, containing the liquid crystal cell, is connected to a temperature regulated oil bath and is positioned between the magnet pole pieces. After the analyser, an aperture removes any stray light component and finally, a photodiode detects the intensity of the transmitted signal. The photodiode has a fast linear response and its output is monitored using a digital multimeter. A neutral density filter has been added in front of the detector to avoid any saturation effects, which occur when the output voltage of the photodiode exceeds 15 V.

The electromagnet can generate magnetic fields up to 1.3 T with stability of ± 0.0005 T and uniformity of ± 0.0002 T. The gap between the magnet pole pieces is 4 cm. A calibrated Hall probe, connected to a teslameter, measures the magnetic field at one of the magnet poles with an accuracy of about 1%. A function generator allows a square wave electric field to be applied across the sample cell and its amplitude is measured with another digital multimeter. This crossed-field method will be explained in detail in Section 3.4.4.

The experiment has been almost fully automated. The magnet power supply and the electric field generator are computer-controlled. The magnetic field B is increased by increments of 0.0004 T and the system is left to stabilise for 10 s before a measurement is carried out. For each value of B, five runs are averaged. The values of the light intensity at the photodiode and the magnetic field are automatically acquired and saved into a file. The temperature is constantly monitored to check that it is stable to within 0.1 °C.

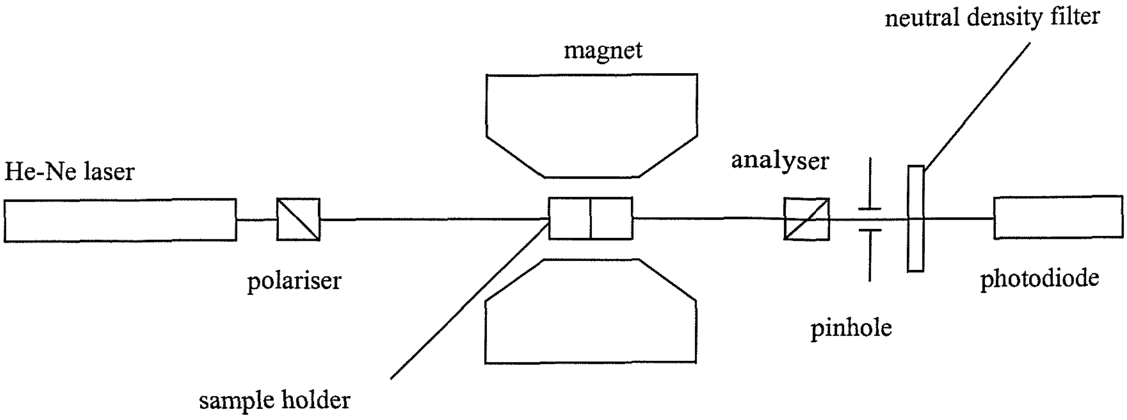

Figure 3.10: Schematic diagram of the apparatus.

Sample holder

The sample holder, shown in Figures 3.11 (a) and (b), was specifically designed for the Freedericksz transition experiment.[24] It consists of two parts, an outer heating jacket and an inner brass cell holder. This system guarantees that good thermal and vibrational stability is achieved at the sample cell. The external jacket is a hollow brass drum with chambers for the oil circulation; it also has two circular windows and a cylindrical opening to insert the inner cell holder. This can be seen in Figure 3.11 (a), which depicts the outer jacket, containing the inner cell holder, in place between the magnet pole pieces. The oil is heated in a Braun Thermomix 1441 circulating bath[25] and the maximum temperature available is 150 °C. The bath is connected to flexible insulated hoses and the fluid is pumped into the chambers through two pipes located at the base of the jacket. The liquid crystal cell is enclosed between two flat brass plates, perforated with two large apertures. Thin brass sheets with smaller holes have been added on both sides of the cell to reduce thermal gradients. The different elements constituting the cell holder are pictured in Figure 3.11 (b). When the cell holder is in place in the heating jacket, its apertures are positioned in front of the two transparent windows of the jacket and in this way, allow the light to pass though the sample. A Pt 100 platinium resistance thermometer is located in a groove close to the cell and measures the temperature to an accuracy of ± 0.1 °C. The soldered wires from the cell are attached to two clips, located inside the top of the brass holder and directly connected to the BNC terminals visible in Figure 3.11 (a). One of the BNC terminals enables the application of electric fields to the cell. The second BNC and the switch were previously used to perform consecutive measurements of dielectric constants and threshold fields.[23]

It is important to note that good thermal stability of the sample necessitates the presence of a cooling system, which circulates water around the magnetic coils and the power supply unit of the magnet.[23] In fact, the magnetic coils are subjected to large currents that can produce heat in the magnetic pole pieces and this heat energy can easily be transferred to the adjacent sample holder. A flow of water is diverted to cool the oil bath through its counter-cooling coil to ensure better thermal regulation and to allow measurements close to room temperature.

(a) Outer heating jacket containing the cell holder in place between the magnet pole pieces

(b) Detail of the different components of the inner brass cell holder

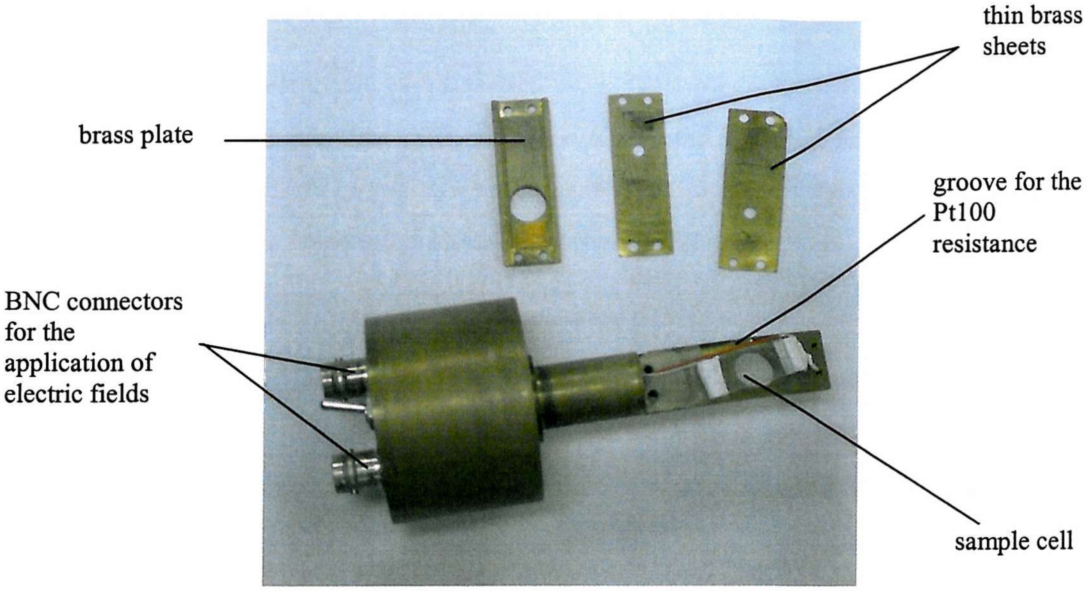

Figure 3.11: Photographs of the sample holder used for Freedericksz transition experiments.

Alignment of the set-up

The alignment procedure for the Freedericksz transition experiment has been described in detail in reference 23. The main requirements are outlined below:

- the optical rails on each side of the magnet have to be horizontal, levelled, centred and collinear;
- the optical rails and the laser beam must be normal to the direction of the magnetic field;
- the sample cell must lie normal to the incident laser light and parallel to the magnetic field.

3.4.2 Observation of the FT using optical techniques

The bend geometry was mainly used in this thesis in order to measure directly k_{33}, which could not be determined from DLS experiments alone. This configuration for the Freedericksz transition was defined explicitly in Chapter 2 Figure 2.6.

Consider a linearly polarised light wave at normal incidence to a homeotropically-aligned cell. For $B < B_C$, the light propagates at a speed characterised by the ordinary refractive index n_o since the polarisation is perpendicular to the optic axis i.e. to the director. For B > B$_C$, the molecules distort and tend to align along the field. This causes a variation in the index of refraction experienced by the laser beam passing through the sample. The liquid crystal cell acts as a variable retardation plate. If the light is polarised along the y-axis, it experiences n_o as previously; however if it is polarised along the x-axis, it travels at a speed associated locally with an effective refractive index n_{eff} that is a combination of ordinary and extraordinary refractive indices n_o and n_e:

$$n_{eff}(z) = n_o n_e [n_o^2 \sin^2 \varphi(z) + n_e^2 \cos^2 \varphi(z)]^{-1/2}. \qquad \textbf{(3.15)}$$

This situation is depicted in Figure 3.12. A light beam polarised in an arbitrary direction and incident upon a distorted nematic sample will be split into an ordinary ray (o) and extraordinary ray (e).

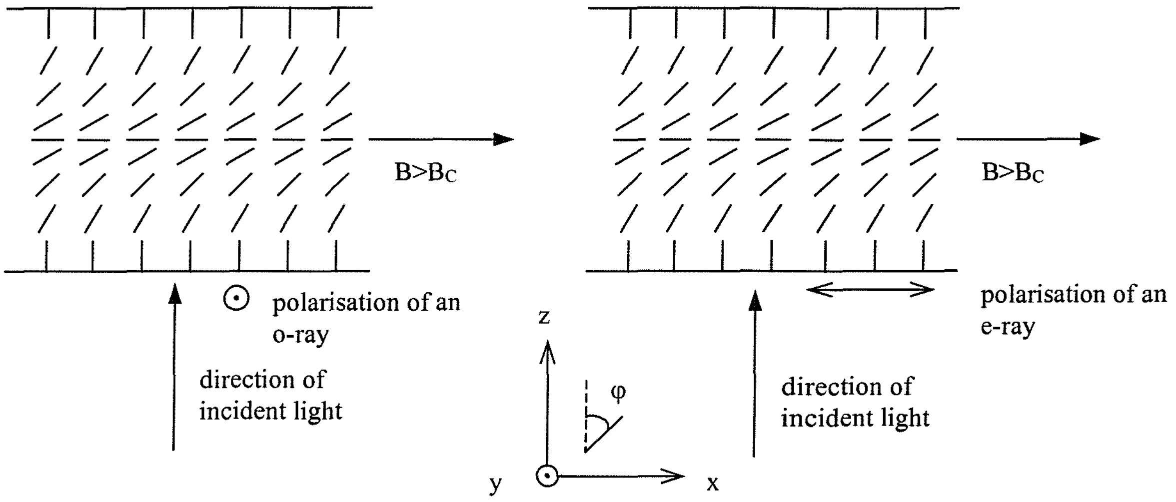

Figure 3.12: Propagation of an o-ray (a) and of an e-ray (b) at normal incidence to the cell for B > B$_C$.

Experimentally, from the interference of the two beams at the analyser, the difference in optical path length δ is obtained from:

$$\delta = \frac{2\pi}{\lambda} \int_0^d \left| n_{eff} - n_o \right| dz, \qquad \textbf{(3.16)}$$

where λ is the incident light wavelength in vacuum.

Near threshold for weak deformations, the expression for the phase difference or retardation δ(B) can be written:[23, 26]

$$\delta(B) = \frac{2\pi d n_o}{\lambda} \frac{n_e^2 - n_o^2}{n_e^2} \frac{k_{33}}{k_{11}} \left(\frac{B}{B_C(0)} - 1 \right), \qquad \textbf{(3.17)}$$

$$\text{with } B_C(0) = \frac{\pi}{d}\sqrt{\frac{\mu_0 k_{33}}{\Delta\chi}}\,. \qquad \textbf{(3.18)}$$

In this case, $\delta(B)$ is proportional to the applied magnetic field B. The critical field B_C and therefore the bend elastic constant are determined from the linear portion of the retardation curve $\delta(B)$ extrapolated to $\delta(B_C) = 0$. The bend-to-splay elastic constant ratio can be derived from the gradient of the line, provided the refractive indices are known.

The variations in transmitted light intensity I are related to the phase difference and thus to any changes in birefringence of the liquid crystal. For a birefringent sample viewed between crossed polarisers, the resulting intensity I at the detector is described by:

$$I = I_0 \sin^2 2\alpha \sin^2(\delta/2), \qquad \textbf{(3.19)}$$

where I_0 is the maximum intensity of transmitted light; α is the angle between the polarisation direction of the incident light and (x, z), which is the plane of reorientation of the optic axis. Below the critical field, no light is transmitted since δ is zero. As the magnetic field is increased above threshold, the transmitted intensity is characterised by a succession of minima and maxima. If the polariser is set at 45°, the oscillation amplitude of I is at a maximum. Typical data for the intensity plotted as a function of magnetic field are presented in Figure 3.13.

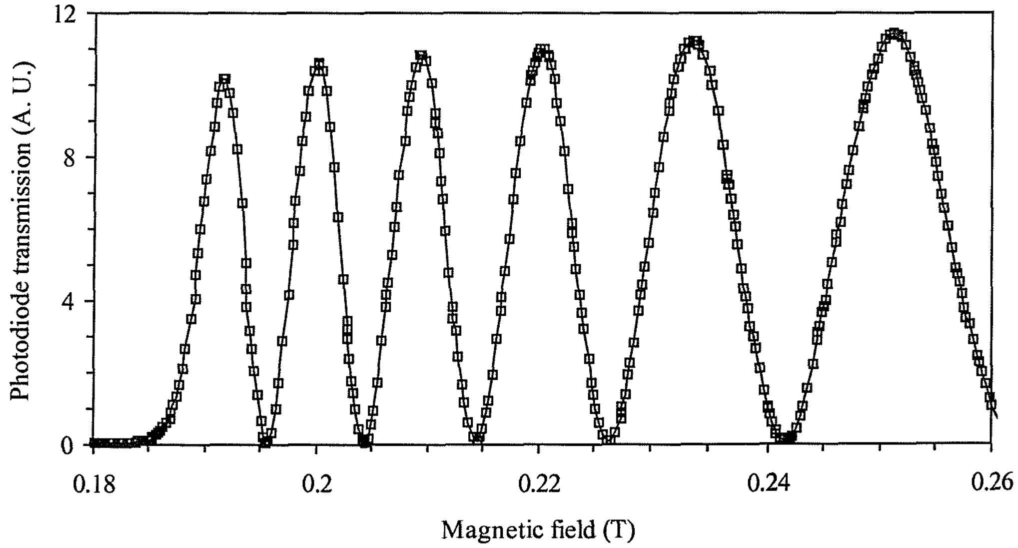

Figure 3.13: Intensity data versus magnetic field obtained for 5CB at T = 30 °C (V = 1 V); the curve and plots correspond both to experimental points.

3.4.3 Data analysis

First, the retardation data $\delta(B)$ is extracted from the transmitted intensity following the procedure adopted in reference 23. The analytical treatment is done using an Excel worksheet specially developed in-house for this purpose by Dr. S. Meyer. A summary of the principal steps performed for data analysis is given below:

1. The intensity data are normalised i.e. $0 < I(B) < 1$ to ensure the peaks have the same height.
2. Then $\sin(\delta/2)$ is determined by taking the square root of the intensity. Since the calculation only yields the positive roots, every second peak has to be inverted to take into account the negative values of the function $\sin(\delta/2)$.
3. Finally, δ is calculated. Note that since the inverse sin function only returns values for the retardation between $-\pi/2$ and $\pi/2$, it is necessary to correct these data by adding the appropriate phase information.

The retardation $\delta(B)$ is plotted against magnetic field in Figure 3.14. The value of the threshold field B_C is determined by extrapolating the linear fit to the curve just above the critical field. The error in B_C, which includes random experimental errors and the uncertainty in the extrapolation procedure, is estimated to be ± 1.5%.

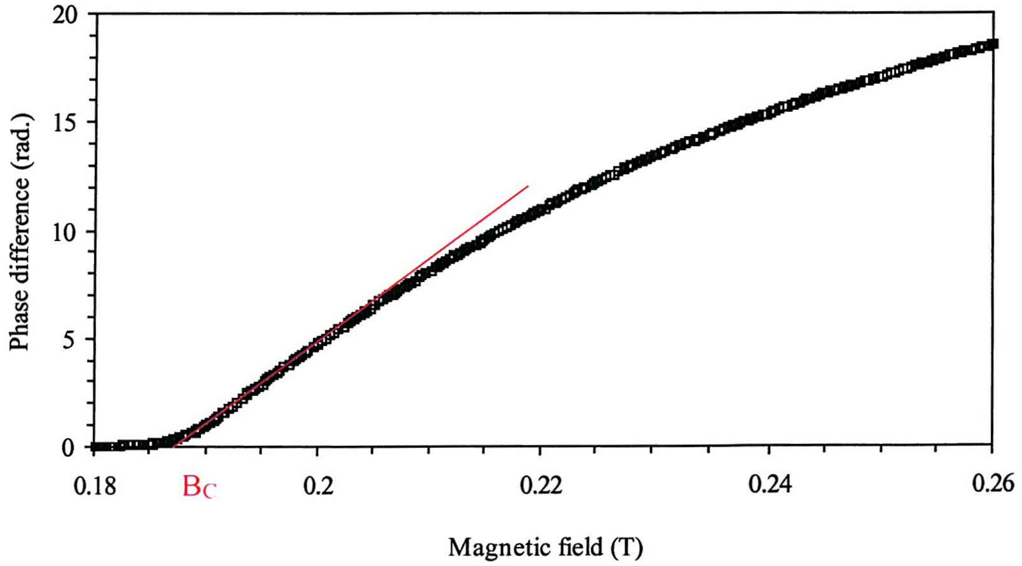

Figure 3.14: Phase difference curve derived from intensity data (see Figure 3.13) for 5CB at T = 30 °C (V = 1 V); the intercept of the line fitted to the linear portion of the graph yields the value of threshold field B_C.

3.4.4 Experimental method

As shown in Equation (3.18), the magnetic anisotropy $\Delta\chi$ should be known in order to calculate the bend elastic constant. Direct measurements of $\Delta\chi$ are difficult and usually inaccurate for measuring small anisotropies.[1] A solution is to use a crossed-field method, i.e. to apply simultaneously an electric field **E**, such that **E** is perpendicular to **B** and to the cell's substrates.[27] For $\Delta\varepsilon > 0$ and for an initially homeotropic sample, the presence of E counteracts the magnetic field B and therefore causes an increase of the threshold field B_C. This results in an extra term in the threshold field equation:

$$[B_C(V)]^2 = [B_C(0)]^2 + \frac{\mu_0 \varepsilon_0 \Delta\varepsilon}{\Delta\chi}\left(\frac{V}{d}\right)^2, \qquad \textbf{(3.20)}$$

where d is the cell thickness expressed in microns.

Experimentally, an ac square wave signal of 1 kHz was applied via a Turlby Thandar[21] programmable function generator TG1304, which can generate voltage amplitude ranging from 1 mV to 10 V. B_C is measured at different applied voltages V. Figure 3.15 shows that each plot of B_C^2 against V^2 obtained for 5CB at different temperatures gives a straight line that can be fitted using Equation (3.20). Considering the experimental uncertainty of about 2% for each data point, the gradient of this graph is independent of temperature. The magnetic susceptibility $\Delta\chi$ can be determined from the gradient of this curve since the dielectric anisotropy $\Delta\varepsilon$ and cell thickness d are measured separately. The bend elastic constant can be finally deduced using Equation (3.18)

An initial run is performed by increasing the magnetic field manually to get an estimate of the threshold field; this step is required in order to set the appropriate parameters for the computer control program, namely the initial and final values of magnetic field as well as the increment. For each temperature five voltages were applied (0, 0.5, 0.75, 1 and 1.2 V). At each new temperature, the apparatus is left at least half an hour to equilibrate. The acquisition time for each run at one temperature is between one and two hours and the data analysis can be performed in less than 10 minutes.

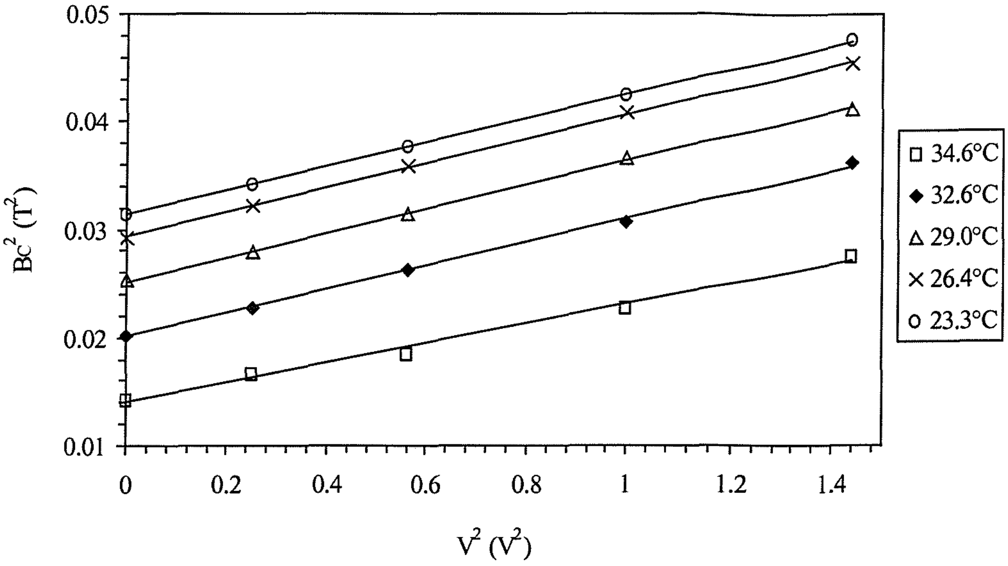

Figure 3.15: Squared threshold magnetic field versus squared voltage for 5CB at different temperatures; the lines are the fitted curves to the experimental data.

3.4.5 Electro-optic measurements[28]

Electro-optic experiments were carried out to investigate the switching behaviour of nematic materials with low dielectric anisotropy, which will be discussed in Chapter 6. The samples are enclosed in planar aligned cells and the electric field is applied normal to the initial orientation of the director. This geometry allows in principle the observation of the splay Freedericksz transition.

The basic set-up was introduced in 3.2.4 and consists of a polarising microscope equipped with a heating stage. A photodiode was added to the microscope's photo tube to monitor the intensity of transmitted light. Alternatively, an Olympus[8] OM-1 photographic camera was mounted to obtain images of the different textures. Electric fields were applied using a Turlby Thandar[21] programmable function generator TG1304 and the signals were further amplified to 130 V_{rms} by means of a wide band voltage amplifier EW 1134B, identical to the one employed in DLS experiments (see Section 3.3.4). A Hewlett Packard[11] two-channel, 100 MHz digitising oscilloscope was used to measure the amplified voltage and the output from the photodiode. The whole set-up for electro-optic measurements is pictured in Figure 3.16.

Figure 3.16: Photo of the experimental set-up for electro-optic measurements.

3.5 Measurements of refractive indices

In nematic liquid crystals, both ordinary and extraordinary refractive indices n_o and n_e can be measured accurately using a Bellingham and Stanley 60/HR Abbé refractometer.[29] This technique is based upon total internal reflection. As sketched in Figure 3.17, a thin layer of sample is sandwiched between an illumination prism and a second (or measuring) prism of higher refractive index. The optical path of an incident ray emerging at the critical angle for total internal reflection is also illustrated in Figure 3.17. In the eyepiece of the instrument, a light-dark boundary that corresponds to this critical angle can be seen. A scale measures precisely the value of angle for total internal reflection. A table supplied with the refractometer converts these angular data into refractive indices at the wavelength of light used. A change in refractive index is directly related to a variation in critical angle.

For nematic materials, the experiment requires a well-aligned homeotropic film. In this case, the director is normal to the prisms. When the incident light is polarised in the horizontal plane, the polarisation is perpendicular to the director and thus, n_o is measured. Alternatively, if the polarisation of the incoming beam is in the vertical plane, the light will experience n_e. The two cases are indicated in Figure 3.18 (a) and (b). This method works well for nematic liquid crystals since it does not rely on absolute intensities, which depend on the turbidity of the mesogenic material studied. Furthermore, only a small quantity of sample is needed. For strongly absorbing samples, such as some types of dye guest-host mixtures, observation of the critical angle may not be possible.

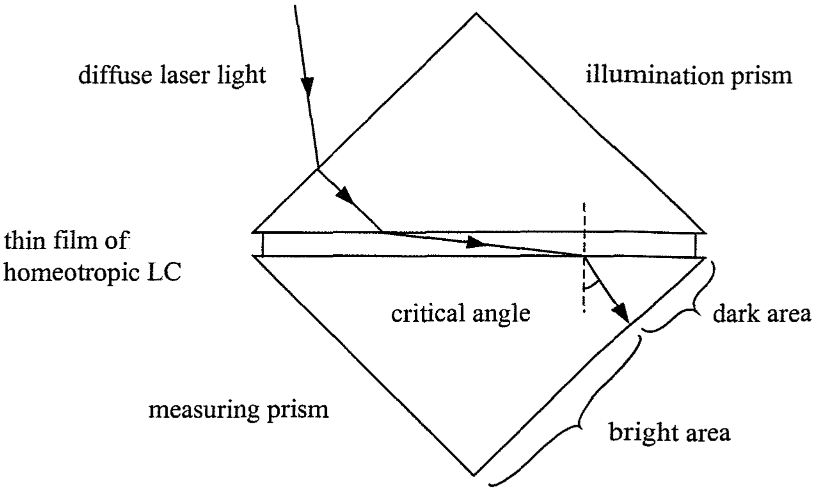

Figure 3.17: Basic principle of the Abbé refractometer.

(a) The ordinary refractive index n_o

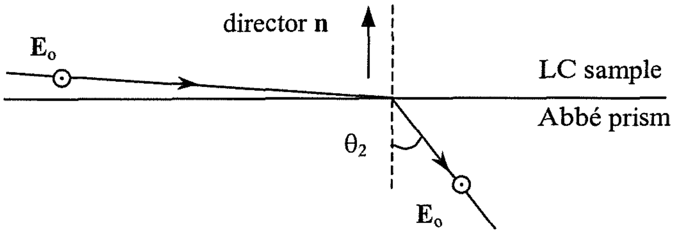

(b) The extraordinary refractive index n_e

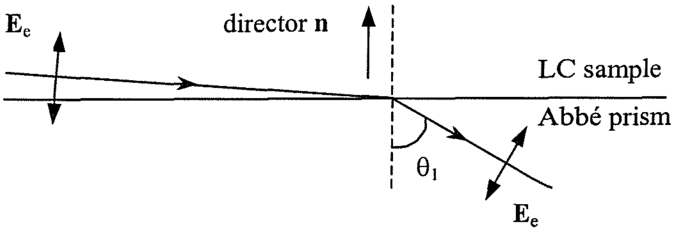

Figure 3.18: Geometry for the measurement of the refractive indices of a nematic LC material.

The experimental set up is summarised in Figure 3.19. The measurements are performed using a 10 mW He-Ne laser at the same wavelength ($\lambda = 632.8$ nm) as in the DLS experiments. A neutral density filter is added at the output of the laser to reduce the light intensity. A beam expander is mounted on the optical rail after the laser source. A polaroid sheet defines the polarisation of the incident light. The beam is then reflected by a plane mirror and steered towards the illumination (or upper) prism of the refractometer. A Braun Thermomix[25] 1419 circulating bath is connected to the Abbé via plastic hoses which pump deionised water around both prisms to heat them to the required temperature. After 30 min, a temperature stability of 0.1 °C can be achieved. The operating temperature is limited to a maximum of about 80 °C, which corresponds to the maximum temperature the optical cement of the refractometer can withstand. A platinum resistance thermometer Pt 100 measures the temperature at the prisms with an accuracy of ± 0.1 °C. The laser and thermal bath are switched on at least half an hour prior to any experiments. The refractometer is calibrated using a sodium light source and a silica piece as reference (of refractive index n = 1.45839 at 20 °C measured at $\lambda = 589.6$ nm). A 0.25% wt/wt solution of lecithin in chloroform is applied to both prisms to form a homeotropic alignment layer. Then, a small drop of liquid crystal is placed onto the measuring prism and covered with the illumination prism. The accuracy on the measured refractive indices is ± 0.0002.

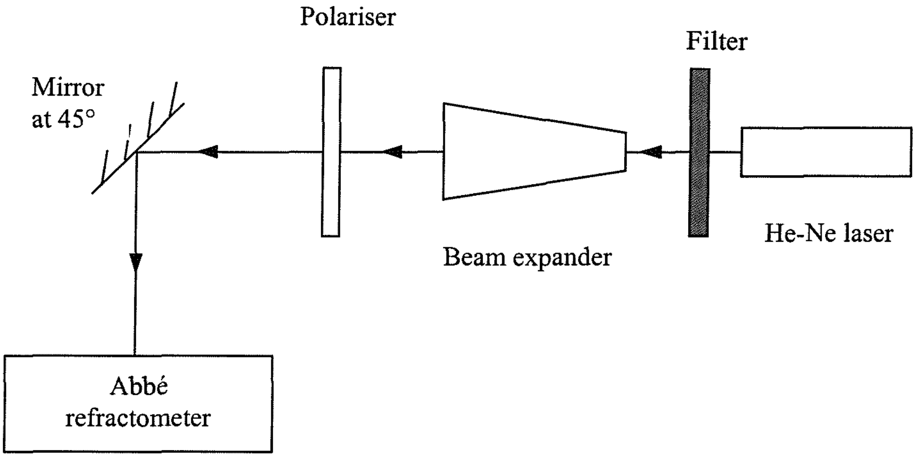

Figure 3.19: Experimental set-up for the measurements of refractive indices.

3.6 Measurements of dielectric constants in nematic liquid crystals

It is important to know the sign and value of the static dielectric anisotropy $\Delta\varepsilon = \varepsilon_{\parallel} - \varepsilon_{\perp}$ since this parameter controls the coupling to an applied electric field. If we recall Equations (2.103) and (2.104) in Chapter 2, the visco-elastic ratios obtained from DLS measurements can be deconvoluted in the presence of a damping electric field, provided the dielectric constants can be determined by an independent technique. The calculation of the threshold magnetic field in Freedericksz transition experiments also requires the knowledge of the dielectric anisotropy $\Delta\varepsilon$.

The static dielectric constants $\varepsilon_{\|}$ and $\varepsilon_{\perp}$ can be measured by a capacitance method using homeotropic and planar cells respectively. The Lucid sample cell, used for dielectric measurements (see Section 3.2.3 for a description of the cell), may be considered as a parallel plate capacitor. The dielectric measurements are carried out for the same temperature range and at the same frequency as for EFDLS experiments.

3.6.1 Experimental technique

The capacitance of the cell is measured using a Wayne-Kerr 6425 multibridge[30] with a probe voltage of amplitude 250 mV and of frequency 10 kHz. The Wayne-Kerr bridge is switched on at least two hours before starting any experiments. Two short leads, soldered to the ITO side of an empty Lucid cell (carrying either a homeotropic or a planar alignment layer), are twisted together and placed within a thin rigid tube to minimise signal fluctuations arising from movement of the wires. The cell is placed inside a Mettler[12] FP82 heating stage and its wires are attached to the Kelvin clip, which consists of a 4-terminal electrical connector for the application of the probe voltage. Since the capacitance measurements are extremely sensitive to any displacement of the cell and leads, the Kelvin clips and soldered wires are secured on the table with adhesive tape and care is taken not to move them between successive runs on the same cell. The bridge and the heating stage are mounted on an optical table to eliminate any mechanical shock or vibration that might affect the experiment.

The capacitance of the empty cell is measured at room temperature. The cell is filled in situ by capillary action at a temperature that is above the material's clearing point. Then, the liquid crystal in the cell is cooled down in the nematic phase and left for several minutes to reach thermal equilibrium. Values of filled cell capacitance are collected over the required temperature range. The temperature measurements are accurate to ± 0.2 °C and the random error on the dielectric constants is estimated to be 0.5%.

3.6.2 Determination of dielectric constants

The dielectric constant can be deduced from the ratio of the capacitance of the filled cell C_{full} to the capacitance of the empty cell C_{empty}. However, the measured capacitances also include contributions from the lead capacitance C_{lead} that increases with the length of the soldered wires.

Therefore, the final value for the dielectric constant is given by:

$$\varepsilon_i = \frac{C_{\text{full, i}} - C_{\text{lead}}}{C_{\text{empty, i}} - C_{\text{lead}}} \quad \text{where i} = \parallel, \perp. \qquad \textbf{(3.21)}$$

For the 7.5 μm Lucid cells used, C_{empty} usually lies in the range 35 to 45 pF and the values for C_{full} range from 120 pF to 700 pF, depending on the material and temperature investigated. C_{lead} is determined (after the empty and filled cell capacitances have been measured) by severing the connection between the soldered leads and the Lucid cell. For short wires of about 5 cm long, $C_{lead} \approx$ 1-2 pF.

3.7 Summary

The experimental techniques that were introduced in this chapter are commonly used for the characterisation and for the measurements of the physical properties of nematic liquid crystals.

First, we have presented the methods to achieve uniform homeotropic and planar orientations of nematic materials and to prepare the cells required in the different experiments. The LC samples, studied in the course of this work have been characterised by optical microscopy and DSC. The thickness of the cells employed in DLS and Freedericksz transition experiments have been measured by a UV-Visible spectrometer and their values usually range from 44.0 μm to 46.0 μm with a variation of ± 1 to 2 μm across their whole area, which corresponds to a 5% uncertainty.

In Section 3.3, the dynamic light scattering apparatus has been described in detail. This set-up allows the use of heterodyne detection and the available range of collection angles are –13° to +40°. The sample holder was specifically constructed for the determination of splay and twist visco-elastic constants and its temperature is measured to an accuracy of 0.05 °C. The relative uncertainty in the scattering wavevector $\mathbf{q}$ is considered to be approximately 0.5% for a scattering angle of 14°. After averaging, the standard deviation for the fitted linewidth of the resulting autocorelation function is less than 2% in most cases.

The Freedericksz transition experiment has been fully discussed in Section 3.4. The magnetic field between the magnet's poles is defined with a resolution of 1%. The value of threshold field can be obtained to an accuracy of ±1.5%.

The refractive indices are measured directly by Abbé refractometry at the same wavelength ($\lambda = 632.8$ nm) as the DLS experiments; the overall uncertainty is ± 0.0002. For both the FT and the Abbé set-ups, the temperature at the sample is stable to within 0.1 °C and is measured to an accuracy of 0.1 °C.

The dielectric permittivities of nematic LCs are determined via a capacitance technique with a random error of about 0.5% while the temperature of the Mettler heating stage is monitored to ±0.2 °C.

The alignment and calibration of the light scattering spectrometer will be explained in the next chapter.

REFERENCES

[1] de Jeu W. H., *Physical Properties of Liquid Crystalline Materials*, Gordon and Breach, New-York (1980)

[2] Goodby J. W., *Practical Microscopy of Liquid Crystals*, Annual Hull Workshop (1997)

[3] Birtwistle P. J. R., *Dynamic Light Scattering from Liquid Crystalline Systems,* PhD Thesis, University of Manchester (1995)

[4] Sefton M. S., *Dynamic Light Scattering from Thermotropic Liquid Crystals*, PhD Thesis, University of Manchester (1985)

[5] Naemura S., *Appl. Phys. Lett.*, **33(1)**, pp. 1-3 (1978)

[6] EEV, Chelmsford, Essex CM1 2QU, http://www.eev.com

[7] Cox P. J., *Dynamic Light Scattering from Nematic Liquid Crystalline Systems,* PhD Thesis, University of Manchester (1997)

[8] Olympus Optical Company Ltd, Southall, Middlesex UB2 4SB, http://www.olympus.co.uk/home.cfm

[9] Linkam, Scientific Instruments Ltd, Waterfield, Tadworth, Surrey KT20 5HT, http://www.linkam.co.uk/

[10] Perkin Elmer Instruments, Beaconsfield, Bucks HP9 2FX, http://instruments.perkinelmer.com/index.asp

[11] Agilent Technologies UK Ltd, Cheadle Royal Business Park, Stockport, Cheshire SK8 3GR http://www.chem.agilent.com/Scripts/Phome.asp

[12] Mettler-Toledo Ltd, Beaumont Leys, Leicester, LE4 1AW, http://www.mt.com/home/mettlertoledo.asp

[13] Bowdler A. R., *Dynamic Light Scattering from Dilute Solutions of Mesomorphic Polymers*, PhD Thesis, University of Manchester (1984)

[14] Bancroft M. S., *Dynamic Light Scattering Studies of Some Nematic Liquid Crystals*, PhD Thesis, University of Manchester (1989)

[15] Model 05-LHP-927, Melles Griot Ltd, Cambridgeshire Business Park, Ely CB7 4EX, http://www.mellesgriot.com/

[16] Chu B., *Laser Light Scattering*, Academic Press, New York (1974)

[17] Electron Tubes Ltd, Ruislip, Middlesex HA4 7TA, http://www.electron-tubes.co.uk/menu.html

[18] Ortec, Advanced Measurement Technology, Berkshire, http://www.ortec-online.com/

[19] Malvern Instruments Ltd, Enigma Business Park, Malvern. Worcs. WR14 1XZ, http://www.malvern.co.uk/home.htm

[20] Nash P. J., *Development of Experimental and Analytical Techniques in Photon Correlation Spectroscopy*, PhD Thesis, University of Manchester (1982)

[21] TTi (Thurlby Thandar Instruments Ltd, Huntingdon, Cambs. PE29 7DR, http://www.tti-test.com/

[22] Blinov L. M., *Electro-Optical and Magneto-Optical Properties of Liquid Crystals*, John Wiley and

Sons Ltd, Chichester (1983)

[23] Allinson H., *A Study of Photochromic Fulgide Doped Liquid Crystals*, PhD Thesis, University of Manchester (1994)

[24] Hopwood A. I., *Electro-optic Effects in Polymer Liquid Crystalline Solutions*, PhD Thesis, University of Manchester (1985)

[25] Rich-Mond Agencies Ltd, Wigan, WN3 4JS, http://www.rich-mond.co.uk/

[26] Deuling H. J., *Sol. St. Phys. Suppl.*, **14**, pp. 77-103 (1978)

[27] Schad Hp., Baur G. and Meier G., *J. Chem. Phys.*, **70**, pp. 2770-2774 (1979)

[28] Musgrave B., *Electro-Optic Studies of the Flexoelectric Effect in Chiral Nematic Liquid Crystals*, PhD Thesis, University of Southampton (2000)

[29] Bellingham and Stanley, Tunbridge Wells, Kent, TN2 3EY, http://www.bs-ltd.com/

[30] Wayne Kerr Electronics, Bognor Regis, West Sussex, PO22 9RL, http://www.waynekerrtest.com/indexf.htm

CHAPTER 4: EVALUATION OF THE DLS TECHNIQUE FOR THE MEASUREMENTS OF VISCO-ELASTIC PROPERTIES IN NEMATICS

4.1 Introduction

The light scattering spectrometer was described in Chapter 3; the next step, explained in Section 4.2 is to align the apparatus prior to making any measurements. When collecting data, it is important to ensure that the autocorrelation function is a single exponential for a homodyne signal arising from a single mode of director fluctuations. Multiple exponentials occur for partially heterodyned signals or for spurious scattering due to impurities or in scattering geometries when mixed fluctuation modes are present. Part 4.3 of this chapter shows that the apparatus yields accurate and reliable results for the splay and twist visco-elastic constants using a well-characterised standard material such as 5CB. In Sections 4.4 and 4.5, the calibrated spectrometer is utilized to investigate the visco-elastic properties of various nematic mixtures. The nematogens of the first series have different chemical compositions, which result in low and high birefringence. Nevertheless, their splay and twist elastic constants are found to be comparable. The second series consists of guest-host mixtures for the study of the influence of dopants on the properties of the host material. The twist elastic constant k_{22} and the associated viscosity coefficient γ_1 are of particular importance because they determine the in-plane switching behaviour in liquid crystal displays (LCDs) along with the dielectric anisotropy.[1, 2]

4.2 Preparation of the light scattering spectrometer

4.2.1 Optical alignment of the spectrometer

In dynamic light scattering (DLS) experiments, it is essential that the input and collection optical paths coincide with the axis of rotation of the goniometer at any scattering angle.

The light scattering apparatus is illustrated in Figure 4.1. The detailed alignment procedure is given by Bowdler[3] in his thesis and only the main steps are outlined below, taking into account the recent modifications of the spectrometer:[4, 5]

a) Firstly, the path of the heterodyne beam is adjusted by tuning the beam steerers BSP5 and BSP6, so that it follows the rotation axis of the goniometer. This is accomplished by observing the resulting spot (also called fiducial point) on a screen mounted on the collection optical rail: the heterodyne beam coincides with the rotation axis when no circular movement of the spot is detected as the goniometer is rotated.

b) The detection arm is aligned collinear to the input rail ($\theta = 0°$ on the Vernier scale) and fixed to the optical table in this position. The input beam is steered, using BSP3 and BSP4, to be parallel to the arm by directing it through a series of pinholes.

c) The half-wave plate, apertures A1 and A2, polariser and lens L1 are attached to the input optical rail. Care has to be taken to ensure that all optical components are mounted normal to the input beam by observing the back reflection of the laser light. The position of the focusing lens L1 can be further adjusted and translated by means of two screws so that it does not cause a displacement of the input spot.

d) With the Vernier scale still set at 0°, the recombination beam splitter BS2 and the first 200 μm pinhole P1 are both attached to the collection optical rail. P1 is positioned in the path of the incident light beam. Both the heterodyne and the input beams should follow the same optical path after BS2 in order to obtain full heterodyne efficiency. This is achieved by tuning the beam steerers BSP7 (located on top of the goniometer) and BSP8 (situated just below BS2) that control the optical path of the heterodyne ray.

e) Finally, the lens L2, analyser, 200 μm pinhole P2 and PMT detector are mounted onto the collection optical rail. The position of the focusing lens L2 is adjusted in order to optimise the detected scattered signal at the pinhole P2.

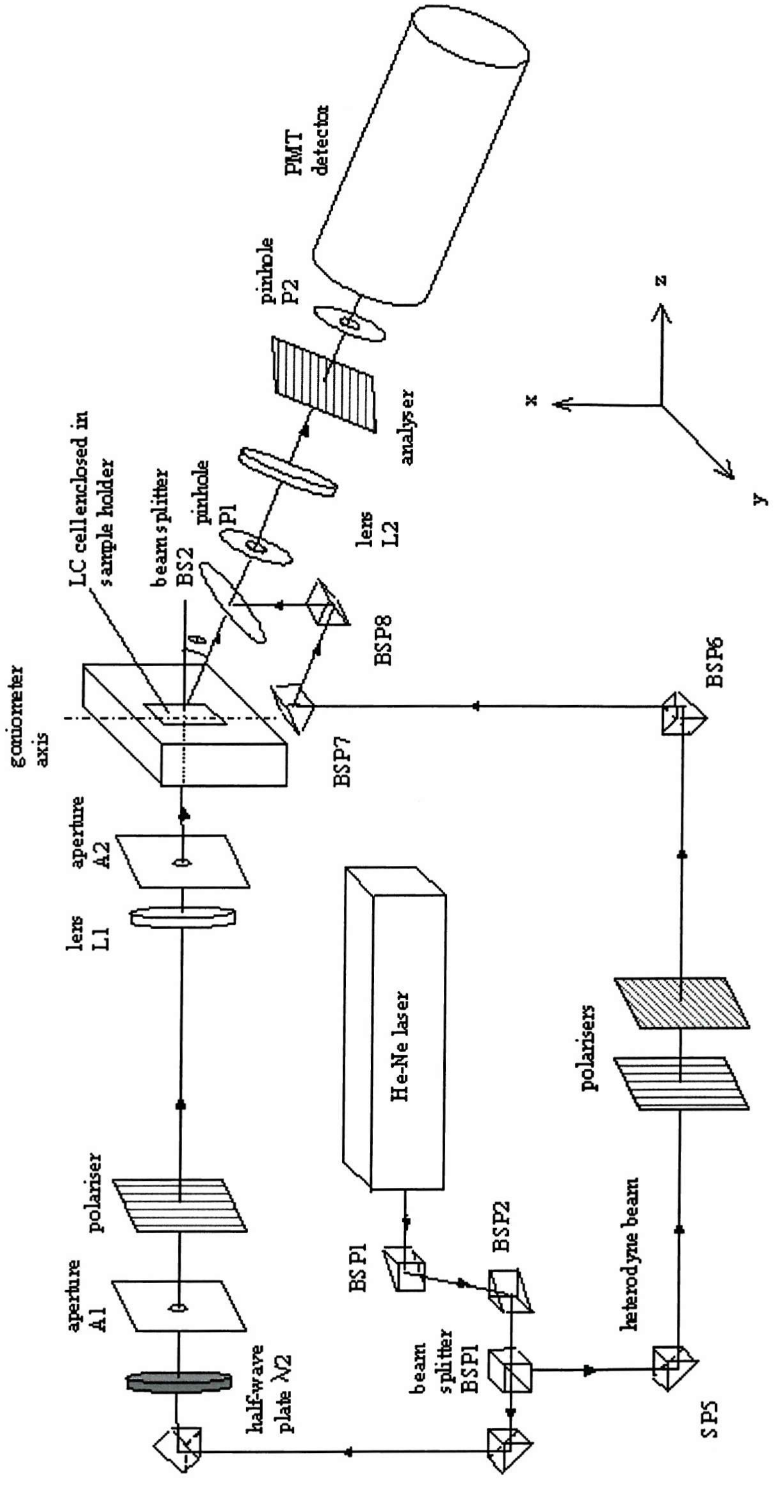

Figure 4.1: Diagram of the light scattering spectrometer (see Figure 3.5).

4.2.2 Aligning the cell with respect to the spectrometer

The spectrometer is initially configured for the study of the twist fluctuations (mode 2): the polariser and analyser are respectively orthogonal and parallel to the scattering plane and the scattering angle is set to 14° to minimise the bend contribution to mode 2.
The appropriate experimental geometry described in Chapter 2, Section 2.7.1 requires the use of homeotropic cells with the director oriented along the incident beam. The sample holder is positioned correctly by using three screws to ensure the back reflection from the cell is incident on the input aperture A2.

The main requirement for aligning the cell in the spectrometer is that the scattering volume has to be precisely located at the intersection of the input beam, the collection optics and the rotation axis of the goniometer (refer to Figure 4.1). This is achieved in the homodyne mode by moving the cell parallel to the input beam along the z-direction until a sharp increase (of about 5 kHz) in count rate is detected at the photon counter.

However, it is also necessary to perform a few experimental runs of short duration times (10-20 s) to maximise the dynamic component of the scattered light due to the fluctuations of the liquid crystal director, rather than the static component caused by impurities or glass flare. The cell alignment was found to be optimal when the normalised amplitude of the correlation function a_{norm} is maximised to 0.8-0.9; a_{norm} is defined as $a_{norm} = a_2/a_1$ where a_1 and a_2 are respectively the fitted background and signal amplitude. Fine adjustments to the sample holder are then made using the micro-positioning screws, which enable translation along x-, y- and z-directions.

4.2.3 Heterodyne mode

Previous studies have shown that when the heterodyne intensity is over 20 times the scattered intensity, there is no dependence of the fitted linewidth on the heterodyne intensity.[6] To confirm this, we have repeated the same experiment, which consists of collecting spectra at different heterodyne intensities. In Figure 4.2, the linewidth is plotted against I_{tot}/I_{sca}, which is the ratio of total intensity to scattered light intensity of the autocorrelation function. The fully heterodyned linewidth is obtained for a scattering-to-heterodyne intensity ratio higher than 1:15, which corresponds to a normalised amplitude a_{norm} of the order of 0.03-0.04. In the pure homodyne detection mode, for which $I_{tot}/I_{sca} = 1$ or $a_{norm} = 1$, the linewidth should be twice the fully heterodyned one.

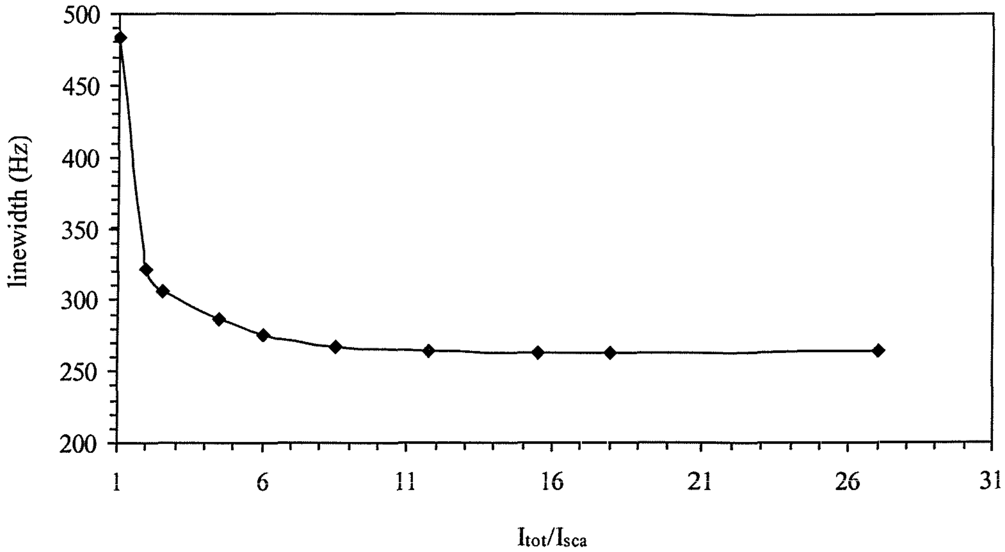

Figure 4.2: Twist linewidth as a function of the ratio between total and scattered intensities obtained using 5CB at temperature T = 24.6 °C.

4.3 Calibration using 5CB

The standard liquid crystal material chosen to calibrate the instrument is 4-pentyl-4'-cyanobiphenyl, also known as 5CB, provided by Merck. This compound, first synthesised by G. Gray and co-workers in 1973, exhibits a high photo and chemical stability. Since that time, it has been widely studied and its physical properties are well-documented.[7-20]

As it has been characterised by a number of different techniques, including DLS and Freedericksz transition, the data measured in this work can be readily compared to the values existing in the literature. Its chemical structure is sketched in Figure 4.3. The melting and clearing temperatures are given below:

Cr 20°C **N** 34.9°C **I**

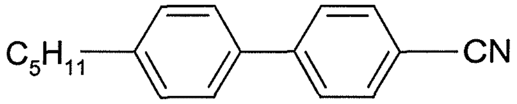

Figure 4.3: Chemical structure of 4-pentyl-4'-cyanobiphenyl (5CB).

In this thesis, most of the experimental results are reported as a function of relative or shifted temperature T_{NI}-T, where T is the measurement temperature and T_{NI} is the clearing point or nematic-to-isotropic transition temperature. Both temperatures are expressed in degrees Celsius. In order to account for the different heating systems used, T_{NI} for a given sample is usually determined for each experimental technique by monitoring a significant change in the measured property (eg. change in capacitance). For most experiments carried out in this work, the absolute error on T_{NI} is 0.4°C (except for polarised microscopy where the Linkam hotstage employed allowed transition temperatures to be accurate to within ± 0.1 °C).

4.3.1 Dielectric constants, refractive indices and orientational order parameter

The components $\varepsilon_{\parallel}$ and $\varepsilon_{\perp}$ of relative dielectric permittivity, obtained in this work, are plotted in Figure 4.4 for 5CB. The uncertainty of ± 0.5% on the dielectric constants is contained within the experimental data points and the absolute error of ± 0.4°C on T_{NI}-T is shown in the same figure. Both $\varepsilon_{\parallel}$ and $\varepsilon_{\perp}$ are lower than the data measured by Sefton[6, 7] also included in Figure 4.4. Figure 4.5 represents the resulting dielectric anisotropy $\Delta\varepsilon = \varepsilon_{\parallel} - \varepsilon_{\perp}$ determined in this work and by other groups. Our values of $\Delta\varepsilon$ are generally about 5% lower than the results quoted in the literature.[4, 7, 8] The dielectric permittivities are extremely sensitive to impurities and are influenced by the chemical purity of the mesogenic material.[9] Consequently, different batches of 5CB may account for a discrepancy of up to 2% in the experimental values of $\varepsilon_{\parallel}$ and $\varepsilon_{\perp}$.[9] The three data sets taken from different references seem in good agreement compared to one another. Since the values of static dielectric permittivity are independent of the probe frequency in the range 100 Hz to 100 kHz,[6] the fact that the measurements were carried out at 10 kHz (this work/Birtwistle) or at 1 kHz (Sefton/Bradshaw *et al.*) should not affect the results.

It should be mentioned that Sefton and Bradshaw *et al.* used a single planar cell with a gap of about 50 μm to evaluate both dielectric components $\varepsilon_{\parallel}$ and $\varepsilon_{\perp}$.[6, 8] This cell has a circular electrode enclosed by a guard ring to prevent fringing field effects. For materials with $\Delta\varepsilon > 0$, an electric field, applied normal to the glass plates, will induce a homeotropic alignment above the Freedericksz threshold. The effective dielectric constant is proportional to the reciprocal of the applied voltage 1/V and the value of $\varepsilon_{\parallel}$ is given by linear extrapolation to infinite voltage.[10] This extrapolation method has an accuracy of about 0.5% and yields results in good agreement with those obtained from the direct measurement with two cells.

In this work, we employed the two cell-method with homeotropic and planar alignment to measure respectively $\varepsilon_{\parallel}$ and $\varepsilon_{\perp}$. The type of cells used in this study may explain the discrepancy regarding our data; these Lucid cells, manufactured with thickness around 7.5 μm, are described in Chapter 3 Section 3.2.3. They differ from those used in single cell measurements in that they have square electrodes, no guard ring and are much thinner. The cells used by Birtwistle were identical to the cells employed in the present work except that they were 14 μm thick. In this case, the values of capacitances of the cells filled with liquid crystal were corrected by 10% to take into account electrode edge effects.[4] However, this calibration procedure seems quite arbitrary since the correction factor should account for the coupling between fringing field effects and a given LC material and thus should be dependent on the dielectric constants of the individual sample. As will be discussed later in Section 4.3.4, the lower values for the dielectric anisotropy do not affect significantly the values of the elastic constants and viscosity coefficients, which are consistent with those determined by other workers. Thus, our dielectric measurements with no further correction are considered scientifically acceptable.

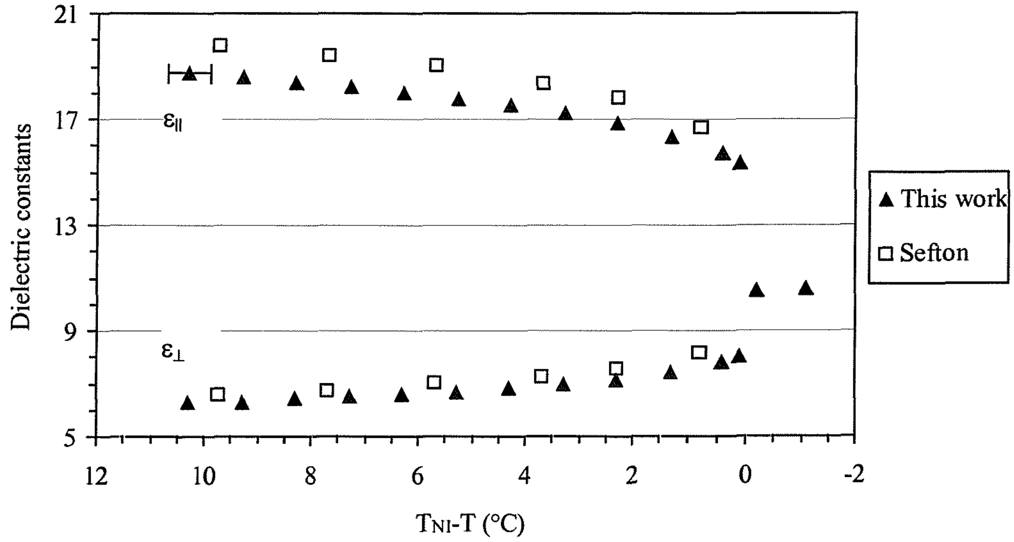

Figure 4.4: Dielectric constants (± 0.5%) for 5CB.

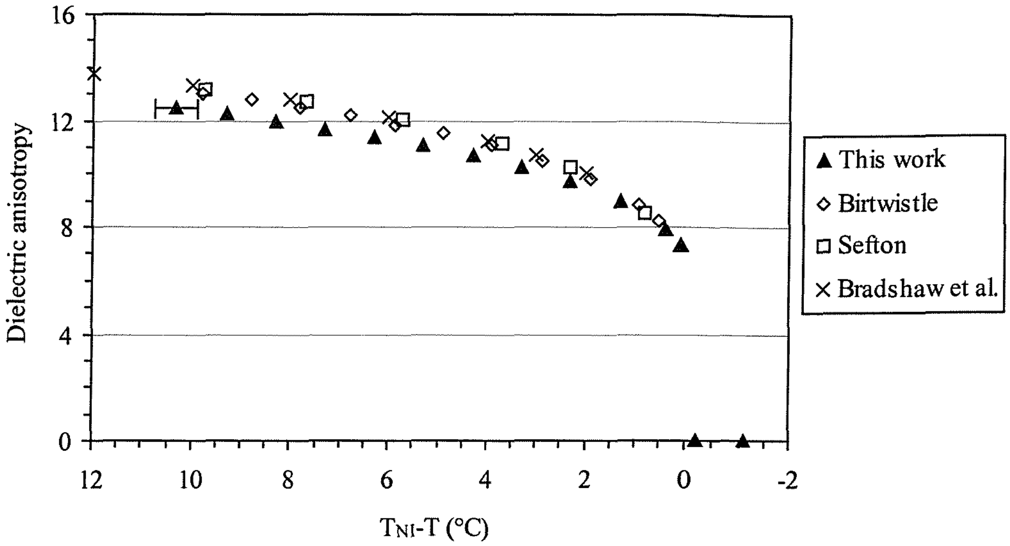

Figure 4.5: Dielectric anisotropy (± 1%) for 5CB.

In Figure 4.6, the experimental ordinary and extraordinary refractive indices for 5CB, measured by Abbé refractometry, are shown against shifted temperature. They agree well with the values reported by other workers using similar techniques.[7]

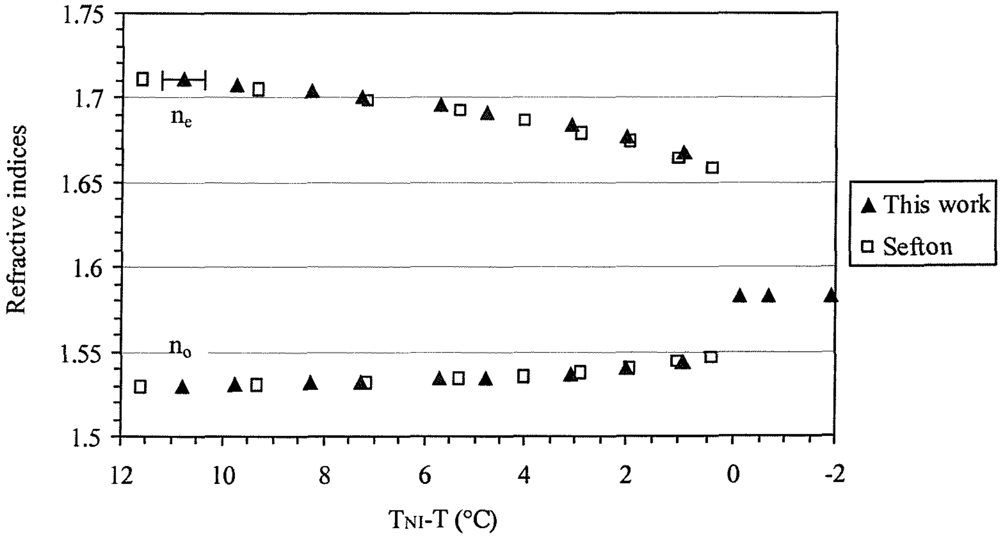

Figure 4.6: Extraordinary n_e and ordinary n_o refractive indices (± 0.0002) for 5CB.

As explained in Chapter 2 Section 2.2, it is possible to deduce the nematic orientational order parameter S from the measured values of refractive indices using the following equation derived from Haller's extrapolation technique (recall Equation 2.3):

$$\mathrm{Log}_{10}\left(\frac{n_e^{\,2}-n_o^{\,2}}{\overline{n^2}-1}\right)=\beta\,\mathrm{Log}_{10}\left(1-\frac{T}{T^*}\right)+\mathrm{Log}_{10}\left(\frac{\Delta\alpha}{\overline{\alpha}}\right). \qquad \mathbf{(4.1)}$$

The three parameters T^*, β and $\Delta\alpha/\overline{\alpha}$ were determined using a powerful non-linear least square fit method (based on the Levenberg-Marquardt algorithm) available from the software Origin 6.0. Then, S was calculated from the following expression:

$$S=\left(1-\frac{T}{T^*}\right)^{\beta}. \qquad \mathbf{(4.2)}$$

The order parameter is drawn in Figure 4.7 for 5CB. The resulting uncertainty on S is typically 0.02. The values obtained by Sefton[6] are also presented for comparison. The agreement between our data and the order parameter determined in the cited reference provides a good assessment of the accuracy and demonstrates the validity of the fitting routine employed.

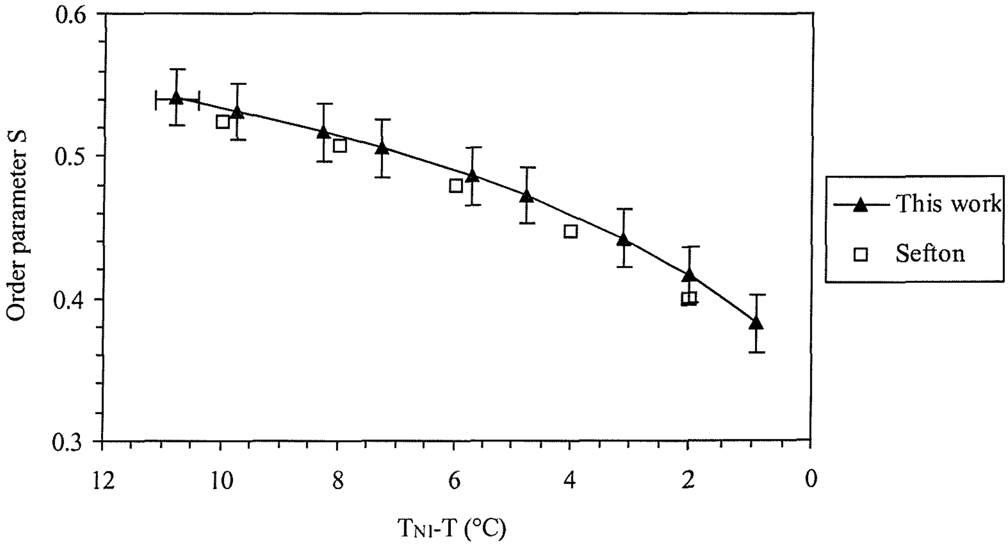

Figure 4.7: Nematic orientational order parameter S (± 0.02) for 5CB.

4.3.2 Light scattering from director fluctuations

In DLS experiments, the visco-elastic ratios can be determined from the measurement of the linewidth associated with the exponential decay of each mode of director fluctuations. Using the experimental geometries introduced in Chapter 2, Section 2.7.1, the splay and twist linewidths are given by

$$\Gamma_1 = \Gamma_{splay} = \frac{k_{11}}{\eta_{splay}} q_\perp^2 \tag{4.3}$$

and $$\Gamma_2 = \Gamma_{twist} = \frac{k_{22}}{\gamma_1} q_\perp^2 \tag{4.4}$$

where k_{11} and k_{22} are the splay and twist Franck elastic constants, η_{splay} and γ_1 are the corresponding viscosity coefficients and $q_\perp = \frac{2\pi}{\lambda}\sin\theta_{lab}$ is the component of the scattering wave vector normal to the director.

The twist and splay elastic constant to viscosity coefficient ratios are illustrated respectively in Figure 4.8 and Figure 4.9 for 5CB against relative temperature. The results obtained for the same material by previous workers using a similar spectrometer are also included on the same graphs.[4, 6, 11] Our twist and splay visco-elastic ratios are measured respectively with ± 1.5% and ± 3% uncertainties, also indicated on both graphs; the values are in excellent agreement with the ones determined by Birtwistle. In both cases, the data were collected on a DLS spectrometer, based on the same experimental design.[4] The twist and splay ratio values measured in this work are systematically about 2% and 5% lower than the ones quoted by Sefton/Bancroft.[6, 11] The main modification between the recent version of the apparatus and the original one employed by Sefton/Bancroft is the sample holder. The minor differences in visco-elastic ratios may be attributed to slight differences in the optical alignment required by the geometry of each sample holder.[4]

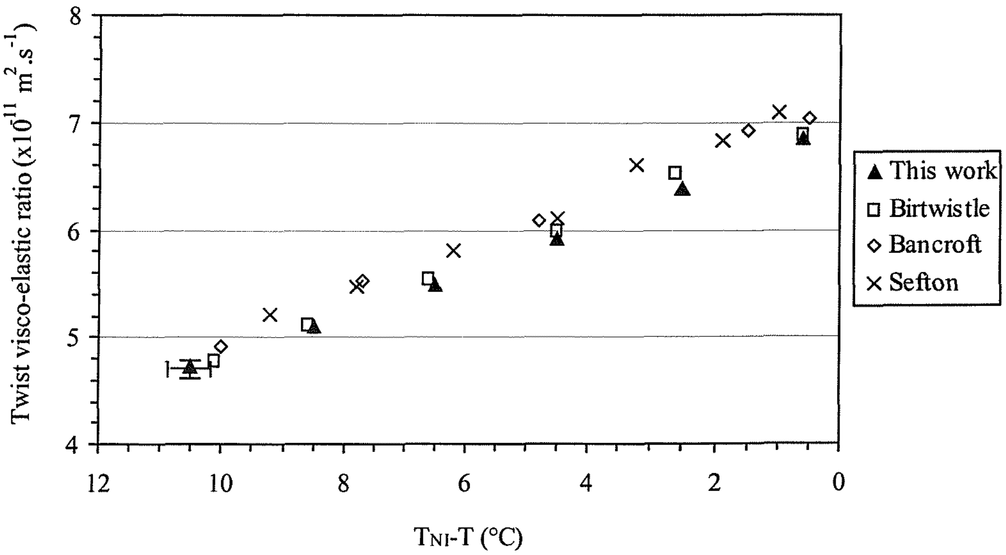

Figure 4.8: Ratio of twist elastic constant to viscosity coefficient for 5CB.

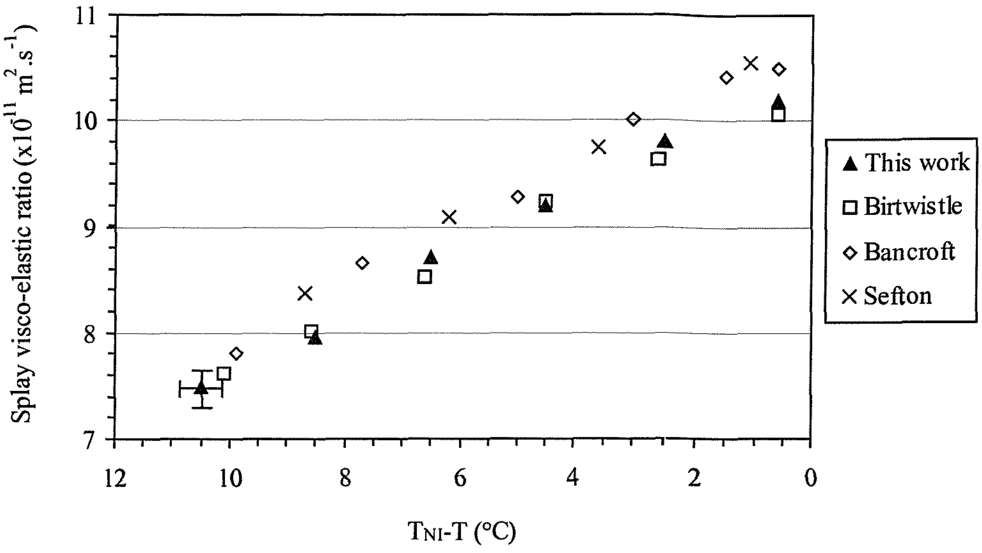

Figure 4.9: Ratio of splay elastic constant to viscosity coefficient for 5CB (± 3% accuracy).

4.3.3 EFDLS

An external electric field E may be applied parallel to the director (for a material with positive dielectric anisotropy) to dampen the thermal fluctuations. In this case, the characteristic decay time is increased and the scattered linewidth becomes:

$$\Gamma_{\text{splay}} = \frac{k_{11}}{\eta_{\text{splay}}} q_{\perp}^2 + \frac{\varepsilon_0 \Delta\varepsilon \varepsilon_{\parallel}}{\varepsilon(\theta_{LC}/2)\eta_{\text{splay}}} E^2 \quad (4.5)$$

$$\Gamma_{\text{twist}} = \frac{k_{22}}{\gamma_1} q_{\perp}^2 + \frac{\varepsilon_0 \Delta\varepsilon}{\gamma_1} E^2, \quad (4.6)$$

where ε_0 is the vacuum permittivity, $\Delta\varepsilon$ is the dielectric anisotropy of the liquid crystal, $\varepsilon_{\parallel}$ and $\varepsilon_{\perp}$ are the dielectric constants parallel and perpendicular to the director and $\varepsilon(\theta_{LC}/2) = \varepsilon_{\perp} + \Delta\varepsilon \sin^2(\theta_{LC}/2)$. θ_{LC} is defined as the scattering angle in the LC medium and is directly related to the scattering angle in the laboratory θ_{lab} via the refractive indices n_e and n_o of the nematic material (see Chapter 2, Equation (2.105)).

From the theory, both the splay and twist linewidths are expected to be proportional to the squared rms voltage V^2. This relationship is well-verified for any values of the applied voltage and at all temperatures within the nematic range as can be seen in Figure 4.10 where Γ_{splay} and Γ_{twist} are depicted against V^2 for 5CB. If the scattered linewidth is represented as a function of the square of the applied voltage, the gradient G_{α} of the plot will yield the viscosity, provided that the cell gap d and the dielectric constants $\varepsilon_{\parallel}$ and $\varepsilon_{\perp}$ of the material are known. For the splay mode, it is also necessary to measure the refractive indices n_e and n_o of the liquid crystal independently. The gradient G_α is calculated from

Splay mode
$$G_1 = \frac{\varepsilon_0 \Delta\varepsilon \varepsilon_{\parallel}}{\varepsilon(\theta_{LC}/2)\eta_{splay} d^2} \quad \textbf{(4.7)}$$

Twist mode
$$G_2 = \frac{\varepsilon_0 \Delta\varepsilon}{\gamma_1 d^2}. \quad \textbf{(4.8)}$$

The elastic constant can be deduced from the visco-elastic ratio given by the intercept of this curve at V = 0. In the presence of an applied electric field, the elastic constants and viscosity coefficients can be determined separately.

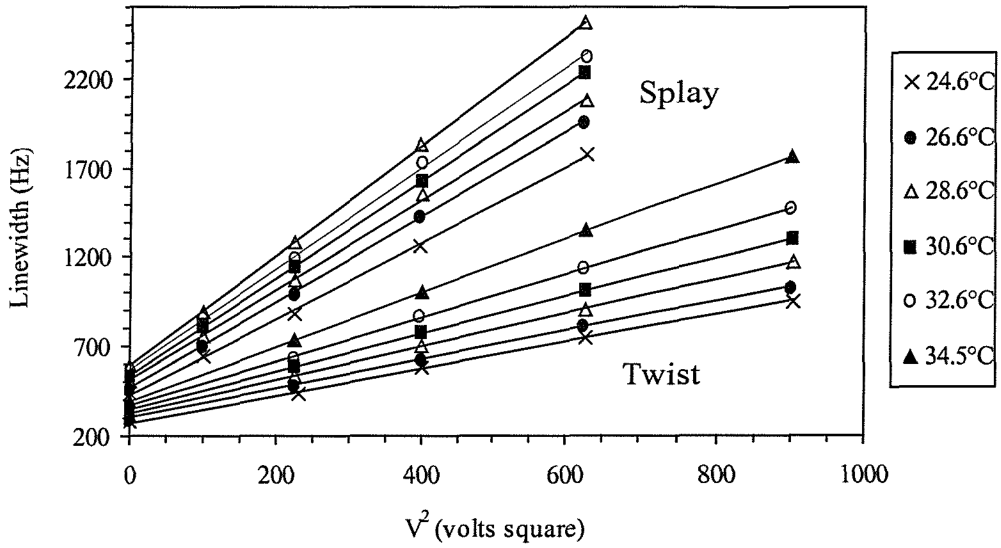

Figure 4.10: Experimentally measured linewidths for the splay and twist modes as a function of squared rms voltage at different temperatures for 5CB.

4.3.4 Elastic constants and viscosity coefficients

Figure 4.11 represents the twist and splay viscosities as a function of shifted temperature for 5CB. The twist viscosity coefficients measured by Birtwistle and Sefton using DLS on the same material are plotted on the same figure.[4, 6] Our twist viscosity values are obtained with an uncertainty of ± 2% while the splay ones are given to within an accuracy of ± 6% and any deviations seen in Figure 4.11 between different data sets are within experimental errors. Therefore, our data can be considered in very good agreement with those of references 4 and 6. The splay viscosity is related to the twist viscosity through

$$\eta_{splay} = \gamma_1 - \frac{2\alpha_3^2}{\alpha_3 + \alpha_4 + \alpha_6}, \tag{4.9}$$

where α_i are the Leslie viscosity coefficients.

As shown in Figure 4.11, $\eta_{splay} = \gamma_1$. The term $\frac{2\alpha_3^2}{\alpha_3 + \alpha_4 + \alpha_6} = \frac{\alpha_3^2}{\eta_2}$ is positive and negligible since α_3 is much smaller than the other coefficients[12] (η_2 is the Miesowicz viscosity coefficient defined in Chapter 2, Equation (2.29)).

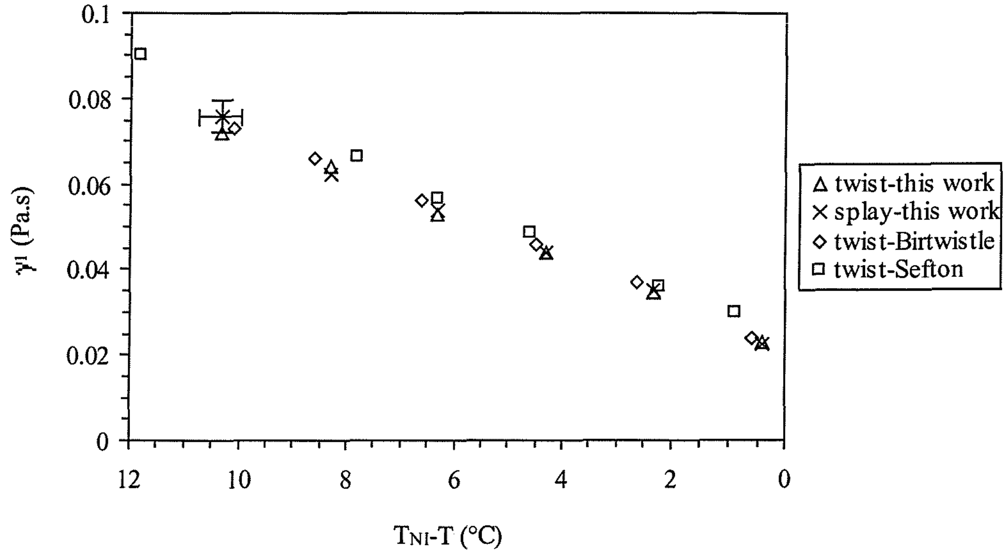

Figure 4.11: Twist (± 2%) and splay viscosity (± 6%) coefficients for 5CB.

The twist and splay elastic constants measured for 5CB in this work are illustrated in Figure 4.12 and Figure 4.13. The error bars for our values of k_{22} and k_{11} correspond respectively to ± 3% and ± 5% uncertainties and they are indicated in the figures. Results from previous DLS experiments using a similar apparatus are also included for comparison. Our elastic constant data agree well with the values taken from Birtwistle's thesis[4] but they are systematically 10% lower than the ones obtained by Sefton[6]. As explained in Section 4.3.2, the discrepancy stems mainly from the differences between the values of splay and twist visco-elastic ratios determined using different experimental set-ups. The twist and splay elastic constants and associated viscosities can be considered sufficiently accurate since the purpose of this thesis is to compare the visco-elastic properties of a wide-range of nematic liquid crystals.

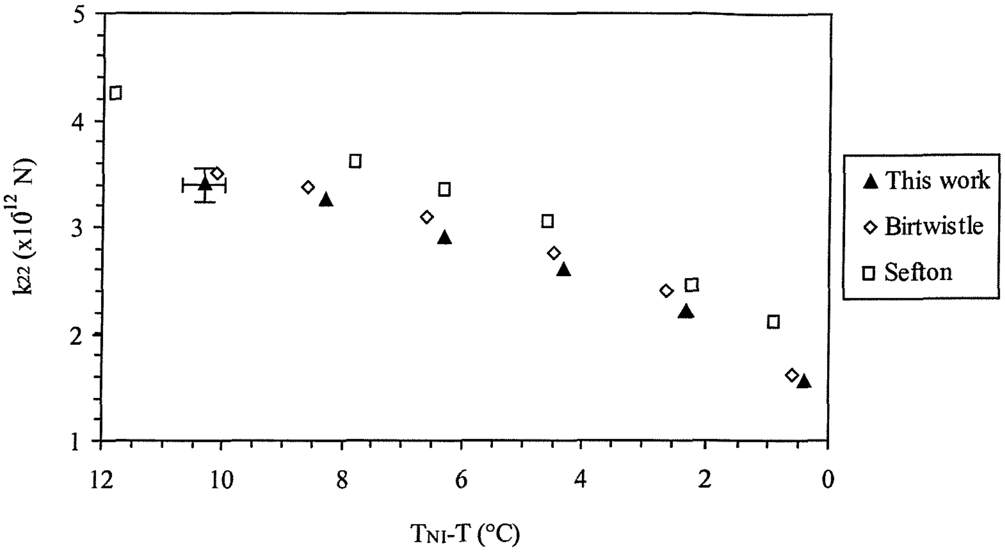

Figure 4.12: Twist elastic constant for 5CB.

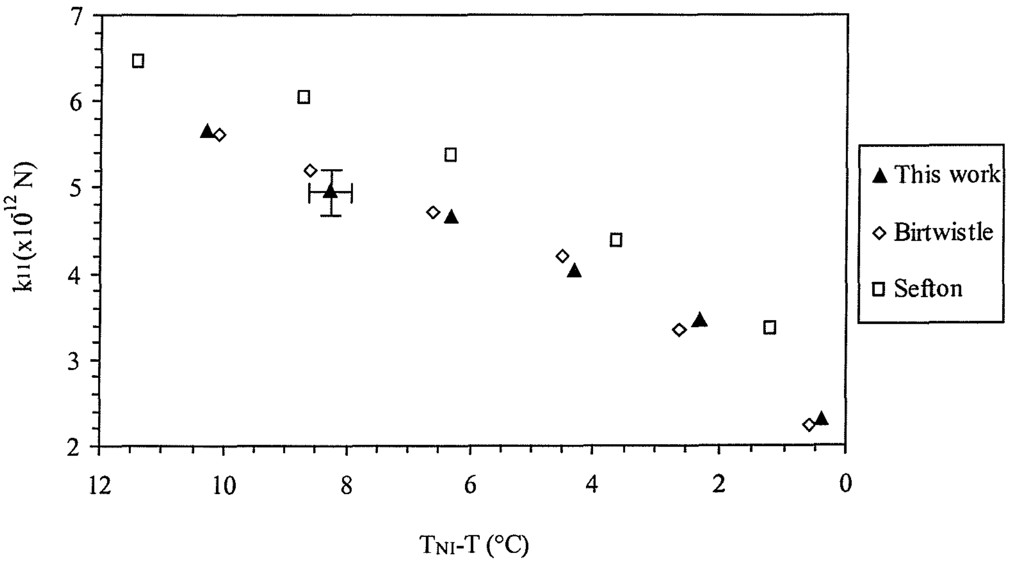

Figure 4.13: Splay elastic constant for 5CB.

It is interesting to compare our results with the visco-elastic data measured with different techniques: static and dynamic light scattering,[12, 13, 14, 15, 16] Freedericksz transition induced by magnetic or electric fields[8, 9, 17, 18] and flow viscometry[19]. The rotational viscosity, twist and splay elastic constants from a number of these experiments are added to the same graphs as our data in Figures 4.14, 4.15 and 4.16.

The twist viscosity derived in the present study is in good agreement with the values determined by other methods. Nevertheless our data exhibit a slightly different temperature dependence, especially at lower temperatures, with a decrease in our twist viscosity of about 13% at T_{NI}-T = 10 °C compared to the value given by Gu *et al.*[16]

The twist and splay elastic constants quoted from various references reveal quite a wide dispersion range and they also have different temperature dependences. The values measured by Madhusudana *et al.* are significantly lower than the ones obtained in all other references.[17] This discrepancy may be attributed to the indirect procedure employed by this group to evaluate the magnetic susceptibility anisotropy $\Delta\chi$.[9, 17] The absolute values of k_{22} reported in this work are within 5% of the measurements of Breddels *et al.*, who observed the twist Freedericksz transition using a conoscopic technique[18] (in which both k_{22} and γ_1 were determined by monitoring the dynamic response of the interference pattern). Furthermore, the thermal behaviour of k_{22} is rather similar between these two data sets. Toyooka *et al.* used four distinct experimental methods based on light scattering to evaluate k_{22}:[15] (electric field) static light scattering, electric field dynamic light scattering and forced Rayleigh scattering. The accuracy of these experimental techniques is about 7% and their results (not presented here) are in good agreement with the data from Chen[12] and Breddels[18]. Our data for k_{11} are about 10-15% lower than the values reported by Chen *et al.* [12] and by Bradshaw *et al.*[8]; whereas, they are in good agreement with the splay elastic constants from Madhusudana *et al.*.[17] The twist and splay elastic constants of 5CB determined by Hakemi *et al.* by anisotropy of turbidity[20] are systematically 2.5 to 6 times larger than the values found in the literature and therefore are not included for discussion.

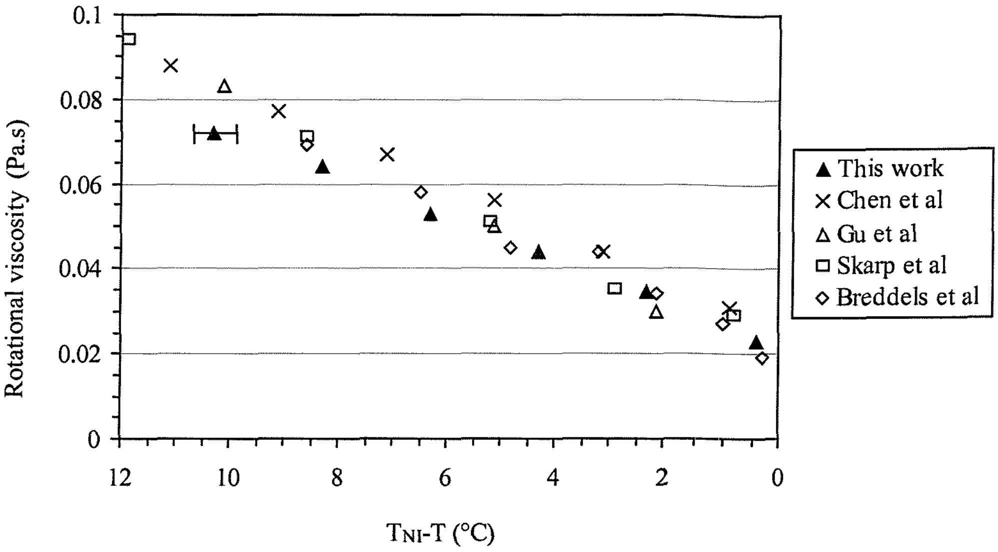

Figure 4.14: Comparison of twist viscosity coefficients for 5CB obtained via different methods.

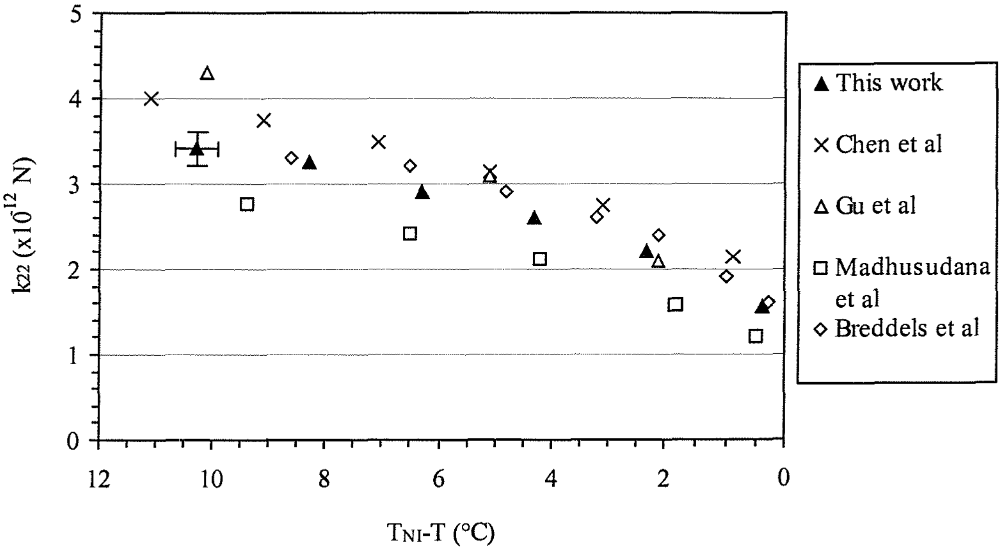

Figure 4.15: Comparison of twist elastic constant values for 5CB measured in various experiments.

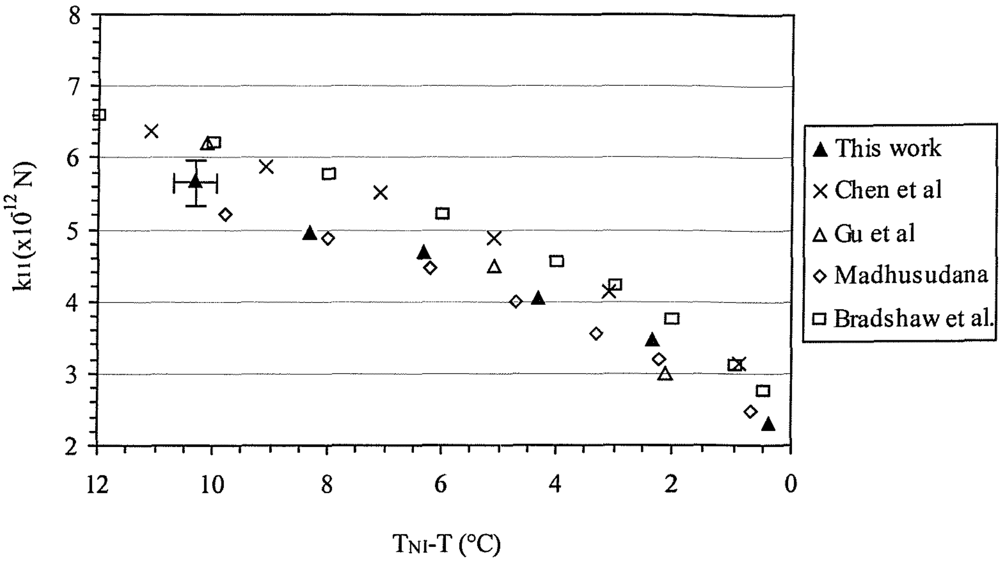

Figure 4.16: Comparison of splay elastic constant for 5CB.

4.3.5 Conclusion

In this section, we have reported on the initial calibration measurements using a standard nematic material 5CB. The dielectric constants are about 5% lower than the reference data while the refractive indices agree well with the values quoted in the literature. The twist and splay visco-elastic ratios are measured in this work with a relative uncertainty of 1.5% and 3% while the elastic constants k_{22} and k_{11} are determined to within ± 3% and ± 5%. The twist viscosity coefficient is obtained with a 2% error. Our values are consistent though slightly lower than the data obtained on other light scattering spectrometers or using different techniques. Minor discrepancies have also been observed in the thermal dependence of the results obtained from various methods. The uncertainty on the visco-elastic constants will depend not only on the associated experimental quantity but also on the accuracy of other related experiments necessary to derive the absolute visco-elastic values, in particular, measurements of material constants (e.g. $\Delta\varepsilon$, $\Delta\chi$, n_e and n_o) and of external parameters, such as temperature and cell thickness.[15]

The reproducibility of the results obtained in this work has been thoroughly checked by repeating the same measurements on three different cells of similar thicknesses filled with 5CB.

4.4 Investigation of a series of mixtures of different birefringence

After calibrating the spectrometer, the visco-elastic constants of a series of nematic mixtures were measured. The three mixtures were provided by Merck Ltd (UK) and each contains several low molar mass mesogenic components based on cyanobiphenyls (A), phenylbenzoates (B) and dicyclohexyls (C). These mixtures are characterised by different optical anisotropies. The aim of this study is to compare the absolute values of the twist and splay elastic constants as well as the ratio k_{22}/k_{11} obtained for each mixture. Table 4.1 below recapitulates the main properties of each sample.

Mixture	Clearing point T_{NI}	Birefringence
Cyanobiphenyls (A)	35 °C	high
Phenylbenzoates (B)	35 °C	medium
Dicyclohexyls (C)	45 °C	low

Table 4.1: A, B and C mixtures with their main constituents and their clearing points.

4.4.1 Dielectric and optical properties

The values for the dielectric anisotropy $\Delta\varepsilon$ (± 1%) and birefringence Δn (± 0.0002) measured for each mixture are given versus relative temperature T_{NI}-T in Figure 4.17 and Figure 4.18 respectively. The experimental uncertainties on both parameters are contained within the data points. The dielectric anisotropy is significantly higher for the mixture of cyanobiphenyls ($\Delta\varepsilon = 8.5$ to 13) than for the samples containing phenylbenzoates or dicyclohexyls. This increase is due to the presence of LC molecules with strongly polar nitrile groups in sample A. The dielectric properties of B and C are quite similar: their $\Delta\varepsilon$ is low (between 1 and 2), almost constant and shows a weaker temperature dependence than in the case of mixture A. The three mixtures have very different optical behaviour: the sample with cyanobiphenyls is a high birefringence mixture ($\Delta n = 0.15$ to 0.2), the mixture of dicyclohexyls is a low birefringence mixture ($\Delta n = 0.03$ to 0.05) while the sample containing phenylbenzoates exhibits intermediate values of Δn (between 0.08 and 0.12).

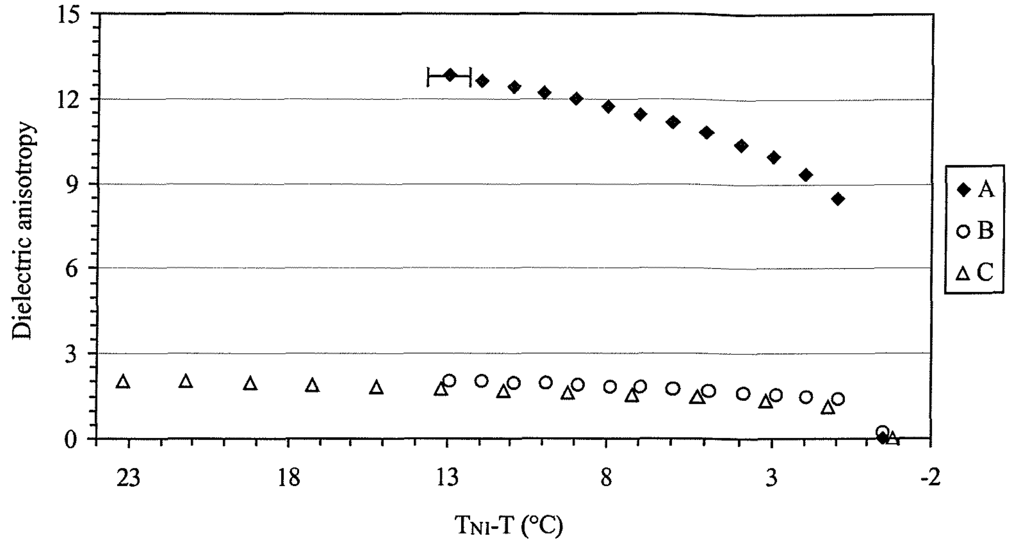

Figure 4.17: Dielectric anisotropy of the A, B and C mixtures.

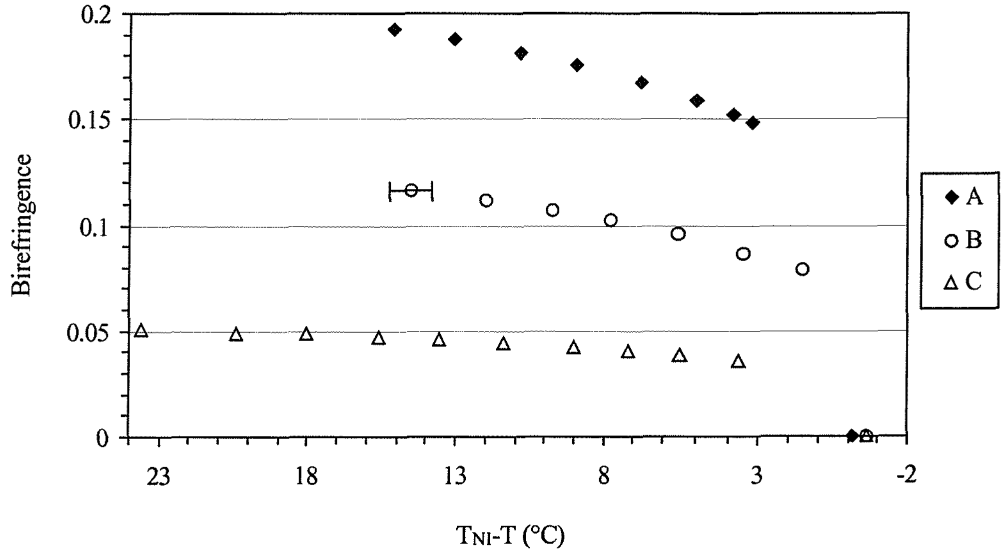

Figure 4.18: Optical anisotropy of the mixtures A, B and C.

4.4.2 Visco-elastic properties

The twist and splay elastic constants k_{11} and k_{22} and associated viscosity coefficients were determined at the same shifted temperature, to enable comparison between the three mixtures. Table 4.2 summarises all visco-elastic results as well as the dielectric anisotropy and birefringence data taken at T_{NI}-T = 13 °C.

	Cyanobiphenyls	Phenylbenzoates	Dicyclohexyls
T (°C)	22	22	32
T_{NI}-T (°C)	13	12.9	13.2
$\Delta n \pm 0.0002$	0.188	0.114	0.046
$\Delta\varepsilon \pm 1\%$	12.8	2.1	1.8
k_{22} (pN)	3.7 ± 0.1	3.5 ± 0.1	3.3 ± 0.2
k_{11} (pN)	5.9 ± 0.3	6.4 ± 0.3	5.9 ± 0.4
k_{22}/k_{11}	0.63 ± 0.03	0.55 ± 0.03	0.56 ± 0.04
γ_1 (mPa.s)	84 ± 2	92 ± 2	18 ± 1

Table 4.2: Summary of the physical properties of the three mixtures at T_{NI}-T = 13 °C.

Neither k_{22} nor k_{11} change significantly with mixture composition. Therefore, the three samples have the same twist-to-splay elastic constant ratio if the experimental errors on k_{22} and k_{11} are taken into account. This ratio does not vary with mixture composition or nature, which is confirmed in this work. k_{22}/k_{11} has been found experimentally to range from 0.5 to 0.7 and to be weakly dependent on temperature for most nematic materials[21] (if pre-transitional effects are excluded).

As expected, the splay viscosity η_{splay} is equal to γ_1 within experimental uncertainties for samples containing cyanobiphenyls and phenylbenzoates. Furthermore, the rotational viscosity γ_1 is of the same order of magnitude for these two mixtures. By contrast, in the case of the dicyclohexyl compounds, γ_1 is reduced by approximately a factor of 5. In general, higher rotational viscosity coefficients are associated with strongly polar materials,[21] such as the cyanobiphenyls. For the dicyclohexyl mixture, η_{splay} is much lower than γ_1, which would lead to a negative value for $\frac{2\alpha_3^2}{\alpha_3+\alpha_4+\alpha_6}$. This result can be interpreted as a greater experimental error for sample C due to the weaker scattered signal from this low birefringence sample, as illustrated in Table 4.3. Though the experimental duration is increased to 3000 s for this mixture, the number of scattered photons is still significantly reduced compared to the samples containing cyanobiphenyls and phenylbenzoates. From the data collected in Table 4.3, there is a direct correlation between the birefringence of a material, its scattering behaviour and the noise factor associated with the measured linewidth. The noise factor, defined in Chapter 3, Equation

(3.10), is a measure of the accuracy of the fitted data with respect to the experimental values.

DLS still gives reliable order-of-magnitude information on the viscosity but in the case of mixture C, the absolute viscosity is obtained with an accuracy of ± 6% while for samples A and B, the uncertainty is only ± 2% as indicated in Table 4.2. This also leads to further error on the elastic constant values for sample C.

	Cyanobiphenyls	Phenylbenzoates	Dicyclohexyls
Scattered signal (for one run)	75 kHz	58 kHz	20 kHz
Experimental duration	40 s x 25 runs	40 s x 30 runs	100 s x 30 runs
Twist linewidth	254.7 Hz	221 Hz	1161.8 Hz
Noise factor	0.01%	0.013%	0.055%

Table 4.3: Experimental data for the three mixtures at T_{NI}-T = 13 °C for the twist mode (using heterodyne detection).

4.4.3 Conclusion

The chemical structures of the mixtures and their polarities have a small effect on the twist and splay elastic constants.[22] Both k_{11} and k_{22} depend to a certain extent on the geometrical factors characteristic of a given mesogenic molecule, although the influence of the molecular shape is extremely complex to quantify in the case of mixtures of several components. The ratio k_{22}/k_{11} is remarkably constant for mixtures of different chemical nature. In contrast, the twist and splay viscosities are directly related to the polarity and the composition of the mixtures. Strongly polar nematic liquid crystals exhibit higher rotational viscosity coefficients.[21] This study also confirmed that the accuracy of the measurements of visco-elastic parameters depends on the birefringence of the material investigated.

4.5 Influence of dopants on the switching properties of LCDs

In the last section of this chapter, the influence of dopants on the visco-elastic properties of a nematic host was investigated using DLS.[23, 24] The measurements were performed on our spectrometer in collaboration with Dr. N. Kunimatsu from Displays, Hitachi, Ltd..

4.5.1 Introduction

The in-plane switching (IPS) mode was developed to improve the performance with respect to poor viewing angle and contrast ratio of the conventional twisted nematic (TN) display.[1, 2, 24] In an IPS cell, the reorientation of the mesogenic molecules, initially in a twisted configuration, occurs above a threshold field applied parallel to the substrate. In this mode, the liquid crystal switching behaviour is governed by the electric field and not by the voltage.[1] The threshold field depends only on the twist elastic constant k_{22} and is given by:

$$E_C = \frac{\pi}{d}\sqrt{\frac{k_{22}}{\varepsilon_0\,|\Delta\varepsilon|}}, \qquad \textbf{(4.10)}$$

where $\Delta\varepsilon$ is the dielectric anisotropy and d represents the thickness of the liquid crystal layer.

The switch-on and switch-off response times are expressed respectively by:[2]

$$\tau_{ON} = \frac{\gamma_1}{\varepsilon_0|\Delta\varepsilon|\,E^2 - \pi^2 k_{22}/d^2} \qquad \textbf{(4.11)}$$

$$\text{and} \quad \tau_{OFF} = \frac{\gamma_1 d^2}{\pi^2 k_{22}}, \qquad \textbf{(4.12)}$$

where γ_1 is the rotational viscosity and V is the applied voltage.

Materials with positive or negative $\Delta\varepsilon$ are both suitable for the IPS mode. Only liquid crystals with $\Delta\varepsilon > 0$ are considered in the present study since they present better switching characteristics, such as faster response time and lower threshold field.

Lower γ_1 coefficients and higher values of $\Delta\varepsilon$ are required to improve response times, while the twist elastic constant k_{22} has an opposing effect on the switch-on and switch-off response times; low k_{22} leads to a decrease in τ_{ON} while it causes an increase in τ_{OFF}.[24]

4.5.2 Materials and clearing points

The host liquid crystal is a commercial mixture ZLI-4792 supplied by Merck. This mixture is based on superfluorinated materials, containing cyclo and phenyl carbocycles with fluoro substituents. The four different dopants used are sketched in Figure 4.19, including their abbreviated names and chemical structures. All of the guest-host mixtures contain about 10% by weight of dopant molecules.

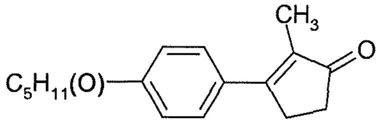

4-pentyl(oxy) phenylcyclopentenone or 5(O)PCP

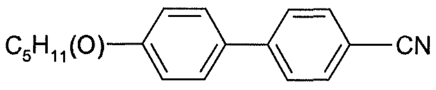

4-pentyl(oxy) 4'-cyanobiphenyl or 5(O)CB

Figure 4.19: Chemical structure of the four dopants used in this work; the brackets indicate the presence of an oxygen atom.

The nematic-to-isotropic transition temperatures are reported in Table 4.4. The addition of 5PCP and 5OPCP decrease T_{NI} of the pure host by about 30 °C whereas the same concentration of 5CB and 5OCB reduces T_{NI} by only 10 °C and 7 °C respectively. The greater effect of the phenylcyclopentenone is due to the fact that 5PCP and 5OPCP are non-mesogenic molecules while both 5CB and 5OCB exhibit a nematic phase, their clearing points being respectively 35 °C and 68 °C.

Sample	Clearing point T_{NI} (±0.1°C)
ZLI-4792	92.2
5CB	35
5OCB	68
ZLI-4792 + 10% 5CB	82.6
ZLI-4792 + 10% 5OCB	85.3
ZLI-4792 + 10% 5PCP	60
ZLI-4792 + 10% 5OPCP	61.8

Table 4.4: Nematic-to-isotropic transition temperatures for ZLI-4792, 5CB, 5OCB and the four doped mixtures.[23]

4.5.3 Results

Dielectric anisotropy

Both dielectric constants parallel and perpendicular to the director were determined using a single uniform planar cell.[23] As mentioned in Section 4.3.1, the single- and two-cell methods should yield identical values for the relative dielectric permittivities $\varepsilon_{\parallel}$ and $\varepsilon_{\perp}$.

The resulting dielectric anisotropy $\Delta\varepsilon$ for ZLI-4792 and the four doped mixtures is plotted in Figure 4.20 as a function of measured temperature T. It can be seen clearly that at any given T, $\Delta\varepsilon$ of the phenylcyclopentenone-doped samples is identical to $\Delta\varepsilon$ for the host material. The values of $\Delta\varepsilon$ in the cyanobiphenyl-doped mixtures are higher than those characterising the host and the 5(O)PCP-doped mixtures i.e. the addition of the (O)CB dopant increases $\Delta\varepsilon$ at a given temperature.

The same experimental data are given versus relative temperature T_{NI}-T in Figure 4.21. On this scale, the addition of any dopant increases the dielectric anisotropy of the pure host ZLI-4792. The $\Delta\varepsilon$ values lie on the same curve for 5(O)CB and 5OPCP and are slightly lower in the case of 5PCP.

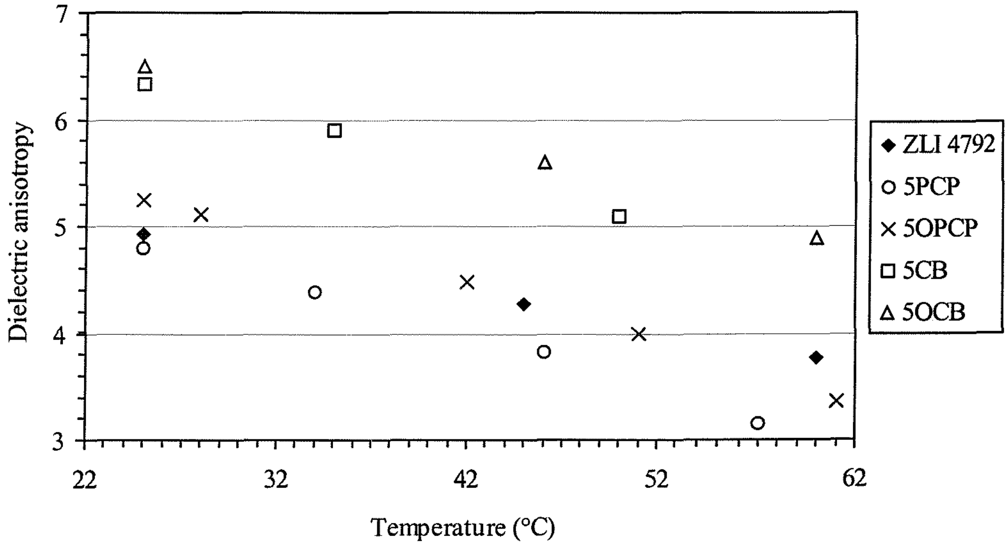

Figure 4.20: Dielectric anisotropy $\Delta\varepsilon$ (± 1%)for pure ZLI-4792 and with 5(O)PCP and 5(O)CB additives against temperature (Courtesy of Dr. N. Kunimatsu).[23]

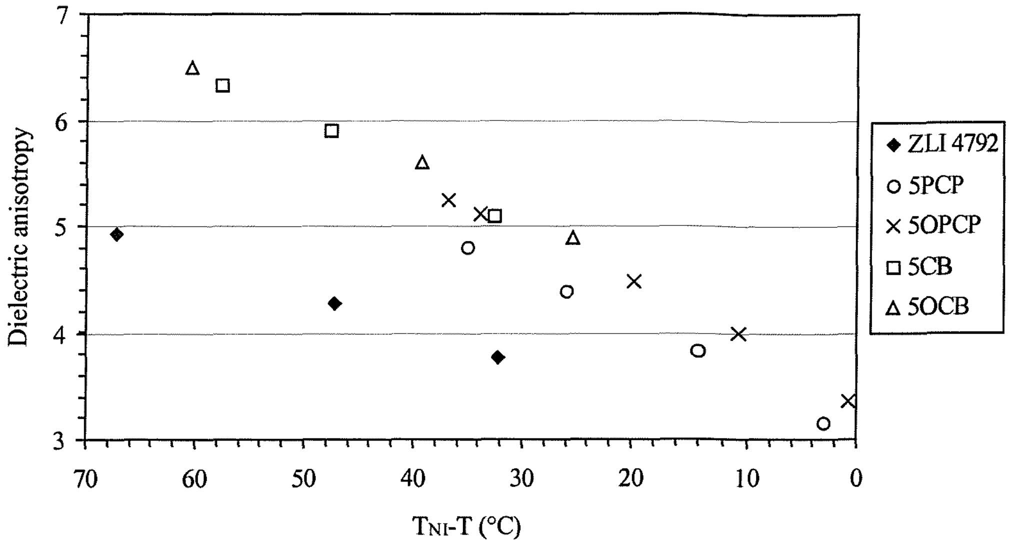

Figure 4.21: Dielectric anisotropy Δε (± 1%) for pure ZLI-4792 and with 5(O)PCP and 5(O)CB additives versus shifted temperature (Courtesy of Dr. N. Kunimatsu).[23]

Twist elastic constant

Figure 4.22 shows the twist elastic constants k_{22} of the four mixtures as a function of temperature. The addition of 5(O)CB has almost no influence on the value of k_{22} of the pure host mixture: k_{22} is identical for the pure ZLI-4792 and the 5OCB-doped sample (except at 61 °C). At all temperatures, the mixture with 5CB exhibits twist elastic constants about 10% lower than these of ZLI-4792. In the case of the phenylcyclopentenone additives, the twist elastic constant of the host mixture is reduced by about 30%.

If k_{22} is represented against relative temperature as depicted in Figure 4.23, the data obtained with the four different guest molecules can be considered to be superimposed onto a master curve. This may be explained by the fact that k_{22} is essentially proportional to S^2 where S is the nematic orientational order parameter, which itself depends on T_{NI}-T.[6, 7, 22] A greater spread of data is noticed at about T_{NI}-T = 32-35 °C, where the value of k_{22} is about 20% lower for 5PCP compared to the pure ZLI-4792; this discrepancy probably arises from an unexpectedly higher value for k_{22} measured for the host mixture at this shifted temperature.

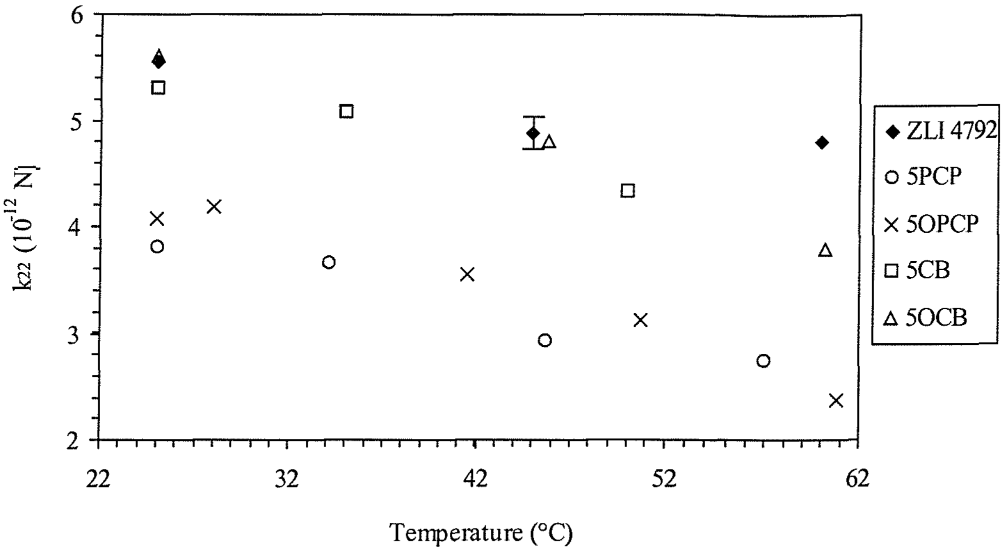

Figure 4.22: Twist elastic constant (± 3%) versus temperature.[23]

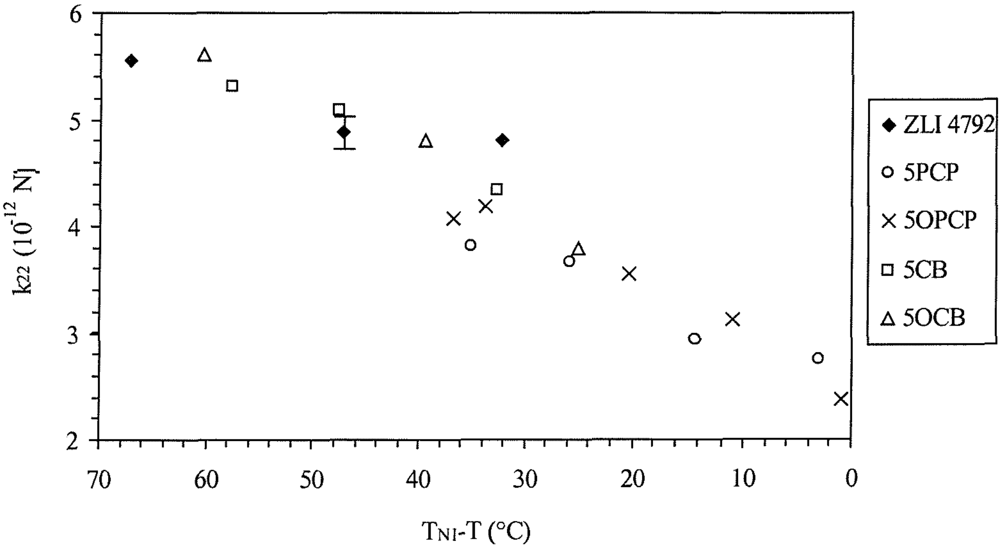

Figure 4.23: Twist elastic constant (± 3%) as a function of relative temperature (redrawn from 23).

Rotational viscosity

In Figure 4.24, the rotational viscosity coefficient γ_1 is illustrated on a log scale as a function of temperature. It shows a weak dependence on the nature of the added dopants: the twist viscosity of the nematic host remains unchanged in the presence of 5(O)CB and 5OPCP while it is decreased by approximately 30% when doped with the same concentration of 5PCP.

The rotational viscosity coefficient γ_1 is plotted on a logarithmic scale at different T_{NI}-T in Figure 4.25. All of the guest molecules are found to increase dramatically the value of γ_1 of the host at a given T_{NI}-T; this increase is about 45% for 5(O)CB and 180% in the case of 5(O)PCP. For nematics, experimental data for γ_1 can usually be described by a type of Arrhenius law that also takes into account the orientational order parameter S.[22, 25] The general form is given by

$$\gamma_1 \propto S^x \exp(E(S)/k_B T), \quad \textbf{(4.13)}$$

where E(S) is an activation energy. E(S) = E_0 or E_0S and x = 0, 1, or 2 depending on the best fit for the data; k_B is the Boltzmann constant. In Chapter 5, the temperature dependence of the rotational viscosity will be discussed in more detail. Equation (4.13) indicates that the rotational viscosity depends on both the relative and the standard temperature scales, the former is linked to the order parameter S while the latter is associated with the pure Arrhenius exponential behaviour which is dominant at lower temperatures.

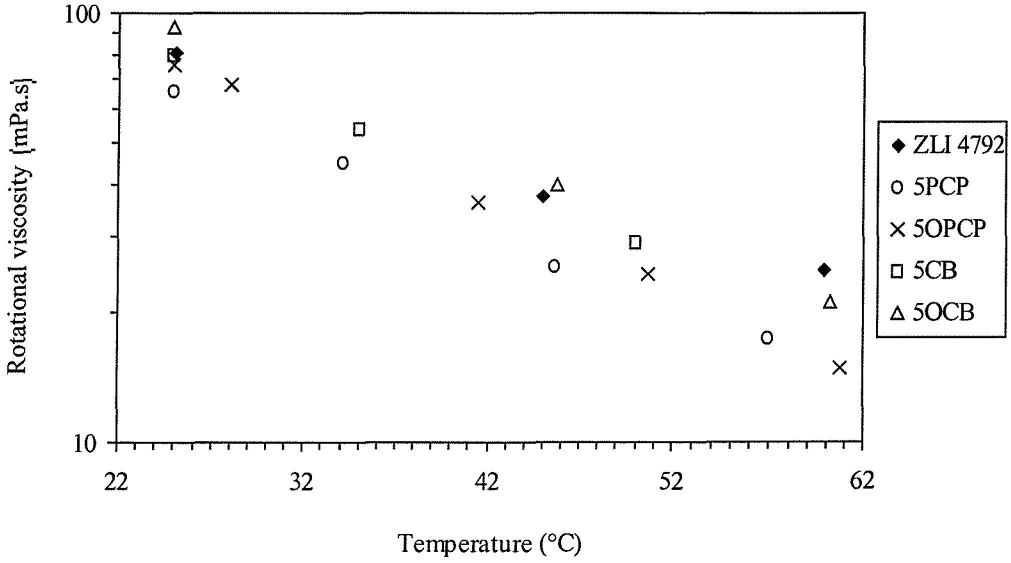

Figure 4.24: Twist viscosity coefficient (± 2%) versus temperature (redrawn from 23).

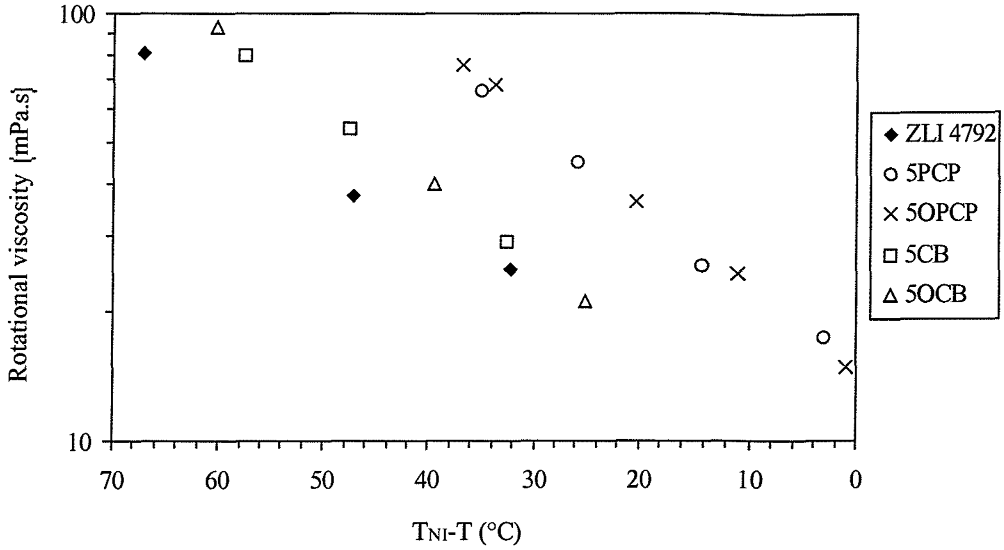

Figure 4.25: Twist viscosity coefficient (± 2%) as a function of shifted temperature (redrawn from 23).

4.5.4 Conclusion

The phenylcyclopentenone molecules cause a greater reduction in the nematic-to-isotropic transition temperature of the host mixture ZLI-4792 than the cyanobiphenyl-based compounds. The temperature dependence of the dielectric and visco-elastic constants may be more complex than originally thought. The results of the comparison between the pure host and the four different doped mixtures are strongly correlated to the type of temperature scale used. The addition of the cyanobiphenyl or of the phenylcyclopentenone dopants has a small influence on the values of the twist elastic constant k_{22} of the host if the orientational order is accounted for by using a relative temperature scale. The temperature dependence of the rotational viscosity γ_1 is more subtle: in the presence of phenylcyclopentenone additives, γ_1 is slightly reduced at a given temperature but it is significantly increased if plotted as a function of shifted temperature. For the mixtures doped with cyanobiphenyl compounds, γ_1 exhibits the same values as for the host ZLI-4792 at all temperatures and exhibits higher values on a relative temperature scale.

From the comparison of the influence of the four additives on the switching properties of the host, the pure host ZLI-4792 seems the most suitable mixture for the in-plane switching mode. The advantage of using ZLI-4792 doped with a few percent of a polar compound such as 5CB or 5OCB would be that it increases the dielectric anisotropy $\Delta\varepsilon$ and therefore lower switching voltages are achieved. However, the response time of the cyanobiphenyl-doped samples is not expected to improve significantly: on one hand, higher $\Delta\varepsilon$ leads to faster switch-on time but on the other hand, the addition of polar molecules causes an increase of the rotational viscosity γ_1 at the same relative temperature.

4.6 Summary

This chapter shows that DLS is suitable for the investigation of the splay and twist visco-elastic behaviour of quite diverse types of low-molar mass nematic liquid crystalline materials. The conclusions of these preliminary measurements are summarised below:

- Before carrying out any experiment, it is crucial to check the optical alignment of the spectrometer. The collection of accurate measurements also requires careful positioning of the sample cell within the apparatus. Once aligned, the spectrometer should be calibrated using a well-known material such as 5CB. After that, it can be used to perform routine measurements on a regular basis since the optical alignment is stable for several months.

- The values of twist and splay elastic constants and viscosity coefficients determined in this work for 5CB are in good agreement with those obtained by previous workers using DLS. They are accurate to within 10% of the values measured by other experimental techniques.

- Three mixtures, consisting of cyanobiphenyls (A), phenyl benzoates (B) and dicyclohexyls (C) were investigated. The dielectric anisotropy is significantly higher for sample A than for samples B and C, which contain non-polar molecules. The birefringence Δn of the three mixtures is significantly different: $\Delta n = 0.15$ to 0.2 for A, $\Delta n = 0.08$ to 0.12 for B and $\Delta n = 0.03$ to 0.05 for C. Both k_{22} and k_{11} remain unchanged with mixture composition and therefore k_{22}/k_{11} is almost constant with values between 0.5 and 0.6. The values of rotational viscosity γ_1 are similar for A and B but is reduced by a factor of 5 in the case of sample C. The associated experimental uncertainty on γ_1 is estimated to be 2% for high birefringence samples and 6% for low Δn materials.

- The next series of samples consists of a nematic host mixture ZLI-4792 doped with the same concentration of four additives (5CB, 5OCB, 5PCP and 5OPCP), in an attempt to improve the in-plane switching characteristics of a device. A comparison of the twist elastic constants k_{22} and the rotational viscosities γ_1 measured for the pure host and the four different doped mixtures indicates that this result is greatly influenced by the temperature scale used. Since k_{22} depends mainly on the relative temperature, it shows similar values for the pure host and the doped mixtures when plotted on this temperature scale. In contrast, γ_1 is dependent on both the standard and the relative temperature. The addition of dopants causes an important increase in γ_1 at the same relative temperature, this effect being more pronounced in the case of the phenylcyclopentenone molecules.

REFERENCES

[1] Oh-e M. and Kondo K., *Appl. Phys. Lett.*, **67(26)**, pp. 3895-3897 (1995)

[2] Oh-e M. and Kondo K., *Appl. Phys. Lett.*, **69(5)**, pp. 623-625 (1996)

[3] Bowdler A. R., *Dynamic Light Scattering from Dilute Solutions of Mesomorphic Polymers*, PhD Thesis, University of Manchester (1984)

[4] Birtwistle P. J. R., *Dynamic Light Scattering from Liquid Crystalline Systems,* PhD Thesis, University of Manchester (1995)

[5] Cox P. J., *Dynamic Light Scattering from Nematic Liquid Crystalline Systems,* PhD Thesis, University of Manchester (1997)

[6] Sefton M. S., *Dynamic Light Scattering from Thermotropic Liquid Crystals*, PhD Thesis, University of Manchester (1985)

[7] Coles H. J., Chapter 4 in *The Optics of Thermotropic Liquid Crystals*, edited by Elston S., and Sambles R., Taylor and Francis, London (1998)

[8] Bradshaw M. J., Raynes E. P., Bunning J. D. and Faber T. E., *J. Physique*, **46**, pp. 1513-1520 (1985)

[9] Bogi A. and Faetti S., *Liq. Cryst.*, **28(5)**, pp. 729-739 (2001)

[10] Clark M. G., Raynes E. P., Smith R. A. and Tough R. J. A., *J. Phys. D: Appl. Phys.*, **13**, pp. 2151-2164 (1980)

[11] Bancroft M. S., *Dynamic Light Scattering Studies of Some Nematic Liquid Crystals*, PhD Thesis, University of Manchester (1989)

[12] Chen G-P., Takezoe H. and Fukuda A., *Liq. Cryst.*, **5(1)**, pp. 341-347 (1989)

[13] Coles H. J. and Sefton M. S., *Mol. Cryst. Liq. Cryst. Lett.*, **1(5)**, pp. 151-157 (1985)

[14] Coles H. J. and Sefton M. S., *Mol. Cryst. Liq. Cryst. Lett.*, **3(3-4)**, pp. 63-68 (1986)

[15] Toyooka T., Chen G-P., Takezoe H. and Fukuda A., *Jap. J. Appl. Phys.*, **26(12)**, pp. 1959-1966 (1987)

[16] Gu D., Jamieson M., Rosenblatt C., Tomazos D., Lee M. and Percec V., *Macromol.*, **24**, pp. 2385-2390 (1991)

[17] Madhusadana N. V. and Pratibha R., *Mol. Cryst. Liq. Cryst.*, **89**, pp. 249-257 (1982)

[18] Breddels P. A. and Mulkens J. C. H., *Mol. Cryst. Liq. Cryst.*, **147**, pp. 107-112 (1987)

[19] Skarp K., Lagerwall S. T. and Stebler B., *Mol. Cryst. Liq. Cryst.*, **60**, pp. 215-236 (1980)

[20] Hakemi H., Jagodzinski E. F. and DuPré D. B., *J. Chem. Phys.*, **78(3)**, pp. 1513-1518 (1983)

[21] Hirschmann H. and Reiffenrath V., Chapter 3 in the *Handbook of Liquid Crystals*, **2A**, pp. 199-229, edited by Demus D., Goodby J., Gray G. W., Spiess H-W. and Vill V., Wiley-VCH, New-York (1998)

[22] de Jeu W. H., *Physical Properties of Liquid Crystalline Materials*, Gordon and Breach, New-York (1980)

[23] Kunimatsu N., *Magnetic Resonance and Light Scattering Studies of Nematics*, PhD Thesis, University of Southampton (2000)

[24] Coles H. J., Dunmur D. A., Kagawa H., Kondo K., Kunimatsu N., Luckhurst G. R. and Schott C., *Mol. Cryst. Liq. Cryst.*, **347**, pp. 157-166 (2000)

[25] Prost J., Sigaud G. and Regaya B., *J. Physique Lett.*, **37**, pp. L-341 (1976)

CHAPTER 5: DYE GUEST-HOST NEMATIC MIXTURES

5.1 Introduction

Dichroic dyes strongly absorb light, of a specific wavelength, polarised along a given direction. When they are dissolved in small quantity in a liquid crystal host, the dye molecules become aligned with the LC matrix and will reorient with the mesogenic molecules upon the application of an external field. This electro-optical phenomenon is called the dye guest-host effect (DGH) and was first demonstrated in 1968 by Heilmeier and Zanoni.[1] Since that time, the display industry has been increasingly interested in dichroic DGH systems since they can greatly improve the brightness and viewing angles of liquid crystal displays (LCDs). They can provide a colour image without the use of polarisers. One of the possible applications is to incorporate these materials to make bright reflective LCDs with no backlight.
The performance of these displays depends on the dye parameters (such as chemical and photochemical stability, wavelength of maximum absorption, dichroic ratio, order parameter and solubility), the host liquid crystal characteristics and the compatibility between the dye and the host.[2] The nematic-to-isotropic transition temperature and some of the physical properties of the liquid crystal host may be affected by the addition of dye. It is especially important to determine quantitatively the influence of dye concentration on the dielectric and visco-elastic properties of the nematic host since these parameters determine the threshold field and the response time of a device. In general, the addition of dye is expected to have a weak influence on the dielectric anisotropy or elastic constants of the host and to cause a noticeable increase of its viscosity coefficients.[3]

The first part of this chapter explains the dye guest-host effect by introducing the concept of the order parameter associated with the dye's absorption and by showing the principle of a DGH display.

In Sections 5.3 and 5.4, we report on the first measurement of the splay and twist elastic constants and viscosity coefficients by electric field dynamic light scattering for dye-doped nematic mixtures. We have investigated a series of orange azo dye mixtures and a series of purple anthraquinone dye mixtures; in both cases, the concentration of dye varies from 1 to 3% wt/wt and the host used is 4-pentyl 4'-cyanobiphenyl, known as 5CB. The transition temperatures, absorbance spectra and dielectric constants of all samples have also been measured. The dichroic ratio and the order parameter of the dye's transition moment have been calculated from the absorbance data.

In the next section, the temperature dependence of the elastic constants and of the twist viscosity has been studied for the azo-doped samples. Prior to this, the refractive indices had been determined and then the orientational order parameter of each mixture has been calculated following Haller's extrapolation method, outlined in Chapter 2.

The effects of each type of dye on the visco-elastic constants and on the dye absorption order parameter are discussed in Section 5.6. A comparison between the values of the order parameter of the host and of the dye's absorption illustrates the interactions between the dichroic and mesogenic molecules.

The samples containing anthraquione dye absorb light strongly and thus no birefringence data could be obtained. Nevertheless, this dye appears more suitable for display applications since it offers a better dark state than the azo dye. The bend elastic constant and viscosity coefficient have been determined by combining DLS and Freedericksz transition for the anthraquinone DGH mixtures. The experimental procedure and the results are included in the final part of the chapter.

5.2 Dye guest-host effect

5.2.1 Nematic orientational order parameter and absorption order parameter of the dye

The guest dyes are oriented by the liquid crystal matrix and therefore the director of the dyes coincides with the director of the host **n**. As mentioned in Chapter 1 Section 1.3.2, the orientational order parameter of the nematic liquid crystal host can be defined as

$$S_{LC} = \frac{1}{2} < 3\cos^2\theta - 1 >, \qquad \textbf{(5.1)}$$

where θ is the angle between the long molecular axis of the liquid crystal L_m and the director **n** as illustrated in Figure 5.1. Similarly, the orientational order parameter of the dye is given by

$$S_D = \frac{1}{2} < 3\cos^2\phi - 1 >, \qquad \textbf{(5.2)}$$

where ϕ is the angle between the long molecular axis of the dye D_m and the director **n** (see Figure 5.1). S_D may be different from S_{LC} because thermal fluctuations may have a different impact on the dichroic and mesogenic molecules, depending on their respective molecular structures.[2]

The dichroic dye efficiency is determined mainly by the order parameter of the transition moment of the dye absorption S_T, which defines the colour and absorption of the dye. By analogy with Equation (5.2), if the transition moment makes an angle ϕ_T with the director **n**, S_T can be written as:

$$S_T = \frac{1}{2} < 3\cos^2\phi_T - 1 >. \qquad \textbf{(5.3)}$$

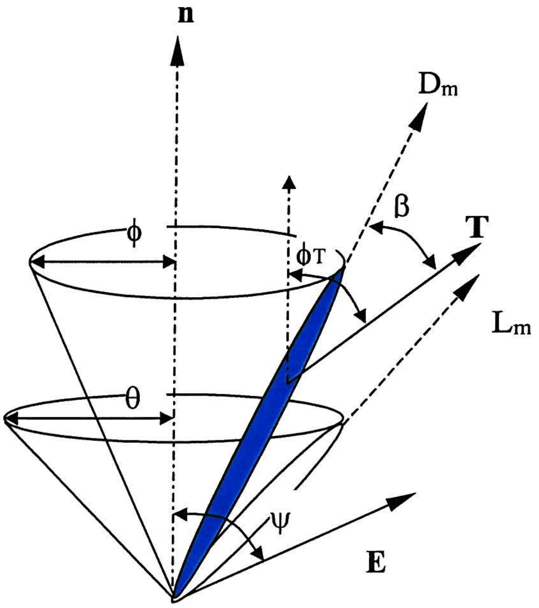

Figure 5.1: Geometrical representation of the mesogenic and dichroic molecules as well as of the dye transition moment **T**, in the presence of polarised incident light.

The dye absorbs incident light polarised at an angle ψ with respect to the director orientation. The absorbance (also called optical density) is expressed as:[2]

$$A(\beta,\psi) = Tcd\left[\left(\frac{S_D}{2}\right)\sin^2\beta + \left(\frac{1-S_D}{3}\right) + \left(\frac{S_D}{2}\right)(2-3\sin^2\beta)\cos^2\psi\right], \qquad (5.4)$$

where T is the magnitude of the transition moment, c is the dye concentration and d is the cell thickness. β is the angle between the direction of the absorption T and the dye long molecular axis D_m as shown in Figure 5.1. The dichroic ratio is defined by

$$D = \frac{A_{\parallel}}{A_{\perp}} = \frac{A(\beta,\psi=0°)}{A(\beta,\psi=90°)}$$

$$\text{or } D = \frac{2+4S_D-6S_D\sin^2\beta}{2-2S_D+3S_D\sin^2\beta}, \qquad (5.5)$$

where $A_{\parallel}$ and $A_{\perp}$ are respectively the absorbance along and normal to the director measured at the wavelength of maximum absorption λ_{max}. D is influenced by the order parameter of the nematic host S_{LC} but on the other hand, it is independent of dye concentration and of sample thickness.[4]

Experimentally, S_T is obtained from absorbance data as follows:

$$S_T = \frac{A_{\parallel}-A_{\perp}}{A_{\parallel}+2A_{\perp}} = \frac{D-1}{D+2}. \qquad (5.6)$$

Using Equations (5.5) and (5.6), the dye order parameter S_D is related to S_T via

$$S_D = S_T\frac{2}{2-3\sin^2\beta}, \qquad (5.7)$$

The order parameter S_T is directly related to the dichroic ratio, while S_D depends on the molecular structure of the dye.[5] In the general case, $\beta \neq 0$ and so $S_T \neq S_D$. However, for elongated positive dyes, the angle β is extremely small leading to a negligible term sin β. In this particular case, $S_T = S_D$ and the dichroic ratio can be written:

$$D = \frac{1+2S_D}{1-S_D}. \qquad (5.8)$$

The effects of internal field have to be taken into account and the order parameter becomes

$$S_{T\,corr} = \frac{n_eA_{\parallel}-n_oA_{\perp}}{n_eA_{\parallel}+2n_oA_{\perp}}, \qquad (5.9)$$

where n_e and n_o are the extraordinary and ordinary refractive indices of the liquid crystal host. The values of n_e and n_o have been measured by refractometry (this technique is described in detail in Chapter 3, Section 3.5) at $\lambda = 632.8$ nm, which differs from λ_{max}. The wavelength dispersion effects have been evaluated on the system 5CB + 2% anthraquinone dye ($\lambda_{max} = 553$ nm) at T_{NI}-T = 11.7 °C by using the data for n_e and n_o, measured at 632.8 nm and 546.1 nm, for pure 5CB[6] to determine the order parameter S_{Tcorr}. The results, given in Table 5.1, show that the influence of wavelength dispersion on S_{Tcorr} is negligible and that the values of refractive indices at $\lambda = 632.8$ nm can be used as a good approximation. Bahadur *et al.* conducted a similar study on various mixtures consisting of a single azo or anthraquinone dye dissolved in a liquid crystalline host E8; the S_{Tcorr} values were then calculated from refractive indices measured at λ = 436-644 nm and were found to be within 2% of each other.[7]

Wavelength (nm)	n_e	n_o	S_{Tcorr}
632.8	1.711	1.5296	0.553
546.1	1.7302	1.5383	0.555

Table 5.1: Comparison between the order parameter S_{Tcorr} obtained from refractive index data measured at $\lambda = 632.8$ nm and $\lambda = 546.1$ nm for 5CB + 2% anthraquinone dye (at T_{NI}-T = 11.7 °C).

5.2.2 Basic principle of DGH displays

The main component of the absorption **T** of the dye is either parallel (positive dichroic or pleochroic) or lies in the plane normal to the long molecular axis D_m of the dye (negative dichroic).[4] Positive and negative dichroic dyes absorb light polarised respectively along and normal to D_m as depicted in Figure 5.2. The dyes are usually characterised by a narrow absorption region in the visible spectrum, with a maximum occurring at wavelength λ_{max}.

(a) Positive dye ($A_{\parallel} > A_{\perp}$)

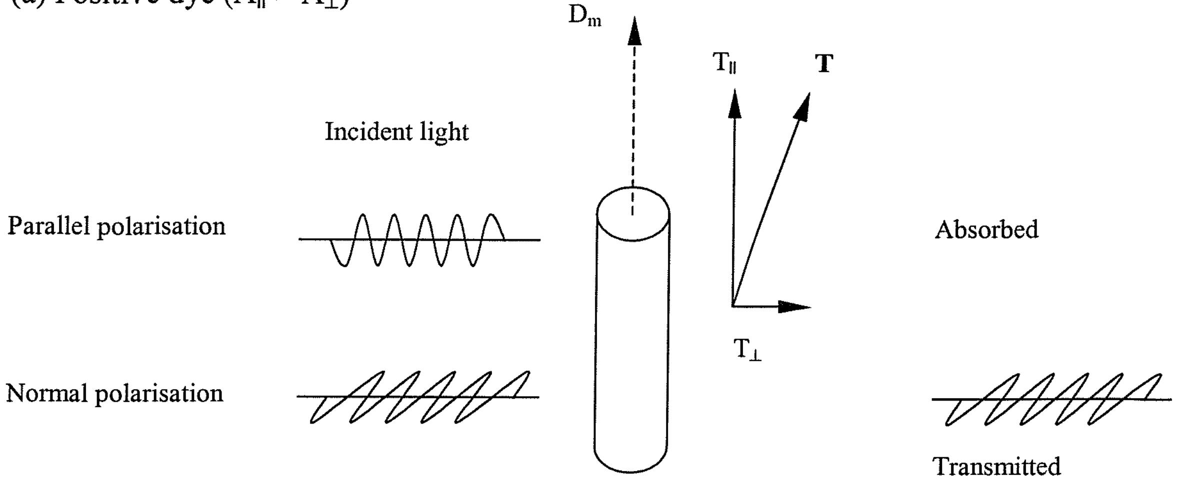

(b) Negative dye ($A_{\parallel} < A_{\perp}$)

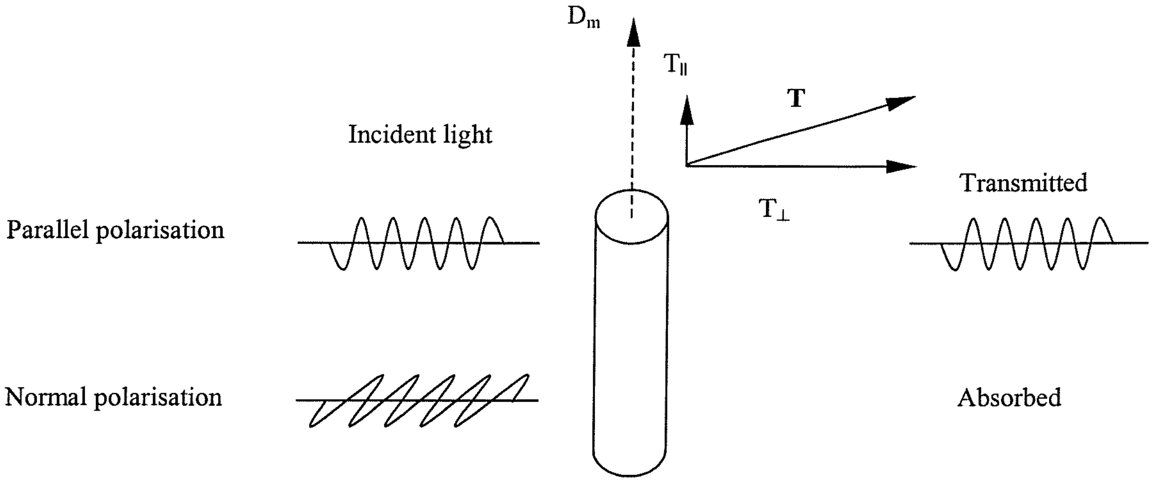

Figure 5.2: (a) Positive dichroic dye absorption mode
(b) Negative dichroic dye absorption mode.

DGH devices require low dye concentration of typically 0.5-2% wt/wt, depending on the solubility and absorption coefficient of the dye[2]. Positive elongated dichroic dyes are usually preferred since the major component of their transition moment **T** coincides with the long molecular axis of the dye ($\beta \approx 0°$). In this case, they will exhibit a higher dichroic ratio and dye absorption order parameter. High values for D are desirable to improve brightness and to achieve good colour contrast in a DGH device.[5]

The principle of a simple dichroic DGH display, the so-called Heilmeier display, is represented schematically in Figure 5.3. This mode requires a positive dye and a host LC with positive dielectric anisotropy $\Delta\varepsilon$. Initially, the alignment of the liquid crystal and dye molecules is planar and the cell appears dark due to the absorption of the dye. In the presence of an applied electric field, the director reorientation towards a homeotropic configuration causes a change in the absorption direction of the dye molecule and the display becomes transparent. The dye behaves as a switchable polariser and in principle, no polarisers are necessary to observe the electro-optical switching. However, the use of a single polariser enhances the absorption and improves the contrast. The addition of dye results in brighter displays with intrinsic colour. In display devices, it is advantageous to employ a black dichroic dye. This is usually achieved by mixing dyes of three colours (such as orange, green-blue and purple) with high order parameter, good absorption, photostability and solubility properties.

The two main classes of dyes commonly used are the azo dye (high dye order parameter) and anthraquinone dye (good photochemical stability);[3, 5] their molecular structures are given in Figure 5.4. It is mainly the core of the dye molecule that determines its colour (with slight differences in hue) while lateral substituents have little influence.[5, 8] In liquid crystals, the absorption peak is usually shifted by about 20 nm towards longer wavelengths; this leads to minor differences in colour compared to the same dye dissolved in a solvent such as chloroform.[8] Azo dyes with satisfactory photostability can provide yellow, orange and red colours, while anthraquinone dyes can produce blue, purple and red colours. Some of the azo compounds may undergo photodecomposition and/or cis-trans changes when exposed to UV light of specific wavelengths.[2, 3]

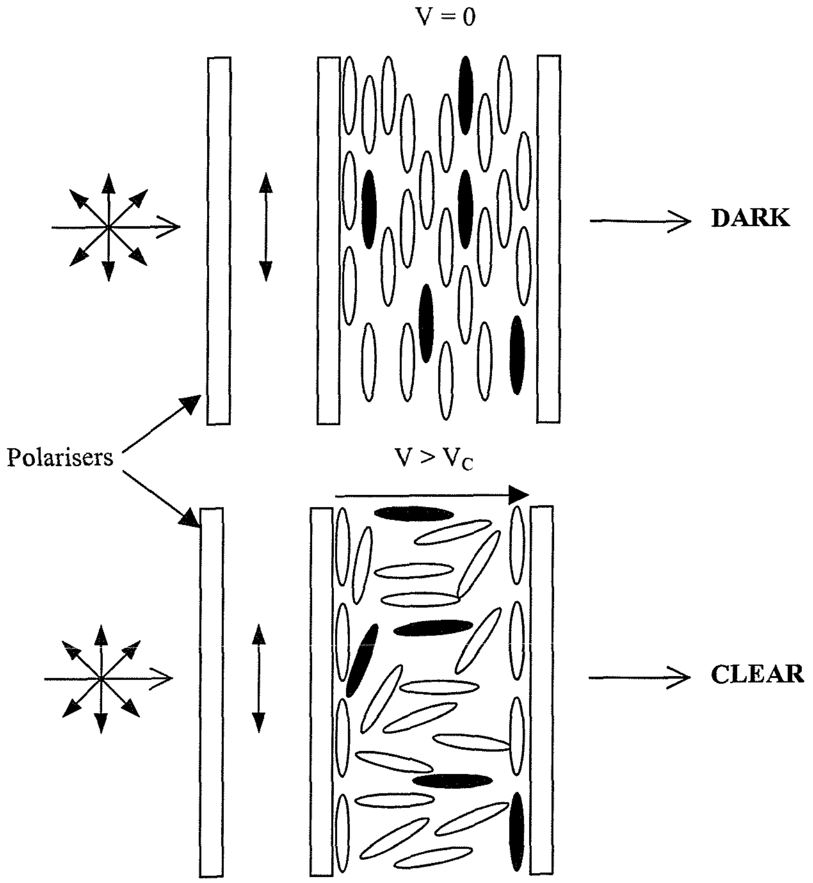

Figure 5.3: Basic operational principle of a Heilmeier display.[1, 4]

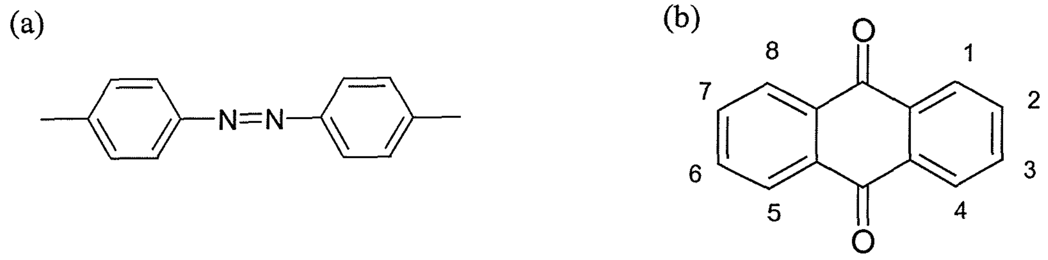

Figure 5.4: Core chemical structure for the (a) azo dye (b) anthraquinone dye.

5.3 Azo mixtures

5.3.1 Characterisation of the azo DGH nematics

Materials and their transition temperatures

The pure host 5CB and the azo DGH samples were provided by Toshiba and were used without any further purification. No mixture preparation was required since the dye was already dissolved in the host. The exact structure of the azo dye molecule is illustrated in Figure 5.5. The properties of the host 5CB has been described in detail in Chapter 4, Section 4.3. Another sample of 5CB, which was heated at 140 °C for 30 min in order to dissolve the dye, was also supplied. As the physical properties of the heated 5CB (i.e. transition temperature, dielectric anisotropy, elastic constants and viscosity coefficients) are identical to the standard 5CB, the data obtained for this sample are not included in this work. The mixtures investigated contain up to 3% wt/wt concentration of orange azo dye. The nematic-to-isotropic transition temperatures T_{NI} are summarised in Table 5.2. The temperature range of the nematic phase increases with dye concentration. Therefore, the addition of dye can stabilise the nematic phase to higher temperatures.

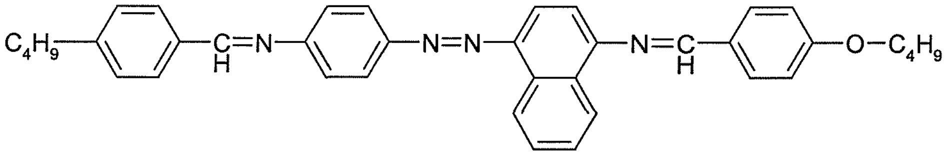

Figure 5.5: Chemical structure of the azo dye investigated.

Sample	Clearing point T_{NI} (°C)
5CB pure	34.9 ± 0.1
5CB + 1% azo dye	35.6 ± 0.1
5CB + 2% azo dye	36.8 ± 0.1
5CB + 3% azo dye	38.0 ± 0.1

Table 5.2: Nematic-to-isotropic transition temperatures T_{NI} for pure 5CB and for the azo containing mixtures.

Dichroic ratio and dye order parameter of the azo doped mixtures

The maximum absorption, determined from the absorbance spectra of all the azo-doped 5CB mixtures, occurs at $\lambda_{max} = 457 \pm 1$ nm.

As explained in Section 5.2.1, the dichroic ratio D and the order parameter S_T of the dye absorption can be deduced respectively from

$$D = \frac{A_{\parallel}}{A_{\perp}} \tag{5.5}$$

and $$S_{T\,corr} = \frac{n_e A_{\parallel} - n_o A_{\perp}}{n_e A_{\parallel} + 2n_o A_{\perp}}. \tag{5.9}$$

The dichroic ratio D and the corrected order parameter of the dye absorption S_{Tcorr} have been determined for all azo DGH samples. An example of typical data sets for D and S_{Tcorr}, measured for the 2% azo-doped sample, are shown respectively in Figures 5.6 (a) and (b) as a function of shifted temperature T_{NI}-T. The dichroic ratio D and order parameter S_{Tcorr} are found to increase with increasing dye concentration, although other studies[5, 7] have reported results indicating that these parameters are independent of the amount of dye; at about T_{NI}-T = 6 °C, $S_{Tcorr} = 0.6$ for 3% azo compared to $S_{Tcorr} = 0.51$ for 1% azo. For this reason, to obtain the values of D and S_{Tcorr} for the azo dye in 5CB, an average over the three dye concentrations has been calculated and found to agree very well with the corresponding values measured for the intermediate concentration. Thus, in the following discussion, when no dye concentration is clearly stated, this means that the data are quoted for 2% azo dye content.

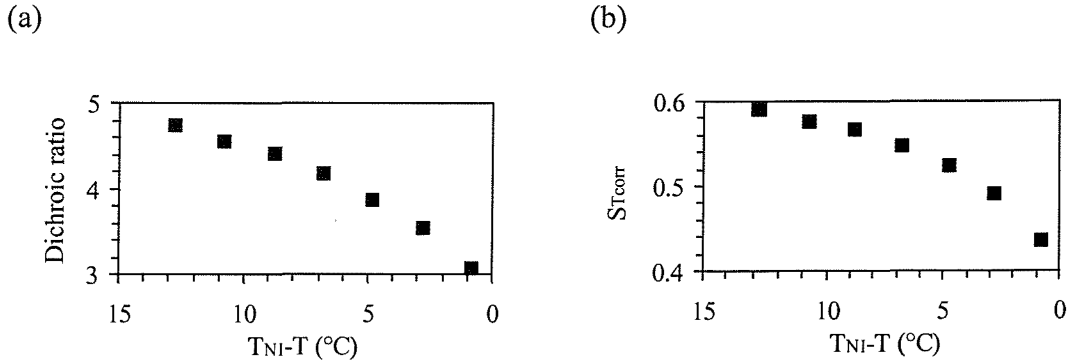

Figure 5.6: (a) Dichroic ratio D (± 5%) obtained for 5CB+2% azo dye

(b) Corrected values of the dye absorption order parameter S_{Tcorr} (± 3%) for the same sample.

Dielectric permittivities

The dielectric constants parallel $\varepsilon_{\parallel}$ and perpendicular $\varepsilon_{\perp}$ to the director are represented in Figure 5.7 for pure 5CB and all azo dye concentrations. The values of $\varepsilon_{\parallel}$ and $\varepsilon_{\perp}$ and the resulting dielectric anisotropy $\Delta\varepsilon = \varepsilon_{\parallel} - \varepsilon_{\perp}$ are clearly independent of the dye concentration.

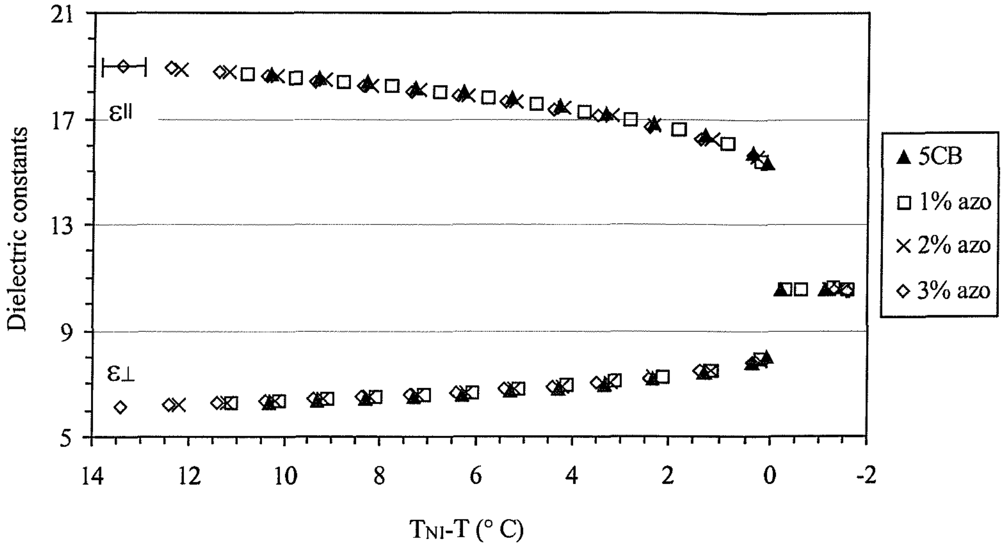

Figure 5.7: Dielectric constants $\varepsilon_{\parallel}$ and $\varepsilon_{\perp}$ (± 0.5%) for the azo DGH mixtures and for pure 5CB against T_{NI}-T.

5.3.2 Twist and splay visco-elastic constants

The rotational viscosity coefficient γ_1 and the elastic constants k_{11} and k_{22} are plotted in Figure 5.8 and Figure 5.9 for all mixtures. Within experimental errors, the graphs obtained for the host and for different dye concentrations are superimposed. This means that the azo dye has a negligible effect on the viscous and elastic properties of the liquid crystal host. The splay viscosity η_{splay} has also been measured and for all samples studied, $\eta_{splay} \approx \gamma_1$ taking into account the experimental uncertainties.

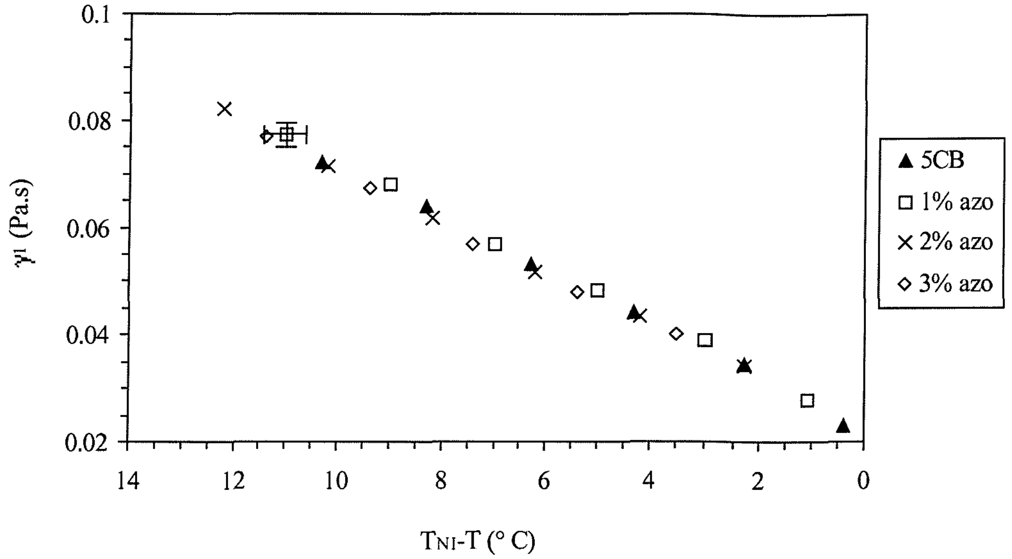

Figure 5.8: Rotational viscosity γ_1 (± 2%) for azo DGH samples versus shifted temperature.

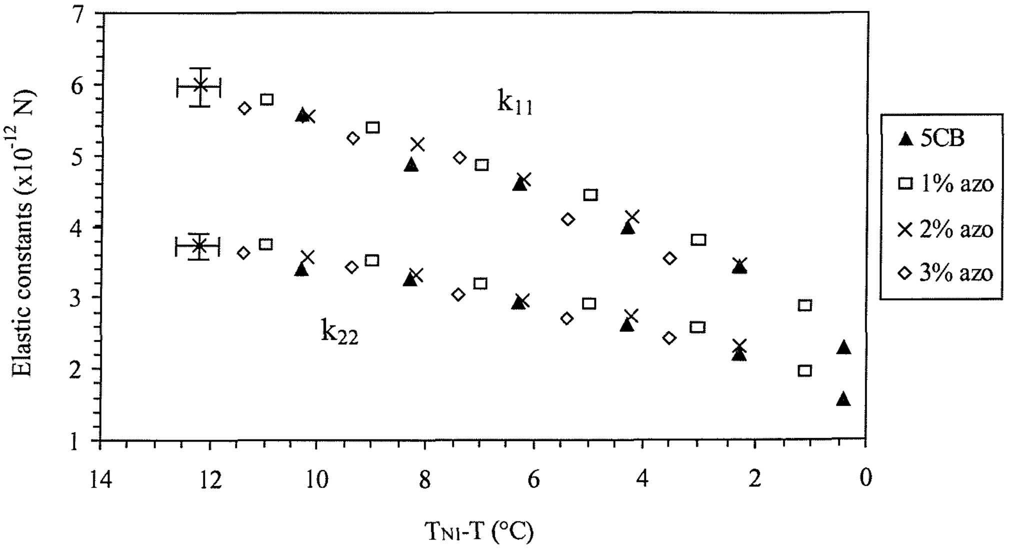

Figure 5.9: Splay (± 5%) and twist (± 3%) elastic constants at different azo dye concentrations as a function of T_{NI}-T.

5.4 Anthraquinone mixtures

5.4.1 Physical properties of the anthraquinone DGH samples

Materials and their transition temperatures

The DGH mixtures, supplied by Toshiba, were used without any further purification. The structure of the anthraquinone dye molecule investigated is presented in Figure 5.10. Concentrations of 1 to 3% by weight of this purple-coloured dye dissolved in a host nematic 5CB were studied. The nematic-to-isotropic transition temperature T_{NI} increases with dye concentration as illustrated in Table 5.3.

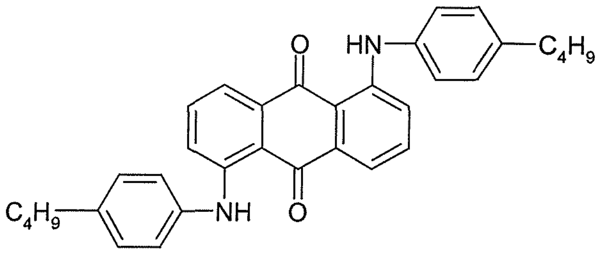

Figure 5.10: Molecular structure of the anthraquinone dye.

Sample	Clearing point T_{NI} (°C)
5CB pure	34.9 ± 0.1
5CB + 1% anthra dye	35.8 ± 0.1
5CB + 2% anthra dye	36.7 ± 0.1
5CB + 3% anthra dye	37.5 ± 0.1

Table 5.3: Nematic-to-isotropic transition temperatures T_{NI} for pure 5CB and for the anthraquinone mixtures.

Dichroic ratio and dye order parameter of the anthraquinone mixtures

The maximum absorption occurs at a wavelength $\lambda_{max} = 553 \pm 1$ nm. No particular absorption problems were observed in DLS experiments using homeotropic cells when the samples are exposed to a He-Ne laser ($\lambda = 632.8$ nm).

The dichroic ratio D and the order parameter of the dye absorption S_{Tcorr} were determined from the absorbance spectra of the anthraquinone samples following the same method as for the azo DGH mixtures (see Equations (5.5) and (5.9)). D and S_{Tcorr} are respectively illustrated in Figures 5.11 (a) and (b) for the 2% anthraquinone-doped sample against shifted temperature. They exhibit a weaker dependence on dye concentration than the samples containing azo dye.

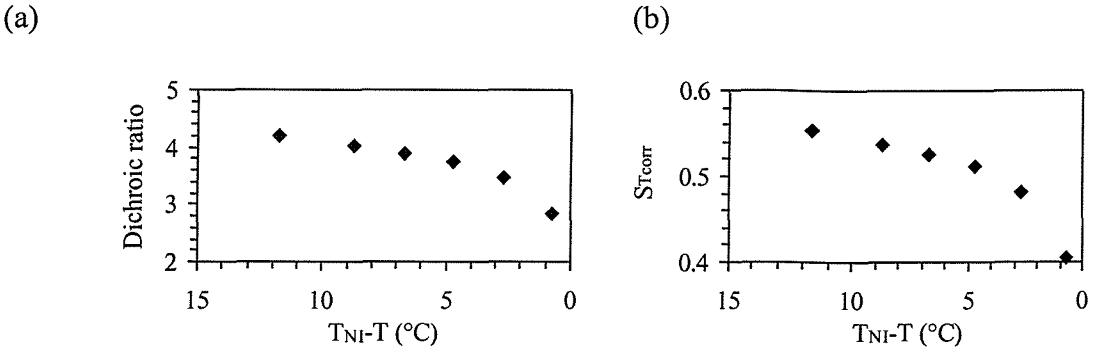

Figure 5.11: (a) Dichroic ratio D (± 5%)

(b) Order parameter S_{Tcorr} (± 3%) for the 2% anthraquinone dye mixture.

Dielectric permitivities

As can be seen in Figure 5.12, neither of the components of the dielectric permittivity $\varepsilon_{\parallel}$ and $\varepsilon_{\perp}$ of the doped mixtures are affected by the presence of up to 3% of anthraquinone dye.

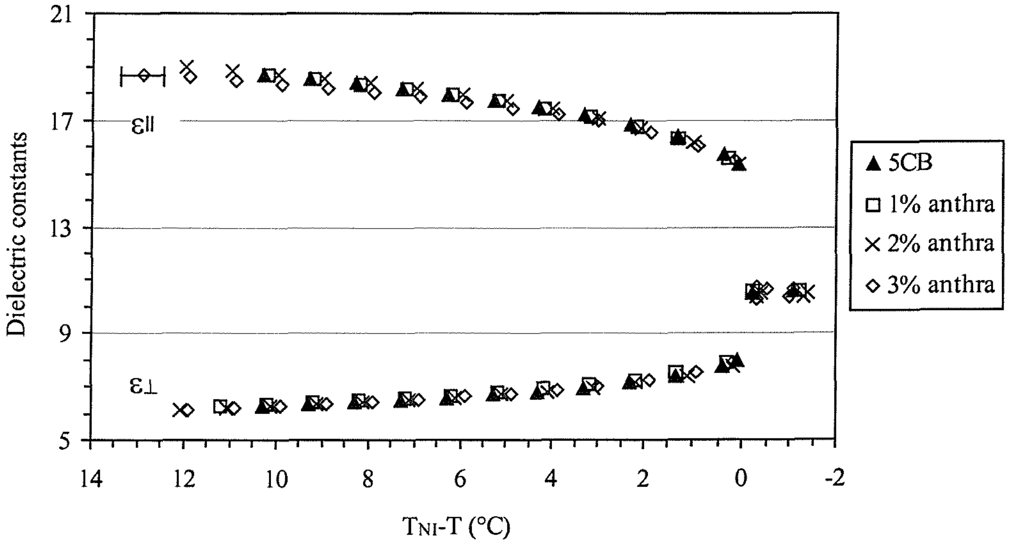

Figure 5.12: Dielectric constants $\varepsilon_{\parallel}$ and $\varepsilon_{\perp}$ (± 0.5%) for all anthraquinone DGH samples against relative temperature T_{NI}-T.

5.4.2 Twist and splay visco-elastic constants

Figure 5.13 represents the twist viscosity coefficient versus T_{NI}-T for 5CB and the anthraquinone-doped samples. γ_1 decreases by about 5% for the mixture containing 3% dye compared to the host, although the viscosity data of the 1% and 2% samples can be considered (within the uncertainty limits) to be equal to the values of the host. The twist and splay elastic constants k_{22} and k_{11} are both given in Figure 5.14 on a shifted temperature scale. The values of k_{11} are more disperse than the data for k_{22} but none of the elastic constants are affected by the addition of dye.

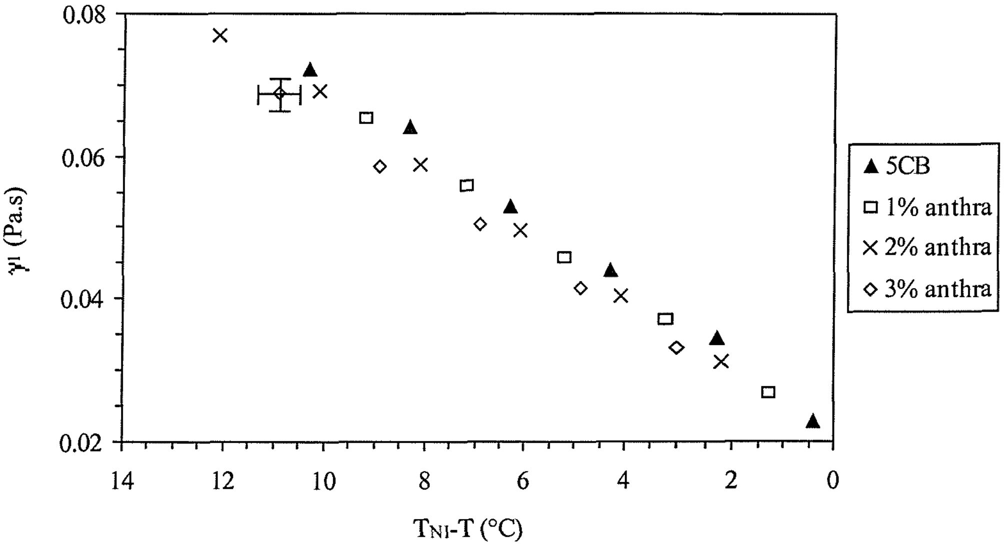

Figure 5.13: Twist viscosity γ_1 (± 2%) for the pure 5CB and the three dye-doped mixtures as a function of T_{NI}-T.

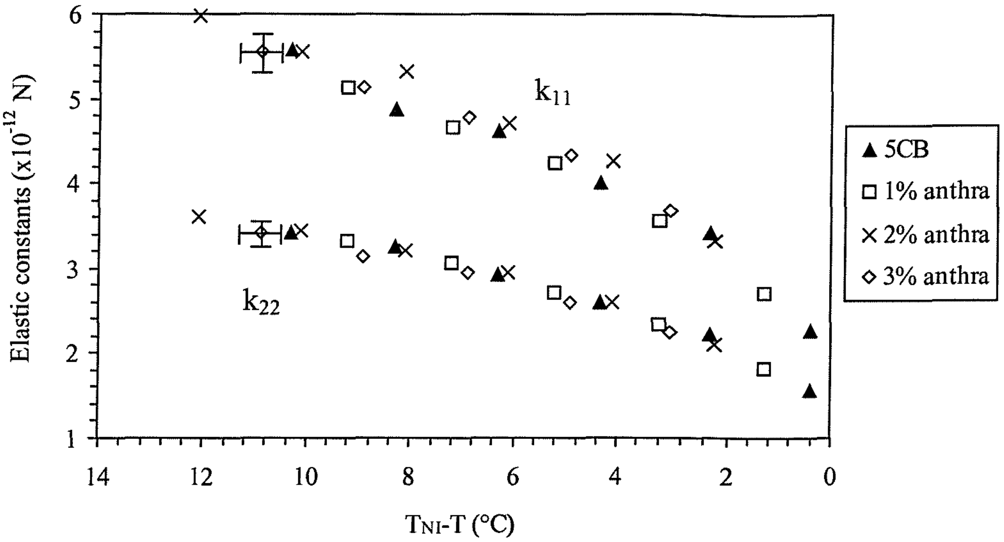

Figure 5.14: Splay (± 5%) and twist (± 3%) elastic constants for all samples against shifted temperature.

5.5 Temperature influence on the visco-elastic properties

5.5.1 Refractive indices and orientational order parameter

The extraordinary and ordinary refractive indices n_e and n_o as well as the nematic orientational order parameter S are plotted in Figure 5.15 and Figure 5.16.

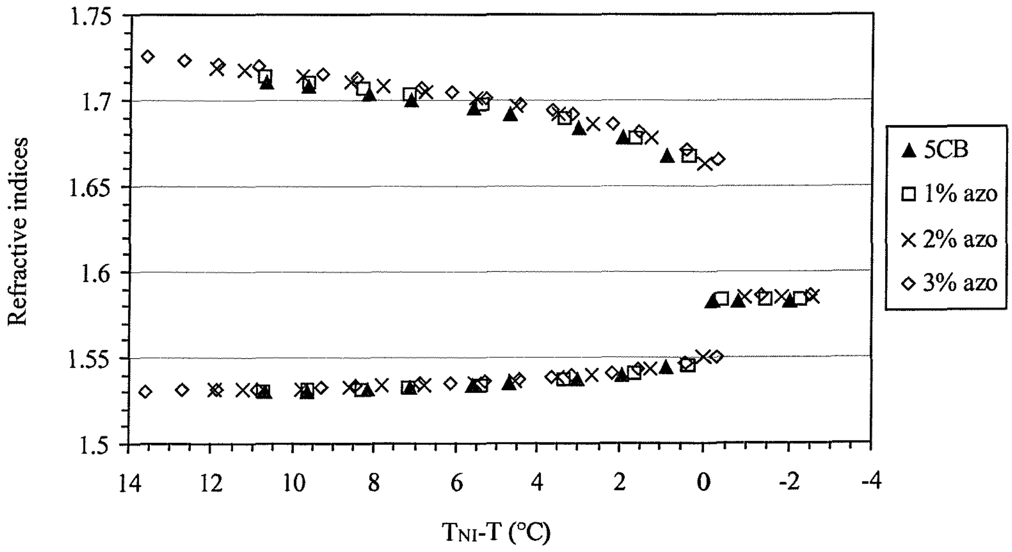

Figure 5.15: Refractive indices n_e and n_o (± 0.0002) for 5CB and for the azo-doped samples.

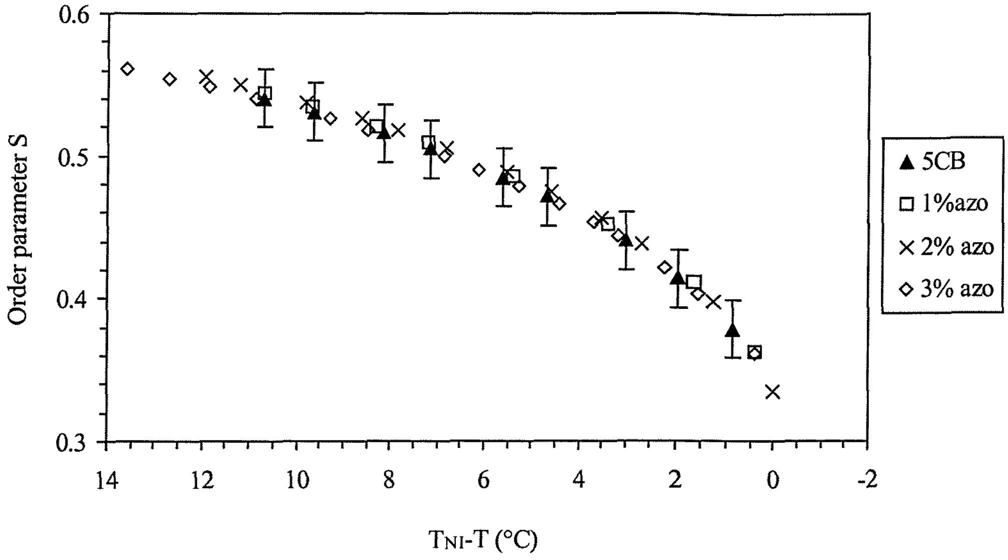

Figure 5.16: Nematic orientational order parameter for pure 5CB and for the azo mixtures as a function of T_{NI}-T.

The presence of azo dye seems to cause a very small increase in n_e while it does not affect n_0. As a result, the birefringence $\Delta n = n_e - n_0$ of the azo doped samples is about 3% higher than for the pure liquid crystal host, taking into account that the accuracy on the measured values is less that 1%. However, this small change in birefringence does not affect the optical properties of the host LC.

The orientational order parameter S, calculated from refractive index data using Haller's analysis, remains unchanged upon the addition of up to 3% of azo dye. In fact, at low dye concentrations, the elongated azo dye molecules are aligned by the liquid crystal matrix and do not disturb the orientational order of the host material. Recalling Chapter 2, Equation (2.2), S can be derived according to:

$$S = \left(\frac{T^* - T}{T^*} \right)^{\beta} . \qquad \textbf{(5.10)}$$

The fitting parameters, used in Haller's method, are the exponent β and the temperature T^* associated with a "continuous" nematic-to-isotropic transition. The values for T* (obtained to within ± 0.1°C) are recapitulated in Table 5.4 for 5CB and for the three azo-doped mixtures. The parameter β is independent of dye concentration and is equal to β=0.187 ± 0.005. For all samples, the temperature T^* is higher than the clearing point T_{NI} and follows the same evolution i.e. it increases as a function of dye concentration. From

Equation (5.10), it is obvious that greater transition temperatures induce an upward shift in S.

Sample	Temperature T^* (°C)
5CB	35.8
5CB + 1% azo	36.5
5CB + 2% azo	37.6
5CB + 3% azo	39.0

Table 5.4: Transition temperatures T^* derived from Haller's method for the azo DGH samples.

5.5.2 Temperature dependence of the visco-elastic constants

Several phenomenological models have been developed to describe the thermal dependence of the twist viscosity γ_1. For nematics, experimental data show that γ_1 follows generally a type of Arrhenius law that takes into account the orientational order parameter S, such that:[6, 9, 10, 11]

$$\gamma_1 \propto S^x \exp\left(E(S)/k_B T\right), \qquad \mathbf{(5.11)}$$

where E(S) is an activation energy. $E(S) = E_0$ or E_0S and x = 0, 1, or 2 depending on the best fit for the data.

Maier-Saupe theory predicts that E(S) is proportional to S and γ_1 is expected to scale with $S^2 \exp\left(E_0 S/k_B T\right)$.[9] However, there is strong empirical evidence for x = 1, $E(S) = E_0$ to account for the thermal behaviour of the twist viscosity for several nematic materials including 5CB.[10] For our 5CB data, the best fit for the rotational viscosity is achieved with x = 0 and $E(S) = E_0S$ i.e.

$$\gamma_1 \propto \exp\left(E_0 S/k_B T\right). \qquad \mathbf{(5.12)}$$

This unexpected dependence may be explained by the fact the temperature range investigated is relatively narrow (~ 10 °C) and close to the nematic-to-isotropic transition. Under these conditions, the Haller's method used to derive the orientational order parameter S may not give reliable and consistent results (see Chapter 2, Section 2.2).[12] It should be mentioned that our twist viscosity values for pure 5CB and for the azo-doped samples also seem to vary linearly with temperature (refer to Figure 5.8).

Cui *et al.* also measured the visco-elastic properties of 5CB by DLS and found that their twist viscosity data were best fitted using x = 2 and $E(S) = E_0$ over a similar temperature range of 10 °C.[11] The activation energy calculated for 5CB and the azo DGH mixtures is 0.16 eV ± 2% (compared with 0.46 eV[6, 13] and 0.27 eV[11] obtained by other groups for 5CB). The discrepancy not only between the theoretical predictions and the experimental findings but also between the measurements made by various groups on the same material suggests that other models should be investigated in order to describe accurately the temperature dependence of the twist viscosity.

From the mean field theory, Saupe and Nehring predicted that the elastic constants are expected to scale as the squared order parameter[9] i.e. $k_{ii} \propto S^2$. For 5CB and all azo mixtures, this relation is verified for both k_{11} and k_{22} as illustrated in Figure 5.17, where k_{ii}/S^2 is plotted versus T_{NI}-T. Using Equation (5.10), the variation of elastic constants with temperature can be written

$$k_{ii} \propto (1 - T/T^*)^{2\beta}. \qquad \textbf{(5.13)}$$

It is clear that the elastic constants, like the order parameter, increase with T* and consequently with dye concentration since β does not change significantly.

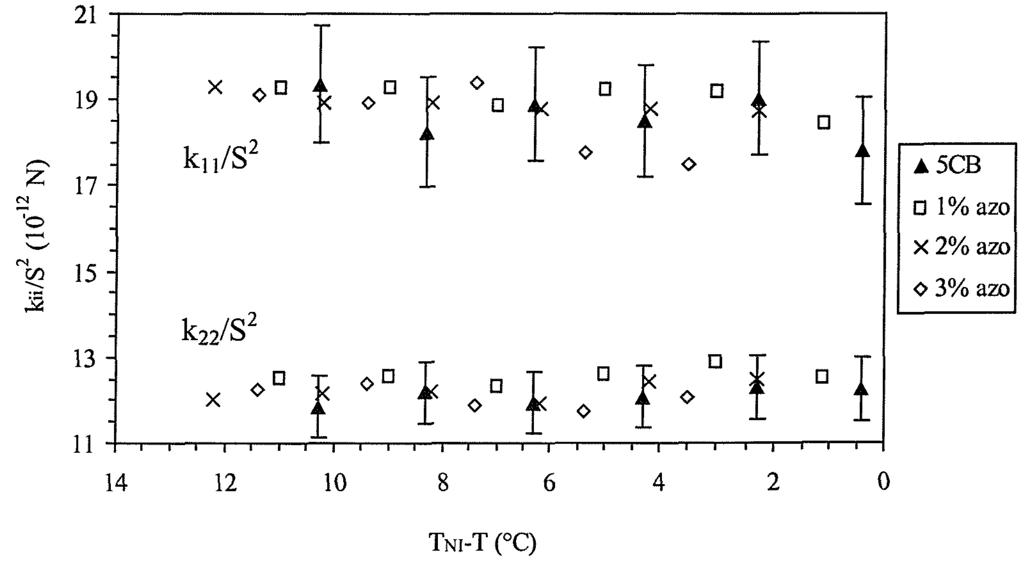

Figure 5.17: Ratio of twist and splay elastic constants to the squared order parameter against shifted temperature.

The twist-to-splay elastic constant ratio k_{22}/k_{11} is presented in Figure 5.18 for the 5CB and the azo samples; it is nearly constant within experimental errors for all mixtures as expected[14] and takes values between 0.6 and 0.7 in this work.

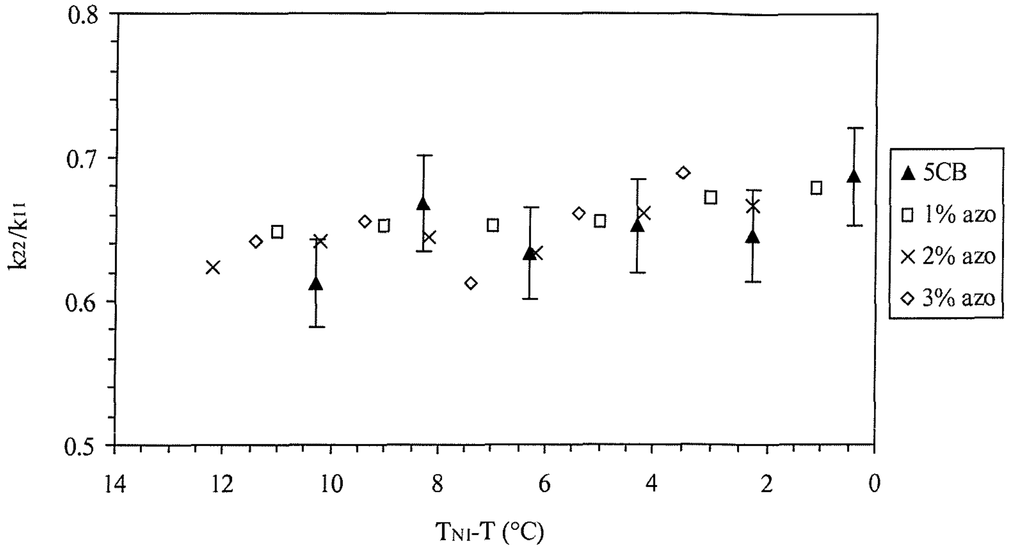

Figure 5.18: Twist-to-splay elastic constant ratio (± 6%) as a function of shifted temperature.

5.6 Comparison between the azo and anthraquinone-doped systems

From the data in Tables 5.2 and 5.3, both dyes produce a similar raise in the clearing point of the host 5CB. They do not exhibit large dipole moments and thus they do not change the dielectric permittivities of the host liquid crystal[15] (see Figure 5.7 and Figure 5.12).

5.6.1 Dichroic ratio and dye order parameter

The dependence of the dichroic ratio D and of the order parameter S_{Tcorr} on dye content is less significant for the anthraquinone dye than for the azo dye; for example, at a shifted temperature of about 11.5 °C, for the mixtures containing 1% and 3% anthraquinone, S_{Tcorr} is equal to 0.53 and 0.57 respectively while at T_{NI}-T = 6 °C, S_{Tcorr} = 0.6 for 3% azo compared to S_{Tcorr} = 0.51 for 1% azo. As explained in Section 5.3.1, in both instances, average values for D and S_{Tcorr} are taken over the different dye concentrations.

Table 5.5 summarises the data for the maximum absorption wavelength λ_{max}, dichroic ratio D and transition moment order parameter S_{Tcorr} determined at T_{NI}-T = 8.8 °C for the azo and anthraquinone dyes. The values of λ_{max} and D measured by other groups on analogous azo and anthraquinone dyes, illustrated in Figure 5.19 are compiled in Table 5.6.[4, 5, 7, 16, 17, 18] The transition moment order parameter S_T is also included in the same table. Although, S_T is slightly lower than the corrected values S_{Tcorr}, both parameters behave similarly. Their difference varies in the range 0.02 to 0.05, depending the dye and the host material considered.[7]

Within each class of dye, the values of λ_{max} are almost identical. Previous investigations showed experimentally that the absorption occurs in the central part of the dichroic molecule;[5, 8] terminal chains do not affect the direction of the transition moment **T** of the dye absorption but they have a direct influence on the dye orientational order parameter S_D.[5] The data in Table 5.6 were obtained at room temperature in various liquid crystalline host materials of different polarities, which explain the minor differences in λ_{max}.[19]

Schematically, the dye can be represented as a cylinder of length L and of breadth a. If we define a dye geometrical factor as L/a, there is a correlation between the order parameter of the transition moment S_{Tcorr} and L/a:[5] S_{Tcorr} increases with L/a. Consequently, azo dyes will generally exhibit a higher dye absorption order parameter and a higher dichroic ratio than the anthraquinone type. This results from the combination of two effects: the increased length of the azo molecule yields higher values for S_{Tcorr} while the greater breadth of the anthraquinone acts to reduce S_{Tcorr}.[7] However, in this work, the value of S_{Tcorr} and D for the azo dye is only slightly higher than that measured for the anthraquinone dye at the same shifted temperature, as reported in Table 5.5. This is because the absorption order parameter of the dye S_{Tcorr} also depends on the nematic orientational order parameter of the host S_{LC}.[7]

For both dyes investigated in this thesis, the values of S_{Tcorr} are systematically lower than the data of S_T quoted in Tables 5.6 (a) and (b) obtained for analogous dyes. This difference can be removed by taking into account the shifted temperature T_{NI}-T at which the measurements were performed. Most of the liquid crystal materials used as hosts to obtain the data of Tables 5.6 (a) and (b) are commercial mixtures with wider nematic range than 5CB and with clearing points $T_{NI} > 60$ °C. S_T is usually measured at ambient temperature i.e. T = 20-25 °C, which corresponds approximately to a shifted temperature T_{NI}-T = 35-40 °C for these host mixtures and to T_{NI}-T = 10-15 °C in the case of 5CB. For example, both anthraquinone dyes in Table 5.6 (b) from Cox's reference were studied in E7, which consists of a eutectic mixture of cyanobiphenyls. The nematic orientational order parameter S_{LC} of the host is found in this work to be 0.53 for 5CB compared to a value of about 0.51 quoted by Allinson *et al.* for E7[20] at the same T_{NI}-T = 10 °C. As expected, these cyanobiphenyl-based hosts have values of S_{LC} in close agreement with each other. At T_{NI}-T = 35-40 °C, the absorption order parameter of the anthraquinone dyes S_T reported by Cox is about 0.67[16] while the order parameter S_{LC} of E7 is higher than 0.63[20] (see Table 5.6 (b)). Thus, $S_T > S_{LC}$, in agreement with our observations.

	Azo	Anthra
λ_{max} (nm)	457	553
D	4.4	4.0
S_{Tcorr}	0.566	0.536

Table 5.5: Comparison of dye parameters for both azo and anthraquinone dyes at T_{NI}-T = 8.8 °C.

(a)

Azo dye of Figure 5.19 (a)	λ_{max} (nm)	D	S_T	References
$R_1 = R_2 = OC_2H_5$	451	11.3	0.77	Cox[16, 17]
$R_1 = R_2 = OC_4H_9$	450	12.1	N/A	Uchida *et al.*[4]
Figure 5.19 (b)	446	N/A	0.71	Seki *et al.*[5]

(b)

Anthra dye of Figure 5.19 (c)	λ_{max} (nm)	D	S_T	References
$R_3 = C_2H_5$	554	N/A	0.67	Cox[16, 18]
	553	6.5	N/A	Uchida *et al.*[4]
$R_3 = OC_5H_{11}$	557	N/A	0.68	Cox[16, 18]
$R_3 = C_4H_9$	556	N/A	0.66	Constant *et al.*[18]

Table 5.6: Maximum absorption wavelength, dichroic ratio and dye absorption order parameter measured for (a) azo and (b) anthraquinone dyes in various nematic hosts.

(a) Generic structure for the azo dye

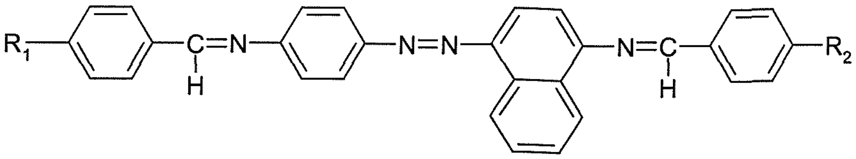

(b) Azo dye from reference 5

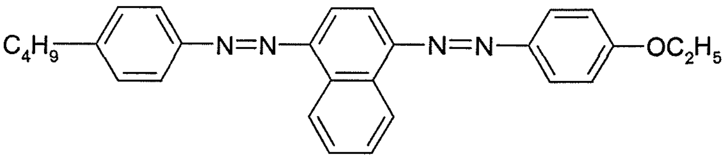

(c) Generic structure for the anthraquinone

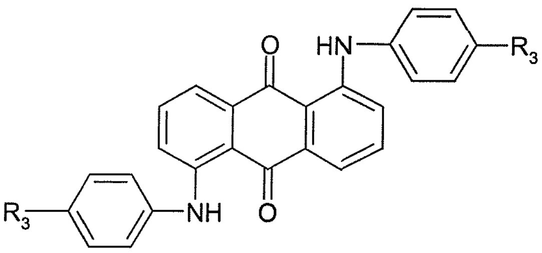

Figure 5.19: General formula of the dyes discussed in Tables 5.6 (a) and (b).

Good contrast between the on and off states in a DGH display requires a dye order parameter S_{Tcorr} higher than 0.73.[21] In practice this criterion is seldom fulfilled by the anthraquinone dyes. Values of S_{Tcorr} between 0.7 and 0.76 were only reported for compounds with alkoxyphenyl groups substituted in position 2 and 6 of the anthraquinone core[8] (compared to position 1 and 5 for our dyes). This type of dye is soluble up to 7% in E7. S_{Tcorr} is found to increase with the length of the substituted chains. An example of such a dye is given in Figure 5.20.

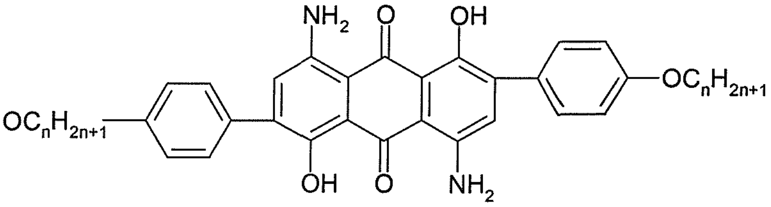

Figure 5.20: 2, 6- substituted anthraquinone dye with high order parameter.

The ratio of S_{Tcorr}/S_{LC} is plotted in Figure 5.21 against T_{NI}-T in order to compare the order parameters of the host and of the dye absorption. S_{Tcorr}/S_{LC} is greater than 1 and tends to increase with temperature, this latter effect being more pronounced for the anthraquinone dye than for the azo dye investigated. This can be understood in the following way: for dyes whose length exceeds the length of the LC molecules, $S_{Tcorr}/S_{LC} > 1$ and this ratio increases at higher temperatures which means that the dyes are less affected by thermal fluctuations than the LC molecules. Whereas, for dichroic molecules shorter than the mesogenic molecules, $S_{Tcorr}/S_{LC} < 1$ and in this case, the dyes are more sensitive to these fluctuations.[7, 15]

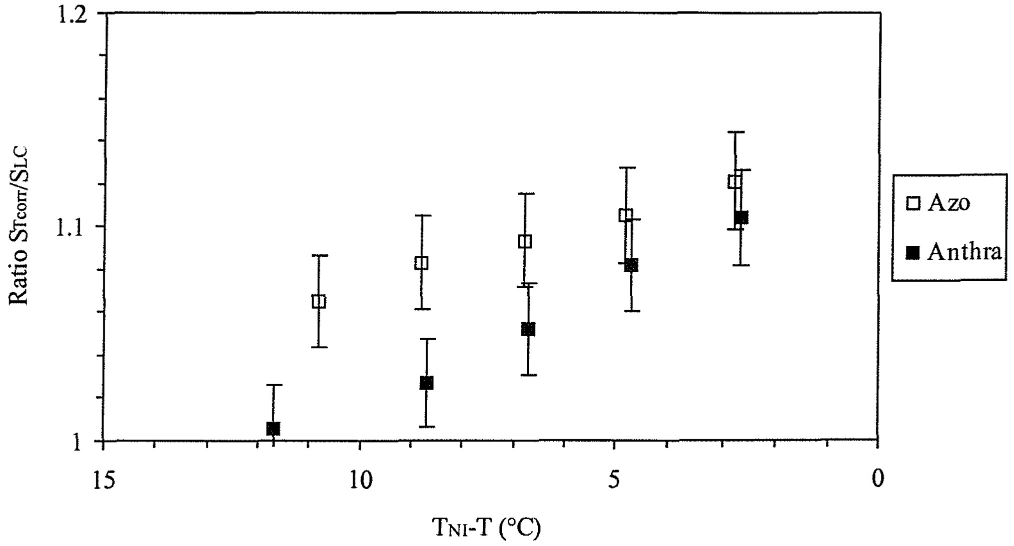

Figure 5.21: Ratio (± 2%) between the dye absorption and the nematic orientational order parameters versus shifted temperature.

5.6.2 Twist and splay visco-elastic constants

In Figure 5.22, the twist viscosity γ_1 is depicted against dye concentration at several temperatures for both dyes. In this graph, the lines represent linear fits to the experimental data and they show that γ_1 increases proportionally with the percentage of added dye (by about 15% for 3% azo dye and by only 5% for 3% anthraquinone dye at 26.6 °C). Thus, the value of rotational viscosity is higher for the azo dye than for the anthraquinone dye at the same temperature and concentration.

The twist and splay elastic constants k_{22} and k_{11} are given in Figure 5.23 and in Figure 5.24 as a function of dye concentration for both dyes. At a given temperature, k_{22} and k_{11}

increase with the addition of azo and anthraquinone dyes and they appear to be approaching saturation values at 3% concentration, the highest concentration investigated. However, the rise in the values of elastic constants with dye percentage is not observed on a shifted temperature scale as illustrated in Figure 5.9 and Figure 5.14 since both k_{22} and k_{11} are proportional to the squared order parameter S^2, which is directly related to T_{NI}-T. The dependence of k_{22} and k_{11} on dye concentration is similar for both dyes, which indicates that none of the dye molecules show preferential ordering within the host. The elastic constants are less affected by the addition of the guest dye than are the corresponding viscosity coefficients.[3]

At T = 34.5 °C, the increase in γ_1, k_{22} and k_{11} appears more pronounced due to a sharp drop in the visco-elastic parameters of 5CB due to pretransitional effects in the vicinity of the nematic-to-isotropic transition.

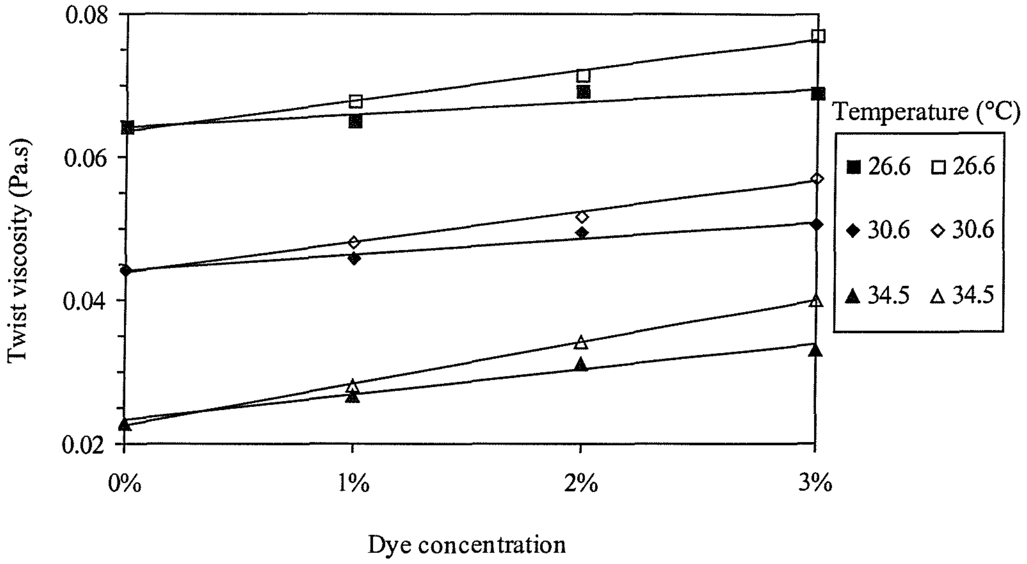

Figure 5.22: Rotational viscosity coefficients (± 2%) versus dye concentration for the azo (open symbols) and for the anthraquinone (filled symbols) doped mixtures at several temperatures.

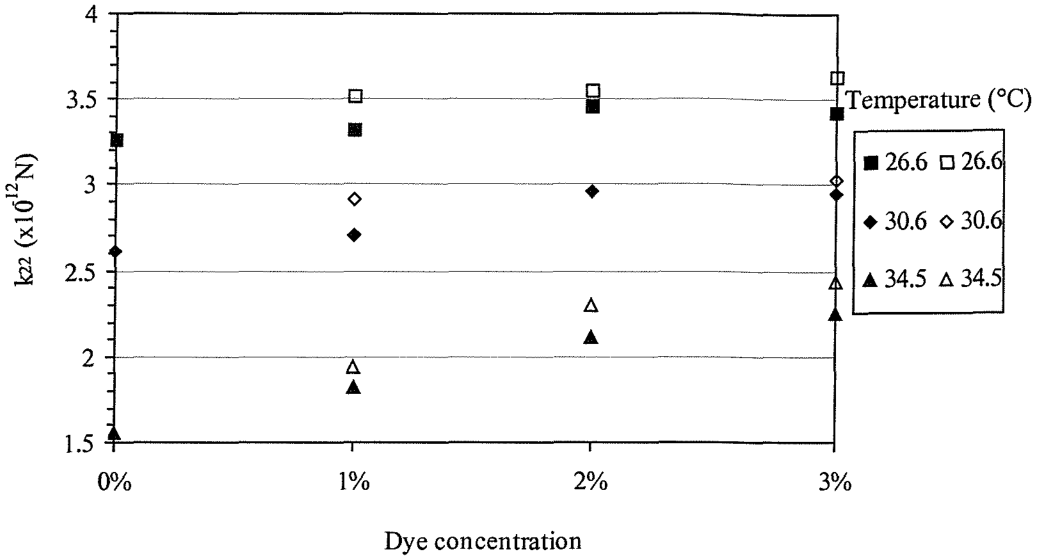

Figure 5.23: Twist elastic constant (± 3%) against dye content at different temperatures (same caption as Figure 5.22).

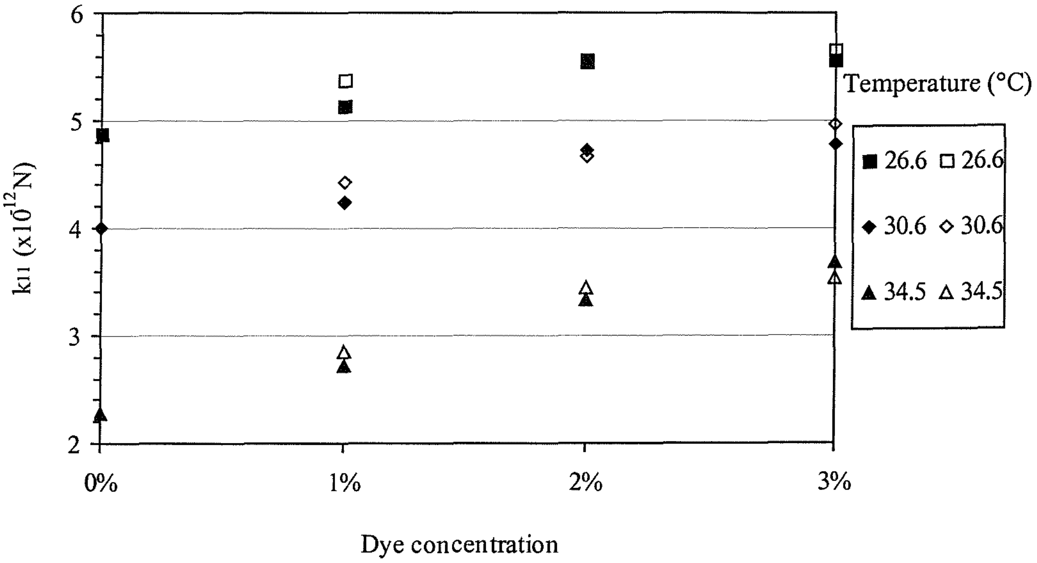

Figure 5.24: Splay elastic constant (± 5%) as a function of dye concentration at different temperatures (same caption as Figure 5.22).

5.6.3 Discussion and comparison with other DGH systems

The influence of dye solute on the nematic-to-isotropic transition temperature is determined not only by the size, shape and concentration of dye molecules but also by the intermolecular interactions between the guest and host molecules.[19] First of all, the pure azo and anthraquinone dyes investigated in this work are expected to have very high melting points; for instance, the pure anthraquinone dye, sketched in Figure 5.10, is reported to exhibit a melting point of 158 °C.[18] Thus the addition of a few percent of this dye will increase the value of T_{NI} of the host material.

In the case of the azo dye, the complementary structure of the elongated dye molecule with respect to the host nematic enhances the effects of the shape anisotropy of the host, leading to an increase in the nematic-to-isotropic transition temperature and elastic constants. It has been shown that highly anisotropic guest molecules can stabilise the nematic phase leading to an increase in the nematic-to-isotropic transition temperature T_{NI} and in the order parameter on the host.[22] A DGH system composed of a 5% photochromic mesogenic azo-benzene dye in 5CB was investigated and it was found that:[22]

- A small elevation of T_{NI} occurred in the dye-doped mixture.
- The splay visco-elastic properties (derived from Raman scattering measurements) were not altered by the addition of dye.

These results agree well with our findings, although we do not know whether the azo dye used in our study has itself a nematic phase with a high clearing point.

The anthraquinone dye studied here exhibits the same physical properties as the azo dye. This behaviour is in contradiction with the results reported by other workers on similar systems. For DGH mixtures consisting of more bulky dyes in a nematic host (for instance photochromic fulgide[23] or anthraquinone[24] dyes, the host used being E7 in both cases), the addition of a few percent of guest dye has been observed to lower the nematic-to-isotropic transition temperature and to reduce significantly the splay elastic constant k_{11} of the host liquid crystal.

5.7 Bend visco-elastic constants for the anthraquinone dye-doped series

Although this work on DGH systems has been focused on the measurements of the twist and splay elastic constants and the corresponding viscosities, the bend elastic constant k_{33} is also an important physical parameter. In this thesis, the measurements of bend elastic constant k_{33} and viscosity coefficient η_{bend} are only performed for the pure 5CB and for the anthraquinone-doped mixtures.

Bend elastic constant

k_{33} can be derived from the magnetic field threshold value B_C (refer to Chapter 2, Equation 2.35) using the following expression:

$$B_C = \frac{\pi}{d}\left(\frac{k_{33}\mu_0}{\Delta\chi}\right)^{1/2}. \tag{5.14}$$

The experimental determination of the bend elastic constant k_{33} via the Freedericksz transition method was explained thoroughly in Chapter 3, Section 3.4.

Figure 5.25 compares the values of k_{33} for 5CB reported in this work and in the literature.[25-28] Chen *et al.* determined k_{33} by studying the angular dependence of the linewidth measured in DLS experiments.[25] While Gu *et al.* and Bradshaw *et al.* directly derived the bend elastic constant from magnetic Freedericksz transition measurements, using a similar technique to ours.[26, 27] The technique used by Durbin *et al.* is based on the optical Freedericksz transition (OFT); the LC molecules, initially aligned homeotropically, tend to reorient parallel to the polarisation of the input laser beam above a threshold intensity I_{th} given by:[28]

$$I_{th} = \frac{c n_e^4}{n_o^3}\left(\frac{\pi}{d}\right)^2 \frac{k_{33}}{n_e^2 - n_o^2}, \tag{5.15}$$

where c is the velocity of light in vacuum, n_e and n_o are the extraordinary and ordinary refractive indices of the nematic LC and d is the layer thickness. For a 250 μm thick sample of 5CB, $I_{th} = 155$ W/cm^2. The value of k_{33} can be deduced from Equation (5.15). The next sub-section discusses how the effects of OFT are enhanced in DGH systems.

The values of k_{33}, measured in this thesis to an accuracy of about 3%, agree rather well with the data quoted by Gu *et al.*;[26] they are respectively about 15% and 30% lower than the values measured by Bradshaw *et al.*[27] and Chen *et al.*[25]

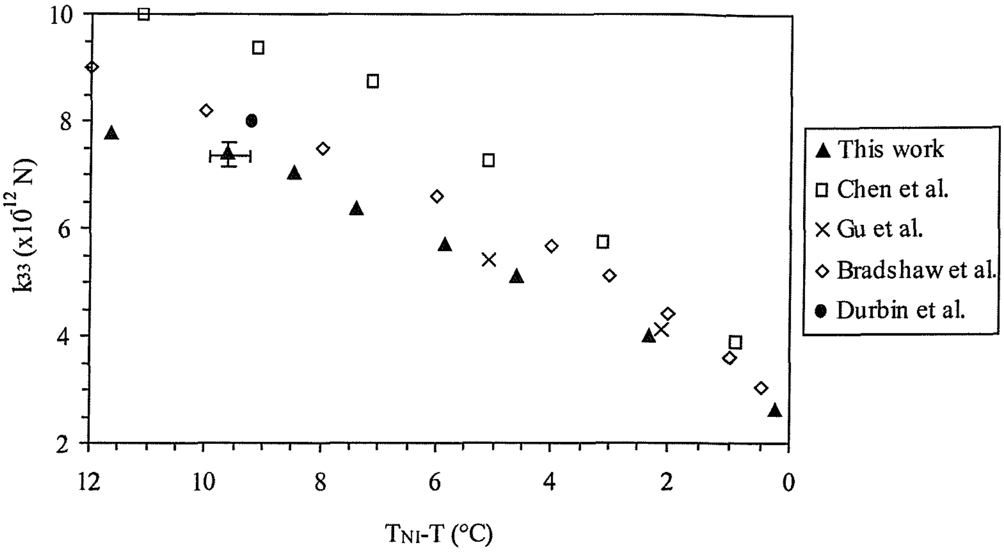

Figure 5.25: Bend elastic constant versus T_{NI}-T measured for 5CB by different groups using various methods.

The bend elastic constant is presented as a function of shifted temperature in Figure 5.26 for the anthraquinone doped mixtures. The addition of dye causes a 10% decrease of k_{33} with saturation between 2 and 3% dye concentration. This reduction in k_{33} results from the disruption of the host nematic by the anthraquinone dye molecules with respect to the bend distortion.

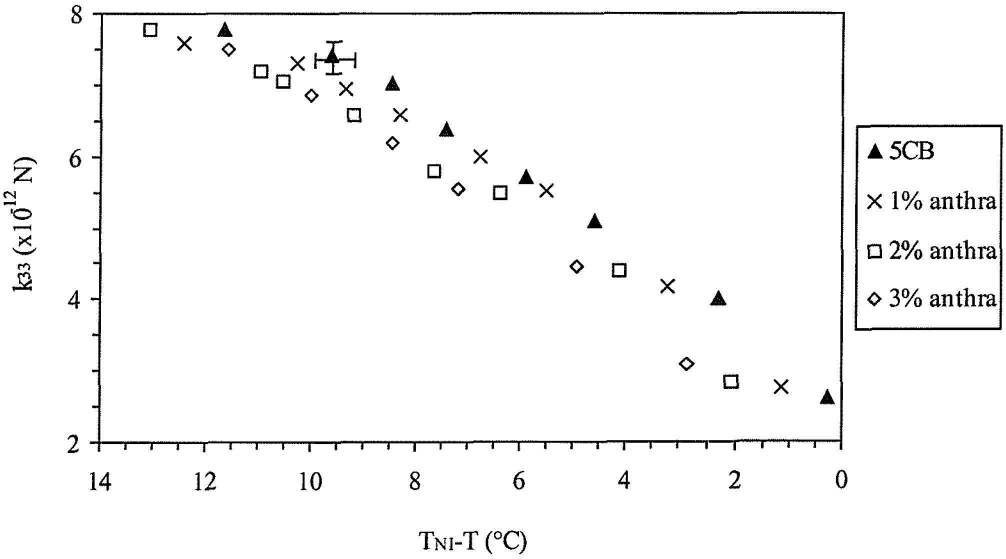

Figure 5.26: Bend elastic constant for the pure 5CB and for the anthraquinone doped mixtures as a function of T_{NI}-T.

Bend viscosity coefficient η_{bend}

The first condition to isolate the bend mode is the use of planar cells. As described in Chapter 2, Section 2.7.2, the best scattering geometry (mode 2) requires:

- A scattering angle $\theta_{lab} = \cos^{-1}(n_e / \sqrt{2n_e^2 - n_o})$ for which $q_\perp = 0$
- Vertical input and horizontal scattered light polarisations.

For 5CB, θ = 43-35° for T = 24.6-34.5 ° C. However such high scattering angles are not achievable with our current spectrometer. Thus, a different scattering geometry (mode 1) has been used:

- A scattering angle θ_{lab} of about 12°
- Horizontal input and scattered light polarisations.

In this configuration, the intensity correlation function is described more accurately by a double exponential function with two adjustable parameters for the decay linewidth: the first component Γ_{bend} is associated with the pure bend mode fluctuations while the second component represents a slower mode (less than 5 Hz). Therefore, it is easy to distinguish between these two dynamic modes. The value of Γ_{bend} determined from a single exponential fit is underestimated. Another fitting program, called SDFIT[29], was required to determine the linewidth caused by the bend fluctuations. The quality of the resulting fit can be assessed by plotting the residuals.

The bend visco-elastic ratio k_{33}/η_{bend}, measured for 5CB to an accuracy of ± 5% in this work, is given in Figure 5.27 on an expanded scale against shifted temperature. Data from Hirataka *et al.*[30], Sefton[13] and Birtwistle[29] included on the same graph for comparison, were obtained from linewidth measurements using the scattering geometry based on mode 2 in DLS experiments. The values of k_{33}/η_{bend} obtained in this thesis with the mode 1 scattering geometry are systematically 20% lower than the data reported by other groups even after correcting for the double exponential.

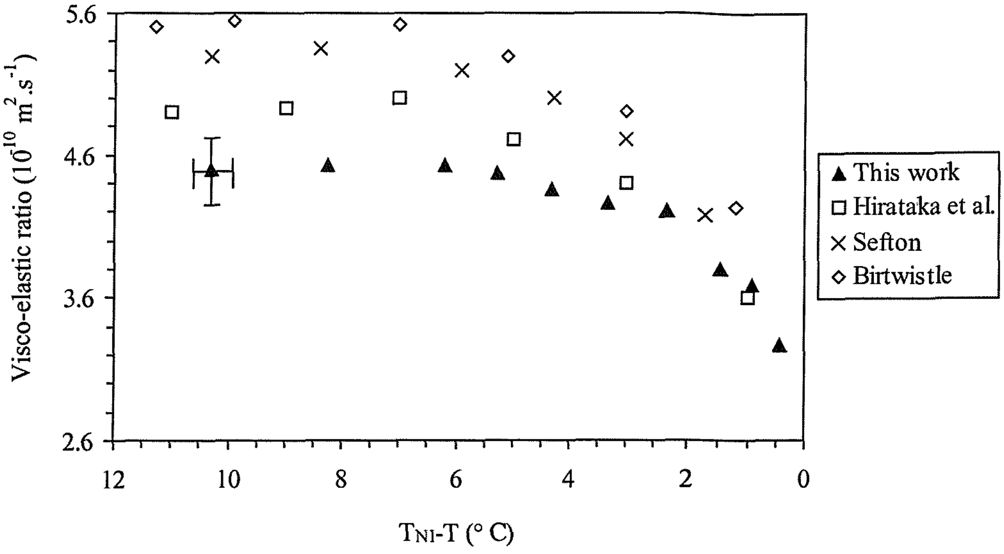

Figure 5.27: Bend visco-elastic ratio determined for 5CB by various workers using DLS.

Figure 5.28 compares the bend viscosity η_{bend} determined in this thesis for 5CB to the values reported by other groups. Our values (given with an accuracy of ± 6%) are in excellent agreement with the data from Gu *et al.*[26] except at lower temperatures: this group also used magnetic Freedericksz transition for the measurement of k_{33} and they deduced η_{bend} ± 2% from the bend visco-elastic ratio.[26] Skarp *et al.* measured directly the Miesowicz and the Leslie coefficients via flow viscometry[31] and these results were used to calculate the bend viscosity using the relation defined in Chapter 2, Equation 2.77:

$$\eta_{\text{bend}} = \gamma_1 - \alpha_2^2 / \eta_1 \,. \qquad \textbf{(5.16)}$$

No uncertainties are quoted with the data from reference 31. Even if the errors on η_{bend} were 10% (included in Figure 5.28), the data from Skarp *et al.* are more disperse than our values and show a different thermal behaviour.

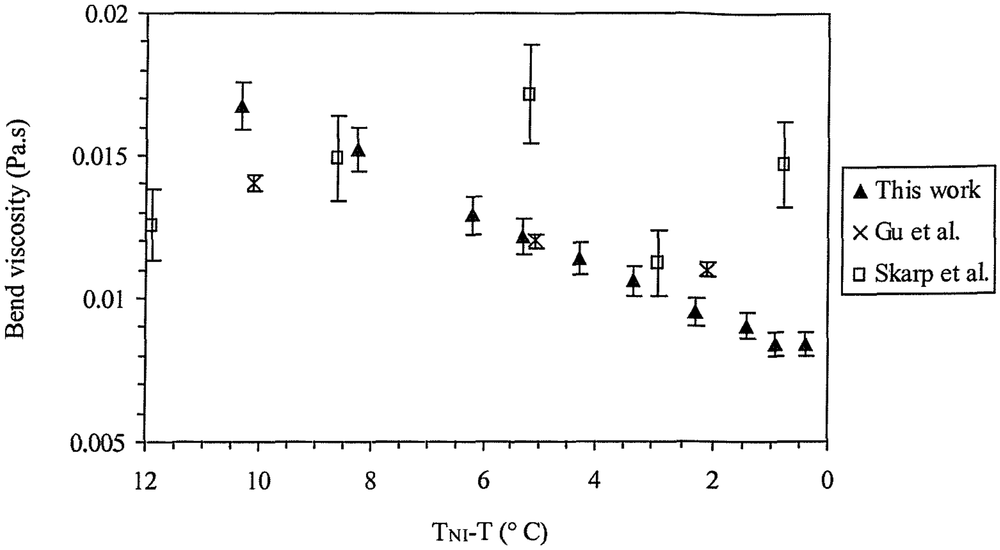

Figure 5.28: Bend viscosity coefficient versus shifted temperature for 5CB measured by different techniques.

The measurements of η_{bend} could not be performed on 50 μm thick planar samples containing 1-3% anthraquinone dye since at all dye concentrations, the optical Freedericksz transition (OFT) causes the apparition of self-diffraction rings similar to the diffraction pattern observed in homeotropic nematic liquid crystals above a certain light intensity threshold I_{th}.[28, 32] It was demonstrated that the presence of a dichroic dye can drastically reduce the value of I_{th} compared to the case of the pure nematic host; this effect may be explained by the existence of a strong dye-induced optical torque caused by the interaction between the excited dye molecules and the mesogenic host molecules.[33] The photoinduced-reorientation of the dye molecules can occur in planar or homeotropic aligned samples, depending on the sign and value of the optical torque, which itself is related to the molecular structure and the concentration of dye. From Equation (5.15), the threshold intensity is inversely proportional to the squared sample thickness d. Therefore, measurements of the bend viscosity have to be carried out on thinner samples of about 6 μm contained in the Lucid cells (described in detail in Chapter 3, Section 3.2.3). Table 5.7 shows for 5CB, the dependence of the bend visco-elastic ratio k_{33}/η_{bend} and of the viscosity coefficient η_{bend} on cell thickness. By comparing Table 5.7 to Figure 5.27 and Figure 5.28, it can be seen that both values of k_{33}/η_{bend} and η_{bend} obtained for the thinner sample are farther from the literature data. Though no diffraction rings were observed using the Lucid cells filled with anthraquinone DGH materials, the absolute values of η_{bend} are not as good as those obtained with thicker cells and will be used solely for comparative studies. Hall *et al.* studied numerically the influence of cell thickness on the accuracy of elastic constants ratios measured in static light scattering experiments.[34] They reported larger experimental uncertainty for thinner cells of thickness of about 7μm and for external scattering angles either less than 10° or comprised between 20° and 60°.

Cell thickness	$k_{33}/\eta_{bend} \pm 5\%$ ($\times 10^{-10}$ m^2.s^{-1})	$\eta_{bend} \pm 6\%$ ($\times 10^{-2}$ Pa.s)
45.0 μm	4.5	1.8
6.0 μm	3.7	2.0

Table 5.7: Bend visco-elastic ratio and viscosity coefficient measured for 5CB using cells of different thicknesses at T = 24.6 °C.

The values of η_{bend} measured for pure 5CB and the three concentrations of anthraquinone dye are presented in Figure 5.29. At the same shifted temperature, the bend viscosity decreases slightly with increasing dye concentration: η_{bend} is slightly lower for both mixtures containing 2% and 3% dye than it is for the pure host. This is related to the fact that the addition of 2 or 3% of dye causes the same decrease in the bend elastic constant. While the values of k_{33}/η_{bend} are unaffected by the dye concentration since they change by less than 5% for the host and for all anthraquinone DGH samples and thus they can be considered within experimental errors.

In Table 5.8, the splay, twist and bend visco-elastic data are summarised for 5CB at two different temperatures. The measured elastic constants and the viscosity coefficients verify respectively the following relationships:

$$k_{33} > k_{11} > k_{22}$$

$$\gamma_1 \geq \eta_{splay} > \eta_{bend} \qquad \textbf{(5.17)}$$

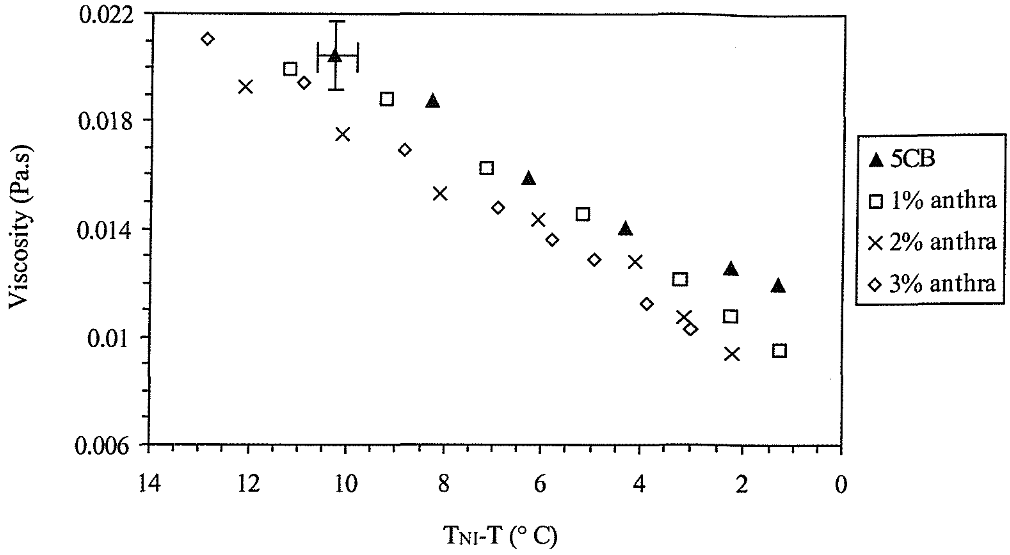

Figure 5.29: Bend viscosity coefficient (± 6%) measured for pure 5CB and for all anthraquinone samples against T_{NI}-T.

	T = 24.6 °C	T = 32.6 °C
k_{11} ± 5% (10^{-12} N)	5.6	3.4
k_{22} ± 3% (10^{-12} N)	3.4	2.2
k_{33} ± 3% (10^{-12} N)	7.5	4.0
k_{33}/k_{22} ± 6%	2.2	1.8
k_{33}/k_{11} ± 7%	1.3	1.2
γ_1 (10^{-2} Pa.s) ± 2%	7.2	3.5
η_{bend} (10^{-2} Pa.s) ± 6%	1.7	1.0

Table 5.8: Splay, twist and bend elastic constants and viscosity coefficients for 5CB at two temperatures.

5.8 Summary

For the first time, electric field dynamic light scattering has been used to determine the twist and splay elastic constants k_{22} and k_{11} and the rotational viscosity coefficient γ_1 of nematic systems doped with azo or anthraquinone dyes. On a shifted temperature scale, the addition of either dye has no influence on any visco-elastic parameters k_{11}, k_{22} and γ_1 of the liquid crystal host 5CB. Nevertheless, at a given temperature, the presence of azo or anthraquinone dye causes an elevation of all visco-elastic constants, this effect being more pronounced for the viscosity coefficients.

Measurements of the bend visco-elastic ratios using DLS have been performed on 5CB and on the anthraquinone-doped systems; these experiments are difficult since, in the scattering geometry employed in this work, molecular reorientation occurs in thick samples due to the strong interaction between the optical laser field and the dye molecules. At the same shifted temperature, the bend elastic constant k_{33} and the bend viscosity η_{bend}, are both found to decrease with increasing concentration of anthraquinone dye.

The main effect of each guest dye is to induce an augmentation of the nematic-to-isotropic transition temperature. The results obtained in this thesis for the anthraquinone dye are very similar to the data measured in the azo case, though the molecular structures of these dichroic molecules are very different. The elongated azo dye molecules increase the stability of the nematic phase range due to their shape compatibility with the rod-like mesogenic molecules of the host. However, the bulkier anthraquinone guest molecules would be expected to disturb further the liquid crystal matrix, resulting in reduction of the clearing point and of the elastic constants of the host liquid crystal.

Since none of the dyes has a strong dipole moment, the dielectric permittivities of the dye-doped mixtures are found to be identical to the values measured for the pure host. The birefringence and the orientational order parameter, determined for the azo-doped mixtures, are independent of dye concentration. Although the refractive indices could not be measured for the samples containing anthraquinone dye, we can assume that these results are also applicable in this case.

For 5CB and the azo-doped mixtures, the splay and twist elastic constants are found to scale as the squared order parameter, as predicted by Saupe and Nehring. The rotational viscosity γ_1 can be described as a function of temperature T and of order parameter S; this experimental fitting procedure depends on the temperature range considered. Different theoretical and phenomenological models have been reported in the literature.

The absorption order parameter S_{Tcorr} and dichroic ratio D of the anthraquinone dye are slightly lower than the values measured in the azo case. For the azo dye investigated, the angle β is likely to be zero and thus, the order parameters of dye absorption S_{Tcorr} and of the dye S_D are equal.[5] For the anthraquinone dye, the value of β is probably small but non zero.

To achieve good contrast between the on and off states at room temperature, a practical device based on the DGH effect requires:[21]

- a dye order parameter S_{Tcorr} of at least 0.73
- a dichroic ratio D higher than 6
- a host order parameter S_{LC} of about 0.65.

The values of S_{Tcorr} and D of our system of anthraquinone and azo dyes in 5CB are insufficient for display applications. These conditions are fulfilled by similar azo dyes dissolved in host mixtures with a wider nematic temperature range and with higher values of S_{LC} but not by the anthraquinone dyes, as reported in Table 5.6 (a) and (b).

For mixtures containing azo or anthraquinone dyes, the ratio of S_{Tcorr}/S_{LC} is greater than one and increases with temperature and consequently both dyes are less influenced by thermal fluctuations than the host LC molecules.

In conclusion, our results are encouraging for the use of DGH mixtures in devices since the performance of displays will not be significantly altered by the presence of a few percent by weight of dye. Longer dyes of the type studied in this work are more advantageous for display applications since they are more resistant to thermal fluctuations and enhance the stability of the nematic phase range of the host liquid crystal.

REFERENCES

[1] Heilmeier G. H. and Zanoni L. A., *Appl. Phys. Lett.*, **13(3)**, pp. 91-92 (1968)

[2] Bahadur B., Guest-Host Effect, Chapter 3 in the *Handbook of Liquid Crystals*, **2A**, pp. 257-302, edited by Demus D., Goodby J., Gray G. W., Spiess H-W. and Vill V., Wiley-VCH, New-York (1998)

[3] Ivaschchenko A. V. and Rumyantsev V. G., Dyes in Liquid Crystals in *Mol. Cryst. Liq. Cryst.* (1987)

[4] Uchida T. and Wada M., *Mol. Cryst. Liq. Cryst.*, **63**, pp. 19-44 (1981)

[5] Seki H., Uchida T. and Shibata Y., *Mol. Cryst. Liq. Cryst.*, **138**, pp. 349-365 (1986)

[6] Coles H. J., Chapter 4 in *The Optics of Thermotropic Liquid Crystals*, edited by Elston S. and Sambles R., Taylor and Francis, London (1998)

[7] Bahadur B., Sarna R. K. and Bhide V. G., *Mol. Cryst. Liq. Cryst.*, **75**, pp. 121-132 (1981)

[8] Cognard J. and Hieu Phan T., *Mol. Cryst. Liq. Cryst.*, **70**, pp. 1-19 (1981)

[9] de Jeu W. H., *Physical Properties of Liquid Crystalline Materials*, Gordon and Breach, New-York (1980)

[10] Prost J., Sigaud G. and Regaya B., *J. Physique Lett.*, **37**, pp. L-341 (1976)

[11] Cui M. and Kelly J. R., Proceedings of the 17th Liquid Crystal Conference, Strasbourg, *Mol. Cryst. Liq. Cryst.*, **331**, pp. 49-57 (1999)

[12] Tough R. J. A. and Bradshaw M. J., *J. Physique*, **44**, pp. 447-454 (1983)

[13] Sefton M. S., *Dynamic Light Scattering from Thermotropic Liquid Crystals*, PhD Thesis, University of Manchester (1985)

[14] Hirschmann H. and Reiffenrath V., Chapter 3 in the *Handbook of Liquid Crystals*, **2A**, pp. 199-229, edited by Demus D., Goodby J., Gray G. W., Spiess H-W. and Vill V., Wiley-VCH, New-York (1998)

[15] Blinov L. M., *Electro-optical and Magneto-optical Properties of Liquid Crystals*, John Wiley and Sons, Chichester, 1983

[16] Cox R. J., *Mol. Cryst. Liq. Cryst.*, **55**, pp. 1-32 (1979)

[17] Uchida T., Shishido C., Seki H. and Wada M., *Mol. Cryst. Liq. Cryst. Lett.*, **34**, pp. 153-158 (1977)

[18] Constant J., Pellatt M. G. and Roe I. C. H., *Mol. Cryst. Liq. Cryst.*, **59**, pp. 299 (1980)

[19] Bauman D., Martyński T. and Mykowska E., *Liq. Cryst.*, **18(4)**, pp. 607-613 (1995)

[20] Allinson H. and Gleeson H. F., *Liq. Cryst.*, **14(5)**, pp. 1469-1478 (1993)

[21] Kelly S. M., *Flat Panel Displays: Advanced Organic Materials*, RSC Materials Monographs, Connor J. A., Cambridge (2000)

[22] Taylor M. R., *Photochromic Liquid Crystals: as Studied by Time Resolved Raman Scattering and Birefringence*, PhD Thesis, University of Manchester (1993)

[23] Allinson H. and Gleeson H. F., *J. Mater. Chem.*, **5(12)**, pp. 2139-2144 (1995)

[24] Hubbard S. D., *The Influence of Dye Solutes on the Static and Dynamic Electro-Optic Properties of Nematic Mesophases*, PhD Thesis, University of Manchester (1986)

[25] Chen G-P., Takezoe H. and Fukuda A., *Liq. Cryst.*, **5(1)**, pp. 341-347 (1989)

[26] Gu D., Jamieson M., Rosenblatt C., Tomazos D., Lee M. and Percec V., *Macromol.*, **24**, pp. 2385-2390 (1991)

[27] Bradshaw M. J., Raynes E. P., Bunning J. D. and Faber T. E., *J. Physique*, **46**, pp. 1513-1520 (1985)

[28] Durbin S. D., Arakelian S. M. and Shen Y. R., *Phys. Rev. Lett.*, **47(19)**, pp. 1411-1414 (1981)

[29] Birtwistle P. J. R., *Dynamic Light Scattering from Liquid Crystalline Systems,* PhD Thesis, University of Manchester (1995)

[30] Hirakata J. I., Chen G. P., Toyooka T., Kawamoto S., Takezoe H. and Fukuda A., *Jap. J. Appl. Phys.*, **25(7)**, pp. L607-L610 (1986)

[31] Skarp K., Lagerwall S. T. and Stebler B., *Mol. Cryst. Liq. Cryst.*, **60**, pp. 215-236 (1980)

[32] Durbin S. D., Arakelian S. M. and Shen Y. R., *Opt. Lett.*, **6(9)**, pp. 411-413 (1981)

[33] Jánossy I. and Kósa T., *Opt. Lett.*, **17(17)**, pp. 1183-1185 (1992)

[34] Hall R., Miyachi K., Newton D., Takezoe H. and Fukuda A., *Jap. J. Appl. Phys.*, **31**, pp. 329-335 (1992)

CHAPTER 6: INVESTIGATION OF NEMATIC MATERIALS WHICH EXHIBIT A CHANGE OF SIGN IN $\Delta\varepsilon$

6.1 Introduction

Previous chapters discussed the physical properties measured for a wide variety of systems consisting of low molar mass mesogens over the whole nematic phase range. The main focus of these studies was the influence of mixture composition or of guest molecules (mesogenic or dichroic) on the visco-elastic parameters determined by dynamic light scattering and Freedericksz transition techniques.

In this chapter, a new approach has been followed: through material engineering, novel types of LC materials have been synthesised in-house for different display applications and their structure-property relationships have been established. These compounds are more complex molecules, with the dielectric anisotropy $\Delta\varepsilon$ playing a major role in their electro-optic performance. The two classes of nematic liquid crystals investigated are materials with low dielectric crossover frequency (improperly called "dual-frequency" materials) and bimesogens or dimers, with high flexoelectric coefficients and low dielectric anisotropy.

In most nematics, the dispersion associated with the parallel component of dielectric constant $\varepsilon_{||}$ occurs at frequencies f_c above 100 kHz at ambient temperature:[1] below f_c, the dielectric anisotropy is positive and above f_c, it becomes negative. By contrast, some nematic liquid crystals (e.g. phenylbenzoates) are characterised by low crossover frequencies, with values typically ranging from 2 kHz to 20 kHz.[1, 2, 3] Such materials are of interest since the use of dual-frequency addressing schemes can improve device performance, especially response times and multiplexability in TN displays.[1, 2]

In short pitch chiral nematic liquid crystals (i.e. with pitch <1 μm), the flexoelectric effect consists of a fast and linear coupling with an applied electric field that causes an in-plane rotation of the optic axis, provided the sample is initially in a uniformly lying helix configuration.[4] One difficulty to overcome is the unwinding of the helix due to dielectric coupling that becomes dominant at higher fields.[4] The use of symmetrical dimers can drastically reduce the molecular dielectric anisotropy[5] and thus much higher rotation angles of the optic axis can be achieved.[6] Depending on the combination of shape and dipole moment, the dimers can also be characterised by high flexoelectric coefficients. New bimesogenic compounds have recently been synthesised[7] that exhibit switching angles of 90° in a bipolar field of amplitude 9 $V.\mu m^{-1}$.

To begin with, alignment issues will be discussed in Section 6.2: the materials studied in this chapter do not align homeotropically although the "dual-frequency" materials did initially. Therefore, the dielectric measurements will be performed on chiral-doped samples. In Section 6.3, the nematic host mixture used with the "dual-frequency" material will be characterised and the crossover frequency will be determined for a wide range of concentrations. Finally in the last part of the chapter, the dielectric anisotropy and visco-elastic ratio will be measured for the novel bimesogens that show improved flexoelectric properties.

6.2 Alignment issues and dielectric constant measurements

6.2.1 Surfactants as homeotropic alignment layers

Bimesogens

The dimers consist of two polar mesogenic units linked by a flexible carbon chain, as illustrated in Figure 6.20. The non-chiral bimesogenic molecules tend to align spontaneously parallel to the substrate and only planar alignment can be achieved in these systems. Several surface treatment agents were tried to promote homeotropic alignment:[8, 9]

- 0.25% wt/wt lecithin in chloroform
- 1 g/100 ml cetyltrimethylammonium bromide (CTAB) in methanol.
- 1% g/l chloro-dimethyl-octadecylsilane in tetrahydrofuran (THF)

These three agents are surfactant molecules that comprise a polar head group and an aliphatic chain: they interact respectively with the glass substrate via their polar groups and with the bimesogens via their carbon tails.[8] Only the silane-based surfactant becomes chemically bonded to the substrate[9] and thereby offers higher anchoring strength. The main drawback with this material is that it reacts readily with air and water.[9] The use of lecithin and CTAB has been discussed in Chapter 3, Section 3.2.1. No homeotropic alignment of the bimesogens could be obtained with any of these surfactants. A possible explanation is that steric interactions between the spacer chain of the bimesogen and the carbon chain of the surfactant act to promote planar alignment.

We also used cells constructed of clean glass without any alignment layer since the polar end groups of the bimesogens might directly make contact with the glass substrate and adopt a homeotropic orientation. However, this attempt did not work and instead, planar orientation of the sample was achieved.

Dual-frequency materials

Schematically, the structure of the compound investigated is a calamitic mesogenic core terminated by a carbon chain at both ends and we call it 5PFP5. This abbreviation is directly related to the structure of the material, which will be presented in Section 6.3.1, Figure 6.3.

Some difficulties were also encountered to induce homeotropic alignment in the low crossover frequency material 5PFP5. The surfactant solutions described previously were used except for the silane-based surfactant. The Lucid cells were filled with 5PFP5 by capillary interactions at different temperatures:

(a) lecithin-treated cell, filled at 85°C
(b) lecithin-treated cell, filled at 170°C
(c) CTAB-treated cell, filled at 170°C

The clearing point of the LC material is 164°C but the lecithin starts to decompose above ~90°C. Care was taken to ensure that cell (b) was left for only a few seconds on the hot plate until filled. After filling, all cells were placed onto a Mettler heating stage to be inspected by polarising microscopy. On heating from room temperature, all cells exhibit good homeotropic alignment at the melting point (~56.3°C) and this texture is maintained up to 65-70°C, depending on the cell. Then, upon further increase of the temperature, there is a spontaneous transition from homeotropic to planar orientation in all three cells. The homeotropic alignment is irreversibly lost at higher temperatures.

6.2.2 Measurement of dielectric constants

Since the nematic compounds, considered in this chapter, do not align homeotropically, it was not possible to measure directly the dielectric constant $\varepsilon_{\parallel}$ as was done previously on nematic liquid crystals. Instead, both dielectric constants can be determined in chiral nematic materials on a single cell using two different configurations.[10]

Principle

In chiral nematics as with achiral nematics, $\varepsilon_{\parallel}$ and $\varepsilon_{\perp}$ are defined as the static dielectric components parallel and perpendicular to the director. The corresponding dielectric anisotropy is given by $\Delta\varepsilon = \varepsilon_{\parallel} - \varepsilon_{\perp}$. Because of the helical structure of the material, two specific orientations, shown in Figures 6.1 (a) and (b), are required for the measurement of the dielectric constants:

- In the standing helix configuration (SH), also known as Grandjean texture, $\varepsilon_{\perp}$ is measured.
- In the uniformly lying helix configuration (ULH), the average dielectric constant is determined from:[10]

$$\varepsilon_{\text{ave}} = \frac{\varepsilon_{\parallel} + \varepsilon_{\perp}}{2}. \qquad \textbf{(6.1)}$$

Thus, $\varepsilon_{\parallel}$ can be obtained using the following formula:

$$\varepsilon_{\parallel} = 2\varepsilon_{\text{ave}} - \varepsilon_{\perp}. \qquad \textbf{(6.2)}$$

Example photomicrographs of both textures[11] are presented in Figure 6.1. In the SH orientation, the light propagates parallel to the helix axis which is normal to the substrates. The reflected wavelength depends on the pitch of the helix and on the birefringence of the sample. The ULH configuration corresponds to a monodomain texture of negative birefringence with its optic axis lying uniaxially in the plane of the cell.[11]

The experimental set-up is based on a capacitance technique and has been detailed in Chapter 3, Section 3.6. The only difference is that a small polarising microscope has been added to the sample holder to check the quality of the texture during the measurements.

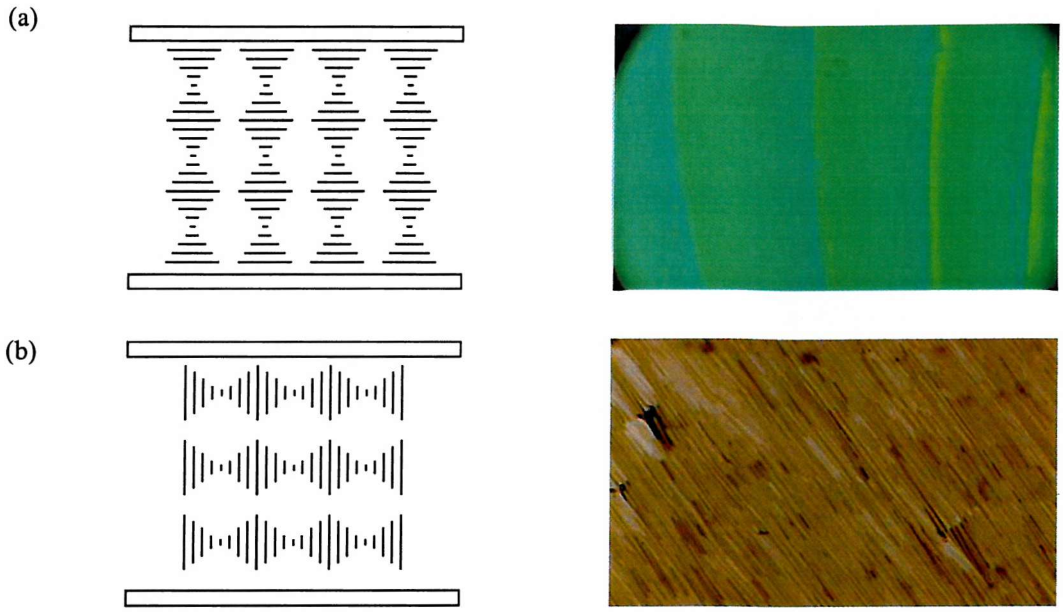

Figure 6.1: Geometries employed for the measurement of dielectric constants in chiral nematic samples. The corresponding optical textures are also shown (courtesy of Dr. B. Musgrave)[11]

(a) Standing helix

(b) Uniformly lying helix.

Experimental

The chiral sample was obtained by doping the original nematic mixture with a low concentration of suitable chiral molecules. The two non-polar chiral additives used in this work, BDH-1305 and BDH-1281, were supplied by Merck Ltd (UK). These two chiral dopants do not have mesomorphic behaviour and their melting points are 89 °C and 120 °C for BDH-1305 and BDH-1281 respectively. They exhibit high helical twisting power, of 57 μm^{-1} for BDH-1305 and of 72 μm^{-1} for BDH-1281 (these values were measured in the host mixture E63)[12]. Therefore, only small amount 1-6% by weight, of either chiral dopant is required to produce a chiral nematic with short to medium pitch. At these low concentrations, the non-polar chiral additives are not expected to strongly influence the dielectric properties of the host material. Typically, the pitch of the chiral-induced systems ranges from about 0.35 to 2 μm.

In most chiral samples studied in this thesis, it was possible to achieve good uniformly lying helix texture by applying an external orienting voltage accompanied by weak mechanical shearing during cooling of the sample from the isotropic phase[10, 11](the rate used was 1 °C.min^{-1}). Depending on the type of materials, cells with different boundary conditions were utilized since the storage of the ULH aligned texture depends on the interactions between the alignment layers and the nematogenic molecules.[7] We also have to take into account that 5 V is the maximum rms voltage available with the Wayne-Kerr bridge used to carry out dielectric constant measurements. For $\Delta\varepsilon>0$, it is necessary to switch between the probe voltage of 0.25 V at 10 kHz and the orienting voltage of 5 V at 500 Hz to maintain the ULH texture. For $\Delta\varepsilon<0$, only the probe voltage remains. In the case of the so-called dual frequency material 5PFP5, the frequency of the aligning voltage was reduced to 100 Hz to ensure that at all temperatures, $\Delta\varepsilon$ remains positive. The experimental conditions required for the ULH alignment are summarised in Table 6.1 for the chiral-doped samples 5CB + 6% BDH-1305, 5PFP5 + 3% BDH-1281 and bimesogens + 1.5% BDH-1281. If the alignment degraded during the measurement, the material was heated back into the isotropic phase and then cooled down again to the desired temperature following the same procedure as described above to ensure a good ULH orientation.

The Grandjean or SH texture forms spontaneously in cells treated to promote planar alignment in the absence of orienting voltage or when the chiral sample is subjected to strong mechanical shearing.

Host nematic	% Chiral dopant	Type of aligning layer	Orienting field
5CB	6% BDH-1305	homeotropic	5V, 500 Hz
5PFP5	3% BDH-1281	none	5V, 100 Hz
Bimesogens	1.5% BDH-1281	planar (AP)	5V, 500 Hz

Table 6.1: Conditions for the formation of ULH orientation in the liquid crystalline samples investigated.

Test measurement

We measured the dielectric constants $\varepsilon_{||}$ and $\varepsilon_{\perp}$ for a well-known achiral mesogen 5CB and for the same compound doped with 6% BDH-1305. The dielectric data, presented in Figure 6.2, show that the dielectric anisotropy was found to be about 10% lower in the chiral nematic mixture that in the pure host at T_{NI}-T = 3 °C. The two data sets seem to converge as the temperature decreases, though no measurements could be carried out at lower temperatures due to the low clearing point of the chiral mixture (T_{N^*I} = 27.8 °C). The dielectric anisotropy Δε, measured for a material containing a few percent of non-polar chiral molecules, can be extrapolated within 10% uncertainty for the pure nematic compound at the same shifted temperature far from the clearing point. This accuracy is sufficient to measure qualitatively the variations of dielectric constants with temperature or with frequency or for comparison between different samples. The underlying assumption is that at low concentrations of a non-polar chiral additive (between 1-6% depending on its helical twisting power), the chiral-induced nematic will have the same dielectric properties than the nematic host liquid crystal. The uncertainty on this measurement stems mainly from the quality of the uniformly lying helix texture required to determine the average dielectric constant.

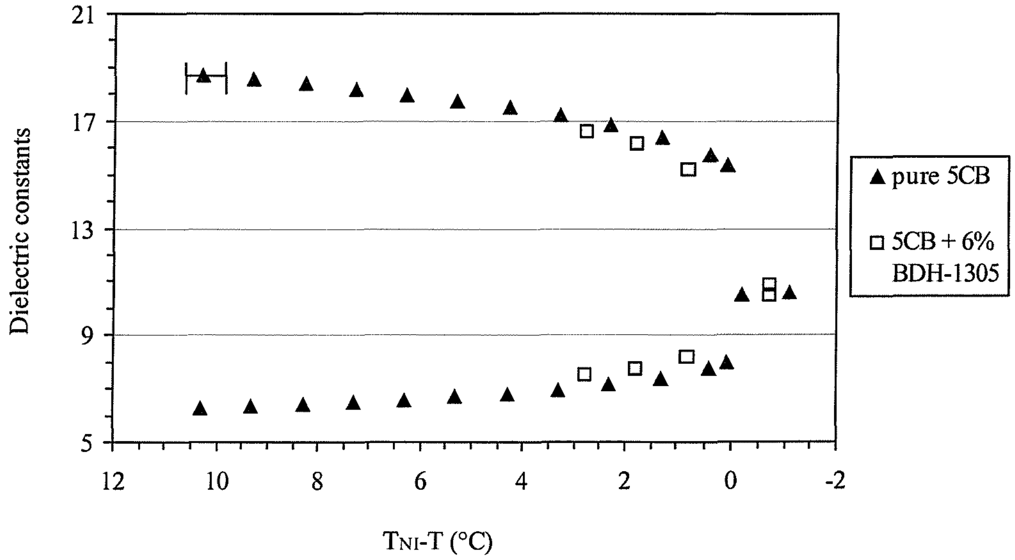

Figure 6.2: Dielectric constants (± 0.5%) versus shifted temperature for pure 5CB and for 5CB doped with 6% BDH-1305.

6.3 Nematic "dual frequency" mixtures

6.3.1 Materials and transition temperatures

The low crossover frequency material 4-n-pentylphenyl 2-fluoro-4-(4-n-pentylbenzoyloxy) benzoate, abbreviated as 5PFP5, was synthesised in-house by Dr. S. Perkins and was used without further purification. Its molecular structure is given in Figure 6.3. The original benzoate compound it is based upon, contains a chlorine atom instead of a fluorine one.[2]

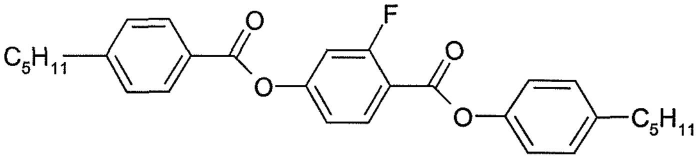

Figure 6.3: Chemical structure of 5PFP5.

5PFP5 is used at different concentrations in a nematic host mixture, MDA-00-984, supplied by Merck Ltd (UK). The host exhibits a wide nematic phase range, low negative dielectric anisotropy and low viscosity. Moreover, good planar and homeotropic alignment can be readily achieved with this host mixture.

Four concentrations by weight of 5PFP5 in MDA-00-984 were prepared: 5%, 10.6%, 17.3% and finally 49.5%. The nematic-to-isotropic phase transition temperatures of achiral and chiral samples investigated were measured by optical microscopy and are shown in Table 6.2. The melting and clearing points $T_{Cr\text{-}N}$ and $T_{N\text{-}I}$, determined by DSC for the nematic mixtures, are also included in the same table and the corresponding phase diagram is plotted in Figure 6.4. The values measured by optical microscopy are consistent with DSC data. The nematic host MDA-00-984 and the mixtures containing up to 20% 5PFP5 crystallise well below 0 °C. The sample with 50% 5PFP5 can be investigated at ambient temperature since it crystallises at about 15 °C while the pure ester 5PFP5 is only nematic above ~53°C.

In the following, the shifted temperatures are based on the clearing points taken from optical microscopy measurements.

	Optical microscopy		DSC	
	$T_{N\text{-}I}$ (in °C)	$T_{N*\text{-}I}$ (in °C)	$T_{Cr\text{-}N}$ (in °C)	$T_{N\text{-}I}$ (in °C)
MDA-00-984	59		< -40°C	58.4
5% 5PFP5	61.8		< -20°C	60.4
10.6% 5PFP5	67.6		< -20°C	64.2
17.3% 5PFP5	76.5	78.6	< -20°C	72
49.5% 5PFP5	108.3	103.7	15.1	109.8
pure 5PFP5	164	159.8	52.6	163.7

Table 6.2: Melting and clearing points determined by DSC and by optical microscopy for the nematic and chiral-doped mixtures.

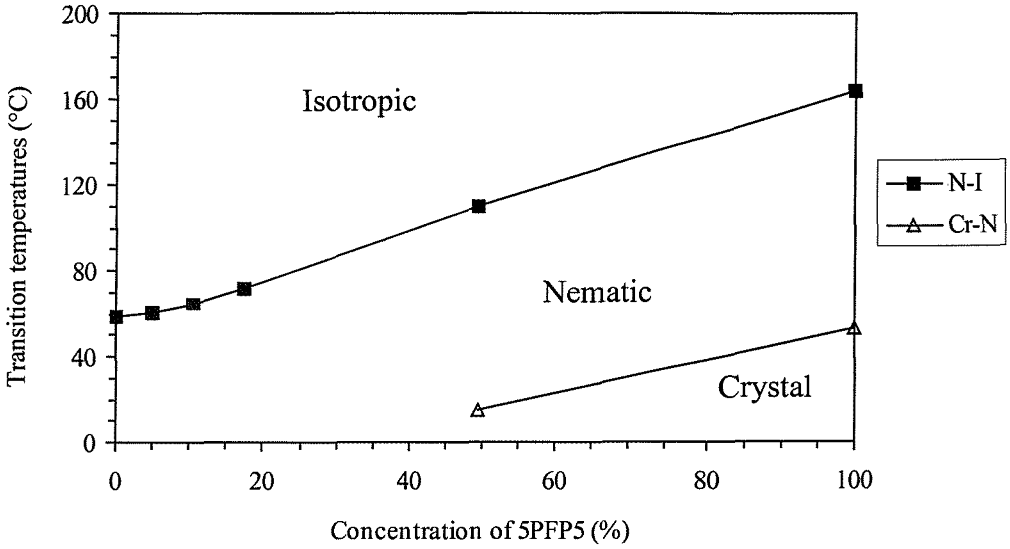

Figure 6.4: Phase diagram of the nematic 5PFP5/MDA-00-984 mixtures (data measured by DSC).

6.3.2 *Characterisation of the host*

Dielectric and optical anisotropies

The dielectric constants $\varepsilon_{\parallel}$ and $\varepsilon_{\perp}$ of MDA-00-984 (measured at 1 kHz) and the associated dielectric anisotropy $\Delta\varepsilon$ are plotted against T_{NI}-T in Figures 6.5 (a) and (b) respectively. At all temperatures, $\varepsilon_{\perp}$ is slightly greater than $\varepsilon_{\parallel}$. As a result, $\Delta\varepsilon$ is weakly negative and is comprised between –0.8 and –0.3 across a 35 °C temperature range.

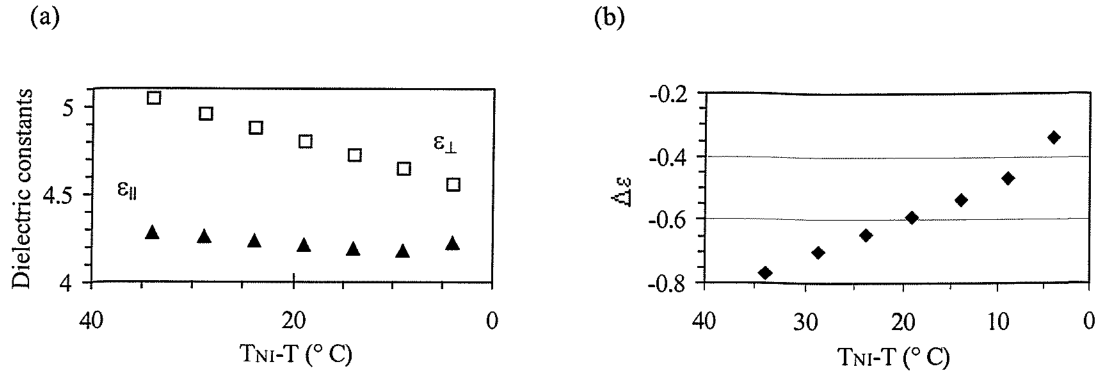

Figure 6.5: (a) Dielectric constants $\varepsilon_{\parallel}$ and $\varepsilon_{\perp}$ (± 0.5%)

(b) Corresponding dielectric anisotropy of the mixture MDA-00-984.

The refractive indices and the optical anisotropy of MDA-00-984 (measured at 632.8 nm) are given in Figure 6.6 (a) and (b). This host is a medium birefringence mixture with an average optical anisotropy Δn=0.125.

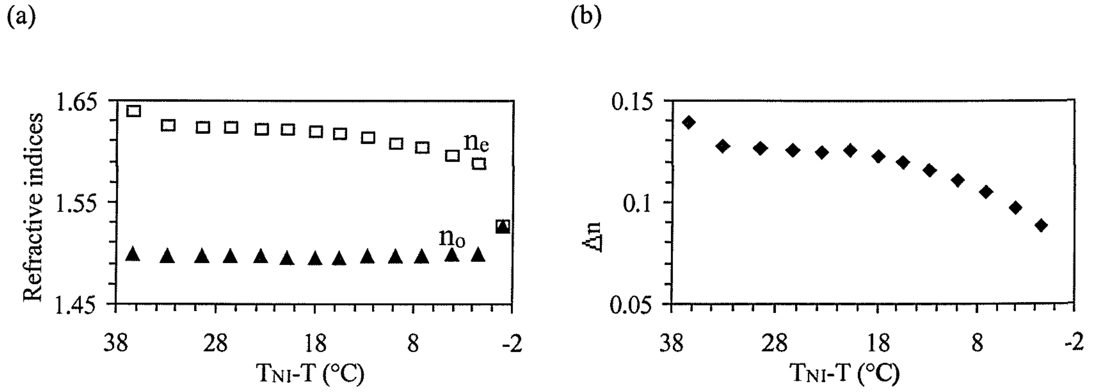

Figure 6.6: (a) Refractive indices n_e and n_o (± 0.0002)

(b) Associated birefringence for MDA-00-984.

Visco-elastic properties

Figures 6.7 (a) and (b) illustrate respectively the bend elastic constant k_{33} and the twist and splay visco-elastic ratios k_{22}/γ_1 and k_{11}/η_{splay} as a function of shifted temperature for MDA-00-984. These data are also quoted in Table 6.3 and the values measured for 5CB at a similar T_{NI}-T have been included for comparison (see Chapter 4, Section 4.3.2 and Chapter 5, Section 5.7). k_{33} is increased by about 30% in the case of the MDA mixture compared to 5CB. Both k_{22}/γ_1 and k_{11}/η_{splay} are twice greater for the MDA-00-984 mixture than for 5CB. This is caused by a combination of higher elastic constants and lower viscosity coefficients of the neutral components that are used for MDA-00-984.

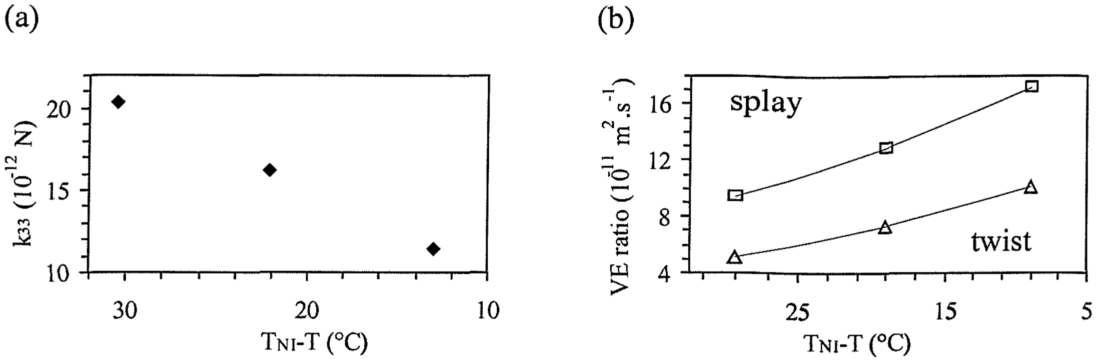

Figure 6.7: Visco-elastic data for the host mixture MDA-00-984 against T_{NI}-T

(a) Bend elastic constant (± 3%)

(b) Twist (± 1.5%) and splay (± 3%) visco-elastic (VE) ratios.

Material	T_{NI}-T (°C)	Twist VE ratio (10^{-11} $m^2.s^{-1}$)	Splay VE ratio (10^{-11} $m^2.s^{-1}$)	Bend elastic constant (10^{-12} N)
5CB	10.3	4.7	7.5	-
	11.6	-	-	7.8
MDA-00-984	9	10.1	17.1	-
	12.9	-	-	11.4

Table 6.3: Visco-elastic data measured for 5CB and for MDA-00-984.

Since the dielectric anisotropy of this mixture is negative, it is not possible to apply a damping field in the present homeotropic geometry to obtain separately the twist and splay viscosity coefficients and elastic constants.

6.3.3 Dual frequency mixtures

Theory for dielectric relaxation

A molecular dipole can reorient itself via two possible rotations:[13]

- about the short molecular axis
- about the long molecular axis.

These two mechanisms correspond respectively to the relaxation of the parallel component $\varepsilon_{\parallel}$ and perpendicular component $\varepsilon_{\perp}$ of dielectric permittivity. These reorientation processes are characterised respectively by the time constants $\tau_{\parallel}$ and $\tau_{\perp}$, with $\tau_{\parallel} > \tau_{\perp}$, since the first mode is significantly hindered in the nematic phase.[13]

For single relaxation process, the frequency dependence of the parallel and perpendicular dielectric component can be expressed as follow:[1, 14]

$$\varepsilon_i(\omega) = \varepsilon_i(\infty) + \frac{\varepsilon_i(0) - \varepsilon_i(\infty)}{1+\omega^2\tau_i^{\ 2}}, \text{ with i= ||, } \perp, \qquad \textbf{(6.3)}$$

where $\omega = 2\pi f$, $\varepsilon_i(0) = \varepsilon_i(\omega = 0)$ and $\varepsilon_i(\infty) = \varepsilon_i(\omega = \infty)$ are the static and high frequency values, $\tau_i = 1/\omega_i$ $(i = ||, \perp)$ is the relaxation time associated with each mode.

Some materials exhibit relaxation frequencies below 100 kHz for $\varepsilon_{||}$. Since the dielectric dispersion of $\varepsilon_\perp$ generally occurs at frequencies higher than 100 kHz, the value of $\varepsilon_\perp$ can be assumed constant at low frequencies[1] i.e. $\varepsilon_\perp(\omega) = \varepsilon_\perp$ and Equation (6.3) can be rewritten for $\varepsilon_{||}$ as:

$$\varepsilon_{||}(\omega) = \varepsilon_{||}(\infty) + \frac{\varepsilon_{||}(0) - \varepsilon_{||}(\infty)}{1+\omega^2\tau_{||}^2}, \qquad \textbf{(6.4)}$$

$\tau_{||} = 1/\omega_0$ and ω_0 is defined such that:

$$\varepsilon_{||}(\omega_0) = \frac{\varepsilon_{||}(0) + \varepsilon_{||}(\infty)}{2}. \qquad \textbf{(6.5)}$$

$\varepsilon_{||}(0) - \varepsilon_{||}(\infty)$ is the dispersion step and from the Maier and Meier theory, it can be shown that

$$\varepsilon_{||}(0) - \varepsilon_{||}(\infty) \propto \mu_{||}^2, \qquad \textbf{(6.6)}$$

where $\mu_{||}$ is the longitudinal component of the permanent dipole moment.[1]

The dispersion of the dielectric anisotropy can be derived from Equation (6.4):

$$\Delta\varepsilon(\omega) = \Delta\varepsilon_\infty + \frac{\Delta\varepsilon(0) - \Delta\varepsilon_\infty}{1 + \frac{\omega^2}{\omega_0^2}}. \qquad \textbf{(6.7)}$$

At low frequencies $\omega < \omega_c$, $\Delta\varepsilon(0) > 0$ while at high frequencies $\omega > \omega_c$, $\Delta\varepsilon(\infty) < 0$.

At $\omega = \omega_0$,
$$\Delta\varepsilon(\omega_0) = \frac{\Delta\varepsilon(0) + \Delta\varepsilon(\infty)}{2}. \qquad \textbf{(6.8)}$$

The relationship between the relaxation frequency f_0 and the crossover frequency f_c is given by:

$$f_c = f_0\sqrt{\frac{\Delta\varepsilon(0)}{|\Delta\varepsilon(\infty)|}}. \qquad \textbf{(6.9)}$$

Therefore, if the dielectric anisotropies $\Delta\varepsilon$ (0) and $\Delta\varepsilon(\infty)$ are of same magnitude but of opposite sign, $f_c = f_0$.

The temperature dependence of the crossover and relaxation frequencies can be described by an Arrhenius law:[1, 15]

$$f_c \propto f_0 \propto \exp(-E/k_B T), \qquad \textbf{(6.10)}$$

where E is an activation energy.

Basic device principle using dual-frequency addressing

The "dual-frequency" LC material is initially in a twisted nematic (TN) geometry i.e. the molecules are aligned at 90° to each other on the upper and on the lower substrates. The LC molecules reorient to lie parallel to the field above a threshold voltage $V_{th,L}(V_H = 0)$ applied at low frequency $f < f_c$. If another signal of high frequency $f > f_c$ and of amplitude V_H is superimposed, the threshold voltage for the Freedericksz transition becomes $V_{th,L}(V_H)$:[2]

$$V_{th,L}^2(V_H) = V_{th,L}^2(0) + \left|\Delta\varepsilon(\infty)/\Delta\varepsilon(0)\right| V_H^2, \qquad \textbf{(6.11)}$$

where $\Delta\varepsilon(0)$ and $\Delta\varepsilon(\infty)$ are respectively the low and high frequency dielectric anisotropy.

Since $\Delta\varepsilon(\infty) < 0$, the presence of V_H will stabilise the initial twisted orientation of the liquid crystal and thus, will shift the threshold voltage $V_{th,L}$ to higher values. Furthermore, the steepness of the electro-optical transmission curve also increases with V_{th}, allowing improved multiplexability capability, compared to TN displays using standard nematic materials.[1, 2]

Fast turn off response times can be achieved by applying only high frequency voltage V_H ($f > f_c$). In this case, the dielectric anisotropy is negative and above a threshold value $V_{th,H}$, the LC molecules realign parallel to the plane of the cell.[1, 2]

Results and discussion

The measurements of dielectric constants were carried out at different frequencies up to 300 kHz, the maximum frequency of our capacitance bridge. As expected, the values of the perpendicular component $\varepsilon_\perp$ are independent of frequency in this frequency range for all mixtures investigated.

The dielectric constants $\varepsilon_\parallel$ and $\varepsilon_\perp$ were measured on homeotropic and planar samples, using the method outlined in Chapter 3 Section 3.6, for the host MDA-00-984 and the two lowest concentrations of 5PFP5. The dielectric anisotropy $\Delta\varepsilon$ is plotted in Figure 6.8

versus shifted temperature. The addition of 5PFP5 causes an increase in Δε of the host mixture, which becomes less negative and tends towards zero. However, Δε does not change sign as a function of frequency for any of these mixtures.

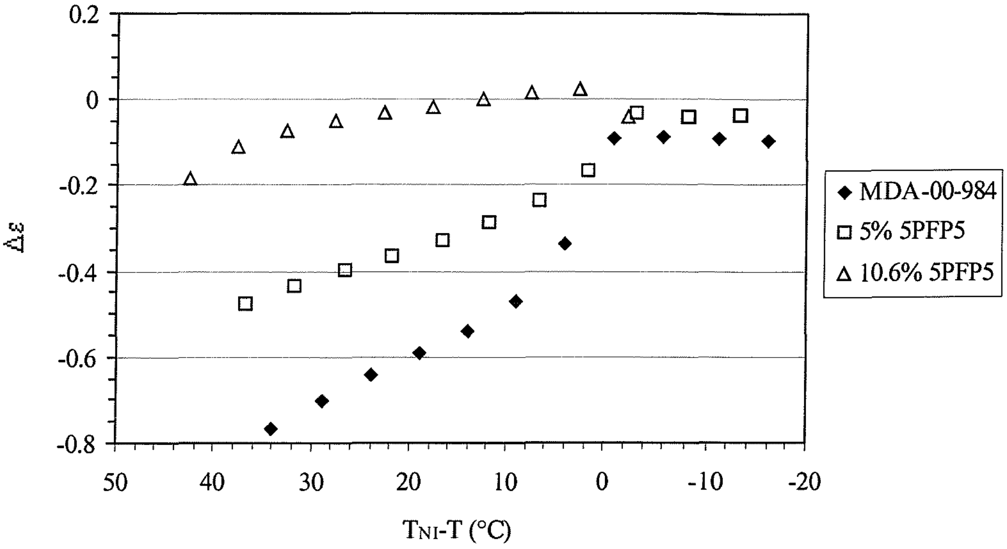

Figure 6.8: Dielectric anisotropy (± 1%) for the pure host, 5% and 10.6% 5PFP5 containing mixtures.

For concentration of 5PFP5 greater than 10%, no homeotropic alignment could be achieved and the dielectric measurements were performed on chiral-doped samples following the method explained in Section 6.2.2. The dielectric behaviour of the mixture with 17.3% 5PFP5 doped with 3% BDH-1281 is similar to the host mixture as shown in Figure 6.9 at different frequencies. The negative Δε increases with temperature. The dependence of Δε on frequency indicates that it is slightly positive or zero at low frequencies and it becomes negative at higher frequencies. From Figure 6.9, the crossover frequency seems to be around or below 10 kHz. To confirm that this mixture exhibits "dual-frequency' behaviour, an achiral mixture of analogous composition, 18.5% 5PFP5 in MDA-00-984, was also prepared and investigated in electro-optical experiments.[16] The data for this mixture are extracted from reference 16: the transmission, measured at a voltage of amplitude 20 V peak-to-peak is plotted in Figure 6.10 as a function of frequency; since this voltage is above the threshold value for the Freedericksz transition, the sample is homeotropic for $f < f_c$ and it becomes planar for $f > f_c$. From this diagram, f_c can be determined and it is found to increase with temperature.

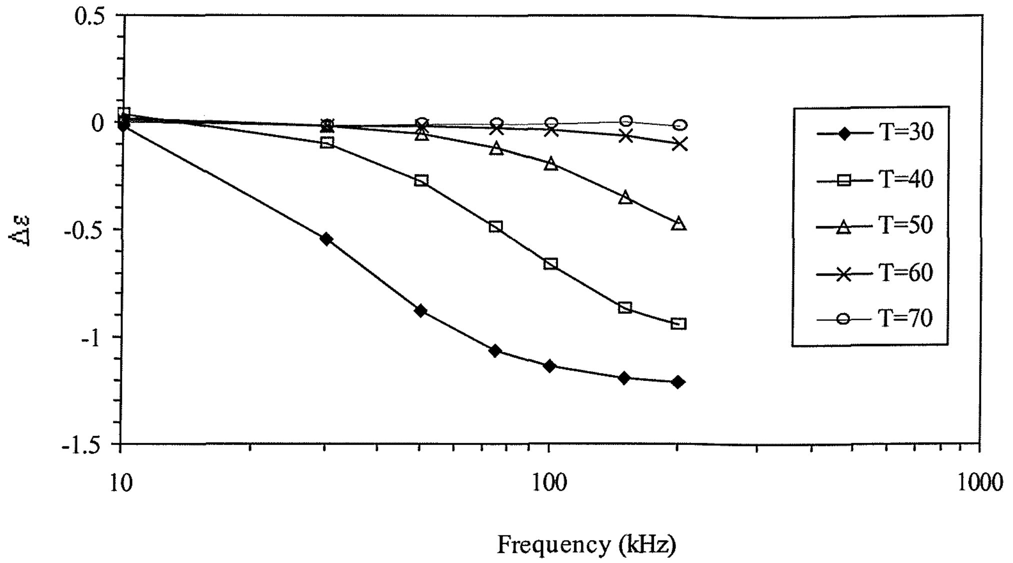

Figure 6.9: Dielectric anisotropy (± 1%) against frequency at several temperatures for the 17.3% 5PFP5 in MDA-00-984 (+3% chiral additive BDH-1281).

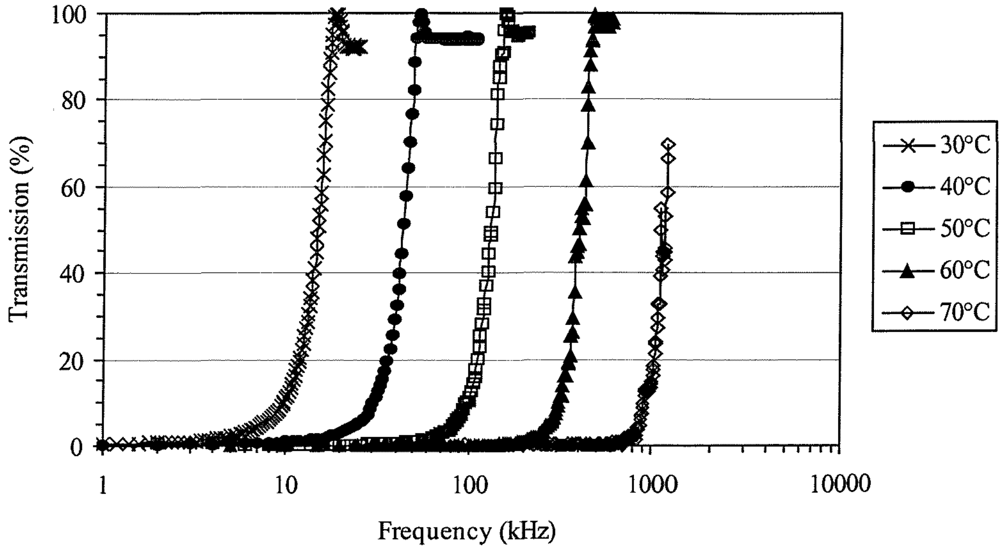

Figure 6.10: Transmission data versus frequency obtained at 20 Vpp for 18.5% 5PFP5 in MDA-00-984 at different temperatures (reproduced with permission of 16).

The dielectric anisotropy Δε of 5PFP5 doped with 3% BDH-1281 is presented in Figure 6.11 against T_{NI}-T for frequencies ranging from 10 kHz to 300 kHz. The dispersion of Δε is given in Figure 6.12 at different temperatures for the same mixture.

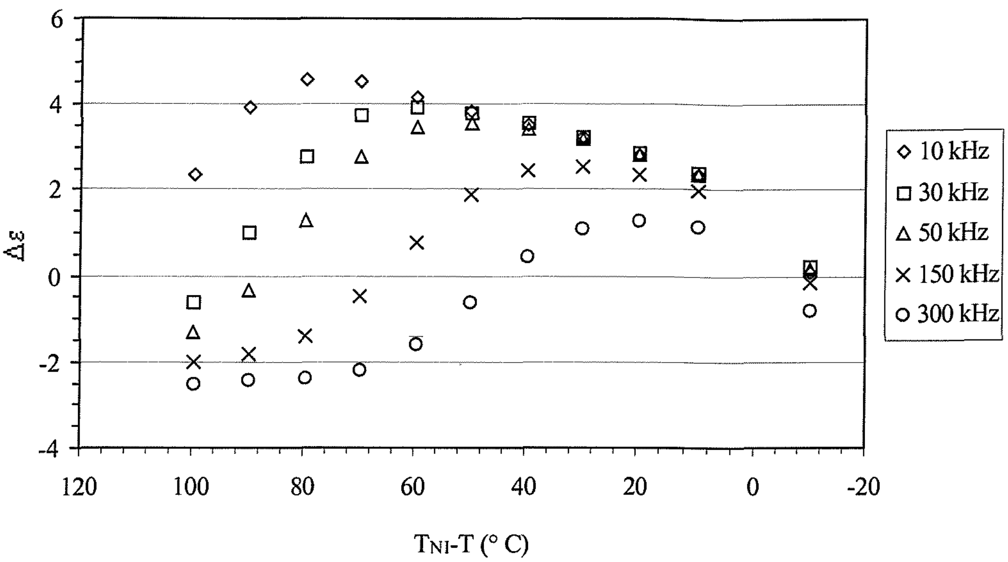

Figure 6.11: Dielectric anisotropy against T_{NI}-T measured at several frequencies for 5PFP5 (+3% BDH-1281).

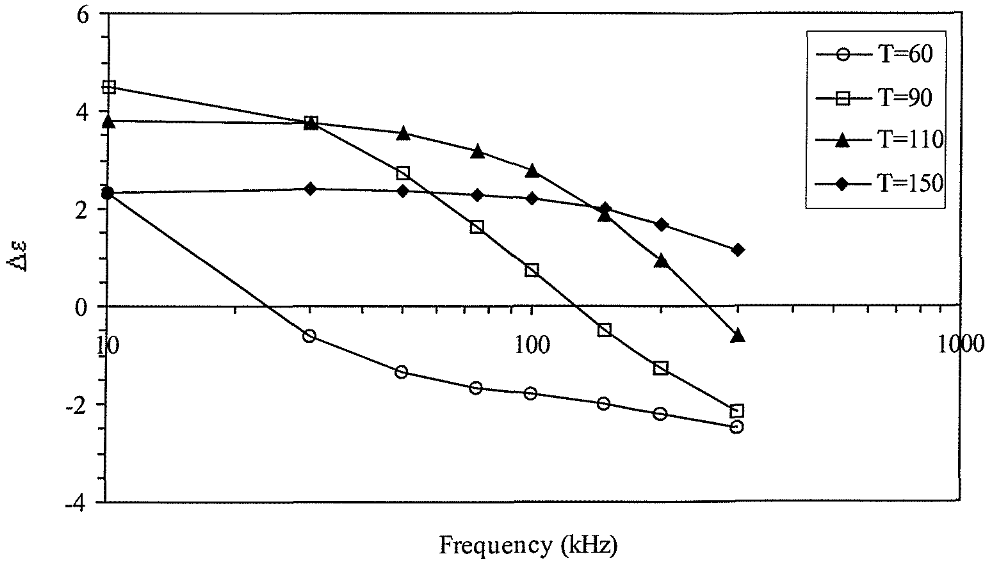

Figure 6.12: Dielectric anisotropy as a function of frequency at different temperatures for 5PFP5 doped with 3% BDH-1281 (the solid lines are here to guide the eye).

The data from Figure 6.12 can be analysed using Equation (6.7) and this fitting procedure yields three parameters $\Delta\varepsilon$ (0), $\Delta\varepsilon$ (∞) and $\tau=1/f_0$. The value of f_c can be determined from Equation (6.9) and the results are plotted in Figure 6.13 on a logarithmic scale as a function of the inverse temperature for the two chiral-doped samples, 5PFP5 and 49.5% 5PFP5, and for the nematic mixture with 18.5% 5PFP5. This graph also shows that in both instances, f_c scales as:

$$f_c \propto \exp(-E/k_BT), \qquad \textbf{(6.12)}$$

with activation energies E increasing from 0.48 eV, 0.71 eV to 0.98 eV for pure 5PFP5 and the mixtures containing 49.5% and 18.5% 5PFP5 respectively. Clearly, the lower the concentration of 5PFP5, the higher the activation energy.

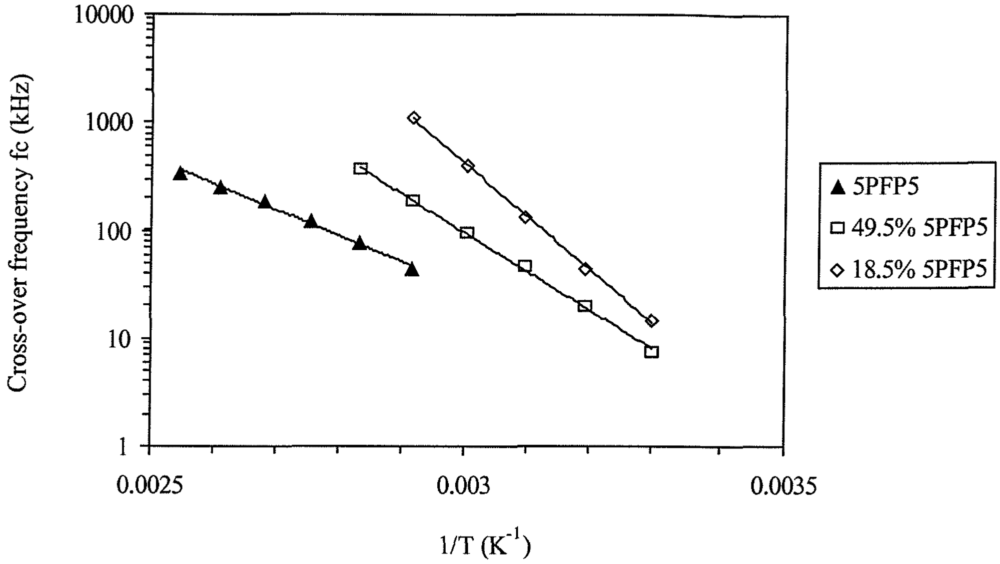

Figure 6.13: Linear fit of the crossover frequency f_c versus 1/T for 5PFP5, 49.5% 5PFP5 and 18.5% in MDA-00-984.

The values of crossover frequencies are summarised in Table 6.4 and Figure 6.14 for 5PFP5, 49.5% and 18.5% 5PFP5 in the host mixture. At comparable shifted temperatures, f_c decreases when the concentration of 5PFP5 is reduced.

5PFP5		49.5% 5PFP5		18.5% 5PFP5	
T_{NI}-T (°C)	f_c (kHz)	T_{NI}-T (°C)	f_c (kHz)	T_{NI}-T (°C)	f_c (kHz)
89.8	43	73.7	8	46.5	15
79.8	75	63.7	20	36.5	44
69.8	122	53.7	45	26.5	132
59.8	183	43.7	93	16.5	405
49.8	254	33.7	185	6.5	1120
39.8	338	23.7	367		
19.8	513				
9.8	545				

Table 6.4: Values of crossover frequency for 5PFP5, 49.5% 5PFP5 and 18.5% 5PFP5 as a function of shifted temperature.

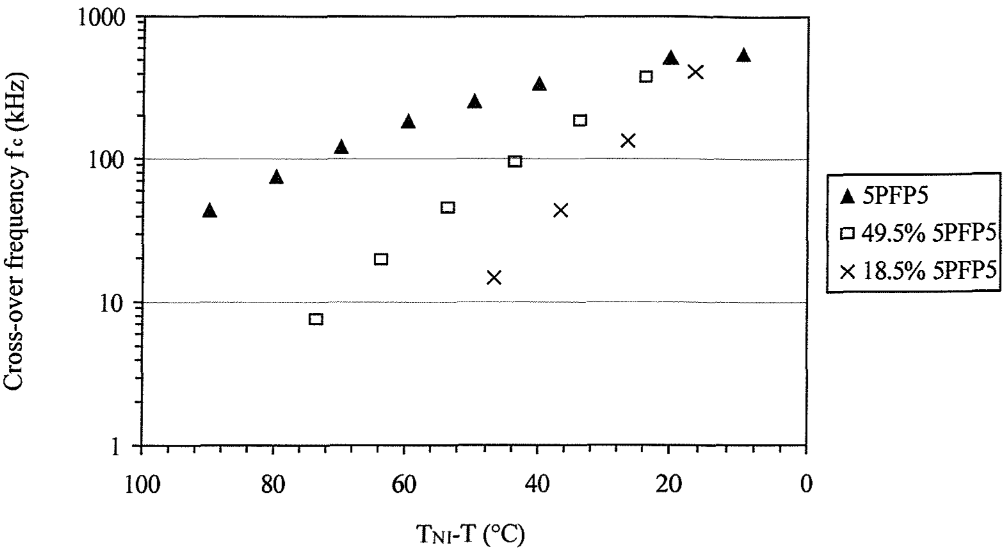

Figure 6.14: Crossover frequency (in kHz) versus T_{NI}-T for different concentrations of 5PFP5.

It is interesting to compare the activation energies E and crossover frequencies f_c obtained for 5PFP5 with the data quoted in the literature on other "dual-frequency" phenylbenzoate mixtures. The value of E measured for the pure 5PFP5 is lower than for analogous compounds. For a similar ester with butyl end chains and no lateral substituent, E is found to be 0.75 eV and f_c ranges from 100 kHz to 1 MHz at shifted temperatures of 99.1 °C and 65.4 °C respectively.[15] A mixture based on the original chlorine-substituted three ring ester compound (consisting of 50% pentyl and 50% octyl components), exhibits an activation energy of 0.83 eV and a crossover frequency of 2.5 kHz at room temperature.[2] Some commercial mixtures of phenylbenzoates, namely ZLI-518, W1 and ZLI-612, also have E = 0.84 to 0.88 eV and the lowest value for f_c, achieved at 25 °C, is about 10 kHz[3]. Schadt studied binary mixtures of pyridazines and four-ring esters with nitrile terminal groups and measured E = 0.96 eV and f_c = 1.2 to 2.3 kHz at 22 °C (or at T_{NI}-T = 52.5 to 60.2 °C).[1] In general, at the same shifted temperature, higher values of activation energies seem to be associated with lower values for f_c.[13]

The behaviour of the crossover frequency is more difficult to compare since it strongly depends on the temperature of the measurements. At the same shifted temperature, the values of f_c for 5PFP5 tend to be higher than those measured in reference 2 and this may be explained by the presence of the fluorine atom. For our compound, f_c remains in the kHz range even at the highest temperature in the nematic phase (i.e. at T_{NI}-T ≈ 10.5 °C).

The plot of the static dielectric anisotropy versus concentration of 5PFP5 is illustrated in Figure 6.15. At low concentrations of "dual-frequency" material, Δε is dominated by the behaviour of host MDA-00-984 and is weakly negative at 10 kHz; whereas at high concentrations, Δε is positive at 10 kHz and behaves characteristically as a "dual-frequency" material, changing sign with frequency (although this is not shown in Figure 6.15). The threshold concentration at which the system 5PFP5/MDA-00-984 will exhibit "dual-frequency" behaviour is probably between 15% and 20% 5PFP5. Δε increases with the quantity of 5PFP5 above 15%, as shown in Figure 6.15 at different T_{NI}-T.

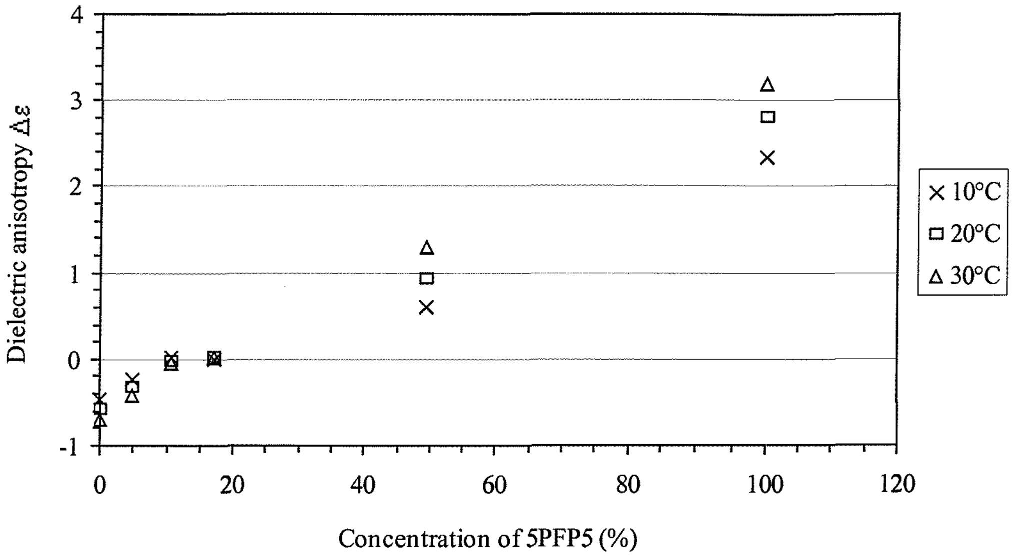

Figure 6.15: Dielectric anisotropy against 5PFP5 concentration measured at 10 kHz for three different shifted temperatures T_{NI}-T.

6.3.4 Summary

In this section, we investigated mixtures of different concentrations of a "dual-frequency" material, namely 4-n-pentylphenyl 2-fluoro-4-(4-n-pentylbenzoyloxy) benzoate, abbreviated as 5PFP5, dissolved in a nematic host mixture MDA-00-984. 5PFP5 has the following phase sequence:

Cr 52.6 °C N 163.7 °C I.

The host MDA-00-984 is characterised by a clearing point of 59 °C, an average birefringence Δn of 0.125 and low and negative Δε varying from –0.8 to –0.3 for temperatures ranging from 25 °C to T_{NI}. For this host mixture, the bend elastic constant k_{33} was measured via the Freedericksz transition technique while the splay and twist visco-elastic ratios were determined by dynamic light scattering. Further work is needed in order to derive the individual splay and twist viscosity coefficients and elastic constants for this mixture with negative dielectric anisotropy. For instance, k_{11} could be calculated at the same shifted temperature from the gradient of the retardation curve plotted versus magnetic field in Freedericksz transition experiments since this gradient is proportional to the ratio of bend-to-splay elastic constant k_{33}/k_{11} (refer to Chapter 3, Equation (3.17)). Knowing k_{11}, the splay viscosity coefficient can be calculated from the visco-elastic ratio and by using the approximation that $\eta_{splay} \approx \gamma_1$, the twist elastic constant k_{22} can finally be obtained.

For 5PFP5 in MDA-00-984, two concentration regimes can be distinguished:

- below 15% 5PFP5, the dielectric anisotropy is weakly negative at all frequencies and the mixture cannot be dual-frequency addressed.
- above 15% 5PFP5, the dielectric anisotropy changes sign at the crossover frequency f_c. Far from the clearing point, f_c varies between 5 and 20 kHz for 18.5% and 49.5% 5PFP5 in MDA-00-984. The crossover frequency is higher for pure 5PFP5 i.e. f_c is about 40 kHz at temperatures just above the melting point. The activation energies associated with this relaxation process are between 0.5 and 1 eV, decreasing with increasing concentration of the compound 5PFP5.

The mixtures containing between 20% and 50% of 5PFP5 in MDA-00-984 are the most interesting for potential display applications since at these concentrations, these systems are likely to exhibit a room temperature nematic phase with T_{NI} higher than 70 °C and their dielectric anisotropy will change sign at crossover frequencies in the kHz range.[16]

The bend-to-splay elastic constant ratio k_{33}/k_{11} controls the gradient of the electro-optical curve. For conventional TN devices driven at low frequency, the steepness is increased for lower values of k_{33}/k_{11} while for STN displays, the steepness is optimised for higher values of k_{33}/k_{11}.[1, 17] Low viscosity coefficients are desirable to achieve fast response times. It would be interesting to measure the elastic constants and viscosities for different mixtures of 5PFP5 and MDA-00-984 in the "dual-frequency" concentration range.

6.4 Mixtures of bimesogens with enhanced flexoelectric properties

6.4.1 Flexoelectric effect in chiral nematics

In nematic liquid crystals, dipolar flexoelectric coupling may occur if the molecules possess a suitable combination of shape asymmetry and permanent dipole moment. In the absence of an electric field, the resulting nematic medium is non-polar. A splay or bend distortion may polarise macroscopically the medium and reciprocally, the application of an electric field may induce a deformation of the LC material[18, 19]. It is worth mentioning that flexoelectricity also exists in non-polar LC materials via quadrupolar coupling that contributes to this effect.[20]

In nematic liquid crystals, the flexoelectric polarisation is given by:[18, 19]

$$\mathbf{P}_{\mathbf{flexo}} = e_s\mathbf{n}(\nabla\cdot\mathbf{n}) + e_b\mathbf{n}\times(\nabla\times\mathbf{n}), \tag{6.13}$$

where e_s and e_b are respectively the splay and bend flexoelectric coefficients. The flexoelectric effect is illustrated in Figure 6.16 and Figure 6.17 for splay and bend induced deformations.

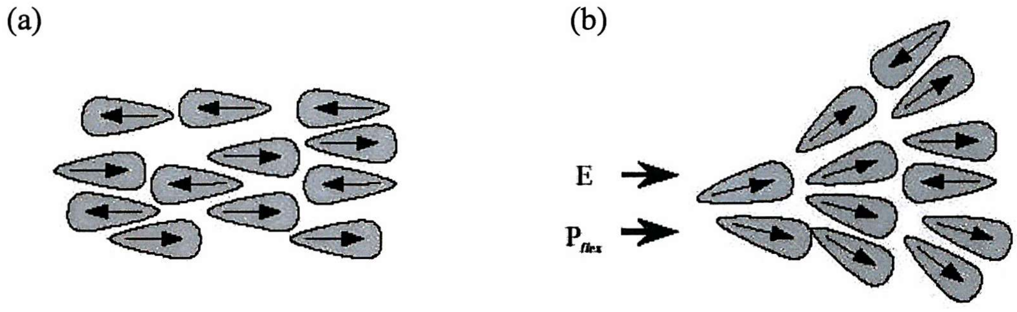

Figure 6.16: Flexoelectrically-induced splay deformation in an LC medium consisting of wedge shape molecules exhibiting a permanent dipole moment parallel to the molecular long axis

(a) in the absence of applied electric field, there is no resulting polarisation

(b) in the presence of a field **E**, there is a macroscopic polarisation $\mathbf{P}_{\mathbf{flexo}}$

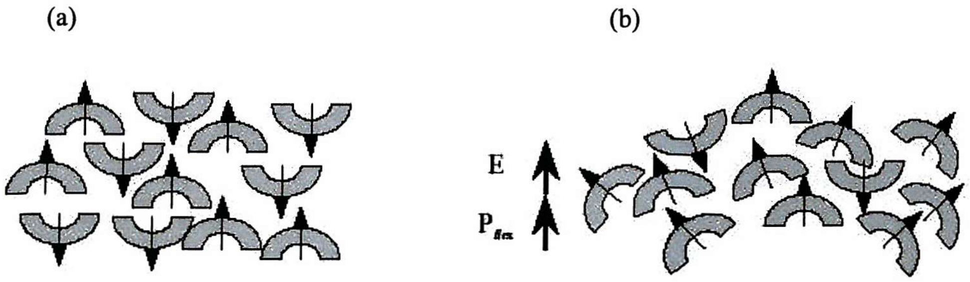

Figure 6.17: Flexoelectrically-induced bend deformation in an LC medium consisting of bent shape molecules with a permanent transverse dipole moment
(a) in the absence of applied electric field, there is no resulting polarisation
(b) in the presence of a field **E**, there is a macroscopic polarisation $\mathbf{P_{flexo}}$.

The flexoelectric switching effect can be observed in short pitch chiral nematic materials using a uniform lying helix configuration and can be considered linear with applied field E for small field amplitudes. In this geometry, the application of an electric field can induce an in-plane rotation of the optic axis,[4] as pictured in Figure 6.18. The rotation angle ϕ can be expressed as:[4, 21, 22]

$$\tan\phi = \frac{eP_0E}{2\pi k}, \qquad \textbf{(6.14)}$$

where P_0 represents the pitch of the helix, $k = (k_{11} + k_{33})/2$ and $e = (e_s + e_b)/2$ are respectively the effective elastic constant and effective flexoelectric coefficient of the chiral nematic phase. k_{11} and e_s are associated with the splay distortion while k_{33} and e_b are related to the bend deformation. The response time τ ($\tau \sim 100\ \mu s$) characteristic of the flexoelectric switching is given by:[22, 23]

$$\tau = \frac{P_0^2\gamma}{4\pi^2 k}, \qquad \textbf{(6.15)}$$

where γ is the effective viscosity coefficient corresponding to the helix distortion. γ is different from the well-known rotational viscosity coefficient γ_1 but is expected to behave in the same way.

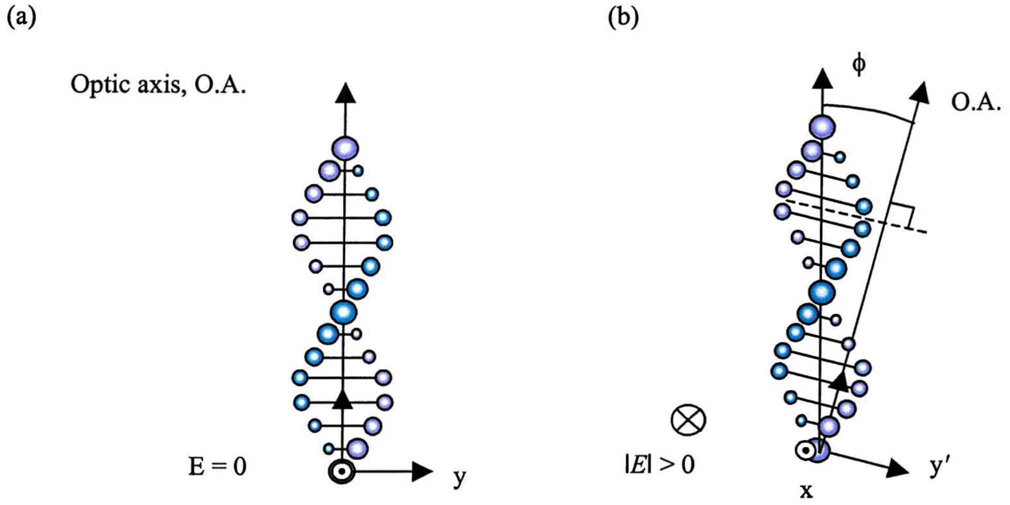

Figure 6.18: Geometry used to study the flexoelectro-optical effect in chiral nematics (taken from reference 11).
(a) without any electric field
(b) in the presence of an electric field

The optimisation of the flexoelectric effect requires short and temperature independent helical pitch, large flexoelectric coefficients, low viscosity coefficients and small dielectric anisotropy.[22] The constraint on dielectric anisotropy arises because the dielectric coupling mechanism, quadratic in applied electric field amplitude, becomes predominant at higher fields and causes the helix to unwind. The critical field associated with helix unwinding is given by:[24]

$$E_C = \frac{\pi^2}{P_0}\left(\frac{k_{22}}{\varepsilon_0 \Delta\varepsilon}\right)^{1/2}, \tag{6.16}$$

where k_{22} is the twist elastic constant and $\Delta\varepsilon$ is the dielectric anisotropy of the material.

The flexoelectric effect in short pitch chiral nematics is promising for display applications since this mode offers many advantages:[10]

- in-plane switching
- wide viewing angles
- continuous grey scale capability
- tilt angle independent of temperature
- very fast response time (~100 μs).

Improved flexoelectric behaviour can be obtained by using symmetric dimer molecules with low molecular dielectric anisotropy.[6] A novel achiral bimesogenic mixture (doped with a suitable chiral agent) can display interesting flexoelectric properties such as rotation angles ϕ of 45° for applied fields of about 9 $V.\mu m^{-1}$.[7]

The flexoelectric coupling and its associated response time are influenced by the Frank splay and bend elastic constants as can be seen in Equations (6.14) and (6.15). The response time of this switching mechanism is proportional to the viscosity coefficient γ. The dielectric coupling depends on the helical pitch, the twist elastic constant and the dielectric anisotropy.

In this section, electro-optic experiments and dynamic light scattering studies were performed on the achiral mixture in order to understand the visco-elastic properties of these dimers. Dielectric anisotropy was also measured on the chiral-induced sample.[25]

6.4.2 *Materials investigated*

Dimers

Novel series of achiral symmetric bimesogens with various spacer lengths have recently been synthesised.[26] Their structure is sketched in Figure 6.19 and their generic formula is given by FFBOnOBFF where n is the number of carbon atoms in the spacer chain.

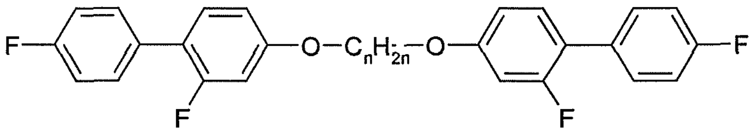

Figure 6.19: Chemical structure of the novel bimesogenic liquid crystal investigated of generic formula FFBOnOBFF.

If the spacer is assumed in its all-*trans* form, the two types of conformers, to be considered in a simple model are the linear and the bent dimers, illustrated in Figure 6.20. In the nematic phase, the first class is predominant among even dimers while the second type is more important among odd dimers, although both types adopt a wide range of conformations due to the flexibility of their spacer.[27] A recent model, based on dielectric relaxation measurements, suggested the necessity to take into account that odd and even symmetric dimers also differ by the shapes of their linear and bent conformers.[28] As a result, dimeric systems usually exhibit strong odd-even effects in their macroscopic properties that reflect these changes in average molecular shape. The bimesogens with an even chain length have higher nematic-to-isotropic transition temperatures[27] and higher elastic constants[5] than the adjacent homologues with an odd number of CH_2 groups.

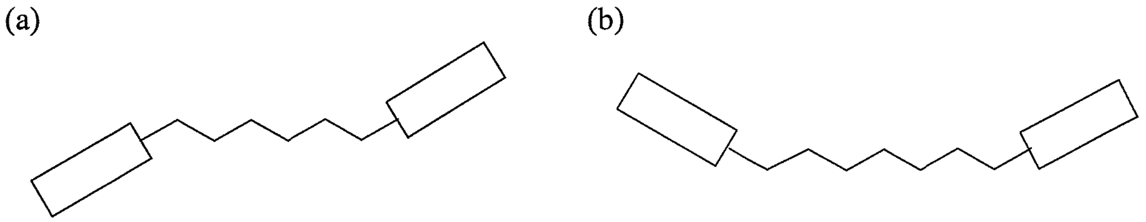

Figure 6.20: Schematic representation of
(a) even dimer (linear)
(b) odd dimer (bent).

Dimers with spacer lengths n = 7 and n = 11, were available for this work. We have prepared and investigated a binary eutectic mixture made of:

- 60% wt FFBO7OBFF
- 40% wt FFBO11OBFF.

In the following, this nematic mixture will denoted BO7/11. The same mixture, doped with 1.5% chiral additive BDH-1281, will be referred to as BO7/11*.

The nematic-to-isotropic transition temperature of each single compound is relatively low (T_{NI} < 80 °C) compared to other dimers reported in the literature.[5, 27, 29] For the eutectic mixture BO7/11, the following transition temperatures were measured using differential scanning calorimetry (DSC):

Cr –30.5 °C **N** 56.4 °C **I.**

However, this mixture crystallises slowly at room temperature.

Dielectric Constant Measurements

These measurements were performed on the chiral mixture BO7/11*. The clearing point for this sample was measured to be 55.5 °C.

Figure 6.21 and Figure 6.22 show respectively the static dielectric permittivties and the dielectric anisotropy Δε as a function of shifted temperature T_{NI}-T for this sample.

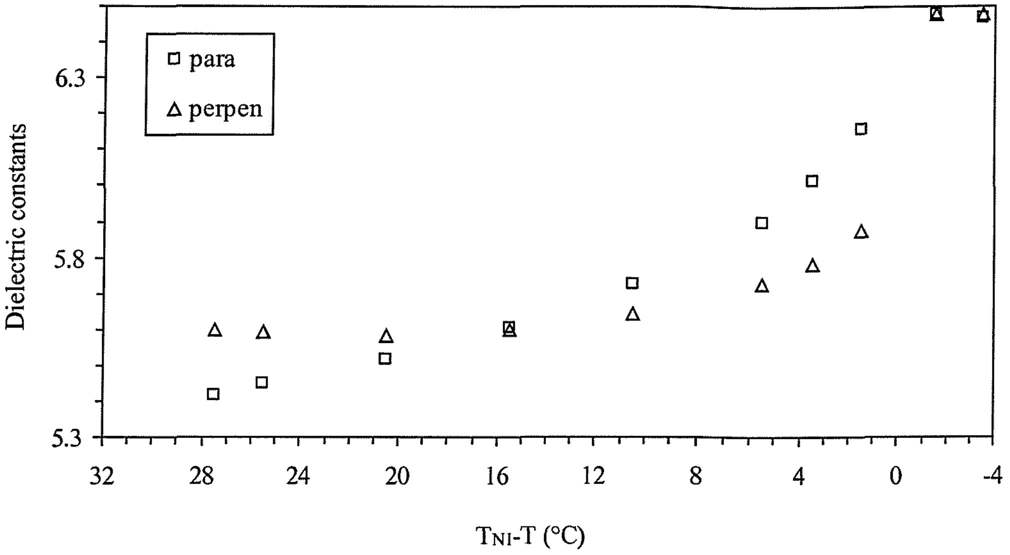

Figure 6.21: Dielectric constants $\epsilon_{\|}$ and $\epsilon_{\perp}$ (± 0.5%) versus shifted temperature for BO7/11* (data obtained at 10kHz with a 6μm planar cell).

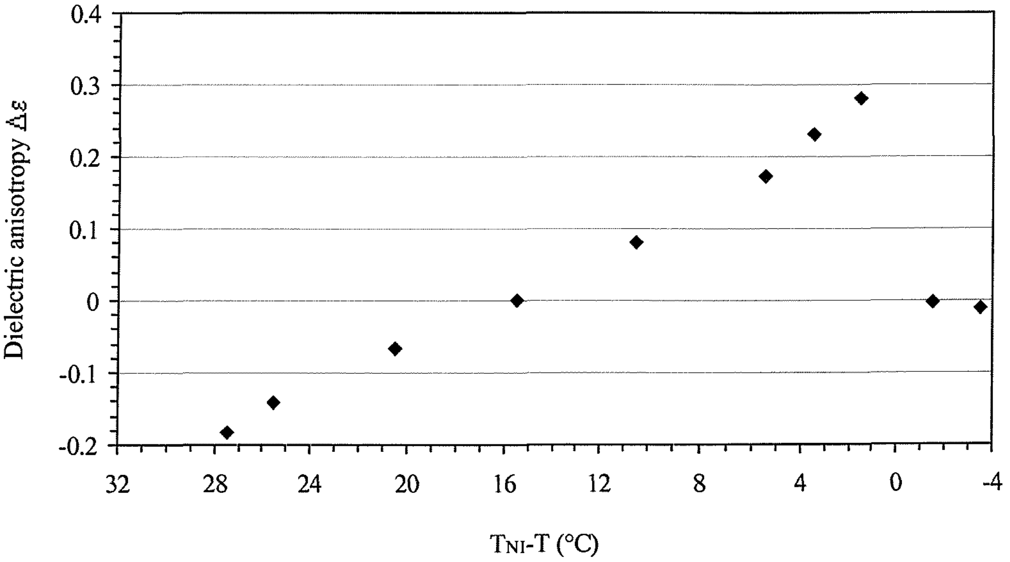

Figure 6.22: Dielectric anisotropy Δε against shifted temperature for BO7/11*.

The dielectric constant in the isotropic phase ϵ_{iso} is larger than both $\varepsilon_{\|}$ and $\varepsilon_{\perp}$ in the nematic phase. $\Delta\varepsilon = \varepsilon_{\|} - \varepsilon_{\perp}$ decreases almost linearly with decreasing temperature and changes sign at T_{NI}-T = 15.5 °C. Its values are rather low and vary between –0.2 and 0.3. For bimesogens with a flexible spacer, changes in the conformational distribution may explain the evolution of Δε against temperature.[27, 30] Dielectric studies have been performed on CBOnOCB, with n=10[30] and n=11[28], which is a homologous series of symmetrical dimers, based on the cyanobiphenyl mesogenic core. The generic structure of this compound is illustrated in Figure 6.23 and closely resembles the FFBOnOBFF dimer. For n=10, the static dielectric constant decreases when the dimer is cooled from the isotropic to the nematic phase, as observed for our sample. For n=11, an increase of the static permittivity is first noticed at T_{NI} and then its value decreases as the temperature is lowered. For both dimers, this can be understood as a random coil distribution adopted by the spacer in the isotropic phase, which allows a variety of possible orientations for the mesogenic terminal groups, resulting in higher values of permittivities. In the nematic phase, the reduction in dielectric constant is due to the dimer exhibiting a more extended shape. CBOnOCB with n=10 and n=11 exhibit positive Δε ranging approximately from 1 to 1.7 and 1.5 to 2.3 respectively.

For our bimesogens FFBOnOBFF, the energy ground state of the nematic phase is associated with the bent conformers. Thus, as the temperature is decreased well into the nematic phase, the population of bent conformers augment resulting in $\Delta\varepsilon < 0$ at lower temperatures.[27]

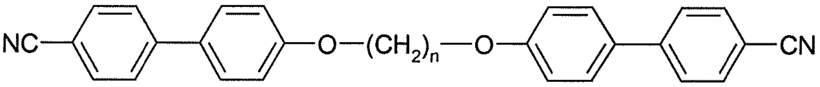

Figure 6.23: Structure of the α, ω-bis[(4-cyanobiphenyl)-4'-yloxy]alkanes dimers, referred to as CBOnOCB.

Similar temperature dependence of the dielectric anisotropy was found in the commercial chiral mixture TM216;[10] Δε is positive above 31 °C and becomes negative below this critical temperature. In TM216, $-0.11 < \Delta\varepsilon < 0.08$ was measured in the temperature range T = 28 °C-39 °C. These values are of the same order of magnitude as those obtained for our sample BO7/11*. However, the rotation angles ϕ that have been measured in TM216 are much lower and require much higher fields than our materials: in the former instance, [10] $\phi \approx 30°$ obtained with applied fields of 120 V.μm^{-1} whereas for our chiral-doped mixture[7] BO7/11*, $\phi > 45°$ at E = 10 V.μm^{-1}.

The increase of Δε with temperature and the fact that it is positive near the chiral nematic-to-isotropic transition is an advantage for the flexoelectric effect. As explained in Section 6.2.2, the sample is aligned on cooling and a good lying helix texture alignment can be obtained just below the clearing point (when $\Delta\varepsilon > 0$) by applying an electric field. At lower temperatures, for which $\Delta\varepsilon \approx 0$, large tilt angles can be measured at higher fields. Nevertheless, negative dielectric anisotropy is a drawback because the application of an electric field will cause a realignment of the helix in the Grandjean texture.

6.4.3 Electro-optic experiments

This method uses the dielectric coupling to an external electric field to induce a reorientation of the molecules. Experimentally, voltages up to 130 V rms were applied to a planar aligned cell of thickness 44.7 μm filled with the achiral mixture BO7/11 in the temperature range 35 °C-50 °C. For this sample, the crossover temperature was found to be 42.6 °C, which corresponds to 13.8 °C on a shifted temperature scale. These values agree quite well with the data obtained from dielectric experiments on the chiral-doped mixture BO7/11*: $\Delta\varepsilon$ changes sign at about 40 °C i.e. at T_{NI}-T = 15.5 °C.

Even for $\Delta\varepsilon > 0$, Freedericksz transition did not occur in BO7/11; instead Williams domains started to appear at a certain threshold voltage V_{th}. Stationary Williams domains are electrohydrodynamic distortions arising from the coupling between a low frequency ac field and the anisotropy of electrical conductivity.[19] Though these effects are generally associated with materials of negative dielectric anisotropy, they can also occur in weakly positive nematics if the applied field is perpendicular to the initial director alignment.[19] V_{th} is almost independent of the frequency of applied field in the range 100 Hz-10 kHz investigated. The evolution of the Williams domains as a function of applied rms voltage can be seen in Figure 6.24. At higher fields, the domains disappear but no Freedericksz transition from planar to homeotropic orientation was observed.

When $\Delta\varepsilon < 0$, at similar frequencies, the effect of the field was to align the sample and to suppress any disclinations or defects present in the cell. No Williams domains are formed at maximum applied voltages of 130 V rms.

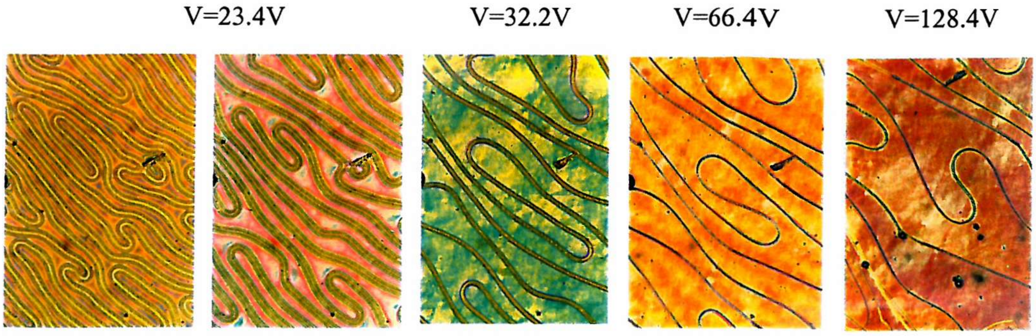

Figure 6.24: Williams domains observed between crossed polarisers (director initially at 45°) with an ac square wave signal of 1 kHz at T = 45 °C at different voltages for BO7/11.

6.4.4 Dynamic Light Scattering: bend visco-elastic ratio

DLS experiments were performed using a 10 μm thick planar cell filled with the achiral bimesogen mixture BO7/11. For pure bend fluctuations, the linewidth obtained with mode 1 or 2 is given by:

$$\Gamma_{1,2} = k_{33} q_{\parallel}^{2} / \eta_{\text{bend}}, \qquad \textbf{(6.17)}$$

where η_{bend} is the bend viscosity coefficient and $q_{\parallel}$ is the component of the scattering wavevector **q** parallel to the nematic director $\mathbf{n_0}$. The scattering plane is defined as ($\mathbf{n_0}$, **q**). The initial director orientation is planar and perpendicular to the incident beam.

As discussed in Chapter 2, Section 2.7.2, there are two possible scattering geometries to determine the pure bend contributions to mode 1 or mode 2. Dimers are analogous to oligomeric or polymeric systems, which exhibit much higher viscosity coefficients than low-molar mass mesogens, resulting in lower visco-elastic ratios and linewidths. Since $\Gamma_{1,2} \propto \sin^2\theta_{\text{lab}}$, the linewidth also decreases with scattering angles. In mode 1, at $\theta_{\text{lab}} = 10°$, the measured frequency broadening Γ_1 associated with pure bend fluctuations is found to be about 20 Hz at T = 34 °C for BO7/11 (see Table 6.5). At such low linewidths, the mechanical and electrical noise becomes significant and distorts the scattered light correlation function, resulting in inaccurate evaluation of the linewidths.[31]

Mode 2 geometry with VH polarisations was chosen for this measurement. In this case, the use of crossed polarisers offers the advantage that the noise factor and the experimental uncertainty on the visco-elastic ratios are reduced compared to a parallel polariser configuration in mode 1, as reported in Table 6.5. In this case, the autocorrelation function decays as a single exponential and the bend mode can be isolated at a certain scattering angle θ_{LC} that is dependent solely on the refractive indices n_e and n_o of the material:

$$\theta_{LC} = \cos^{-1}\left(\frac{n_e}{(2n_e^2 - n_o^2)^{1/2}}\right). \qquad \textbf{(6.18)}$$

The measurement of refractive indices by Abbé refractometry requires homeotropic alignment of the liquid crystalline sample and could not be performed on the bimesogenic mixture BO7/11, since only planar orientation could be achieved with this material. θ_{LC} was deduced from the linewidth, measured by DLS, for a wide range of scattering angles θ_{lab}: at θ_{LC}, the autocorrelation function should be a single exponential. The values for θ_{LC} decrease with increasing temperature and are found to be between 26°-29° for a temperature range of 28 °C-54 °C. For instance, at $\theta_{lab} = 27.5°$, the experimental linewidth Γ_{bend} for the pure bend mode is 148.1 Hz (refer to Table 6.5).

Scattering geometry	Noise factor	Linewidth (Hz)	Visco-elastic ratio (10^{-12} $m^2.s^{-1}$)
Mode 1 (E-E, $\theta_{lab} = 10°$)	0.054%	18.5	6.2
Mode 2 (O-E, $\theta_{lab} = 27.5°$)	0.023%	148.1	7.1

Table 6.5: Comparison of the noise factor, linewidth and visco-elastic ratio measured in the two scattering geometries available to study the pure bend fluctuations for the mixture BO7/11 at T = 34 °C after averaging 25 runs of 40s each.

For nematic liquid crystals with $\Delta\varepsilon < 0$, it is possible in principle to deconvolute the bend visco-elastic ratio k_{33}/η_{bend} by applying an electric field **E** normal to the director planar orientation. In this configuration represented in Figure 6.25, **E** lies within the scattering plane defined by ($\mathbf{n}_o$, $\hat{\mathbf{e}}_1$). Since **E** is always normal to ($\mathbf{n}_o$, $\hat{\mathbf{e}}_2$), no quenching of the bend fluctuations will occur in mode 2. The electric field must be applied using mode 1 geometry to observe a dampening of the director bend distortions. Martinand and Durand studied a material with negative dielectric anisotropy, namely MBBA, by dynamic light scattering in the presence of a stabilising ac electric field using mode 1 conditions.[32] The authors were able to deduce values for the bend elastic constant and viscosity coefficient k_{33} and η_{bend} from the following equation:

$$\Gamma_1 = \frac{K_{33}}{\eta_{bend}} q_{\|}^2 + \frac{(-\Delta\varepsilon)\,\varepsilon_{\perp}}{4\pi\varepsilon_{\|}\eta_{bend}} E^2. \qquad \textbf{(6.19)}$$

For BO7/11, when $\Delta\varepsilon < 0$, no damping of the scattered light intensity could be observed in mode 2 as expected. Using mode 1, the application of electric fields of up to 10 $V.\mu m^{-1}$ are still insufficient to dampen the director fluctuations since the intrinsic dielectric anisotropy of the dimers is rather low.

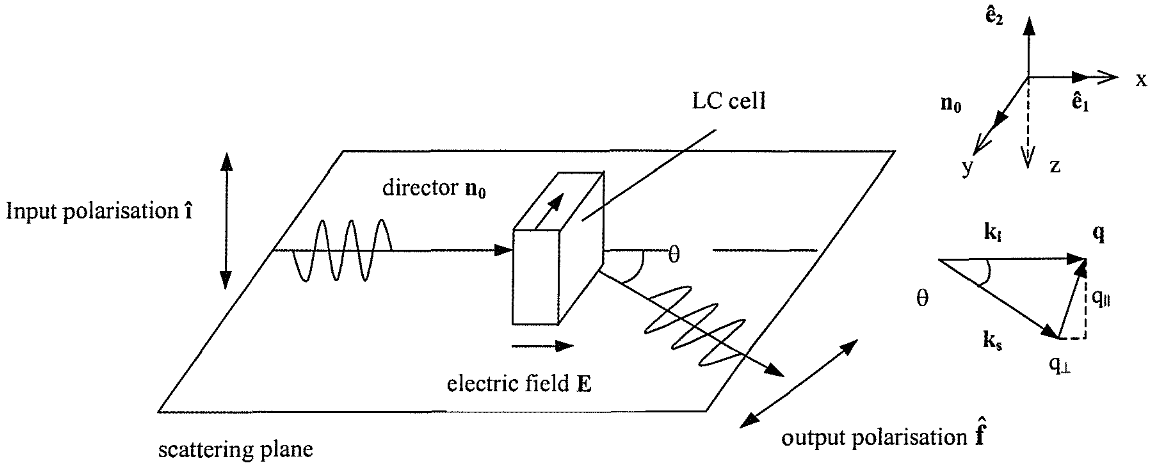

Figure 6.25: Mode 1 scattering geometry for the study of pure bend distortions in the presence of an electric field for material with $\Delta\varepsilon < 0$.

Figure 6.26 shows the ratio of bend elastic constant to viscosity coefficient k_{33}/η_{bend} on a logarithmic scale as a function of shifted temperature for BO7/11. In this system, k_{33}/η_{bend} is reduced by almost a factor ten on cooling the mixture to 30 °C below the N-I transition. The values of the bend visco-elastic ratio of this sample are decreased by about an order of magnitude compared to low molar mass mesogens; for instance, for 5CB, $k_{33}/\eta_{bend} = 5.10^{-10}\ m^2.s^{-1}$ measured at T_{NI}-T = 10 °C (see Chapter 5, Section 5.7).

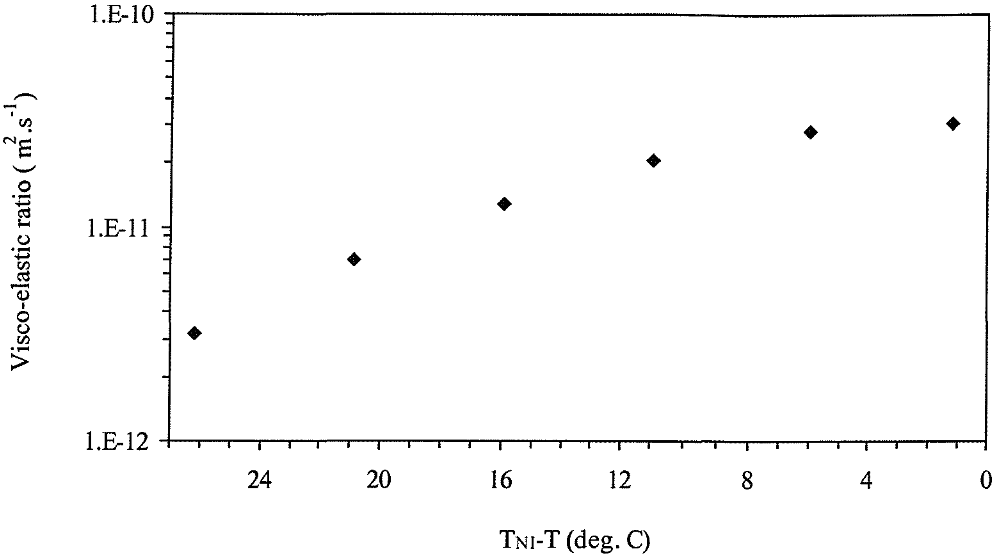

Figure 6.26: Bend visco-elastic ratio k_{33}/η_{bend} (± 5%) against T_{NI}-T.

DiLisi *et al.* measured the splay, twist and bend visco-elastic constants of a series of achiral dimers based on the monomer unit labelled 5005 and containing n = 10 and n = 9 where n is the number of carbon atoms in the space chain.[29, 33] The structure of the even dimer is pictured in Figure 6.27. The degree of flexibility of the spacer linking the two monomers was shown to have a major influence on the visco-elastic parameters. Values of bend visco-elastic data are given in Table 6.6 for our bimesogenic mixture as well as for the monomer and both even and odd dimers examined by DiLisi *et al.*.[29, 33]

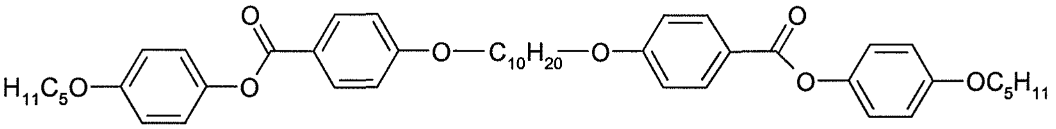

Figure 6.27: Molecular structure of the even dimer containing two monomer units 5005.[33]

Materials	T_{NI}-T (°C)	k_{33}/η_{bend} (m^2.s^{-1})	k_{33} (x10^{-12}N)	η_{bend} (Pa.s)
5005 monomer	10	$5.8\text{x}10^{-10}$	7	0.012
5005 even dimer	10	$1.1\text{x}10^{-10}$	11	0.1
5005 odd dimer	10	$3.9\text{x}10^{-11}$	4.7	0.12
BO7/11	10.9	$2.0\text{x}10^{-11}$	N/A	N/A

Table 6.6: Values of bend visco-elastic data extracted from published data for the 5005 samples[29, 33] and measured for the new bimesogens.

The bend visco-elastic ratio of our sample is of the same order of magnitude as for the 5005 odd dimer. In the case of the odd dimer, the bend elastic constant k_{33} is just less than half that of the even dimer and less than that of the 5005 monomer; this may be explained by the fact that the odd dimer will tend to adopt a bent shape in the all-trans conformation.[27, 29] Theoretical models[34, 35] also predicted a reduction in the bend elastic constant with respect to the monomer for odd dimers due to their bent conformation. The bend viscosity of the 5005 dimers is an order of magnitude greater than for the 5005 monomer. By analogy with other dimeric or polymeric systems, k_{33}/η_{bend} would be dominated by a larger increase in the bend viscosity coefficient than in the elastic constant for the mixture BO7/11.

The splay elastic constant k_{11} can be obtained from the threshold voltage V_{th} in the splay Freedericksz transition configuration in the following way (see Chapter 2, Equation (2.40)):

$$k_{11} = \frac{V_{th}^2}{\pi^2}\varepsilon_0\Delta\varepsilon . \tag{6.20}$$

For instance, the splay elastic constant k_{11} was measured for a homologous series of dimers CBOnOCB[5], based on the cyanobiphenyl mesogenic core, sketched in Figure 6.23. The dependence of k_{11} on n shows a clear odd-even effect and for instance, its values are respectively 11.1 pN and 14.3 pN for $n = 9$ and $n = 10$ at the same reduced temperature $T/T_{NI} = 0.943$[5] (this corresponds to $T\text{-}T_{NI}$ of 25.6 °C and 26.2 °C).

In chiral systems, the response time for flexoelectrically controlled switching can be evaluated from Equation (6.15). A similar mixture of bimesogens, doped with 3% BDH-1281 was investigated.[7] The pitch of the mixture was $P_0 \approx 0.9$ µm. If we assume that the bend visco-elastic ratio in the achiral mixture has the same order of magnitude as the chiral-doped sample i.e.

$$\frac{k_{33}}{\eta_{bend}} \approx \frac{k}{\gamma}, \tag{6.21}$$

and using Equation (6.15), the response time τ is calculated to be about 1 ms at $T_{NI}\text{-}T = 10.9$ °C. Considering the approximations made, this is in good agreement with the direct value measured by electro-optical experiments; at a shifted temperature of 12°C, τ was found to be between 2 and 4 ms depending on the electric field amplitude.[7]

6.4.5 Summary

In this section, results from dielectric, electro-optic and dynamic light scattering measurements are reported for a mixture of bimesogenic molecules. The dielectric anisotropy $\Delta\varepsilon$, measured on the chiral-doped sample, changes sign with temperature and its values range between –0.2 and 0.3 over a 28 °C temperature range. For $\Delta\varepsilon$ weakly positive, no electric field Freedericksz transition could be induced but Williams domains are observed instead. The bend elastic constant to viscosity coefficient ratio increases from 3.2×10^{-12} to 3.1×10^{-11} $m^2.s^{-1}$ as the temperature increases by 26 °C. This significant augmentation may be attributed to a larger reduction in the bend viscosity coefficient than in the corresponding elastic constant at higher temperatures. Further work is necessary to determine directly the visco-elastic parameters of these novel dimers.

6.5 Conclusion

In this chapter, novel types of liquid crystalline compounds were investigated:

- Materials with dual-frequency behaviour
- Bimesogens with improved flexoelectric properties.

The fluorinated-substituted ester 5PFP5 has a crossover frequency f_c as low as 40 kHz. The value of f_c can be further reduced down to about 10 kHz by adding this compound to the host mixture MDA-00-984 at concentration above 15% to retain its “dual-frequency” property. At the same time, the resulting mixture has a better operating nematic phase range. In particular, mixtures containing between 20% and 50% 5PFP5 would be suitable for “dual-frequency” addressed devices since these offer low crossover frequency combined with room temperature operation.

The novel bimesogenic materials present promising features for the flexoelectric effect in chiral nematics. The dielectric anisotropy of the mixture examined is low and exhibits a sign reversal with temperature. For practical applications, it would be more interesting to synthesise new dimers with good flexoelectric properties and with a low dielectric anisotropy that changes sign depending on the frequency of applied field.

Although their molecular structure is completely different, the “dual-frequency” materials and the bimesogens present some similarities. In both cases, the physical parameter to consider is the dielectric anisotropy $\Delta\varepsilon$, which exhibits a sign reversal as a function of frequency or of temperature. As a result, $\Delta\varepsilon$ is found to be close to zero in some specific conditions and William domains may occur for weakly positive or negative values. These instabilities have also been observed in "dual-frequency" compounds, such as in the phenylbenzoates studied by De Jeu *et al.*[36]. However, in the first case, high values of $\Delta\varepsilon$ are required in order to decrease the threshold voltage and a display using dual-frequency addressing scheme should operate using both frequencies with positive and negative $\Delta\varepsilon$. While, in the second example, the dielectric anisotropy should be minimised and only positive $\Delta\varepsilon$ regime can be used for the flexoelectro-optic effect in chiral nematics to ensure the helix stays in-plane.

REFERENCES

[1] Schadt M., *Mol. Cryst. Liq. Cryst.*, **89**, pp. 77-92 (1982)

[2] Bücher H. K., Klingbiel R. T. and VanMeter J. P., *Appl. Phys. Lett.*, **25(4)**, pp. 186-188 (1974)

[3] Haase W. and Poetzsch D., *Mol. Cryst. Liq. Cryst.*, **38**, pp. 77-85 (1977)

[4] Patel J. S. and Meyer R. B., *Phys. Rev. Lett.*, **58**, pp. 1538-1540 (1987)

[5] Tsvetkov N. V., Zuev V. V., Ksenofontov I. V. and Tsvetkov V. N., *Liq. Cryst.*, **25(6)**, pp. 727-732 (1998)

[6] Coles H. J., Musgrave B., Coles M. J. and Willmott J., *J. Mater. Chem.*, **11**, pp. 2709-2716 (2001)

[7] Musgrave B., Coles M. J., Perkins S. P. and Coles H. J., *Mol. Cryst. Liq. Cryst.*, Proceedings for ILCC Sendai 2000, **366**, pp. 735-742 (2001)

[8] de Jeu W. H., Chapter 2 in *Physical Properties of Liquid Crystalline Materials*, Gordon and Breach, New-York (1980)

[9] Goodby J. W., *Practical Microscopy of Liquid Crystals*, Annual Hull Workshop (1997)

[10] Rudquist P., Buivydas M., Komitov L. and Lagerwall S. T., *J. Appl. Phys.*, **76**, pp. 7778-7783 (1994)

[11] Musgrave B., *Electro-Optic Studies of the Flexoelectric Effect in Chiral Nematic Liquid Crystals*, PhD Thesis, University of Southampton (2000)

[12] Merck datasheet

[13] Kresse H., Chapter 3 in the *Handbook of Liquid Crystals*, **2A**, pp. 91-112, edited by Demus D., Goodby J., Gray G. W., Spiess H.-W. and Vill V., Wiley-VCH, New-York (1998)

[14] Blinov L. M., Chapter 2 in *Electro-Optical and Magneto-Optical Properties of Liquid Crystals*, John Wiley and Sons Ltd, Chichester (1983)

[15] de Jeu W. H. and Lathouwers Th. W, *Mol. Cryst. Liq. Cryst.*, **26**, pp. 225-234 (1973)

[16] Noot C., PhD Thesis, *in preparation*, University of Southampton (2002)

[17] Hirschmann H. and Reiffenrath V., Chapter 3 in the *Handbook of Liquid Crystals*, **2A**, pp. 199-229, edited by Demus D., Goodby J., Gray G. W., Spiess H-W. and Vill V., Wiley-VCH, New-York (1998)

[18] Meyer R. B., *Phys. Rev. Lett.*, **22(18)**, pp. 918-921 (1969)

[19] Chandrasekhar S., Chapter 3 in *Liquid Crystals*, Second edition, Cambridge University Press (1994)

[20] Prost J. and Marcerou J. P., *J. Physique*, **38**, pp. 315-324 (1977)

[21] Komitov L., Lagerwall S. T., Stebler B. and Strigazzi A., *J. Appl. Phys.*, **76(6)**, pp. 3762-3768 (1994)

[22] Musgrave B., Lehmann P. and Coles H. J., *Liq. Cryst.*, **26(8)**, pp. 1235-1249 (1999)

[23] Patel J. S. and Lee S-D, *J. Appl. Phys.*, **66(4)**, pp. 1879-1881 (1989)

[24] de Gennes P. G., *Sol. State Comm.*, **6**, pp. 163-165 (1968)

[25] Schott C., Perkins S. P. and Coles H. J., *Mol. Cryst. Liq. Cryst.*, Proceedings for ILCC Sendai 2000, **366**, pp. 715-724 (2001)

[26] Coles H. J., Coles M. J., Perkins S., Musgrave B. and Coates D., *EU Patent EP 9911 9114.9.*, filed 4/10/99

[27] Imrie C. T. and Luckhurst G. R., Chapter 10 in the *Handbook of Liquid Crystals*, **2B**, pp. 801-833, edited by Demus D., Goodby J., Gray G. W., Spiess H.-W. and Vill V., Wiley-VCH, New-York (1998)

[28] Dunmur D. A., Luckhurst G. R., de la Fuente M. R., Diez S. and Perez Jubindo M. A., *J. Chem. Phys.*, **115**, pp. 8681-8691 (2001)

[29] DiLisi G. A., Terentjev E. M., Griffin A. C. and Rosenblatt C., *J. Phys. II*, **3**, pp. 597-602 (1993)

[30] Bauman D., Wolarz E. and Bialecka-Florjanczyk, *Liq. Cryst.*, **26**, pp. 45-49 (1999)

[31] Birtwistle P. J. R., *Dynamic Light Scattering from Liquid Crystalline Systems,* PhD Thesis, University of Manchester (1995)

[32] Martinand J. L. and Durand G., *Sol. State Comm.*, **10**, pp. 815 (1972)

[33] DiLisi G. A., Rosenblatt C., Griffin A. C. and Hari U., *Phys. Rev. A*, **45**, pp. 5738-5745 (1992)

[34] Helfrich W., *Mol. Cryst. Liq. Cryst.*, **26**, pp. 1-5 (1973)

[35] Gruler H., *J. Chem. Phys.*, **61(12)**, pp. 5408-5412 (1974)

[36] de Jeu W. H. and Lathouwers Th. W, *Mol. Cryst. Liq. Cryst.*, **26**, pp. 235-243 (1973)

CHAPTER 7: CONCLUSION AND FUTURE WORK

7.1 Summary of the thesis

In the course of this work, the visco-elastic behaviour of different nematic LC materials was investigated using two complementary techniques, dynamic light scattering (DLS) and Freedericksz transition (FT). The current investigation using these two methods has highlighted the following points:

(a) The DLS apparatus has to be carefully aligned and calibrated prior to any experimental run. The use of heterodyne detection, while it is complicated to implement experimentally, is advantageous in terms of the calculation of the autocorrelation function and in order to suppress any static scattering signal due to impurities or glass flares. DLS in the presence of an external field can yield separately the viscosity coefficients and the elastic constants of splay and twist. The scattering geometry required to isolate either mode employs homeotropic cells and low scattering angles (for instance $\theta_{lab} = 14°$).

(b) The DLS technique was applied to a wide variety of nematic systems including, for the first time, dye guest-host mixtures. The twist viscosities measured ranged from 0.018 Pa.s for non-polar mixtures to 0.15-0.2 Pa.s for dimers[1] at similar shifted temperatures of 10 °C. The twist and splay elastic constants varied respectively from 3 to 4 pN and from 5 to 6.5 pN at T_{NI}-T = 10 °C for most materials investigated in this thesis.

(c) For materials with high or medium birefringence, the value of twist and splay viscosities and associated elastic constants can be measured within 5% accuracy by DLS experiments; while for nematic samples with low birefringence ($\Delta n < 0.05$), these visco-elastic parameters are determined with a relative uncertainty of about 10%.

(d) The field-induced Freedericksz transition can be used routinely to measure accurately all three elastic constants. In this work, only measurements of the bend elastic constant k_{33} have been carried out with this technique (to an accuracy of 5%) since k_{11} and k_{22} can be determined by DLS in the presence of an electric field.

(e) The main limitation with the current DLS spectrometer is the restriction in scattering angles which prohibits the investigation of the pure bend mode at large angles. Preliminary measurements have been performed using two geometries based on mode 1 and mode 2, as described in Table 7.1. The bend visco-elastic ratios measured for 5CB using mode 1 are systematically 10 to 20% lower than values reported in the literature. This is due to the contributions from other modes to the measured linewidth. Therefore whenever possible, it is preferable to employ the mode 2 configuration with crossed polarisers and larger scattering angles.

Mode 2	Mode 1
VH polarisations $\theta_{LC}^{bend} = \cos^{-1}(n_o / n(\theta_{LC}))$	HH polarisations scattering angles $\theta_{LC} < 15°$

Table 7.1: Configurations available for the study of the pure bend mode in planar cells.

(f) In DLS experiments using the bend geometry, no electric field was applied to dampen the director fluctuations for $\Delta\varepsilon > 0$ materials, since this method necessitates transverse electrodes, which were not available in the course of this work. The data for k_{33} from Freedericksz transition experiments were used in order to derive the bend viscosity from the visco-elastic ratio.

(g) The optical Freedericksz transition occurs in thick planar cells ($d \approx 40$ μm) containing anthraquinone DGH samples when attempts are made to employ mode 1 (with horizontal input polarisation) to measure the bend visco-elastic ratio. The phase difference produced by the reorientation of the LC molecules causes interference rings in the scattered optical signal, which results in a distorted autocorrelation function of the intensity and in inaccurate linewidth. This effect is suppressed in thin cells ($d \approx 6$ μm) of DGH mixtures but in this case, the values of

k_{33}/η_{bend} for 5CB are further reduced compared to the values measured in thick samples.

The main difficulty experienced with materials such as the bimesogens or the phenyl benzoate 5PFP5 concerns the achievement of homeotropic alignment. Consequently, the measurements of dielectric constants have been carried out on chiral-doped samples in two geometries, the Grandjean texture or standing helix and the uniformly lying helix configuration. This method makes it possible to extrapolate to within 10% uncertainty, the value $\Delta\varepsilon$ for the achiral mixture.

The results obtained with the nematic materials studied in this thesis are recapitulated below:

(a) Mixtures of different chemical nature, based on cyanobiphenyls, phenylbenzoates and dicyclohexyls respectively, exhibit comparable twist and splay elastic constants at the same shifted temperature; this confirms that the ratio k_{22}/k_{11} is remarkably constant for most nematic LCs and has been found to vary from 0.55 to 0.63 in this work. The birefringence, dielectric anisotropy and rotational viscosity, which characterise each mixture, are dependent on the chemical composition of the sample.

(b) Four dopants, 5PCP, 5OPCP, 5CB and 5OCB, dissolved in ZLI-4792 (13% mol concentration) were investigated to examine the influence of the presence of guest molecules on the twist visco-elastic properties of the nematic host mixture. The two non-mesogenic additives 5PCP and 5OPCP cause a greater depression of the nematic-isotropic transition temperature than 5CB and 5OCB, which both possess a nematic phase. This study shows the importance of the temperature scale used to interpret the results. For the twist elastic constant, the shifted temperature scale is more appropriate since k_{22} varies as the squared order parameter S^2; in this case, k_{22} is slightly decreased upon the addition of 5(O)CB and this effect is more pronounced for 5(O)PCP, causing a 20% reduction. For the twist viscosity, when plotted versus temperature, γ_1 is reduced by up to 30% upon the addition of 5PCP; whereas on a relative temperature scale, the presence of 5(O)CB and 5(O)PCP produce a sharp rise in γ_1 of about 45% and 180% respectively.

(c) Measurements of visco-elastic properties were performed for two series of dye guest-host mixtures, containing 1% to 3% non-polar azo and anthraquinone dyes in 5CB. The addition of either dye results in an increase in clearing point of the host material while the dielectric anisotropy, birefringence and order parameter remain unchanged. The presence of azo or anthraquinone dye does not affect the splay and twist elastic constants or viscosity coefficients of the host material on a shifted temperature scale, while a small increase is observed at the same standard temperature. By contrast, the bend elastic constant and associated viscosity are reduced by about 10% for the sample containing 3% anthraquinone dye, compared with pure 5CB. The dye order parameter S_{Tcorr} is strongly related to S_{LC}, the orientational order parameter of the host, and is found to be similar for both types of dyes; $S_{Tcorr} = 0.566$ and 0.536 for the azo and anthraquinone doped mixtures at T_{NI}-T = 8.8 °C. Both dyes also show damped thermal fluctuations relative to the LC host molecules.

(d) Mixtures of different concentrations of the "dual-frequency" material 5PFP5 in a nematic host mixture MDA-00-984 have been investigated. The host is characterised by values of $\Delta\varepsilon$ between –0.8 and –0.3 and an average birefringence of 0.125. The phenyl benzoate compound 5PFP5 has a nematic phase from 52.6 °C to 164.7 °C. Mixtures containing 15% or more of 5PFP5 possess "dual-frequency" behaviour with cross-over frequencies less than 20 kHz at temperatures far below T_{NI}; the activation energies range from 0.5 and 1 eV depending on the concentration.

(e) The dielectric anisotropy and bend visco-elastic ratio have been measured respectively for the chiral-doped and on the achiral mixture of difluorobiphenyl bimesogens BO7/11. $\Delta\varepsilon$ changes sign as a function of temperature and varies from approximately -0.2 to 0.3. The visco-elastic ratio k_{33}/η_{bend} is reduced by an order of magnitude when the temperature is decreased by 30 °C into the nematic phase. This may be attributed to a greater augmentation of the viscosity compared to the elastic constant upon cooling of the sample. No Freedericksz transition from planar to homeotropic could be induced by applying electric fields up to 130 V rms in the frequency range 100 Hz-10 kHz and instead Williams domains are formed.

Several phenomenological models have been developed to account for the temperature dependence of visco-elastic parameters in nematic liquid crystals; this thesis emphasises that these models should be used cautiously since they are influenced by the temperature range considered and also by the method used to derive the order parameter (for instance Haller's extrapolation technique).

In the next section, we will explain how the apparatus will be modified towards greater flexibility, simplified alignment procedure and complete automation; we will also show the recent progress in the synthesis/characterisation of novel bimesogens and in the investigation of the flexoelectric effect in DGH systems.

7.2 Future developments

7.2.1 Modification of the light scattering apparatus

As highlighted in the course of this work, the current DLS experiment is particularly suitable for measurements of the splay and twist visco-elastic constants at low scattering angles for materials with positive dielectric anisotropy. However, the range of available collection angles are limited to −13° to +40° due to the design of sample holder employed; in particular, this prohibits measurements of the bend visco-elastic coefficients at larger angles using planar cells.

There are several advantages in optimising the current DLS apparatus for the scattering geometries based on planar-aligned LC samples. First, they generally scatter light more significantly than homeotropic oriented materials and consequently shorter integration times are needed. As discussed in Chapter 2, the splay and bend modes can be isolated using planar cells and crossed polarisers at larger scattering angles, dependent on the refractive indices of the LC material; this configuration eliminates stray signal and yields more accurate results.

Another reason is that the dimers only align in a planar configuration and consequently very few visco-elastic parameters can be determined by dynamic light scattering or Freedericksz transition. The application of a damping electric field to separate the visco-elastic ratios is difficult because most of the difluorobiphenyl dimers investigated have low and positive dielectric anisotropy $\Delta\varepsilon$; the situation is further complicated if $\Delta\varepsilon$

changes sign as a function of temperature, as was observed for the BO7/11 mixture. Static light scattering may be employed as a complementary tool in order to measure the three elastic constants for the novel bimesogens in specific geometries. The main drawback of this method is that it requires absolute values of scattered light intensity[2] and multiple scattering problems may occur. It was shown that this technique combined with DLS allows the determination of the three elastic constants and of five of the independent Leslie viscosity coefficients for 5CB.[3]

The DLS spectrometer is currently being rebuilt as a multi-purpose light scattering apparatus, which will enable static and dynamic measurements, heterodyne and homodyne detection, low and large collection angles.[4] In addition, the new rig should also be adaptable enough to perform other experiments, such as two colour DLS and diffusive wave spectroscopy. Two colour DLS is a particular type of cross-correlation using two lasers of different wavelengths to study the same spatial Fourier component in weakly turbid materials;[5] this technique removes the errors in the detection process due to non-linearities and multiple scattering, which occur in thick samples of nematic LCs. Diffusive wave spectroscopy can be applied in highly scattering media to calculate the diffusion constants and transport mean free path.[6]

The novel features of the light scattering spectrometer are:

- two input and two detection arms for cross-correlation experiments;
- use of optical fibres to simplify the alignment procedure.

The new design of the apparatus is shown in Figure 7.1. The sample holder, illustrated in Figure 7.2, will be modified to satisfy the requirement for low and large scattering angles.[4] It can also be used in conjunction with optical fibres and includes an inner sample chamber, which can accommodate different types of cells (e. g. capillaries). Both types of cell holders contain index matching fluid which is in direct contact with the chamber's brass wall and thus can be heated via nichrome wires.

In the future, the bulky correlator Malvern K7025 will be replaced by a correlator card which can be fitted inside the PC and full automation of the data collection and analysis process will be implemented.

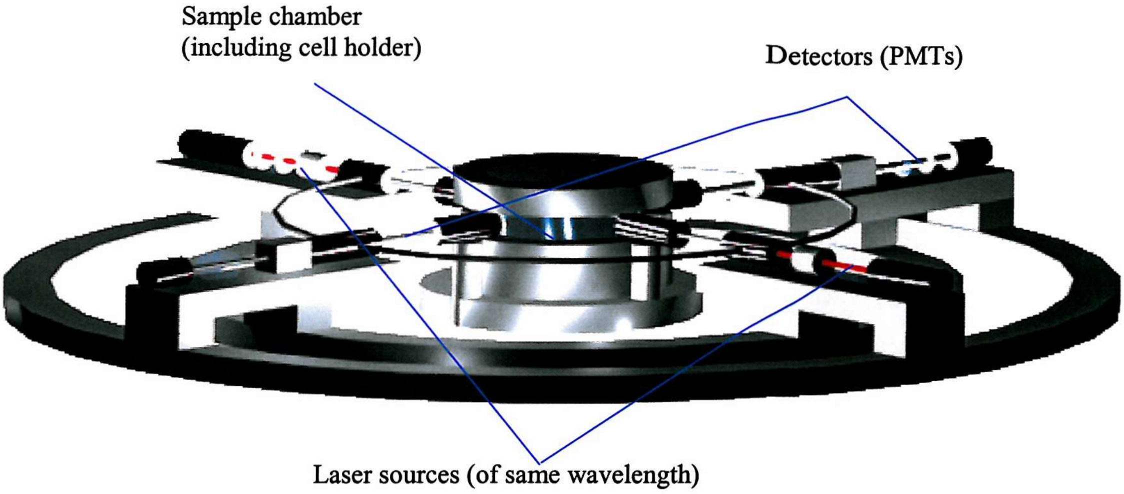

Figure 7.1: New proposed design for the light scattering spectrometer.

Figure 7.2: New sample holder.

7.2.2 Bimesogens for the flexoelectric effect

Further investigation is necessary to fully characterise the achiral bimesogens based on the molecular template FFBOnOBFF and to design new dimers with improved flexoelectric properties.

On-going work is focused on the measurement of the splay elastic constant k_{11} for these systems in order to estimate the average flexoelectric coefficient e from the following expression:

$$\tan\phi = \frac{eP_0E}{2\pi k}. \qquad (7.1)$$

Although this equation describes the flexoelectric effect in chiral nematics, the average of splay and bend elastic constant k is assumed to be the same as for the achiral mixture. The technique used is the electric field Freedericksz transition, which also requires accurate measurements of the dielectric anisotropy $\Delta\varepsilon$.

The conformational changes and distribution occurring in our dimers are still not well understood. The order parameter S of the cyanobiphenyl bimesogens CBOnOCB has been estimated to be between 0.52 and 0.66 for temperatures ranging from 10 °C to 63 °C below T_{NI}.[7] This demonstrates the high degree of orientational order in the nematic phase that can be achieved with these dimers. However, the Maier and Nehring's prediction that the elastic constants scale as S^2 is not valid any longer for the bimesogens.[8] This shows the need to develop new theories that take into account the specific properties of these materials; for instance in their model, Terentjev and Petschek introduced a stiffness parameter to describe the degree of flexibility of the spacer and also an angle between the two mesogenic units forming the dimer.[9] They predicted that the ratio $k_{22}/k_{11} \approx 1/3$ for a rigid odd or even spacer independent of temperature, which agrees with experimental findings. In addition, for a flexible spacer, their theory confirms that for an odd spacer dimer, the bend elastic constant should be significantly reduced for an angle of at least 20° between the two mesogens.

New achiral and asymmetrical dimers, combining the difluorobiphenyl moiety with the cyanobiphenyl mesogenic unit, have been synthesised with n = 9 and n = 10 methylene groups in their spacers;[10] their generic structure is given in Figure 7.3. These materials exhibit the highest values of flexo-elastic ratios reported so far; e/k are respectively 1.25 and 0.6 $C.N^{-1}.m^{-1}$ for n = 9 and n = 10 for the chiral-doped mixtures. Furthermore, smaller pitch and thus higher critical field for the helix unwinding result in larger rotation angles for the odd dimer compared to the even one for a given concentration of chiral additive; for instance, the maximum angle achieved at $T_{N*I}-T = 20$ °C is 21° for n = 9 and 12° for n = 10.

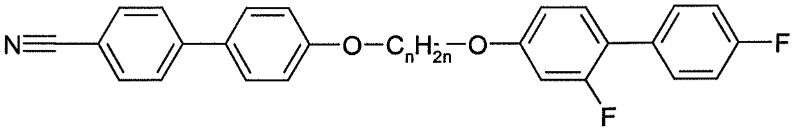

Figure 7.3: Molecular structure of the asymmetric bimesogens.

7.2.3 Bimesogenic dye-doped systems

The flexoelectric effect in dye guest-host chiral nematic mixtures is currently being investigated. The host dimer used (denoted BO7/9) is based on a mixture of n = 7 and n = 9 spacer of the same difluorobiphenyl bimesogens described in Chapter 6. Two types of bimesogenic dyes have been synthesised and their molecular structures are sketched respectively in Figure 7.4 (a) and (b). They both contain a cyanobiphenyl unit connected via a flexible alkyl spacer to either a nitrostilbene group or a highly miscible perylene dye moiety; the former is a dichroic non-fluorescent dye while the latter is a fluorescent monotropic dye.[11] High concentrations (between 15% and 50%) of either dye have been dissolved in the host BO7/9, although phase separation occurs over time. The rotation angles ϕ are found to vary linearly with applied electric field with gradients slightly different from the value obtained for the host dimers. This may be explained by variations in the helical pitch of the dye-doped mixtures and changes in the elastic constants (compared with the pure host). The values for ϕ are comparable to the ones achieved with the bimesogenic host i.e. $\phi = 22.5°$ for an applied field of about 10 V.μm^{-1}. At the same temperature, the response times are slightly increased upon the addition of either dye.

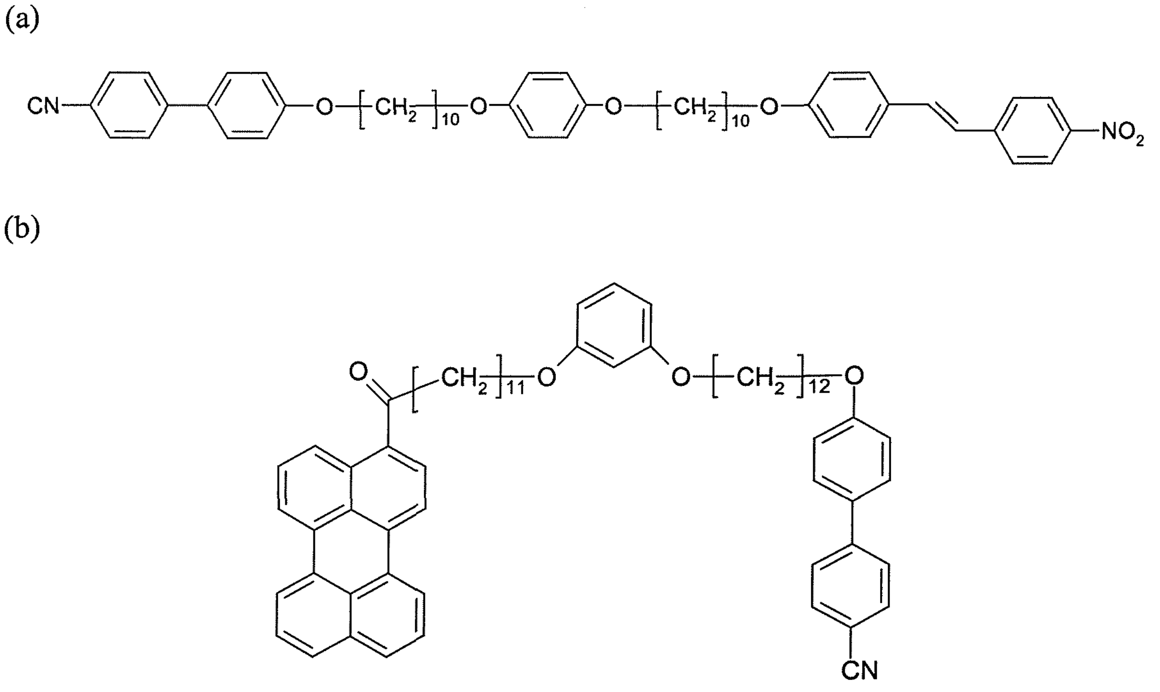

Figure 7.4: Core structures of (a) the nitrostilbene dye (b) the perylene dye.

REFERENCES

[1] DiLisi G. A., Terentjev E. M., Griffin A. C. and Rosenblatt C., *J. Phys. II*, **3**, pp. 597-602 (1993)

[2] Gleeson H. F., Chapter 5 in *Handbook of Liquid Crystals*, **1**, pp. 699-718, edited by Demus D., Goodby J., Gray G. W., Spiess H-W. and Vill V., Wiley-VCH, New-York (1998

[3] Chen G-P., Takezoe H. and Fukuda A., *Liq. Cryst.*, **5(1)**, pp. 341-347 (1989)

[4] Morris S., *Design of a Multi-purpose Light Scattering Experiment for the Investigation of Liquid Crystals*, 1st year PhD report, University of Southampton (2001)

[5] Phillies G. D. J., *Phys. Rev. A*, **24(4)**, pp. 1939-1943 (1981)

[6] Pine D. J., Weitz D. A., Chaikin P. M. and Herbolzheimer E., *Phys. Rev. Lett.*, **60(12)**, pp. 1134-1137 (1988)

[7] Bauman D., Wolarz E. and Bialecka-Florjanczyk, *Liq. Cryst.*, **26**, pp. 45-49 (1999)

[8] Tsvetkov N. V., Zuev V. V., Ksenofontov I. V. and Tsvetkov V. N., *Liq. Cryst.*, **25(6)**, pp. 727-732 (1998)

[9] Di Lisi G. A., Rosenblatt C. and Griffin A. C., *J. Phys. II*, **2**, pp. 1065-1071 (1992)

[10] Blatch A. E., Clarke M. J., Coles M. J. and Coles H. J., *SPIEE Proceedings*, to be published (2002)

[11] P. de Hondt, Peacock M. J. and Coles H. J., *SPIEE Proceedings*, to be published (2002)